BioMed Research International

Molecular Image-Guided Theranostic and Personalized Medicine 2013

Guest Editors: Hong Zhang, Mei Tian, Ignasi Carrio, Ali Cahid Civelek, and Yasuhisa Fujibayashi

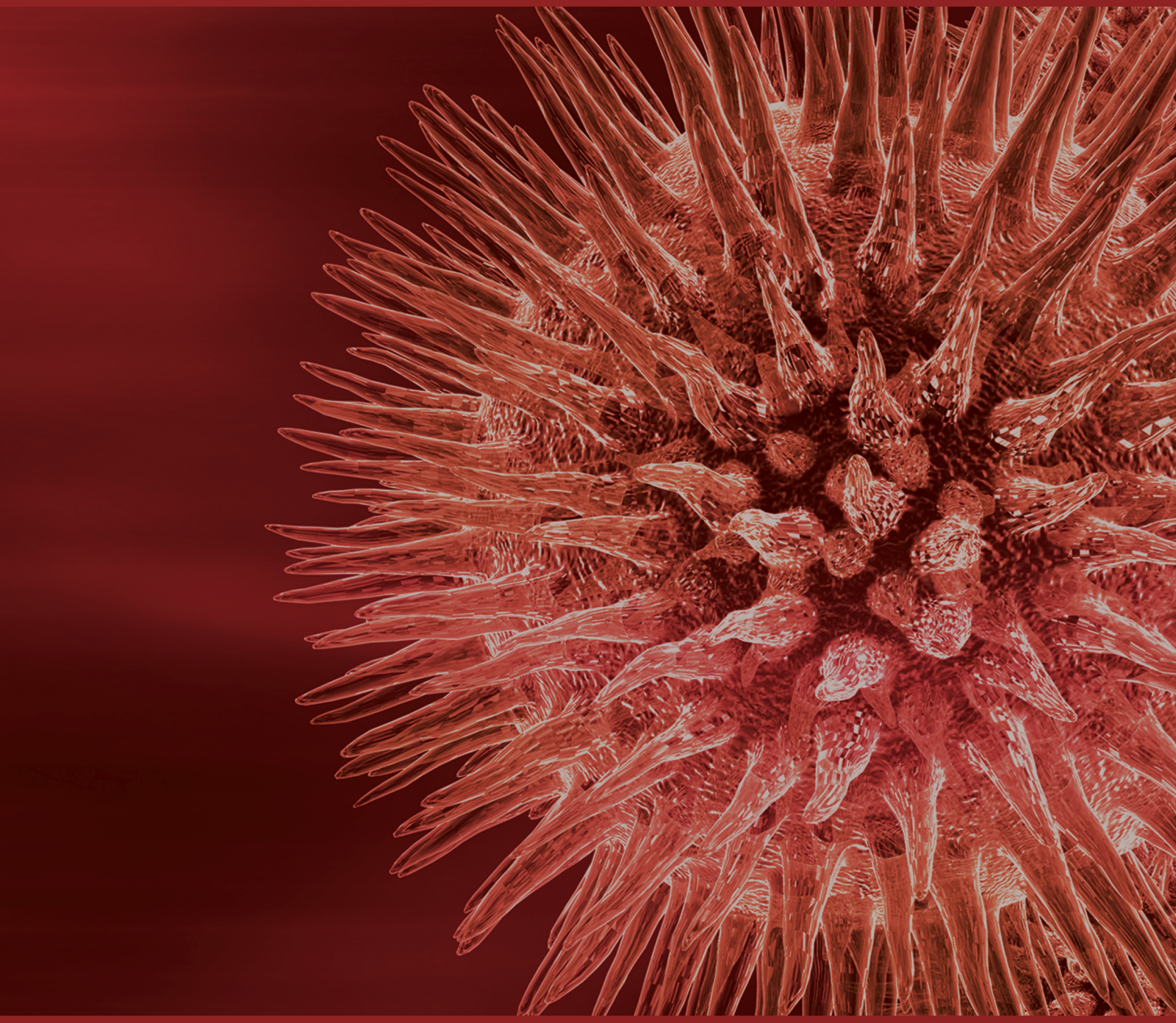

Molecular Image-Guided Theranostic and Personalized Medicine 2013

BioMed Research International

Molecular Image-Guided Theranostic and Personalized Medicine 2013

Guest Editors: Hong Zhang, Mei Tian, Ignasi Carrio, Ali Cahid Civelek, and Yasuhisa Fujibayashi

Contents

Hindawi Publishing Corporation
BioMed Research International
Volume 2014, Article ID 682527, 2 pages
http://dx.doi.org/10.1155/2014/682527

Editorial

Molecular Image-Guided Theranostic and Personalized Medicine 2013

Hong Zhang,[1] Mei Tian,[2] Ignasi Carrio,[3] Ali Cahid Civelek,[4] and Yasuhisa Fujibayashi[5]

[1] *The Second Affiliated Hospital of Zhejiang University, Hangzhou, Zhejiang 310009, China*
[2] *Hangzhou Binjiang Hospital of Zhejiang University, Hangzhou, Zhejiang 310009, China*
[3] *San Paul Hospital, Autonomous University of Barcelona, 08025 Barcelona, Spain*
[4] *University of Louisville Medical Center, Louisville, KY 40202, USA*
[5] *National Institute of Radiological Sciences, Chiba 263-8555, Japan*

Correspondence should be addressed to Hong Zhang; hzhang21@gmail.com

Received 22 April 2014; Accepted 22 April 2014; Published 29 May 2014

Molecular imaging differs from traditional imaging in that imaging agents or probes enable the visualization of the cellular or molecular function and followup of the molecular process in living subjects. It has been shown to be an effective noninvasive technology on improving diagnosis, prognosis, planning, and monitoring of personalized medication. Molecular imaging is a diverse technology which includes various modalities, for instance, positron emission tomography (PET), single photon emission computed tomography (SPECT), magnetic resonance imaging (MRI), computed tomography (CT), ultrasound (US), and optical imaging (Raman, quantum dots, bioluminescence, photoacoustic imaging, etc.). In the era of personalized theranostics (therapeutics and diagnostics), molecular imaging with the specific probe(s) would allow the clinical physicians to select the right patients for the appropriate treatment.

Topics covered in this special issue include advances in biomarkers in preclinical drug discovery, molecular imaging modalities in disease management, image-guided therapy approach of diseases, and imaging technology in drug development. For example, Dr. Z. Cheng's group at Stanford University reported an Affibody molecule, Ac-Cys-$Z_{EGFR:1907}$, targeting the extracellular domain of epidermal growth factor receptor (EGFR), which was newly developed and used for detection of hepatocellular carcinoma (HCC). They observed that EGFR-expressing HCC lesions could be specifically detected by Ac-Cys-$Z_{EGFR:1907}$. PET imaging might have better diagnostic value than optical imaging based on the same Affibody. The early and sensitive detection of HCC based on molecular cancer markers, such as EGFR, is a critical step in improving the currently dismal prognosis of HCC patients. Dr. H. Ma et al. presented a comparison study on ^{99m}Tc-N-DBODC5 and ^{99m}Tc-MIBI in patients with coronary artery disease. Their study results demonstrated that ^{99m}Tc-N-DBODC5 and ^{99m}Tc-MIBI MPI provide comparable diagnostic information for patients undergoing exercise rest for detection of CAD. In addition, ^{99m}Tc-N-DBODC5 does not exhibit the disadvantages of ^{99m}Tc-MIBI in their study.

Stem cell therapy is a promising therapeutic approach for some human major diseases. Molecular imaging plays an important role in terms of noninvasive, in vivo trafficking and evaluation of short-term or long-term therapeutic response. In this issue, molecular imaging in stem cell therapy for spinal cord injury and stroke were reviewed by F. Song et al. and F. Chao et al., who provided up-to-date information and future perspectives on these hot topics. Recently, molecular imaging, especially PET, has been introduced to evaluate the functional or metabolic changes in cerebral ischemia after administration of traditional Chinese medicine. Most of these works were done by the group from the Second Hospital of Zhejiang University School of Medicine. Z. Wang et al. from the same group reviewed molecular imaging in applications of traditional Chinese medicine in neurological disease.

New technologies, such as microfluidics for synthesis of PET tracers and acoustic droplet vaporization, were included

in this special issue. Over the last decade, microfluidics and lab-on-a-chip (LOC) technology have boomed as powerful tools in the field of organic chemistry, which potentially provides significant help to the PET chemistry. Microfluidic radiolabeling technology and its application for synthesis of peptide-based PET tracers are summarized and discussed in the review paper by Dr. Y. Liu et al. Acoustic droplet vaporization (ADV) is a physical process in which the pressure waves of ultrasound induce a phase transition that causes superheated liquid nanodroplets to form gas bubbles. The bubbles provide ultrasonic imaging contrast and other functions. C.-Y. Lin and W. G. Pitt reviewed the literature regarding the use of ADV in clinical applications of imaging, embolic therapy, and therapeutic delivery.

An interesting study on abacus training in Chinese kids using functional magnetic resonance imaging (fMRI) found that abacus training modulates the neural correlations of exact and approximate calculations. Additionally, findings on the influence of ^{131}I radioablation on the important lymphocytes subtypes of regulatory T and B cells in patients with papillary thyroid carcinoma and the prognostic value of interim and final FDG-PET in major histotypes of B cell NHL patients treated with rituximab-containing chemotherapy have been discussed in this special issue.

In summary, molecular imaging could be applied to target characterization, underlying disease progression, and evaluation of therapeutic response after administration of western medication, stem cell, and traditional medicine. This special issue provides a platform of efficacy of personalized medication from molecular imaging technology which may have high impact on patient care and drug development.

Hong Zhang
Mei Tian
Ignasi Carrio
Ali Cahid Civelek
Yasuhisa Fujibayashi

Hindawi Publishing Corporation
BioMed Research International
Volume 2014, Article ID 759514, 13 pages
http://dx.doi.org/10.1155/2014/759514

Review Article

Molecular Imaging in Stem Cell Therapy for Spinal Cord Injury

Fahuan Song,[1,2,3,4] Mei Tian,[1,2,3,4] and Hong Zhang[1,2,3,4]

[1] *Department of Nuclear Medicine, The Second Affiliated Hospital of Zhejiang University School of Medicine, 88 Jiefang Road, Hangzhou, Zhejiang 310009, China*
[2] *Zhejiang University Medical PET Center, Zhejiang University, 88 Jiefang Road, Hangzhou, Zhejiang 310009, China*
[3] *Institute of Nuclear Medicine and Molecular Imaging, Zhejiang University, 88 Jiefang Road, Hangzhou, Zhejiang 310009, China*
[4] *Key Laboratory of Medical Molecular Imaging of Zhejiang Province, 88 Jiefang Road, Hangzhou, Zhejiang 310009, China*

Correspondence should be addressed to Mei Tian; meitian@gmail.com and Hong Zhang; hzhang21@gmail.com

Received 26 July 2013; Accepted 9 December 2013; Published 19 February 2014

Academic Editor: Ali Cahid Civelek

Spinal cord injury (SCI) is a serious disease of the center nervous system (CNS). It is a devastating injury with sudden loss of motor, sensory, and autonomic function distal to the level of trauma and produces great personal and societal costs. Currently, there are no remarkable effective therapies for the treatment of SCI. Compared to traditional treatment methods, stem cell transplantation therapy holds potential for repair and functional plasticity after SCI. However, the mechanism of stem cell therapy for SCI remains largely unknown and obscure partly due to the lack of efficient stem cell trafficking methods. Molecular imaging technology including positron emission tomography (PET), magnetic resonance imaging (MRI), optical imaging (i.e., bioluminescence imaging (BLI)) gives the hope to complete the knowledge concerning basic stem cell biology survival, migration, differentiation, and integration in real time when transplanted into damaged spinal cord. In this paper, we mainly review the molecular imaging technology in stem cell therapy for SCI.

1. Introduction

Spinal cord injury (SCI), which results from trauma or progressive neurodegeneration, is a devastating and life-altering injury. It often affects young and healthy individuals who are suffering from severe functional and sensory deficits. This debilitating condition not only creates enormous physical and emotional cost to individuals but also is a significant financial burden to the society. The annual incidence of SCI is 15–40 cases per million worldwidely [1].

SCI is mainly divided into two types: traumatic SCI and nontraumatic SCI. A global-incident rate (2007) of traumatic SCI is estimated at 23 traumatic SCI cases per million [2]. The most common causes of traumatic SCI are road traffic accidents, falls, occupational mishaps, and sports-related injuries [3]. Most SCI occurs at the cervical level (approximately 55%) with a mortality of 10% in the first year following injury and an expected lifespan of only 10 to 15 years after injury. Thoracic, thoracolumbar, and lumbosacral level injury each accounts for approximately 15% of SCI [3].

Despite the progress of medical and surgical management as well as rehabilitation approaches, many SCI patients still experience substantial neurological disabilities [4, 5]. Moreover, clinical trials of pharmacologic therapeutics within the last two decades have either failed to prove efficacy or provided only modest reductions in functional deficits [6–8].

Previous researches on SCI mainly focused on improving neurological manifestations of SCI while ignoring the pathological changes of spinal cord. According to the progress, SCI could be divided into primary injury phase which is the physical injury and secondary injury phase [9, 10]. The primary injury phase damages both upper and lower motor neurons and disrupts sensory, motor, and autonomic (including respiration, cardiac output, and vascular tone) functions. The secondary injury phase is the amplification of the original injury with a subsequent cascade of molecular and cellular events [11]. Pathophysiological processes occur after the primary injury phase and are rapidly instigated in response to the primary injury in order to control and minimize the damage. However, these are largely responsible

for exacerbating the initial damage and creating an inhibitory microenvironment which prevent endogenous efforts of regeneration and remyelination. Such secondary processes include ischemia, inflammation, lipid peroxidation, disruption of ion channels, fluid and electrolyte disturbances, producing of free radicals, axonal demyelination, necrosis, glial scar formation, and apoptosis [12, 13]. Nevertheless, endogenous repair and regeneration happen during the secondary phase of SCI to minimize the extent of the lesion, reorganize blood supply through angiogenesis, clear cellular debris, reunite and remodel damaged neural circuits, and offer exploitable targets for therapeutic intervention [14, 15]. Thus, these secondary damages are crucial to SCI therapy.

Increasing interest has focused on the development of innovative therapeutic methods that aim to regenerate damaged CNS tissue by taking advantages of recent advances in stem cell and neuroscience research [25, 26]. Preclinical models demonstrated that stem cell transplantation could ameliorate some secondary events of SCI through neuroprotection and restore lost tissue through regeneration [27]. Cumulative researches have demonstrated the feasibility of stem cell therapy and various stem cells have been used to protect against the secondary damage with enhancing the regeneration of a damaged spinal cord. Thus, stem cell transplantation would be one of the promising approaches for the regeneration of an injured spinal cord [28].

Recent studies suggested that stem cell therapy could improve neural function in SCI by replacing damaged cells [29, 30]. Therefore, it becomes more and more important to explore the detailed mechanisms of stem cell therapy for SCI and monitor the fate of these cells *in vivo*, including survival, migration, distribution, rejection, integration, and differentiation.

Fortunately, molecular imaging gives an effective way for such research. Well-established imaging modalities used by researchers for the purpose of molecular imaging are positron emission tomography (PET), magnetic resonance imaging (MRI), whereas others have employed newer modalities based on the transmission of light through tissues, such as *in vivo* bioluminescence imaging (BLI) and fluorescence imaging (FLI). The label of stem cells requires labelling methods making grafted cells distinguishable from host cells to follow transplanted stem cells by the above methods.

PET is a nuclear imaging technique that produces a three-dimensional image or picture of functional processes in the body. The system detects pairs of gamma rays emitted indirectly by a positron-emitting radionuclide (tracer), which is introduced into the body on a biologically active molecule. It can provide metabolic changes and be used for tracing radioactively labeled stem cells *in vivo*. MRI can be used for noninvasive tracking of transplanted cells which are usually labeled with super-paramagnetic nanoparticles as contrast agents in longitudinal studies on living animals. Gadolinium and ferric oxide are two common contrast media used for cell labeling in MRI [31]. Recently, there were several studies using MRI to trace the transplanted stem cells in SCI models [32–34]. Their results showed that the transplanted stem cells could be readily detected *in vivo* using noninvasive MRI techniques. BLI is a newly developing technology for dynamically observing biological behavior. It is based on an enzymatic light production system. The enzyme in action is a luciferase which uses the substrate luciferin to produce light. Then the emitted light is subsequently captured by a highly sensitive CCD camera. Using this technology, cells should be transgenically modified to steadily express luciferase. Then, cells can be tracked in a long periods of time because luciferase expression is preserved during proliferation so that all cells and their descendants express luciferase without dilution. Thus, we can observe the stem cells' dynamic behavior *in vivo* through this method.

2. Stem/Progenitor Cell Therapy in SCI

2.1. Mechanism of Stem Cell Therapy. According to the pathophysiological targets of SCI, transplanted cells should satisfy the following requirements. Firstly, enable regenerating axons to cross any cysts or cavities; secondly, functionally replace dead cells; thirdly, create an environment to support axonal regeneration and myelination. Stem or progenitor cells are capable of modifying the lesion environment, providing structural support, myelination, increasing neurotrophic factors for neuroprotection, and endogenous activation [35–38]. As a result, stem cells have potential for remyelinating lesions and are an attractive cell source for cell therapy of SCI. And recent experimental studies suggested that stem cell therapy can improve neural function in SCI (Table 1). The opportunity to enhance endogenous adaptability through cell-based approaches has led to a great interest in developing stem cell transplantation therapies that could potentiate and synergise with other treatment modalities to maximise neuroplasticity and produce meaningful recovery.

Characteristics and purported mechanisms of action of stem cells will then be discussed, with specific attention paid to axonal regeneration and regrowth, growth factor release, guidance through inhibitory cues, remyelination, and induction of anatomical neuroplasticity.

2.2. Bone Marrow Stem Cells. Transplantation of bone marrow-derived mesenchymal stem cells (BMSCs) for SCI has been previously reviewed [39–43]. Many studies have examined BMSCs in SCI rodents and the results showed improved locomotor recovery [44–46].

There are two types of adult bone marrow stem cells: hematopoietic stem cells (HSCs) and mesenchymal stem cells (MSCs). Zhu et al. compared various properties of human umbilical cord-derived MSCs (HUCMSCs) with human placenta-derived MSCs (HPDMSCs), including cell proliferation, apoptosis, cellular morphology, ultrastructure, and their ability to secrete various growth factors. Their findings indicate that different sources of MSCs have different properties and that care should be taken when choosing the appropriate sources of MSCs for stem cell transplantation [47]. In rodent studies, BMSCs was able to promote a certain degree of axonal regrowth and sprouting, at least in transection models [48]. Lee et al. have used human umbilical cord blood derived mesenchymal stem cells (hUCB-MSCs) to treat dogs with SCI and observed its long-term effects on

Table 1: Stem cell-based cell therapy in experimental SCI models.

Cell type	Cell number	Route	Time after SCI	Weeks after cell injection	Host animal	Cotreatment method	Functional outcome	References
BMSCs	5×10^6	IL	24 h	3	Rabbit	BMSCs were Ngb gene-modified	Significant functional improvement	[16]
OPCs	5×10^5	IL	3 d	4	Rat	No	Functional improvements in SSEP amplitudes and latencies	[17]
iPSC-NS/PCs	1×10^6	IL	9 d	12	Marmoset	No	Promoted functional recovery	[18]
NSCs + OECs	3×10^5	IL	Immediately	4	Rat	Cotransplantation of NSCs and OECs	Improve sensory function	[19]
ESCs	5×10^5	IV	2 h	4	Mice	No	Promoted hind-limb recovery	[20]
iPSCs	5×10^5	IL	9 d	6	Mice	No	Promoting locomotor function recovery	[21]
NS/PCs	8×10^4	IL	9 d	8	Rat	Coinjected with HAMC	Enhanced tissue benefit and functional recovery	[22]
EMSCs	5×10^4	IL	0.5 h	12	Rat	Coinjected with fibrin scaffolds	Improve the behavioral and histological recovery	[23]
BMSCs	1×10^7	IL	7 d	4	Dog	No	Improved functional recovery	[24]

IL: intralesional injection, IT: intratheca injection, IV: intravenous injection, BMSCs: bone marrow mesenchymal stem cells, Ngb: neuroglobin, SSEPs: somatosensory evoked potential, iPSC-NS/PCs: induced pluripotent stem cell-derived neural stem/progenitor cells, HUCBCs: human umbilical cord blood cells, hES: transplanted human embryonic stem, OPCs: cell-derived oligodendrocyte progenitor cells, ESCs: embryonic stem cells, iPSCs: induced pluripotent stem cells, NSPCs: neural stem/progenitor cells, HAMC: hydrogel blend of hyaluronan and methyl cellulose, and EMSCs: ectomesenchymal stem cells.

dogs. It was found that hind-limb recovery in 4 dogs among the five transplanted dogs was significantly improved and the results suggest that transplantation of hUCB-MSCs may have beneficial therapeutic effects [49].

The grafting of MSCs to treat SCI has shown promising results in animals; however, less is known about the effects of autologous MSCs in human SCI. Park et al. explored 10 SCI patients who underwent intramedullary direct MSCs transplantation into injured spinal cords. All patients did not experience any permanent complication associated with MSC transplantation. Three patients showed gradual improvement in activities of daily living, changes on magnetic resonance imaging such as decreases in cavity size and the appearance of fiber-like low signal intensity streaks, and electrophysiological improvement [50].

Despite these potential benefits, there are reported adverse effects of MSCs, such as increased recurrence of hematological malignancies and enhanced tumor growth and metastases [41, 51, 52]. And more preclinical trials of MSC-based therapy need to be preformed.

2.3. Neural Stem Cells and Neural Progenitor Cells. Neural stem cells (NSCs) have been classified as a kind of neural lineage stem cell which is able to self-renew and to give rise to all types of mature neural cells including neurons, astrocytes, and oligodendrocytes [53, 54]. The isolation of adult neural stem cells in mammals was first reported in 1992 by Reynolds and Weiss [55]. NSCs for therapeutic applications are derived from ESCs and progenitor cells are isolated from fetal tissue. Neural progenitor cells (NPCs), like stem cells, have a tendency to differentiate into a specific type of cells.

NSCs and NPCs are found in both fetal and adult CNS [56]. Adult NPCs can be typically harvested from the subventricular zone of the brain or the spinal cord. Embryonic NPCs can be taken from the CNS of rodent embryos and expanded as neurospheres. They all contain precursors for neurons, astroglia, and oligodendrocytes plus stem cells capable of self-renewal [57]. Salazar and his colleagues injected human neural stem cells (hCNS-SCns) into immunodeficient NOD-scid mice 30 days after spinal cord contusion injury in order to test the ability of hCNS-SCns to survive, differentiate, migrate, and promote improved locomotor recovery [54]. They found that hCNS-SCns can survive, differentiate, and promote locomotor recovery when transplanted into an early chronic injury microenvironment. These results suggest that hCNS-SCns graft has efficacy in an early chronic SCI location and expands the "window of opportunity" for intervention.

The extent of glial scar formation and the characteristics of inflammation are the most remarkable difference in the injured spinal cord microenvironment between the subacute and chronic phases. By contrast, the distribution of chronically grafted NSPCs was restricted compared to NSPCs grafted at the subacute phase because a more prominent glial

scar located around the lesion epicenter enclosed the grafted cells. Therefore, glial scar formation and inflammatory phenotype should be considered in order to achieve functional recovery by NSPCs transplantation in cases at the chronic phase [58]. Another study showed that grafted NSPCs mainly differentiate into astrocytes after transplantation at the acute phase [59]. Inflammatory cytokines, such as IL-6, TNF-α, and CXCL1, also increase remarkably in the injured spinal cord [60]. These cytokines might induce NSPCs to differentiate into astrocytes. Furthermore, growth factors like EGF and NT3 have demonstrated beneficial effects on the survival of NSPCs [61, 62].

When transplanted into mice in an animal model of SCI, human NSCs promoted locomotor recovery [63]. The study of Mothe indicated that multipotent NSPCs can be delivered from the adult human spinal cord of organ transplant donors and that these cells differentiate into both neurons and glia following transplantation into rats with SCI [64]. In addition, human fetal brain modified NSPCs transplanted subacutely into the contused cervical spinal cord of adult common marmosets produced significantly greater grip strength than controls [65]. Researchers have shown that these NSCs and NPCs primarily differentiate into oligodendrocytes *in vitro* [66] and *in vivo* [67, 68]. Recently, researchers demonstrated that self-renewing multipotent NSCs and NPCs could be acquired from the adult human spinal cord of organ transplant donors and that these cells differentiate into both neurons and glia following transplantation into rats with SCI [64].

Simultaneously, the aims of axonal regeneration through the injury area have been replaced preclinically by more realistic objectives of remyelination and provision of trophic support for endogenous precursors and axons. It makes NPCs much more promising candidates of cell therapy for SCI and probably heralds their increased use in clinical trials.

2.4. Embryonic Stem Cells. Embryonic stem cells (ESCs) are pluripotent cells derived from the inner cell mass of developing blastocyst embryos that can differentiate into nearly all cell types [69]. Notably, ESCs have great developmental plasticity and can be induced to become NSPCs with specific differentiation potentials, making them a major candidate of cell replacement therapies for SCI. Mcdonald et al. transplanted neural differentiated mouse embryonic stem cells into rats' spinal cord after traumatic injury. The cells that transplanted into the injured spinal cord differentiated into neurons, astrocytes, and oligodendrocytes and showed partial functional recovery [70]. As noted above, SCI causes extensive demyelination and oligodendrocytes are particularly vulnerable to apoptosis. ESCs predifferentiated into oligodendrocyte progenitor cells (OPCs) remyelinated spared axons and improved recovery when transplanted subacutely into the injured rat spinal cord [71, 72]. The studies document the feasibility of predifferentiating hESCs into functional OPCs and demonstrate their therapeutic potential after SCI.

2.5. Induced Pluripotent Stem Cells. The discovery of induced pluripotent stem cells (iPSCs) has opened a new potential therapeutic approach for regenerative neuroscience, although iPSCs have not yet been used clinically in SCI cell therapy. iPSCs were developed in 2006 by Takahashi and Yamanaka, who showed that mouse somatic cells, such as fibroblasts, could be reprogrammed to pluripotency with retroviral expression of four transcription factors OCT4, SOX2, KLF4, and c-MYC and achieve similar morphology, pluripotency, self-renewal, and gene expression as ESCs, without the requirement for an embryo [73].

The clinical use of ESCs is complicated; however, by ethical and immunological concerns, both of which might be overcome by using pluripotent stem cells which can be derived directly from a patient's own somatic cells [74]. Experimental studies using iPSCs-derived neurospheres transplanted subacutely after contusion SCI showed remyelination, axonal outgrowth of serotonergic fibers, and promotion of locomotor recovery.

Different kinds of iPSCs have different performance in SCI treating. Transplantation of "unsafe" iPS-derived neurospheres may result in teratoma formation and sudden loss of locomotor function [21]. Kramer's review highlights emerging evidence that suggests that iPSCs are not necessarily indistinguishable from ESCs and may occupy a different "state" of pluripotency with differences in gene expression, methylation patterns, and genomic aberrations which may reflect incomplete reprogramming and may therefore impact on the regenerative potential of these donor cells in therapies [75]. Furthermore, the first study on iPSC-derived chimeric mice demonstrated that they were prone to cancer and attributed this property to the reexpression of the c-myc reprogramming factor [76]. In brief, iPSCs are likely to carry a higher risk of tumorigenicity than ESCs, due to the inappropriate reprogramming of these somatic cells, the activation of exogenous transcription factors [77, 78]. Thus, safe iPSC-derived clones would need to be screened and selected [21, 78].

Undifferentiated IPSCs, like ESCs, have high tumourigenicity in pathological conditions [79]. Therefore, the safety of IPSCs should be evaluated before clinical IPSCs-based therapy. Of note, Tsuji et al. recently derived "safe" mouse iPSCs and observed trilineage neural differentiation and functional recovery in a contusion model of SCI without teratoma formation [21].

3. Molecular Imaging in Stem Cell Therapy for Spinal Cord Injury

Transplantation of stem cells has a good prospect of clinical application. However, the challenges in the field of molecular imaging are to develop effective imaging strategies with reporter systems and probes which should firstly reveal cellular and molecular processes throughout an entire study period. Secondly, probes should be highly sensitive to small changes in cell function and distribution. Finally, they do not alter the labeled biological process itself significantly. Molecular imaging technologies will greatly facilitate the functional monitoring and evaluation of a wide range from genes to organs for their roles in health and disease. Herein,

molecular imaging has served as a platform to test stem cell therapy for SCI.

3.1. Stem Cell Labelling. Cell labeling can be divided into two types: physical cell labeling and reporter gene imaging. Physical cell labeling is completed before cell administration and can be accomplished with superparamagnetic iron oxide (SPIO) particles for MRI [83, 84], radionuclide labeling for SPECT [85], and PET, nanoparticle labeling for fluorescent imaging [86]. In reporter gene imaging, a gene coding for the synthesis of a detectable protein is introduced into a target cell line or tissue via viral or nonviral vectors. Because the reporter gene integrates into the host cell's chromosome following stable transfection or transduction, the reporter gene is expressed by progeny. As a result, changes in signals following cell administration can be used as indicators of cell proliferation and cell death [87].

3.2. Positron Emission Tomography. Positron emission tomography (PET) imaging, especially ^{18}FDG PET imaging, has been used mainly in cancer [88–90]. PET uses positron emitting radioisotopes as probes for imaging cells *in vivo* to monitor labeled stem cells and it also has been applied widely to detect and quantify subtle abnormalities in CNS diseases. PET has served as a platform to test stem cell therapy for neurological disease allowing more rapid progression in both preclinical and clinical studies. In order to explore the effect of *in vivo* PET in tracking the stem cells transplanted into spinal cord, Bai et al. transplanted human neural progenitor cells into rabbits' injured spinal cord; rabbits were injected with ^{11}C-raclopride intravenously and then underwent PET imaging [91]. ^{11}C-raclopride PET imaging of the live rabbits showed accumulation of radioactivity at the hNPC-TERT cell injection site with a standard uptake value significantly higher than that of control group (the HeLa cell transplantation group) ($P < 0.01$). ^{11}C-raclopride PET imaging of the isolated spinal cords showed rounded focal image of increased radioactivity in the hNPC-TERT cell transplantation group and linear image of radioactivity without clear border in the HeLa cell transplantation group. Meanwhile, fluorescent microscopy showed the same results. These results suggested that PET with radioisotope labeled tracer is useful for functional studies in developing cell-based therapies.

3.3. Magnetic Resonance Imaging. Magnetic resonance imaging (MRI) is a widely used and powerful imaging technique which can provide high resolution and 3D anatomical imaging. It can be used to evaluate the reparation of the injured spinal cord [92]. For monitoring the efficiency of cell transplantation, cellular homing, or targeting, grafted cells can be labeled with superparamagnetic iron oxide nanoparticles (SPION) and detected by means of MRI. In a study of NPC transplantation, SPIO labeling does not affect NPCs' survival and differentiation potential *in vitro* and labeled NPCs were found migrating along white matter tracts as demonstrated by MRI [93]. In addition, cells labeled with SPION can be manipulated in a magnetic field. In research of Vanecek et al., intrathecally transplanted cells labeled with SPION were guided by a magnetic field and successfully targeted near the lesion site in the rat spinal cord. The results showed that targeting efficiency could be increased by using magnets that produce spatially modulated stray fields [84]. Such magnetic systems with tunable geometric parameters may provide the additional level of control needed to enhance the efficiency of stem cell delivery in injured spinal cord. Hu et al. used labeled human umbilical cord mesenchymal stem cells (hUC-MSCs) *in vivo* for tracking hUC-MSCs' fate with noninvasive MRI [94]. SPIO was added to cultures at concentrations equivalent to 0, 7, 14, 28, and 56 mg Fe/ml and incubated for 16 h. *In vivo* MRI 1 and 3 weeks after injection showed a large reduction in signal intensity in the region transplanted with SPIO-labeled hUC-MSCs. The results showed that noninvasive imaging of transplanted SPIO-labeled hUC-MSCs is feasible. Recently, Amemori et al. used neural stem cell line derived from human fetal spinal cord tissue (SPC-01) to treat a balloon-induced SCI [80]. SPC-01 cells labeled with poly-L-lysine-coated SPION were implanted into the lesion 1 week after SCI. Then T2-weighted images were obtained (Figure 1). The transplanted animals displayed significant motor and sensory improvement 2 months after SCI, when the cells robustly survived in the lesion and partially filled the lesion cavity.

3.4. Optical Imaging. Bioluminescence imaging (BLI) uses luciferase-transduced transplanted cells that can be detected noninvasively *in vivo* by virtue of their reporter gene, which is expressed only when cells are alive [95, 96]. Luciferase (Luc) gene is the most commonly used gene for *in vivo* luminescence which is obtained from the North American firefly. This Luc gene encodes a 550 amino acid protein, Luc. Considering the near absence of endogenous light from mammalian cells and tissues, luciferases have a significant advantage as optical indicators in live mammalian cells and tissues, the inherently low background [97]. It is a powerful tool for the detection of exclusively living grafted cells that stably express luciferase in living animals after administration of luciferin (the substrate of luciferase) in the presence of oxygen and ATP as a source of energy [98]. Using the luciferase reaction *in vivo* as a marker of gene expression requires that the substrate is nontoxic and well distributed to the animals' tissues after exogenously adding (usually via intraperitoneal injection). At present, no humoral immune responses, hepatic toxicity, or germ-line integration were observed in models of luciferase reaction. Studies have also suggested that luciferin could be distributed throughout the entire animal and even could not be restricted by the blood-brain or placental barriers [98]. Previous studies demonstrated that the number of photons which emitted from the labeled cells and transmitted through murine tissues was sufficient to detect 1–2.5 $\times$ 10^3 cells in the peritoneal cavity, 1 $\times$ 10^4 cells at subcutaneous sites, and 1 $\times$ 10^6 circulating cells immediately following injection [99, 100]. Recently, noninvasive bioluminescent imaging was successfully applied to investigate the survival of neural stem/progenitor cells following transplantation into the lesioned mouse spinal cord. It was found that the intralesional application of NSPCs among

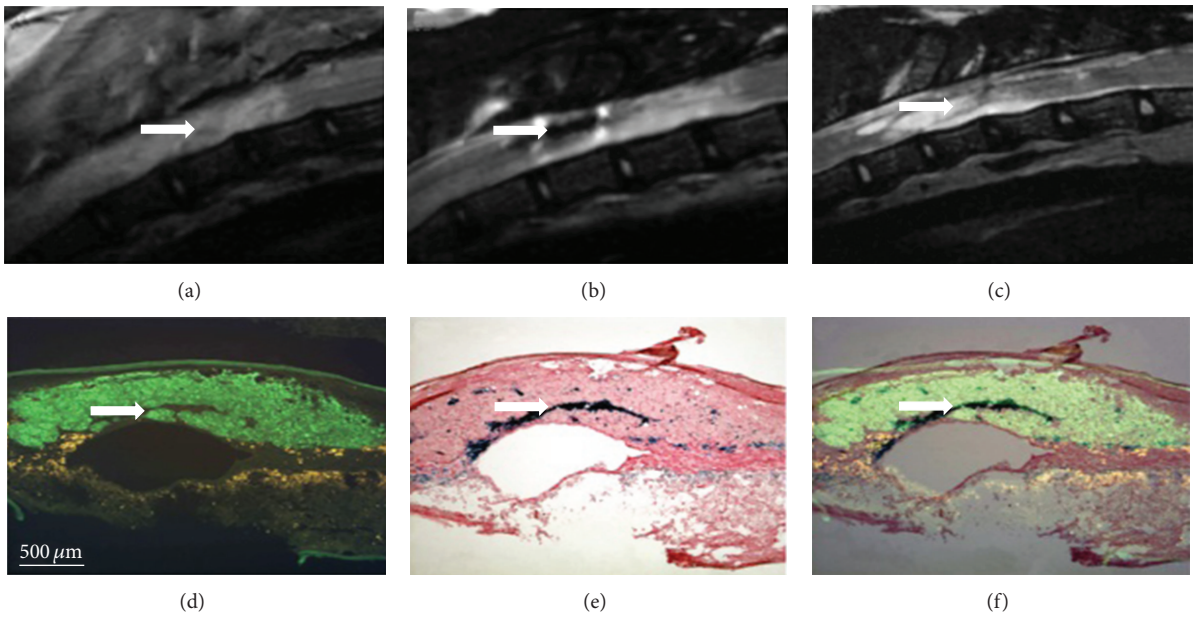

Figure 1: The T2-weighted MR images of the injured rat's spinal cord before and after SPC-01 cell transplantation. The white arrows show labeled transplanted cells and lesion site. (a) The T2-weighted MR images of a spinal cord lesion 5 days after lesion induction before transplantation. (b) Spinal cord with a cell graft 8 weeks after cell transplantation. (c) Control spinal cord lesion 8 weeks after saline injection. (d) Two serial sections were stained with the human mitochondrial marker (MTCO2). (e) The same sections of D were stained with iron. (f) Overlay of MTC02 and iron staining [80].

Table 2: Advantages and limitations of different imaging methods for detection of grafted stem cells (modified from Modo et al. [81] and Spiriev et al. [82]).

Imaging modality	PET	MRI	BLI	FLI
Depth of penetration	No limit	No limit	1-2 mm	<1 mm
Spatial resolution	1-2 mm	10–100 μm	Several mm	2-3 mm
Temporal resolution	sec–min	min–hrs	sec–min	sec–min
Imaging agents	Radionuclide labeled compound	Gadolinium, dysprosium iron oxide particles	Luciferins	Fluorescent protein
Toxicity	No	Yes	No	No
Time range of detection	6–12 months	1-2 months	2–8 weeks	Long-term
Detection limits in terms of cell numbers in vivo	1×10^4–1×10^5	5×10^5–1×10^6	1×10^3–1×10^6	2×10^4–5×10^5

Sec: second, min: minute, and hrs: hours.

3 different procedures (intralesional, intrathecal, and intravenous injection) is the most effective and feasible method for transplanting NSPCs into the SCI site [101]. Okada et al.'s study is a well example of stem cell transplantation study [59]. The third-generation lentiviral vectors enabled efficient transduction and stable expression of both luciferase and a variant of green fluorescent protein in primary cultured NSPCs. Signals from these cells were detectable for up to 10 months or more after transplantation into the injured spinal cords of C57BL/6J mice. Analysis of both acute and delayed transplantation groups revealed drastic reductions in signal intensity within the first 4 days after transplantation, which was followed by a relatively stable bioluminescent signal for 6 wk (Figure 2).

3.5. Multimodality Imaging. No single imaging modality can provide all the information required to track transplanted stem cells and monitor their functional effects. Every imaging modality for stem cell tracing has its own advantages and disadvantages [81, 82] (Table 2). PET has a high sensitivity in tracking biomarkers *in vivo* but lacks the ability of providing detailed anatomic structures. SPIO-labeled stem cells can be detected by means of MRI and get high resolution and 3D anatomical imaging; however, the low sensitivity limits its application on cell tracing. Furthermore, cell division may dilute intracellular markers and then the signals may fail to reflect cells' number and location due to shedding of iron particles [102]. Hence, it is necessary to combine complementary imaging methodologies. Multimodality imaging approaches

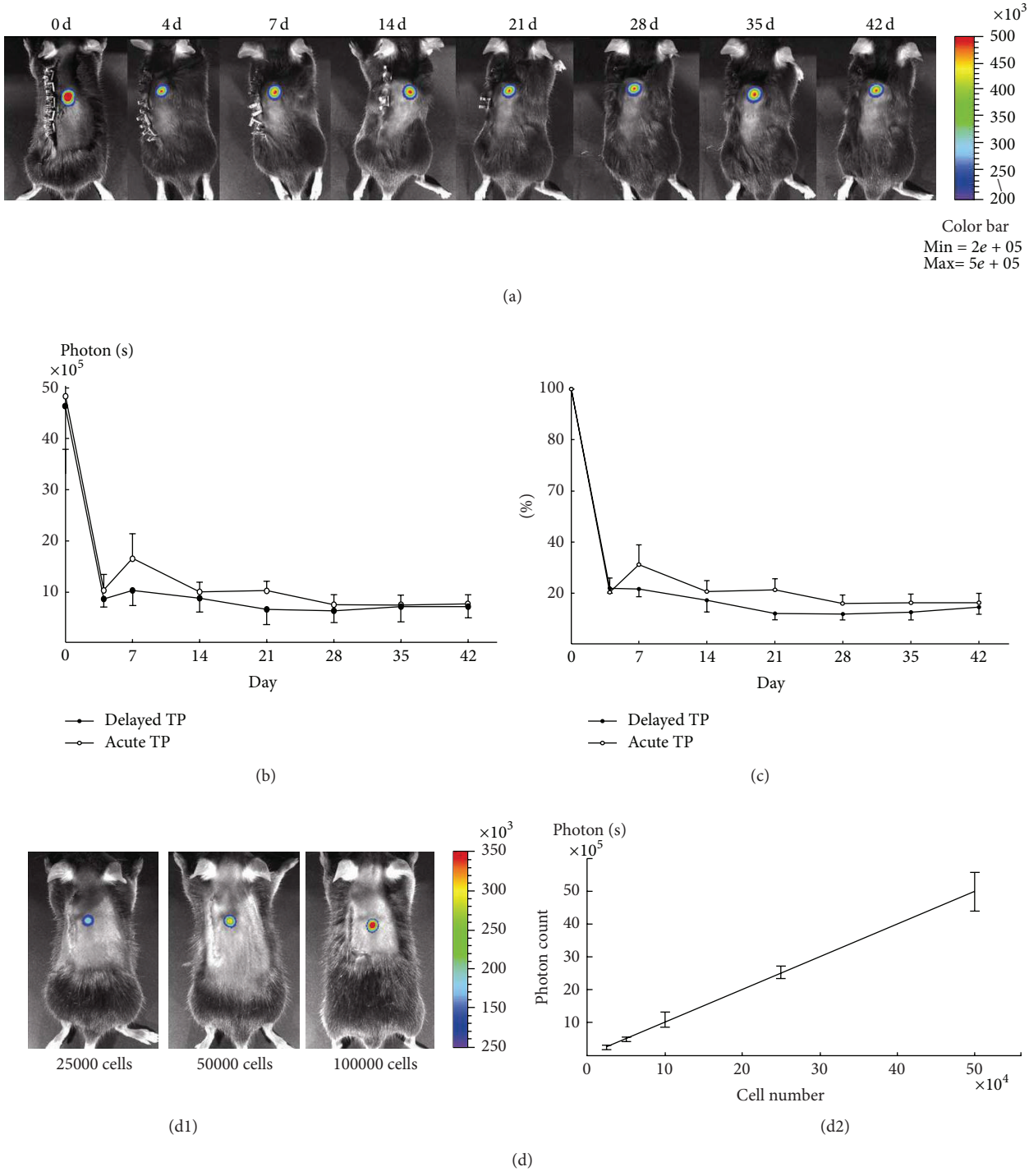

Figure 2: The time course of viability of transplanted NSPCs for SCI. (a) Images of a representative mouse that received acute transplantation (TP) of luciferase-expressing NSPCs confirmed long-term cell viability. Drastic reductions in signal intensity within the first 4 days after transplantation and then relatively stable bioluminescent signals for the following 6 wk were observed in both acute and delayed transplantation groups. There were no differences between acute and delayed transplantation groups in both value of signal intensity (b) and the rate to initial value (c) at each time point. Values are means ± SE ($n = 8$). (d) The correlation between grafted cell numbers and luminescent intensity was confirmed *in vivo*. Values are means ± SE ($n = 4$) [59].

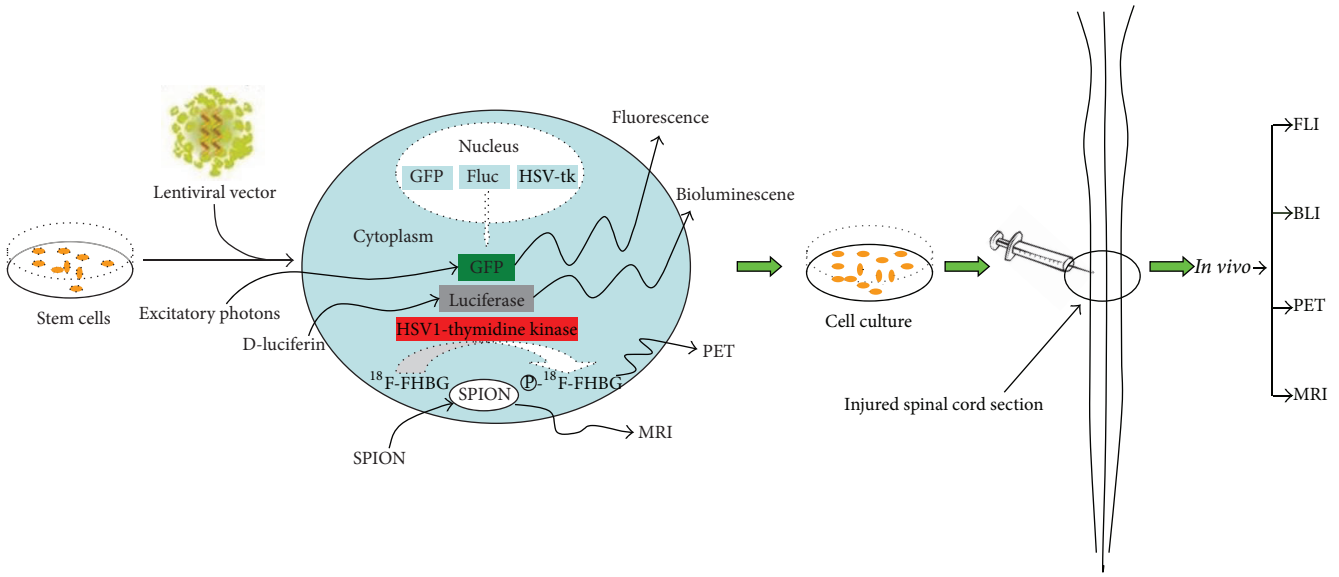

Figure 3: Multimodality of imaging can be applied for tracking stem cell behavior. A work flow chart for labeling cells and introducing labeled cells *in vivo*: firstly, cells are labeled using a marker for positron emission tomography (PET), magnetic resonance imaging (MRI), bioluminescence imaging (BLI), or fluorescence imaging (FLI). Secondly, cells are cultured *in vitro* and injected into the injured spinal cord. Finally, stem cells are then tracked *in vivo* with a camera or scanner.

may minimize the potential drawbacks of using each imaging modality alone and a tailored combination of 2 or more techniques may be the best approach for a given experiment (Figure 3).

Computed tomography (CT) scanners can overcome the lacks of anatomic structures. PET and CT scanners can be used in conjunction to get more detailed, fused images. In a research of Nandoe Tewarie RD, PET was used in combination with CT imaging techniques for longitudinal monitoring of the injured spinal cord. With PET-CT, combined with a simulation-based partial-volume compensation (PVC) method, they can serially measure standardized uptake values of the T9 and T6 spinal cord segments and reveal small, but significant, differences [103]. Because MRI has limitations in determining the viability of labeled transplanted cells, another imaging modality is required. The combination of MRI and PET also allows the acquisition of anatomical, physiological, and metabolic information, all from the same subject [104, 105]. By utilizing CT information acquired by an X-ray detector, the 3-dimensional location can be reconstructed using some bioluminescent tomography (BLT) reconstruction methods such as the adaptive finite element method and Bayesian method [82]. Researchers combined MRI with BLI to simultaneously monitor the location and viability of transplanted cells *in vivo* within the same animal. In recent study, Kim et al. evaluated the therapeutic effects of transplanted human glial precursor cells (hGPs) together with the *in vivo* fate of these cells using MRI and BLI [106]. In order to determine their potential for therapy of multiple sclerosis (MS), they used MRI and BLI side-by-side as complementary imaging techniques to evaluate the effects of transplanted hGPs on experimental autoimmune encephalomyelitis (EAE) pathogenesis. The results demonstrated that intracerebroventricularly (ICV) transplantation of short-lived hGPs can have a remote therapeutic effect through immunomodulation from within the ventricle, without cells directly participating in remyelination.

There are also some problems of nonspecific signals obtained with the different imaging modalities as a result of grafted cells that have died. For example, grafted cells prelabeled with iron oxide nanoparticles that have died post-grafting may result in MRI signals representing macrophage phagocytosis of labeled cell debris. However, PET can use report gene system to avoid such disadvantage, and the high detection sensitivity of PET imaging techniques could offset nonspecific signals of MRI. Hybrid PET/MR imaging might present a formidable technical and suggest potential spinal cord applications exploiting unique properties of the combined instrumentation.

4. Perspective and Summary

The potential of stem cells to reconnect the injured spinal cord and repopulate the area of injury has fascinated SCI researchers. Although some authors believe that endogenous remyelination is effective albeit somewhat slower. The field has learned a great deal about evaluating the fate of stem cells once they are implanted into the cord. How many survive? Do they integrate and migrate? How do they influence the host microenvironment? More and more evidence suggest that the stem cells themselves may be the source of growth factors and have remarkable influence on the injured microenvironment.

The interest in stem cell transplantation for SCI will remain high. This field will obviously continue to evolve, with hopes that further refinement, and understanding will increase the chances that cell transplantation will someday emerge as a fruitful treatment for patients. The complexities of attenuating the tissue damage and secondary complications due to trauma and reconstructing the cytoarchitecture of the injured spinal cord are very challenging. Hopefully, the rapid advances being made in stem cell biology will result in effective experimental and clinical trials of stem cell therapy for SCI.

Molecular imaging is a new discipline which makes it possible *in vivo* of cellular and molecular aspects of pathophysiological processes and therapeutic interventions. PET has high flexibility for the production of specific probes for the detection of different processes in the living subject. However, the production of PET needs advanced chemistry and tight quality control. MRI is also a contending and complementing modality in molecular imaging essential for stem cell studies. It can be used to evaluate the reparation of the injured spinal cord as well as tracing labeled stem cell *in vivo*. Optical imaging has a high molecularly sensitivity, but it provides lesser anatomical localization and is mainly used in small animals.

In summary, the usage of stem cell treatment might restore axonal continuity, connect the area for axonal regeneration, and promote axonal growth back to its distal targets. And the use of a noninvasive imaging method would have the advantage that stem cells transplanting in individual animals can be monitored longitudinally. The multimodality imaging technique allows for studying acute pathological events following a spinal cord lesion, and the development of implanted spinal chamber enables long-term imaging for chronic spinal cord preparations. Therefore, *in vivo* imaging allows the direct observation of dynamic regenerative events of individual stem cells after traumatic injury in the living subject [107]. We predict that future improvement in molecular imaging will make important contributions to our understanding of stem cells' transplantation and allow us to assess the therapeutic effect on a molecular scale.

Abbreviations

SCI: Spinal cord injury
CNS: Center nervous system
PET: Positron emission tomography
MRI: Magnetic resonance imaging
BLI: Bioluminescence imaging
FLI: Fluorescence imaging
CCD: Charge-coupled device
BMSCs: Bone marrow-derived mesenchymal stem cells
HSCs: Hematopoietic stem cells
MSCs: Mesenchymal stem cells
HUCMSCs: Human umbilical cord-derived MSCs
HPDMSCs: Human placenta-derived MSCs
hUCB-MSCs: Human umbilical cord blood derived mesenchymal stem cells
NSCs: Neural stem cells
NPCs: Neural progenitor cells
hCNS-SCns: Human neural stem cells
NSPCs: Neural stem or progenitor cells
NOD-scid: Nonobese diabetic-severe combined immunodeficiency disease
IL-6: Interleukin-6
TNF-α: Tumor necrosis factor-alpha
CXCL1: Chemokine (C-X-C motif) ligand 1
EGF: Epidermal growth factor
NT3: Neurotrophin-3
ESCs: Embryonic stem cells
OPCs: Oligodendrocyte progenitor cells
iPSCs: Induced pluripotent stem cells
OCT4: Octamer-binding transcription factor-4
SOX2: SRY-related high-mobility-group (HMG)-box protein-2
Klf4: Kruppel-like factor-4
c-MYC: Cancer-MYC
SPIO: Superparamagnetic iron oxide
SPECT: Single photon emission tomography
hNPC-TERT: Telomerase-immortalized human neural progenitor cells
SPION: Superparamagnetic iron oxide nanoparticles
hUC-MSCs: Human umbilical cord mesenchymal stem cells
SPC-01: Neural stem cell line derived from human fetal spinal cord tissue
CT: Computed tomography
PVC: Partial-volume compensation
BLT: Bioluminescent tomography
hGPs: Human glial precursor cells
MS: Multiple sclerosis
EAE: Experimental autoimmune encephalomyelitis
ICV: Intracerebroventricularly
IL: Intralesional injection
IT: Intratheca injection
IV: Intravenous injection
Ngb: Neuroglobin
SSEPs: Somatosensory evoked potential
iPSC-NS/PCs: Induced pluripotent stem cell-derived neural stem/progenitor cells
HUCBCs: Human umbilical cord blood cells
hES: Transplanted human embryonic stem
OPCs: Cell-derived oligodendrocyte progenitor cells
HAMC: Hydrogel blend of hyaluronan and methyl cellulose
EMSCs: Ectomesenchymal stem cells
sec: Second
min: Minute
hrs: Hours.

Conflict of Interests

The authors declare that they have no conflict of interests.

Acknowledgments

This work is partly sponsored by Grants from the National Key Basic Research Program of China (2013CB329506), Zhejiang Provincial Natural Science Foundation of China (Z2110230), Health Bureau of Zhejiang Province (2010ZA075, 2011ZDA013), Science and Technology Bureau of Zhejiang Province (2012R10040), National Science Foundation of China (NSFC) (no. 81101023, 81173468, 81271601), and Ministry of Science and Technology of China (2011CB504400).

References

[1] A. Ackery, C. Tator, and A. Krassioukov, "A global perspective on spinal cord injury epidemiology," *Journal of Neurotrauma*, vol. 21, no. 10, pp. 1355–1370, 2004.

[2] B. B. Lee, R. A. Cripps, M. Fitzharris, and P. C. Wing, "The global map for traumatic spinal cord injury epidemiology: update 2011, global incidence rate," *Spinal Cord*, 2013.

[3] L. H. S. Sekhon and M. G. Fehlings, "Epidemiology, demographics, and pathophysiology of acute spinal cord injury," *Spine*, vol. 26, no. 24, supplement, pp. S2–S12, 2001.

[4] C. Morawietz and F. L. Moffat, "The effects of locomotor training after incomplete spinal cord injury: a systematic review," *Archives of Physical Medicine and Rehabilitation*, vol. 94, no. 11, pp. 2297–2308, 2013.

[5] C. Michailidou, L. Marston, L. H. De Souza et al., "A systematic review of the prevalence of musculoskeletal pain, back and low back pain in people with spinal cord injury," *Disability and Rehabilitation*, 2013.

[6] M. B. Bracken, "Steroids for acute spinal cord injury," *Cochrane Database of Systematic Reviews*, no. 3, Article ID CD001046, 2002.

[7] E. Esposito and S. Cuzzocrea, "Anti-TNF therapy in the injured spinal cord," *Trends in Pharmacological Sciences*, vol. 32, no. 2, pp. 107–115, 2011.

[8] T. S. Jensen, C. S. Madsen, and N. B. Finnerup, "Pharmacology and treatment of neuropathic pains," *Current Opinion in Neurology*, vol. 22, no. 5, pp. 467–474, 2009.

[9] C. H. Tator, "Update on the pathophysiology and pathology of acute spinal cord injury," *Brain Pathology*, vol. 5, no. 4, pp. 407–413, 1995.

[10] J. W. McDonald and C. Sadowsky, "Spinal-cord injury," *The Lancet*, vol. 359, no. 9304, pp. 417–425, 2002.

[11] C. H. Tator and M. G. Fehlings, "Review of the secondary injury theory of acute spinal cord trauma with emphasis on vascular mechanisms," *Journal of Neurosurgery*, vol. 75, no. 1, pp. 15–26, 1991.

[12] J. Li and G. Lepski, "Cell transplantation for spinal cord injury: a systematic review," *BioMed Research International*, vol. 2013, Article ID 786475, 32 pages, 2013.

[13] N. Zhang, Y. Yin, S.-J. Xu, Y.-P. Wu, and W.-S. Chen, "Inflammation & apoptosis in spinal cord injury," *Indian Journal of Medical Research*, vol. 135, no. 3, pp. 287–296, 2012.

[14] L. I. Benowitz and P. G. Popovich, "Inflammation and axon regeneration," *Current Opinion in Neurology*, vol. 24, no. 6, pp. 577–583, 2011.

[15] S. Thuret, L. D. F. Moon, and F. H. Gage, "Therapeutic interventions after spinal cord injury," *Nature Reviews Neuroscience*, vol. 7, no. 8, pp. 628–643, 2006.

[16] W. P. Lin, X. W. Chen, L. Q. Zhang et al., "Effect of neuroglobin genetically modified bone marrow mesenchymal stem cells transplantation on spinal cord injury in rabbits," *PLoS One*, vol. 8, no. 5, Article ID e63444, 2013.

[17] A. H. All, F. A. Bazley, S. Gupta et al., "Human embryonic stem cell-derived oligodendrocyte progenitors aid in functional recovery of sensory pathways following contusive spinal cord injury," *PLoS One*, vol. 7, no. 10, Article ID e47645, 2012.

[18] Y. Kobayashi, Y. Okada, G. Itakura et al., "Pre-evaluated safe human iPSC-derived neural stem cells promote functional recovery after spinal cord injury in common marmoset without tumorigenicity," *PLoS One*, vol. 7, no. 12, Article ID e52787, 2012.

[19] Y. Luo, Y. Zou, L. Yang et al., "Transplantation of NSCs with OECs alleviates neuropathic pain associated with NGF down-regulation in rats following spinal cord injury," *Neuroscience Letters*, vol. 549, pp. 103–108, 2013.

[20] D. Bottai, D. Cigognini, L. Madaschi et al., "Embryonic stem cells promote motor recovery and affect inflammatory cell infiltration in spinal cord injured mice," *Experimental Neurology*, vol. 223, no. 2, pp. 452–463, 2010.

[21] O. Tsuji, K. Miura, Y. Okada et al., "Therapeutic potential of appropriately evaluated safe-induced pluripotent stem cells for spinal cord injury," *Proceedings of the National Academy of Sciences of the United States of America*, vol. 107, no. 28, pp. 12704–12709, 2010.

[22] A. J. Mothe, R. Y. Tam, T. Zahir, C. H. Tator, and M. S. Shoichet, "Repair of the injured spinal cord by transplantation of neural stem cells in a hyaluronan-based hydrogel," *Biomaterials*, vol. 34, no. 15, pp. 3775–3783, 2013.

[23] J. Liu, Q. Chen, Z. Zhang et al., "Fibrin scaffolds containing ectomesenchymal stem cells enhance behavioral and histological improvement in a rat model of spinal cord injury," *Cells, Tissues, Organs*, vol. 198, no. 1, pp. 35–46, 2013.

[24] D.-I. Jung, J. Ha, B.-T. Kang et al., "A comparison of autologous and allogenic bone marrow-derived mesenchymal stem cell transplantation in canine spinal cord injury," *Journal of the Neurological Sciences*, vol. 285, no. 1-2, pp. 67–77, 2009.

[25] D. Drago, C. Cossetti, N. Iraci et al., "The stem cell secretome and its role in brain repair," *Biochimie*, vol. 95, no. 12, pp. 2271–2285, 2013.

[26] R. A. Barker, "Stem cells and neurodegenerative diseases: where is it all going?" *Regenerative Medicine*, vol. 7, no. 6, supplement, pp. 26–31, 2012.

[27] H. Q. Cao and E. D. Dong, "An update on spinal cord injury research," *Neuroscience Bulletin*, vol. 29, no. 1, pp. 94–102, 2013.

[28] J. Hernández, A. Torres-Espín, and X. Navarro, "Adult stem cell transplants for spinal cord injury repair: current state in preclinical research," *Current Stem Cell Research and Therapy*, vol. 6, no. 3, pp. 273–287, 2011.

[29] G. Kumagai, P. Tsoulfas, S. Toh, I. McNiece, H. M. Bramlett, and W. D. Dietrich, "Genetically modified mesenchymal stem cells (MSCs) promote axonal regeneration and prevent hypersensitivity after spinal cord injury," *Experimental Neurology*, vol. 248, pp. 369–380, 2013.

[30] J. Liu, D. Han, Z. Wang et al., "Clinical analysis of the treatment of spinal cord injury with umbilical cord mesenchymal stem cells," *Cytotherapy*, vol. 15, no. 2, pp. 185–191, 2013.

[31] L. Yan, Y. Han, Y. He et al., "Cell tracing techniques in stem cell transplantation," *Stem Cell Reviews*, vol. 3, no. 4, pp. 265–269, 2007.

[32] J. Guenoun, A. Ruggiero, G. Doeswijk et al., "In vivo quantitative assessment of cell viability of gadolinium or iron-labeled cells using MRI and bioluminescence imaging," *Contrast Media & Molecular Imaging*, vol. 8, no. 2, pp. 165–174, 2013.

[33] J. Shen, X.-M. Zhong, X.-H. Duan et al., "Magnetic resonance imaging of mesenchymal stem cells labeled with dual (MR and fluorescence) agents in rat spinal cord injury," *Academic Radiology*, vol. 16, no. 9, pp. 1142–1154, 2009.

[34] L. E. Gonzalez-Lara, X. Xu, K. Hofstetrova, A. Pniak, A. Brown, and P. J. Foster, "In vivo magnetic resonance imaging of spinal cord injury in the mouse," *Journal of Neurotrauma*, vol. 26, no. 5, pp. 753–762, 2009.

[35] A. J. Mothe and C. H. Tator, "Review of transplantation of neural stem/progenitor cells for spinal cord injury," *International Journal of Developmental Neuroscience*, vol. 31, no. 7, pp. 701–713, 2013.

[36] S. Forostyak, P. Jendelova, and E. Sykova, "The role of mesenchymal stromal cells in spinal cord injury, regenerative medicine and possible clinical applications," *Biochimie*, vol. 95, no. 12, pp. 2257–2270, 2013.

[37] A. Yamamoto, K. Sakai, K. Matsubara et al., "Multifaceted neuro-regenerative activities of human dental pulp stem cells for functional recovery after spinal cord injury," *Neuroscience Research*, 2013.

[38] M. Nakamura and H. Okano, "Cell transplantation therapies for spinal cord injury focusing on induced pluripotent stem cells," *Cell Research*, vol. 23, no. 1, pp. 70–80, 2013.

[39] A. M. Parr, C. H. Tator, and A. Keating, "Bone marrow-derived mesenchymal stromal cells for the repair of central nervous system injury," *Bone Marrow Transplantation*, vol. 40, no. 7, pp. 609–619, 2007.

[40] J. Vaquero and M. Zurita, "Bone marrow stromal cells for spinal cord repair: a challenge for contemporary neurobiology," *Histology and Histopathology*, vol. 24, no. 1, pp. 107–116, 2009.

[41] R. S. Y. Wong, "Mesenchymal stem cells: angels or demons?" *Journal of Biomedicine and Biotechnology*, vol. 2011, Article ID 459510, 8 pages, 2011.

[42] M. G. Fehlings and R. Vawda, "Cellular treatments for spinal cord injury: the time is right for clinical trials," *Neurotherapeutics*, vol. 8, no. 4, pp. 704–720, 2011.

[43] K. T. Wright, W. El Masri, A. Osman, J. Chowdhury, and W. E. B. Johnson, "Concise review: bone marrow for the treatment of spinal cord injury: mechanisms and clinical applications," *Stem Cells*, vol. 29, no. 2, pp. 169–178, 2011.

[44] M. Chopp, X. H. Zhang, Y. Li et al., "Spinal cord injury in rat: treatment with bone marrow stromal cell transplantation," *NeuroReport*, vol. 11, no. 13, pp. 3001–3005, 2000.

[45] C. P. Hofstetter, E. J. Schwarz, D. Hess et al., "Marrow stromal cells form guiding strands in the injured spinal cord and promote recovery," *Proceedings of the National Academy of Sciences of the United States of America*, vol. 99, no. 4, pp. 2199–2204, 2002.

[46] B. T. Himes, B. Neuhuber, C. Coleman et al., "Recovery of function following grafting of human bone marrow-derived stromal cells into the injured spinal cord," *Neurorehabilitation and Neural Repair*, vol. 20, no. 2, pp. 278–296, 2006.

[47] S. F. Zhu, Z. N. Zhong, X. F. Fu et al., "Comparison of cell proliferation, apoptosis, cellular morphology and ultrastructure between human umbilical cord and placenta-derived mesenchymal stem cells," *Neuroscience Letters*, vol. 541, pp. 77–82, 2013.

[48] K. N. Kang, J. Y. Lee, D. Y. Kim et al., "Regeneration of completely transected spinal cord using scaffold of poly(D,L-Lactide-co-Glycolide)/small intestinal submucosa seeded with rat bone marrow stem cells," *Tissue Engineering A*, vol. 17, no. 17-18, pp. 2143–2152, 2011.

[49] J.-H. Lee, W.-H. Chung, E.-H. Kang et al., "Schwann cell-like remyelination following transplantation of human umbilical cord blood (hUCB)-derived mesenchymal stem cells in dogs with acute spinal cord injury," *Journal of the Neurological Sciences*, vol. 300, no. 1-2, pp. 86–96, 2011.

[50] J. H. Park, D. Y. Kim, I. Y. Sung et al., "Long-term results of spinal cord injury therapy using mesenchymal stem cells derived from bone marrow in humans," *Neurosurgery*, vol. 70, no. 5, pp. 1238–1247, 2012.

[51] R. Ramasamy, E. W.-F. Lam, I. Soeiro, V. Tisato, D. Bonnet, and F. Dazzi, "Mesenchymal stem cells inhibit proliferation and apoptosis of tumor cells: impact on in vivo tumor growth," *Leukemia*, vol. 21, no. 2, pp. 304–310, 2007.

[52] X. Wang, Z. Zhang, and C. Yao, "Survivin is upregulated in myeloma cell lines cocultured with mesenchymal stem cells," *Leukemia Research*, vol. 34, no. 10, pp. 1325–1329, 2010.

[53] C. B. Johansson, S. Momma, D. L. Clarke, M. Risling, U. Lendahl, and J. Frisén, "Identification of a neural stem cell in the adult mammalian central nervous system," *Cell*, vol. 96, no. 1, pp. 25–34, 1999.

[54] D. L. Salazar, N. Uchida, F. P. T. Hamers, B. J. Cummings, and A. J. Anderson, "Human neural stem cells differentiate and promote locomotor recovery in an early chronic spinal cord injury NOD-scid mouse model," *PLoS ONE*, vol. 5, no. 8, Article ID e12272, 2010.

[55] B. A. Reynolds and S. Weiss, "Generation of neurons and astrocytes from isolated cells of the adult mammalian central nervous system," *Science*, vol. 255, no. 5052, pp. 1707–1710, 1992.

[56] F. H. Gage, "Mammalian neural stem cells," *Science*, vol. 287, no. 5457, pp. 1433–1438, 2000.

[57] W. Tetzlaff, E. B. Okon, S. Karimi-Abdolrezaee et al., "A systematic review of cellular transplantation therapies for spinal cord injury," *Journal of Neurotrauma*, vol. 28, no. 8, pp. 1611–1682, 2011.

[58] S. Nishimura, A. Yasuda, H. Iwai et al., "Time-dependent changes in the microenvironment of injured spinal cord affects the therapeutic potential of neural stem cell transplantation for spinal cord injury," *Molecular Brain*, vol. 6, article 3, 2013.

[59] S. Okada, K. Ishii, J. Yamane et al., "In vivo imaging of engrafted neural stem cells: its application in evaluating the optimal timing of transplantation for spinal cord injury," *The FASEB Journal*, vol. 19, no. 13, pp. 1839–1841, 2005.

[60] H. Kumamaru, H. Saiwai, Y. Ohkawa, H. Yamada, Y. Iwamoto, and S. Okada, "Age-related differences in cellular and molecular profiles of inflammatory responses after spinal cord injury," *Journal of Cellular Physiology*, vol. 227, no. 4, pp. 1335–1346, 2012.

[61] K. Kusano, M. Enomoto, T. Hirai et al., "Transplanted neural progenitor cells expressing mutant NT3 promote myelination and partial hindlimb recovery in the chronic phase after spinal cord injury," *Biochemical and Biophysical Research Communications*, vol. 393, no. 4, pp. 812–817, 2010.

[62] S. Kumar, M. A. Kahn, L. Dinh et al., "NT-3-mediated TrkC receptor activation promotes proliferation and cell survival of rodent progenitor oligodendrocyte cells in vitro and in vivo," *Journal of Neuroscience Research*, vol. 54, no. 6, pp. 754–765, 1998.

[63] B. J. Cummings, N. Uchida, S. J. Tamaki et al., "Human neural stem cells differentiate and promote locomotor recovery in spinal cord-injured mice," *Proceedings of the National Academy of Sciences of the United States of America*, vol. 102, no. 39, pp. 14069–14074, 2005.

[64] A. J. Mothe, T. Zahir, C. Santaguida, D. Cook, and C. H. Tator, "Neural stem/progenitor cells from the adult human spinal cord are multipotent and self-renewing and differentiate after transplantation," *PLoS ONE*, vol. 6, no. 11, Article ID e27079, 2011.

[65] J. Yamane, M. Nakamura, A. Iwanami et al., "Transplantation of galectin-1-expressing human neural stem cells into the injured spinal cord of adult common marmosets," *Journal of Neuroscience Research*, vol. 88, no. 7, pp. 1394–1405, 2010.

[66] I. Kulbatski, A. J. Mothe, A. Keating, Y. Hakamata, E. Kobayashi, and C. H. Tator, "Oligodendrocytes and radial glia derived from adult rat spinal cord progenitors: morphological and immunocytochemical characterization," *Journal of Histochemistry and Cytochemistry*, vol. 55, no. 3, pp. 209–222, 2007.

[67] A. J. Mothe and C. H. Tator, "Transplanted neural stem/progenitor cells generate myelinating oligodendrocytes and Schwann cells in spinal cord demyelination and dysmyelination," *Experimental Neurology*, vol. 213, no. 1, pp. 176–190, 2008.

[68] A. J. Mothe, I. Kulbatski, A. Parr, M. Mohareb, and C. H. Tator, "Adult spinal cord stem/progenitor cells transplanted as neurospheres preferentially differentiate into oligodendrocytes in the adult rat spinal cord," *Cell Transplantation*, vol. 17, no. 7, pp. 735–751, 2008.

[69] M. J. Evans and M. H. Kaufman, "Establishment in culture of pluripotential cells from mouse embryos," *Nature*, vol. 292, no. 5819, pp. 154–156, 1981.

[70] J. W. Mcdonald, X.-Z. Liu, Y. Qu et al., "Transplanted embryonic stem cells survive, differentiate and promote recovery in injured rat spinal cord," *Nature Medicine*, vol. 5, no. 12, pp. 1410–1412, 1999.

[71] H. S. Keirstead, G. Nistor, G. Bernal et al., "Human embryonic stem cell-derived oligodendrocyte progenitor cell transplants remyelinate and restore locomotion after spinal cord injury," *Journal of Neuroscience*, vol. 25, no. 19, pp. 4694–4705, 2005.

[72] J. Sharp, J. Frame, M. Siegenthaler, G. Nistor, and H. S. Keirstead, "Human embryonic stem cell-derived oligodendrocyte progenitor cell transplants improve recovery after cervical spinal cord injury," *Stem Cells*, vol. 28, no. 1, pp. 152–163, 2010.

[73] K. Takahashi and S. Yamanaka, "Induction of pluripotent stem cells from mouse embryonic and adult fibroblast cultures by defined factors," *Cell*, vol. 126, no. 4, pp. 663–676, 2006.

[74] K. Hochedlinger and R. Jaenisch, "Nuclear reprogramming and pluripotency," *Nature*, vol. 441, no. 7097, pp. 1061–1067, 2006.

[75] A. S. Kramer, A. R. Harvey, G. W. Plant, and S. I. Hodgetts, "Systematic review of induced pluripotent stem cell technology as a potential clinical therapy for spinal cord injury," *Cell Transplantation*, vol. 22, no. 4, pp. 571–617, 2013.

[76] K. Okita, T. Ichisaka, and S. Yamanaka, "Generation of germline-competent induced pluripotent stem cells," *Nature*, vol. 448, no. 7151, pp. 313–317, 2007.

[77] S. Yamanaka, "Strategies and new developments in the generation of patient-specific pluripotent stem cells," *Cell Stem Cell*, vol. 1, no. 1, pp. 39–49, 2007.

[78] K. Miura, Y. Okada, T. Aoi et al., "Variation in the safety of induced pluripotent stem cell lines," *Nature Biotechnology*, vol. 27, no. 8, pp. 743–745, 2009.

[79] T. Yamashita, H. Kawai, F. Tian, Y. Ohta, and K. Abe, "Tumorigenic development of induced pluripotent stem cells in ischemic mouse brain," *Cell Transplantation*, vol. 20, no. 6, pp. 883–891, 2011.

[80] T. Amemori, N. Romanyuk, P. Jendelova et al., "Human conditionally immortalized neural stem cells improve locomotor function after spinal cord injury in the rat," *Stem Cell Research & Therapy*, vol. 4, no. 3, p. 68, 2013.

[81] M. Modo, M. Hoehn, and J. W. M. Bulte, "Cellular MR imaging," *Molecular Imaging*, vol. 4, no. 3, pp. 143–164, 2005.

[82] T. Spiriev, N. Sandu, and B. Schaller, "Molecular imaging and tracking stem cells in neurosciences," *Methods in Molecular Biology*, vol. 1052, pp. 195–201, 2013.

[83] E. Syková and P. Jendelová, "Magnetic resonance tracking of transplanted stem cells in rat brain and spinal cord," *Neurodegenerative Diseases*, vol. 3, no. 1-2, pp. 62–67, 2006.

[84] V. Vanecek, V. Zablotskii, S. Forostyak et al., "Highly efficient magnetic targeting of mesenchymal stem cells in spinal cord injury," *International Journal of Nanomedicine*, vol. 7, pp. 3719–3730, 2012.

[85] A. S. Arbab, C. Thiffault, B. Navia et al., "Tracking of In-111-labeled human umbilical tissue-derived cells (hUTC) in a rat model of cerebral ischemia using SPECT imaging," *BMC Medical Imaging*, vol. 12, article 33, 2012.

[86] J. K. Jaiswal, H. Mattoussi, J. M. Mauro, and S. M. Simon, "Long-term multiple color imaging of live cells using quantum dot bioconjugates," *Nature Biotechnology*, vol. 21, no. 1, pp. 47–51, 2003.

[87] N. Sun, A. Lee, and J. C. Wu, "Long term non-invasive imaging of embryonic stem cells using reporter genes," *Nature Protocols*, vol. 4, no. 8, pp. 1192–1201, 2009.

[88] M. E. Trinkaus, R. Blum, D. Rischin et al., "Imaging of hypoxia with (18) F-FAZA PET in patients with locally advanced non-small cell lung cancer treated with definitive chemoradiotherapy," *Journal of Medical Imaging and Radiation Oncology*, vol. 57, no. 4, pp. 475–481, 2013.

[89] N. Quartuccio, G. Treglia, M. Salsano et al., "The role of Fluorine-18-Fluorodeoxyglucose positron emission tomography in staging and restaging of patients with osteosarcoma," *Radiology and Oncology*, vol. 47, no. 2, pp. 97–102, 2013.

[90] K. Patel, N. Hadar, J. Lee, B. A. Siegel, B. E. Hillner, and J. Lau, "The lack of evidence for PET or PET/CT surveillance of patients with treated lymphoma, colorectal cancer, and head and neck cancer: a systematic review," *Journal of Nuclear Medicine*, vol. 54, no. 9, pp. 1518–1527, 2013.

[91] J.-Z. Bai, Z.-J. Liu, W.-M. Ding et al., "Tracking neural progenitor cells tranplanted into rabbit spinal cord by detection of dopamine receptors 2 with positron emission computed tomography," *National Medical Journal of China*, vol. 86, no. 29, pp. 2060–2064, 2006.

[92] X. Han, N. Yang, Y. Cui, Y. Xu, G. Dang, and C. Song, "Simvastatin mobilizes bone marrow stromal cells migrating to injured areas and promotes functional recovery after spinal cord injury in the rat," *Neuroscience Letters*, vol. 521, no. 2, pp. 136–141, 2012.

[93] M. E. Cohen, N. Muja, N. Fainstein, J. W. M. Bulte, and T. Ben-Hur, "Conserved fate and function of ferumoxides-labeled neural precursor cells in vitro and in vivo," *Journal of Neuroscience Research*, vol. 88, no. 5, pp. 936–944, 2010.

[94] S.-L. Hu, P.-G. Lu, L.-J. Zhang et al., "In Vivo magnetic resonance imaging tracking of SPIO-labeled human umbilical

cord mesenchymal stem cells," *Journal of Cellular Biochemistry*, vol. 113, no. 3, pp. 1005–1012, 2012.

[95] S. C. Berman, C. Galpoththawela, A. A. Gilad, J. W. M. Bulte, and P. Walczak, "Long-term MR cell tracking of neural stem cells grafted in immunocompetent versus immunodeficient mice reveals distinct differences in contrast between live and dead cells," *Magnetic Resonance in Medicine*, vol. 65, no. 2, pp. 564–574, 2011.

[96] Z. Li, Y. Suzuki, M. Huang et al., "Comparison of reporter gene and iron particle labeling for tracking fate of human embryonic stem cells and differentiated endothelial cells in living subjects," *Stem Cells*, vol. 26, no. 4, pp. 864–873, 2008.

[97] J. R. de Wet, K. V. Wood, M. DeLuca, D. R. Helinski, and S. Subramani, "Firefly luciferase gene: structure and expression in mammalian cells," *Molecular and Cellular Biology*, vol. 7, no. 2, pp. 725–737, 1987.

[98] C. H. Contag and M. H. Bachmann, "Advances in in vivo bioluminescence imaging of gene expression," *Annual Review of Biomedical Engineering*, vol. 4, pp. 235–260, 2002.

[99] M. Edinger, T. J. Sweeney, A. A. Tucker, A. B. Olomu, R. S. Negrin, and C. H. Contag, "Noninvasive assessment of tumor cell proliferation in animal models," *Neoplasia*, vol. 1, no. 4, pp. 303–310, 1999.

[100] T. J. Sweeney, V. Mailander, A. A. Tucker et al., "Visualizing the kinetics of tumor-cell clearance in living animals," *Proceedings of the National Academy of Sciences of the United States of America*, vol. 96, no. 21, pp. 12044–12049, 1999.

[101] Y. Takahashi, O. Tsuji, G. Kumagai et al., "Comparative study of methods for administering neural stem/progenitor cells to treat spinal cord injury in mice," *Cell Transplantation*, vol. 20, no. 5, pp. 727–739, 2011.

[102] V. Mani, E. Adler, K. C. Briley-Saebo et al., "Serial in vivo positive contrast MRI of iron oxide-labeled embryonic stem cell-derived cardiac precursor cells in a mouse model of myocardial infarction," *Magnetic Resonance in Medicine*, vol. 60, no. 1, pp. 73–81, 2008.

[103] R. D. S. N. Tewarie, J. Yu, J. Seidel et al., "Positron emission tomography for serial imaging of the contused adult rat spinal cord," *Molecular Imaging*, vol. 9, no. 2, pp. 108–116, 2010.

[104] J. Jackson, C. Chapon, W. Jones, E. Hirani, A. Qassim, and K. Bhakoo, "In vivo multimodal imaging of stem cell transplantation in a rodent model of Parkinson's disease," *Journal of Neuroscience Methods*, vol. 183, no. 2, pp. 141–148, 2009.

[105] C. Chapon, J. S. Jackson, E. O. Aboagye, A. H. Herlihy, W. A. Jones, and K. K. Bhakoo, "An in vivo multimodal imaging study using MRI and pet of stem cell transplantation after myocardial infarction in rats," *Molecular Imaging and Biology*, vol. 11, no. 1, pp. 31–38, 2009.

[106] H. Kim, P. Walczak, N. Muja, J. T. Campanelli, and J. W. M. Bulte, "ICV-transplanted human glial precursor cells are short-lived yet exert immunomodulatory effects in mice with EAE," *GLIA*, vol. 60, no. 7, pp. 1117–1129, 2012.

[107] C. J. Laskowski and F. Bradke, "In vivo imaging: a dynamic imaging approach to study spinal cord regeneration," *Experimental Neurology*, vol. 242, pp. 11–17, 2013.

Hindawi Publishing Corporation
BioMed Research International
Volume 2013, Article ID 404361, 13 pages
http://dx.doi.org/10.1155/2013/404361

Review Article

Acoustic Droplet Vaporization in Biology and Medicine

Chung-Yin Lin[1,2,3] and William G. Pitt[1]

[1] *Department of Chemical Engineering, Brigham Young University, Provo, UT 84602, USA*
[2] *Department of Neurosurgery, Chang Gung Memorial Hospital, Taoyuan 333, Taiwan*
[3] *Division of Clinical Toxicology, Chang Gung Memorial Hospital, Taoyuan 333, Taiwan*

Correspondence should be addressed to Chung-Yin Lin; linny5782@hotmail.com

Received 24 July 2013; Revised 17 September 2013; Accepted 3 October 2013

Academic Editor: Mei Tian

This paper reviews the literature regarding the use of acoustic droplet vaporization (ADV) in clinical applications of imaging, embolic therapy, and therapeutic delivery. ADV is a physical process in which the pressure waves of ultrasound induce a phase transition that causes superheated liquid nanodroplets to form gas bubbles. The bubbles provide ultrasonic imaging contrast and other functions. ADV of perfluoropentane was used extensively in imaging for preclinical trials in the 1990s, but its use declined rapidly with the advent of other imaging agents. In the last decade, ADV was proposed and explored for embolic occlusion therapy, drug delivery, aberration correction, and high intensity focused ultrasound (HIFU) sensitization. Vessel occlusion via ADV has been explored in rodents and dogs and may be approaching clinical use. ADV for drug delivery is still in preclinical stages with initial applications to treat tumors in mice. Other techniques are still in preclinical studies but have potential for clinical use in specialty applications. Overall, ADV has a bright future in clinical application because the small size of nanodroplets greatly reduces the rate of clearance compared to larger contrast agent bubbles and yet provides the advantages of ultrasonographic contrast, acoustic cavitation, and nontoxicity of conventional perfluorocarbon contrast agent bubbles.

1. Introduction

Acoustic droplet vaporization (ADV) is a relatively recently exploited phenomenon in which a liquid droplet is induced to form a vapor phase as a result of the application of cyclic pressure waveforms (acoustic waves). While this phenomenon has been described in the literature since 1995 as an imaging application [1–3], it acquired the name "acoustic droplet vaporization" in 2000 [4] along with other proposed and demonstrated applications in gas embolism, thrombolysis, and drug delivery. While ADV has many applications in biology, physics, and engineering, this review will center on its application in clinical medicine, with emphasis on imaging and gas embolization, and on the delivery of therapeutics and markers.

Acoustic droplet vaporization has other synonyms in the literature, such as "phase-shift emulsion" and "ultrasonic droplet vaporization." The enthusiasm for ADV and its associated processes comes from its useful and unique applications in some of the more challenging issues of medical imaging and therapeutic delivery. At the same time, increasing access to ultrasonic transducers has made ADV more available to researchers in academia and in the clinic.

In theory, ADV could be employed with any liquid that has a normal boiling point near or below body temperature. The physics are based on the vapor pressure of the liquid, which is a function of temperature, and not necessarily based upon the liquid chemistry. However, for medical applications it is essential to use nontoxic biocompatible liquids that are immiscible with water. Fluorocarbons are good candidates, particularly the perfluorocarbons (PFCs) because they have low solubility in aqueous formulations, and they have relatively low toxicity. Table 1 lists some parameters of candidate alkane perfluorocarbons [5]. Of these, perfluoropentane (PFC5) is perhaps the most commonly used in ADV because of its good combination of high vapor pressure, low solubility in blood, price, and availability. Other phase changing perfluorocarbons that have been explored are

Table 1: Properties of selected perfluorocarbons [5].

Common name	Chemical formula	Normal boiling point (°C)	Vapor pressure at 37°C (kPa)	Expansion ratio*
Perfluorobutane	C_4F_{10}	−1.3	387.98	5.37
Perfluoropentane	C_5F_{12}	29.2	135.05	5.17
Perfluorohexane	C_6F_{14}	57.1	48.09	4.97

*Diameter expansion ratio calculated assuming no Laplace pressure compressing the final gas bubble, internal bubble pressure at 1 atm, and temperature of 37°C.

perfluorodichlorooctane [6] and perfluoro-15-crown-5-ether [7].

2. Physical Chemistry of Acoustic Droplet Vaporization

2.1. Thermodynamics of Vaporization. The first concepts pertaining to ADV are those of thermodynamic phase state (gas, liquid, and solid), phase change, and vapor pressure. Solids and liquids possess a vapor pressure, which is defined as the pressure of the specified gas in equilibrium with its own liquid or solid in a closed system at a specified temperature. The vapor pressure increases as the temperature of the condensed phase increases. Sometimes it is convenient to think of a vapor pressure as the "push" of the solid or liquid molecules trying to escape (the solid or liquid) to the gas phase. When the surrounding pressure is greater than the vapor pressure, the condensed phase remains in its condensed form (liquid or solid), although it may eventually dissipate as the material slowly dissolves and diffuses away into the aqueous phase. However, when the surrounding local pressure decreases below the vapor pressure, then the liquid molecules will quickly escape to form a gas phase (boil), or a solid will quickly sublime to a gas. The "normal boiling point" is the temperature at which the vapor pressure of a liquid is exactly 1 atm pressure; at this temperature the gas and liquid phases are in equilibrium, and a gas phase can form (depending on the volume of the closed system); above this temperature the liquid will transform (or boil) to a gas. Likewise, a gas of a single species will condense to a liquid when the local temperature decreases such that the liquid vapor pressure is below the surrounding gas pressure, or when the local gas pressure increases above the vapor pressure.

Acoustic droplet vaporization employs these concepts of vapor pressure, gas phase, and liquid phase, with the caveat that the change in local pressure causes the phase transformation, not necessarily any changes in temperature. When the local pressure drops below the liquid vapor pressure, the liquid can turn to gas. The acoustic aspect of ADV occurs because sound waves (which are pressure waves) are used to manipulate the local pressure of the liquid, thus controlling the drive to turn a liquid to gas, or gas to liquid.

2.2. Nucleation and Driving Forces. While it is true that a liquid whose vapor pressure is above the surrounding local pressure has a thermodynamic driving force to turn to gas, this transformation may not happen instantaneously for at least two reasons. First, heat needs to be transferred to the liquid because the change from liquid to gas required a certain amount of thermal energy; this is called the enthalpy (or heat) of vaporization.

Second, a nucleation event is required to get the transformation started. It is possible and actually very common for liquids to remain in the liquid state even when above their boiling point (their liquid vapor pressure is above the local pressure) because a nucleation event must first occur to initiate the formation of the gas phase. A liquid above its boiling point is called "superheated." The nucleation of a gas phase requires the formation of a nanoscopic cavity of gas (homogeneous nucleation), which in some cases continues to grow into a macroscopic gas phase (bubble). This process is random and stochastic, with an activation energy barrier that is related to the amount of superheating and the interfacial energy of the gas-liquid boundary [10]. The details are beyond the scope of this review, but the important result is that a liquid can remain superheated if it is very pure. The number of random events that create nucleation cavities in a superheated liquid is proportional to the volume of the liquid and the time length of observation, so a very small droplet has a much greater probability of remaining a superheated liquid for a longer time than has a large volume of liquid. Impurities, foreign surfaces, physical stresses, and higher amounts of superheating increase the probability that a gas bubble will nucleate within a superheated liquid. The probability of forming a nucleation cavity is also a strong function of the amount of superheating above the boiling point, in which superheating is often referred to as the "driving force" for nucleation.

In this review we define true superheating as the state when the vapor pressure of the liquid is above the vapor pressure of the surrounding material, such as when a large droplet (having negligible Laplace pressure) of liquid perfluoropentane in water at 30°C (having a vapor pressure of 1.02 atm) is surrounded by water at a pressure of 1 atm. Engineers also define superheating as any time a liquid is above its normal boiling point, such as pressurized water at 110°C (with a vapor pressure of 1.41 atm) confined in a pipe with a local pressure of 3 atm (304 kPa). However, we will call this situation "apparent superheating" because, although the liquid temperature is above its normal boiling point (at 1 atm), the liquid vapor pressure is still below the local pressure (3 atm), so it will never change to a gas no matter how long one waits.

A small liquid droplet that is immiscible in the surrounding liquid can experience this "apparent superheating" because of Laplace pressure, and thus will never change to

a gas when confined inside the small droplet. Laplace pressure is the additional pressure imposed upon the interior fluid of a droplet because of the surface tension (or interfacial energy) between the two immiscible phases that compresses the liquid or gas inside the droplet. Although there are more sophisticated definitions and explanations of Laplace pressure [11], this qualitative description will suffice for this review. The magnitude of the Laplace pressure is given by $\Delta P = 2\gamma/R$, where ΔP is the increase in pressure inside a spherical droplet of radius R compared to the local pressure of the surrounding fluid and γ is the interfacial energy.

For example, consider a 1-micron-diameter droplet of PFC5 in water at 37°C and 1 atm pressure (local pressure of the surrounding water). The interfacial energy between water and PFC5 at this temperature is estimated to be 56 mN/m [12], and thus the Laplace pressure is calculated to be 224 kPa. This value plus the surrounding water pressure of 101 kPa produces an internal pressure in the droplet of 325 kPa. Even though the local temperature of 37°C produces a PFC5 vapor pressure of 132 kPa, the PFC5 will never turn to gas within this droplet because its vapor pressure remains lower than the local pressure inside the droplet. Although the droplet may slowly shrink due to diffusion of PFC5 into the surrounding water, this droplet will never boil (change to gas) even though it is (apparently) superheated above its normal boiling point of 29.2°C. The PFC5 liquid in this droplet would not turn to gas until it was heated above 66.2°C, so the smallness of the droplet creates an increased boiling point of the liquid. Good examples of apparent superheating and of increased boiling temperatures of perfluorocarbons are given by Sheeran et al. [13, 14]. (Note: vapor pressures and other thermodynamic properties for PFCs are taken from the DIPPR database [5]; properties of water are taken from steam tables [15].)

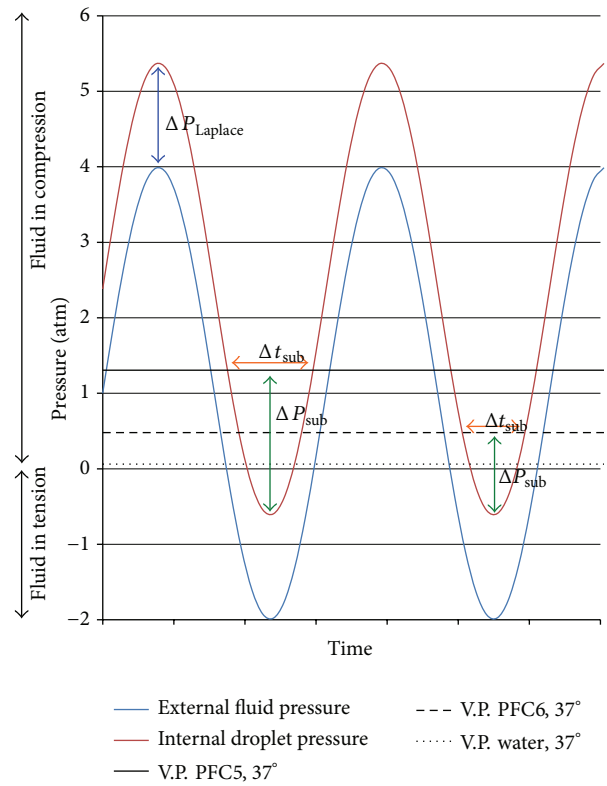

Figure 1: Plot of pressure in an ultrasonic wave. Upper sinusoidal line represents the pressure inside a PFC droplet of 1 μm in diameter. Lower sinusoidal line represents the pressure of the surrounding fluid as the ultrasonic wave passes. The difference is the Laplace pressure. The vapor pressures of PFC5, PFC6, and water are indicated. The vertical arrows indicate the maximum subpressurization, and the horizontal arrows indicate the available subpressurization time.

2.3. Ultrasound and Subpressurization. Now, what does ultrasound have to do with all of this? Ultrasound is defined as pressure waves with a characteristic frequency greater than 20 kHz, the nominal upper threshold of hearing for humans. The wavelength of sound in water at room temperature is given by $\lambda = c/f$, where c is the phase velocity (speed of sound) and f is the frequency. For water at 37°C, c = 1,524 m/s, so wavelengths at 20 kHz, 1 MHz, and 5 MHz are 7.6 cm, 1.5 mm, and 305 μm, respectively. All these lengths are much greater than the size of a 1 μm PFC droplet, so we can consider that there are not significant pressure gradients through the volume of the droplet. The pressure of the fluid surrounding the droplet rises and decreases, and so does the pressure inside the droplet, although at a higher value due to the additional Laplace pressure, as Figure 1 shows. We note that Figure 1 indicates that the pressure can have a negative absolute value. This is possible because the strong cohesive forces in water (and presumably also in PFCs) allow the fluid to be placed in tension (negative pressure) without cohesive failure [16].

Referring to Figure 1 again, we show that during some sections of the acoustic pressure cycle, the internal pressure within the PFC droplet drops below the vapor pressure of the PFC and then increases again to values above the vapor pressure. During the short time window when the internal pressure is less than the vapor pressure (called subpressurization), there is a "driving force" for a gas phase to form. Experimental observations show that often a gas phase is not formed in some cases in which the subpressurization driving force is small (low acoustic amplitude) or the time window is short (high ultrasonic frequency). Thus the instant formation of a gas phase is not guaranteed, suggesting the requirement for a nucleation nidus or other nucleation event. Nucleation theory indicates that at small values of subpressurization in the absence of a heterogeneous nucleation event (particle nidus, shear or shock event, etc.) homogeneous nucleation will eventually occur, but it is a random or stochastic process. The probability of homogeneous nucleation of a growing gas bubble is proportional to the time window (at constant subpressurization) and increases exponentially with the magnitude of subpressurization. Thus ADV events will increase as the ultrasonic frequency decreases, as the number of cycles in a pulse increases, as the peak negative pressure of a wave increases in magnitude, and as the Laplace pressure decreases (due to lower interfacial energy or to larger droplet radius). Many of these postulates have been confirmed experimentally

[17–19]. All of these factors should be considered in the analysis and optimization of ADV.

Several authors have observed subpressurization of perfluorocarbon liquid droplets without gas formation [4, 9, 17–20]. This could be due to "apparent subpressurization," analogous to apparent superheating, in which the Laplace pressure was sufficiently large that the vapor pressure at a temperature above the normal boiling point was still not greater than the local pressure inside the droplet. Or it could have been true subpressurization in the absence of a nucleation event. It is difficult to discern which of these occurred in the literature reports since the interfacial energy (and thus the Laplace pressure) was not always known or reported.

For example, several authors have reported that small PFC5 (b.p. 29.2°C) and PFC4 (b.p. –1.3°C) droplets are stable at 37°C [7, 17, 21–27]. But relatively few have also reported the droplet interfacial energy and size, from which the Laplace pressure can be calculated and true subpressurization can be calculated [15, 19].

2.4. Bubble Growth. High-speed photography of the nucleation of the gas phase shows that the bubble forms within the liquid PFC and not at the liquid PFC/water interface [23]. In some cases 2 bubbles nucleate within the droplet and may coalesce into 1 bubble [19].

Once the gas bubble is nucleated, it will continue to grow as long as the subpressurization exists and there is sufficient heat transfer to satisfy the required heat of formation of the gas phase. Heat transfer is usually not a limiting issue for small droplets of more than a few degrees of superheating [8]. In an acoustic field, the pressure eventually reverses, and the increasing internal pressure of the droplet eventually overtakes the vapor pressure; at this point the gas phase can condense back into liquid, and the liquid droplet is pressurized until the cycle repeats itself. The dynamics of such a system have been observed experimentally [17] and have been modeled for PFC5 and PFC6 droplets in water at 25 and 37°C [8]. As Figure 1 shows, the length of time of subpressurization is a function of the acoustic amplitude and frequency. Greater acoustic amplitude will start bubble growth sooner and have more total time for growth. Similarly, low frequency ultrasound provides a longer time window for growth. Figures 2 and 3 show how sensitive the bubble size is to the amplitude and frequency of the ultrasound as calculated from mathematical models. For example, increasing the acoustic amplitude from 111 kPa to 115 kPa increases the bubble size by more than a factor of 10 (see Figure 2). Decreasing the frequency from 500 kHz to 20 kHz increases the bubble size by more than a factor of 100 (see Figure 3).

After the insonation stops, the final state of the droplet may be a liquid, but there are some cases in which a gas phase may prevail. The first case may be a situation in which a condensed liquid droplet and expanded gas phase are both possible equilibrium states, and the gas phase persisted after cessation of insonation. For example, a 100 nm emulsion droplet of PFC5 coated with a layer phosphatidylcholine is predicted to have an interfacial energy of 3.5 mN/m [28] and

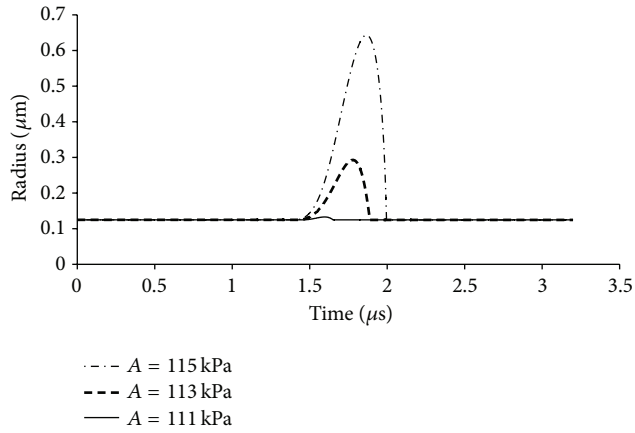

Figure 2: Plot of the radius of an expanding bubble as a function of time and acoustic amplitude. A 125 nm radius droplet of perfluorohexane in water was subjected to 500 kHz pressure waves with amplitudes of 111, 113, and 115 kPa. The temperature was 25°C, and the interfacial tension was 3.5 mN/m. The plot was adapted from [8].

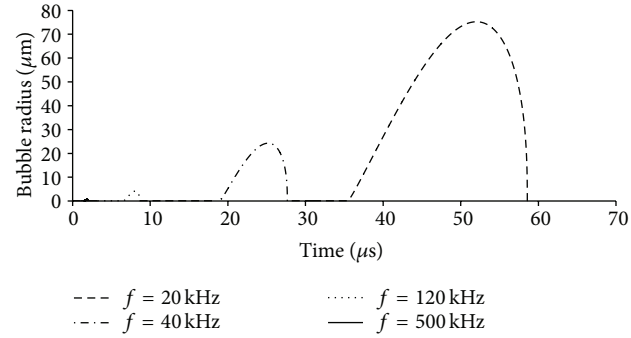

Figure 3: Plot of the radius of an expanding bubble as a function of time and acoustic frequency. A 125 nm radius droplet of perfluorohexane in water was subjected to a 500 kHz pressure wave with an amplitude of 110 kPa. The temperature was 25°C, and the interfacial tension was 3.5 mN/m. The plot was adapted from [8]. Each droplet expansion starts at a different time, because at lower frequencies, longer time is required before the pressure cycle drops low enough to cause the liquid to expand to gas.

thus a Laplace pressure of about 140,000 Pa. At 37°C, the PFC5 vapor pressure is about 132,000 Pa [5], which is less than the sum of the atmospheric pressure (101,000 Pa) and the Laplace pressure; this small droplet in the liquid state, although apparently superheated, is stable. However, if this size of liquid droplet was turned to PFC5 gas at 1 atm pressure, the diameter would be about 517 nm, and the Laplace pressure would be reduced to about 27,000 Pa (assuming the same interfacial energy). The internal pressure in the gas bubble would be about 128,000 Pa, slightly lower than the vapor pressure at 37°C (132,000 Pa); so this gas bubble would also be stable [29].

A more likely and perhaps ubiquitous experimental example is the case in which a noncondensable gas (nitrogen, oxygen, etc.) is dissolved in the liquid surrounding the droplet undergoing liquid-gas-liquid cycles during

insonation. During the time that the gas phase is present, dissolved noncondensable gas (e.g., nitrogen) may diffuse to the gas-liquid interface and enter the expanding bubble of PFC gas. During contraction when the PFC condenses back to liquid during the high pressure phase of the acoustic cycle, the noncondensable gas will not condense along with the PFC and may not completely dissolve back into the surrounding liquid, leaving a very small bubble of noncondensable gas that easily nucleates the next cycle of PFC boiling, leading to an even larger bubble on the next cycle, and subsequently more diffusion of noncondensable gas into the bubble. At the end of several pressure cycles in the insonation pulse, a stable gas bubble may remain that is a mixture of PFC and noncondensable gas. This process has been observed and modeled [4, 23] and may explain several observations showing that gas bubbles following ADV are larger than would be expected given the amount of PFC in the initial liquid droplet [18, 24, 30, 31]. There are reports of other anomalous behaviors of very small PFC5 droplets forming gas bubbles much larger than expected, and this large size persists after the acoustic pulse has passed [24].

2.5. Thresholds for Bubble Formation. If we ignore the required nucleation of a gas phase, the peak negative pressure threshold for ADV can be easily calculated from the vapor pressure, Laplace pressure, and local hydrostatic pressure. Experimental observation of thresholds indicates that ADV does not readily occur until much greater ultrasonic amplitudes are applied. For example, Kripfgans et al. measured ADV thresholds for 8 μm PFC5 droplets in water at 23°C with a reported interfacial tension of 33.8 mN/m [19]. Assuming a local pressure of 101 kPa, the Laplace pressure plus local pressure in the droplet is calculated to be 117.9 kPa, and the vapor pressure at 23°C is 79.4 kPa. This difference is only 38.5 kPa, so any acoustic wave larger than this would drop the internal pressure below the vapor pressure. However, the experimentally observed threshold of 1.7 MPa at 3 MHz is nearly 2 orders of magnitude greater than the calculated theoretical minimum of 38.5 kPa.

In other experiments, Sheeran et al. made 200–300 nm perfluorobutane (PFC4) droplets in water with an estimated interfacial energy of 30 mN/m [17]. The droplet internal pressure of 0.58 MPa, less the 0.28 MPa vapor pressure of PFC4 at 25°C, is only 0.30 MPa, and yet the observed ADV threshold was 1.45 MPa at 1 MHz frequency.

Giesecke and Hynynen made PFC5 droplets stabilized with albumin but did not report an interfacial tension; therefore the Laplace pressure cannot be estimated [18]. However, they found that 2 μm diameter droplets formed vapor without insonation at 72°C. At 37°C with insonation, gas formation was observed at 0.65 MPa at 0.74 MHz and at 1.05 MPa at 1.1 MHz. Other similar observations regarding thresholds have been made [32, 33]. Interestingly, the threshold at high frequency appears to be dependent upon the duration of the insonating pulse [34], again hinting that bubble nucleation is not instantaneous.

3. Acoustic Droplet Vaporization in Clinical Nanomedicine

The majority of clinical research using ultrasound for vascular imaging has employed the use of microbubbles (MBs) as contrast agents to enhance the acoustic signal from the blood. MBs are gas-in-liquid bubbles most often stabilized with albumin, galactose, lipid, or polymers [35]. The average diameters of the MBs are generally around 2.5 μm and can range from 1 to 10 μm. The MBs resonate in an ultrasonic field, rapidly contracting and expanding in response to the pressure changes of the sound waves [36].

While micron-sized gas-phase contrast agents are easily introduced into blood, their large size precludes their entry into the extravascular space [37] and also promotes more rapid clearance. Larger particles are taken up more readily by the cells of the reticuloendothelial system (RES) [38–40]. Therefore, emulsions containing submicron and nanometer-sized perfluorocarbon (PFC) droplets that can change to gas are being studied in diagnostic and therapeutic applications of ultrasound. PFCs that form gas are also studied for ultrasonic molecular imaging, the targeted delivery of some therapeutic agents, and in phase aberration correction. Recently, the use of liquid-phase PFC droplets that remain in the liquid state has been explored as a contrast agent [41]; however, this application is not reviewed herein.

The following review presents four applications of ADV in clinical settings and discusses their future possibilities.

3.1. ADV in Vascular Imaging. In general, the aim of ultrasound contrast agents is to selectively increase the strength of the back-scattered signal that is returned to the detecting transducer. The first clinical application of phase changing emulsions as an ultrasound contrast agent appears to be in 1995 with a product called EchoGen made by Sonus Pharmaceuticals (Bothell, WA). EchoGen was a suspension of PFC5 liquid droplets in water, stabilized by an albumin layer. The reported droplet size was 0.3 μm in diameter, and the bubbles produced were reported to be from 1 to 10 μm, with an average diameter of 6 to 8 μm [42]. Since expansion at 37° produces only a 5-fold expansion in radius from liquid to gas, these large bubble sizes suggest that after phase transformation the smaller bubbles coalesced together and/or absorbed dissolved gas from the surrounding liquid. Although the authors of these early papers supposed that the bubbles were produced by thermal expansion of the liquid to gas, we now know that the droplets in EchoGen are fairly stable at 37°, and most, if not all, of the bubbles were generated by the excitation by the applied ultrasonic imaging pulses. Thus these are examples of acoustic droplet vaporization in its earliest application.

EchoGen was first reported in preclinical application to image the canine renal cortex, providing contrast between the cortex and medulla. It had a half-life of 2 to 3 minutes with an intravenous dose of 0.25 to 0.45 mL/kg [1]. As mentioned, in this and other early papers, bubble formation was attributed to the droplets "undergoing a phase transition to gas above 30°C." There was no comparison to other

conventional contrast agents of that time, so the comparison and advantages to imaging with Albunex were not reported.

In 1996 the first images of color Doppler analysis with EchoGen in human kidneys appeared, using a lower dose than was used in animals (0.05 mL/kg) [31]. By 1998, EchoGen and related PFC5 phase-shift agents, SonoGen, and QW7437 (Sonus Pharmaceuticals) were being used for myocardial opacification in clinical trials [43]. EchoGen was also used to image the prostates of 15 patients using 7-MHz color Doppler linear array transrectal transducers [44]. After injection of 0.05 mL/kg of EchoGen, the entire prostate was examined to study the blood flow in the gland. The combination of the color Doppler sonography and EchoGen provided sufficient contrast in a number of vessels that could not be identified otherwise. No side effects were observed.

Many studies were made on left ventricle opacification; since the PFC5 liquid droplets were much smaller than gas bubbles, they could traverse the lungs and provide contrast by acoustic droplet vaporization in the left heart better than the then-FDA-approved contrast agent Albunex [42, 45, 46]. QW7437 was formulated with a negative surface charge so that it would not adhere to the vascular endothelium [47]. It appeared to deposit in the myocardium and provided myocardial contrast even after the ventricles had been cleared of contrast agent.

The pharmacokinetics of the PFC5 droplets (EchoGen) in human volunteers was investigated as part of the safety evaluation (0.01 to 0.1 mL/kg), showing that the PFC5 clearance of about 30 mL/min/kg was by exhalation [48]. Although adverse effects in humans have not been reported (at therapeutic doses), repeated administrations of high doses (0.5 mL/kg) in dogs produced evidence of accumulation in their lungs and eventual hemodynamic collapse [49]. An alternative method of activating the EchoGen to bubbles was published in 1998 [50]. The physician would pull back the plunger of a 20 mL syringe for a few seconds and then release it, generating a loud popping sound, and then he would inject the contrast agent. This low-pressure activation produced adequate contrast to image the liver and kidneys. It also provided some transpulmonary opacification of the left heart, again suggesting that the microbubbles were cleared to a lesser extent than conventional contrast agents used at that time [42, 47]. Although this application was not strictly "acoustic droplet vaporization," it was a novel application of EchoGen that took advantage of the high vapor pressure of PFC5.

The range of tissues that could be imaged with PFC5 was expanded to basal cerebral arteries in 1999 [51]. As mentioned, we posit that the small size of the PFC5 emulsions and microbubbles produces slower clearance and thus retains sufficiently high concentration to allow imaging where none had previously been done. This study revealed the sensitivity that could be achieved with acoustic droplet vaporization of PFC5 emulsion droplets in transcranial imaging.

Interestingly, published papers of clinical applications of EchoGen, SonoGen, QW7437, and perflenapent were absent after 2003. EchoGen was not approved by the FDA, and apparent interest and funding vanished. It also had competition from Definity, a microbubble contrast agent containing perfluoropropane, which was introduced in 1999 [52] and had reduced clearance by the RES system by virtue of its polyethylene glycol (PEG) coating. However, the use of PFC5 emulsion droplets in other applications started to increase, including the use in vascular occlusion, molecular imaging, and therapeutic delivery.

3.2. ADV in Vascular Occlusion. Another well-studied application of ADV is embolotherapy. Successful application of embolotherapy requires an understanding of the disease to be treated, the distinctive features of the circulation to be embolized, and the embolic material used for the occlusion [53]. Embolotherapy must be carefully done because many arterial emboli could create infarcts in the heart or brain or travel to distant vascular bed where they could cause unwanted arterial occlusion, ischemia, and potentially infarction [54]. However, one method of treating tumors or other malformations is to occlude the blood flow to the tissue with gas bubbles, which can effectively shrink the tumor. As an added advantage, embolotherapy using ADV also enables simultaneous imaging and therapy in cancer treatments.

In practice, embolotherapeutic occlusion is done by focusing ultrasound on arterioles feeding a tumor. As the PFC droplets flow through the targeted vasculature, the droplets expand to gas, which often occludes the further flow of blood and produces ischemic damage to the downstream tissues [4]. PFC droplets that are not activated to gas are too small to cause embolism downstream. Currently, ADV with micron-sized PFC droplets is applied in preclinical use for staging and prognosis of hepatocellular and renal carcinoma [55, 56]. In other types of cancer, ADV is a well-accepted concept; yet current ADV techniques that include using perfluorocarbon droplets as contrast agents, such as perfluoropentane (PFC5), have not been widely validated. Due to the low solubility and diffusivity of PFC gases in water, bubbles can remain stable in an aqueous solution much longer than air bubbles of the same size [57]. These properties endow the PFCs droplets with desirable properties for applications in clinical occlusion.

Samuel et al. prepared 2 μm (mean diameter) albumin-encapsulated PFC5 droplets (1×10^8 droplets/mL) in normal saline. After injection of this solution via the carotid artery, ultrasonically activated bubbles (3.5 MHz, 6 MPa, 3.7 μs pulse length, and 10 Hz pulse repetition frequency) occluded the 125 μm (average diameter) arterioles and the 4–7 μm capillary beds in Sprague-Dawley rats [58]. To obtain microscopic evidence of this occlusion, intravital microscopy was used to image the droplet bubbles that caused occlusion. In addition to occlusion, the different images of erythrocyte extravasation indicate that insonation of the PFC5 droplets produced bubble oscillations and probably inertial cavitation, which resulted in the rupture of arterioles and/or capillaries.

Other studies by the same group showed that ADV following injection of 2 μm PFC5 droplets caused occlusion in canine kidneys [59, 60]. Image-based hyperechogenicity showed that the tissue perfusion was changed after injection and insonation at 3.5 MHz, 7.4 MPa at the focal point, with

a 1 kHz pulse repetition frequency (0.25% duty cycle). Successful ADV demonstrated the potential of this technique to occlude flow [60].

3.3. ADV with Molecular Recognition in Cancer Detection. Early detection of cancer remains one of the most desirable goals for tumor imaging, particularly for identification of early primary tumors and of metastatic spread. Two techniques can be used. First, the tumor vasculature is often malformed and may be detectable by imaging [61]. Second, ligands that specifically bind to the tumor can be attached to the imaging agent to identify tissues of cancerous phenotype. Therefore, there is interest in the potential application of ADV to identify molecular target expression in primary and metastatic cancers. In theory, labeled nanodroplets can penetrate the endothelial barrier and attach to cells expressing surface features indicative of cancerous phenotype [62].

With the growth in ADV-based imaging of cancer as demonstrated in preclinical settings, there is a strong argument for efforts to apply ADV to clinical monitoring of cancer therapies. Early work has demonstrated in animal models that ADV-based angiography can provide sensitive feedback on the effect of ultrasonic therapy in models of pancreatic cancer, breast cancer, kidney function, and so forth [7, 21]. Matsuura et al. used quantum dots, loaded into PFC5 droplets, to show that the droplets could be converted to gas and imaged at 18 MHz with the application of 4.7 MPa acoustic pressure and 32 cycle bursts of ultrasound in hepatoma in mice by ADV [55]. Additional approaches have used antibodies and peptides to target imaging agents for treatment of emerging glioma. An example of this is the use of nanoparticle labeled antivascular endothelial growth factor receptor (EGFR) antibodies for *in vitro* and *in vivo* magnetic resonance molecular imaging. This approach successfully visualized and differentiated C6 glioma tumor types based on their EGFR expression [25]. Intravenous application of labeled anti-EGFR in this same study resulted in a quick delivery to the tumor without the necessity to clear the tissue from adherent tissue or mucus. In this preclinical study, the particles collected in the rat brain, but insonation was never applied to expand the PFC5 droplets to gas to release the drug or permeabilize the blood-brain barrier. A similar construct employing ADV and featuring aptamers for targeting to deliver Doxorubicin has also been described but not employed yet in clinical studies [63].

3.4. ADV in Therapeutic Delivery. Implementation of ADV in the delivery of drugs, plasmids, and other therapeutic agents can be divided into two general categories. The first is the use of ultrasonic ADV to produce gas bubbles on demand at the site of interest and then employ the newly formed gas bubbles as cavitating bodies that accomplish drug delivery by the same mechanisms that gas bubbles normally employ. These include cavitational disruption of drug carriers and sonoporation of cell membranes, the latter leading to increased cell permeability. The second general application of ADV is to use the PFC droplet as a contrast agent, either in the liquid or gas form, to visualize and confirm the location of the desired delivery; then when or if the location is correct, the liquid or gas is subjected to higher intensity ultrasound to generate intense cavitational events that can disrupt carriers or cell membranes. This combination of diagnostics followed by therapeutics (with the same construct) is called theranostics. This section will present clinical (or near clinical) examples of these two general approaches.

A search in September of 2013 revealed that there were yet no published reports of the application of ADV for therapeutic delivery in human medicine. However, there were several reports of ADV in mice, indicating that this technology was approaching, but had not yet arrived, in clinical medicine.

3.4.1. Drug Delivery Using ADV. While there are no publications of ADV for clinical drug delivery, there are some articles that describe the use of ADV for drug delivery to tumors in mice. These are from the laboratory of Dr. Natalya Rapoport of the University of Utah. The first study employed a formulation of doxorubicin-containing block copolymer micelles (poly lactic acid-polyethylene glycol, PLA-PEG) mixed with perfluoropentane [20, 64]. The carriers were formed by sonicating (at 20 kHz) a mixture of drug-loaded micelles and liquid PFC5. The resulting formulation had PFC5 nanosized droplets that they claimed were stabilized by some of the block copolymer and by some of the whole micelles, with the drug distributed in both the micelles and the nanodroplet surface. By adjusting the ratio of PFC5 to micellar suspension, they achieved a mixture of droplets and micelles that was injected into *nu/nu* mice bearing breast and ovarian tumors. In their first two papers they hypothesize that the droplets may have been transformed to "drug-loaded nanobubbles" by thermal activation before they extravasated in mouse tumors. However they did not measure what fraction of PFC5 droplets may have been thermally activated. They also hypothesized that both the micelles and nanobubbles extravasated into the tumor. The presence of the nanobubbles allowed imaging of the tumor at 14 MHz.

To execute the drug release, the tumors were insonated at 3 MHz and 2 W/cm^2 at a 20% duty cycle for 150 sec, resulting in cavitation of the thermally activated bubbles that released the drug they carried and also induced release from the nearby micelles. Following 4 treatments in 2 weeks, the tumors did not continue to grow at the same rate as control tumors (no carrier, no insonation) and as tumors that received the carrier but without insonation. In some cases the tumors grew again after several days, indicating that tumor therapy was transient. While the authors did not mention acoustic bubble vaporization by name, ADV probably did occur with liquid PFC5 nanodroplets that were small enough that the Laplace pressure prevented their thermal activation. Thus these studies are the first known publications of ADV for drug delivery in an animal model. The study also demonstrated the potential of theranostics in which the PFC5 nanodroplets functioned both to provide ultrasound contrast and drug delivery.

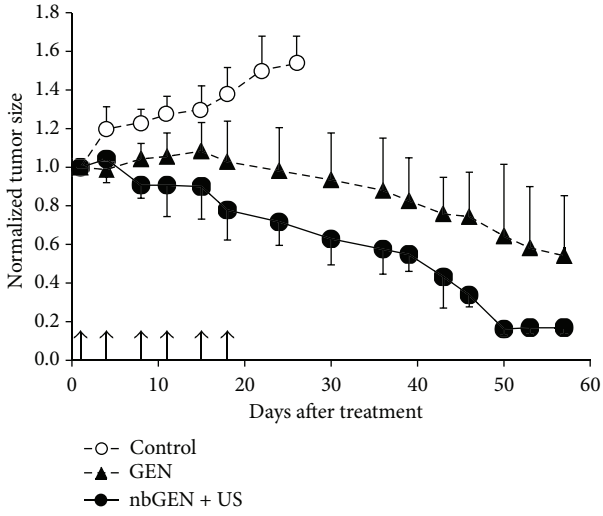

Figure 4: Breast tumor growth in mice for control tumor (open circles), tumors treated with a micellar PTX formulation (filled triangles), and nanodroplet PTX formulation combined with ultrasound (filled circles). Mean values plus/minus standard error are presented ($N = 3$). Arrows indicate days of treatment. Adapted by permission from reference [9].

The same research group did a later study that was similar to the first but which employed paclitaxel (Ptx) instead of doxorubicin, and the insonation parameters were slightly different [9]. Again micelles of Ptx in block copolymers were formed and mixed with a quantity of PFC5, followed by sonication at 20 kHz to form a mixture of micelles and 700 nm (peak average) nanodroplets stabilized by some of the polymer. This study enrolled mice bearing breast, ovarian, and pancreatic tumors. After intravenous injection, the tumors were visualized at 14 MHz and treated with 1 MHz insonation at 3.4 W/cm^2 for 1 min. This treatment was given 4 times in 2 weeks (ovarian cancer model), 6 times in 3 weeks (breast cancer model), or 8 times in 6 weeks (pancreatic cancer model). In all cases, the tumors receiving the formulation with insonation grew at a slower rate or regressed more than other controls. Figure 4 shows an example of tumor regression in the mouse model of breast cancer.

In this second study, the authors discussed acoustic droplet vaporization extensively, including the role of Laplace pressure and temperature. They attributed the positive results to liquid-to-gas transition in the tumor. They also discussed that droplets could be converted to gas by thermal processing and shearing in a syringe needle, in addition to acoustic activation. In a final interesting note, they observed that tumors treated by insonation of their formulation had less evidence of metastatic spread, which argues against the notion that ultrasonic cavitation in tumors can promote metastasis [65].

In a similar study to that mentioned first, a group in Beijing made a slight variation to the constructs of the Rapoport group. They used PLGA-PEG (poly lactic glycolic acid—PEG) instead of PLA-PEG to form doxorubicin-containing micelles; then they added PFC5 and sonicated to form stable droplets of less than 200 nm [66]. They claim that these were thermally activated to form gas bubbles by injection into mice at 37°C. The mice in their experiments hosted H22 tumors (mouse hepatocarcinoma). Again, the nanodroplet formulation combined with 40 kHz ultrasound at 0.7 W/cm^2 effectively suppressed tumor growth for 6 days, while the tumor continued to grow in controls without ultrasonic activation and in controls with neither ultrasound nor formulation. The report makes no mention of droplet vaporization, but probably ADV occurred since their droplet size was so small that Laplace pressure probably retained some of the droplets in a liquid state until ultrasonically activated.

3.4.2. Mechanisms of Drug Delivery. Unfortunately, none of the reports described above provide much accompanying evidence of mechanism *in vivo*. The Rapoport group published several papers of *in vitro* observations including cavitation thresholds [7, 67] and microscopic observations of bubble formation [67–69]. Both the Rapoport and the Du groups propose various scenarios and hypotheses that claim to be consistent with their *in vitro* and *in vivo* observations, but which are difficult to prove *in vivo*; yet these hypotheses must be substantiated before clinical application can commence.

For example, the group from Utah proposed that their nanobubbles enter the tumor by extravasation [20, 64]. The optimal size for extravasation is generally considered to be 100 to 300 nm [70], but particles as large as 750 nm may be extravasated in some tumors [37, 71]. In Rapoport's experiments with Dox-loaded constructs, a formulation of 0.5% polymer and 1% PFC5 was reported to form a bimodal distribution of droplets with peak sizes of 250 and 1328 nm. In the mouse experiments, a formulation of 0.5% polymer and 2% PFC5 was employed, but its size was not reported, so the PFC5 droplets may have been somewhat larger in those experiments. The smaller droplets may have extravasated if they were not thermally activated to gas droplets before insonation. Transformation of a 250 nm droplet to gas would result in a 1250 nm bubble, too large to extravasate. The observation that the combination of ultrasound and formulation was effective in retarding tumor growth suggests that nonactivated droplets did extravasate and became acoustically activated or that gas bubble formation and cavitation may have occurred in the capillaries in the tumor, leading perhaps to capillary disruption or at least increased capillary permeability to the drug or drug carriers (micelles or other droplets).

The Dox-loaded nanodroplets of the Chinese study were on the order of 160 nm in diameter, so they could have extravasated before acoustic activation [66]. However, if they were thermally activated to gas bubbles (as the authors claim), they may have been too large (~800 nm) to extravasate.

In the study of Ptx-loaded nanodroplets, the nanodroplets had a peak diameter of 700 nm [9]. These may have extravasated, although they are larger than the optimal size.

To comment on observations, in pursuing future studies it will be critical to know both the phase state (liquid or gas) and the size of particles in animal studies so that hypotheses

can be carefully formulated and tested. It would also be very useful to collect insonated and noninsonated tumors with the goal of assessing if accumulation of carriers is occurring (via extravasation) and perhaps perform microscopy work to validate the extravasation hypothesis. Another piece of information, perhaps more difficult to collect, is what effect a cavitating PFC5 bubble has upon local tissue within a tumor.

3.5. Other Applications of ADV. There are two other applications of ADV that have great potential for future clinical use. These are the use of ADV to form gas cavities through which much thermal energy can be deposited and the use of ADV in aberration correction. To our knowledge, neither is yet approaching clinical trials.

One intriguing application of ADV is its use as a nucleation agent for bubble-enhanced tumor ablation by high-intensity focused ultrasound (HIFU) [72]. In clinical practice, HIFU has been applied to treat solid malignant tumors, including the liver, prostate, breast, bladder, kidney, and soft-tissue sarcoma [73]. Absorption of the ultrasound energy in the focal area can produce localized temperature elevations and generate tissue necrosis without damaging the surrounding tissues [74]. Therefore, HIFU ablation provides a noninvasive modality with precise targeting of tissues for cancer treatment. Transformation of ultrasonic pressure waves to thermal energy is much more efficient in the presence of bubbles that oscillate and collapse, producing localized viscous heating. Recently, HIFU has been used with ADV of PFC5 nanoemulsions to enhance the heating produced by focused ultrasound *in vitro* and *in vivo* studies [22, 72, 75]. Their work has demonstrated that the nanoemulsions can be an effective nucleating agent for acoustic cavitation and can be employed to enhance HIFU-mediated heating locally. ADV may provide a means of increasing localized thermal ablation for cancer therapy that hopefully will soon be demonstrated in a preclinical setting.

Aberration correction is a mathematical technique applied to ultrasonic imaging data that corrects for the distortions that occur as ultrasound travels through various tissues [76]. Aberration is particularly annoying during imaging within the skull because of the various thicknesses and densities of cranial bone. One method to make the correction is a point-target technique that relies on sparsely distributed fixed points in space, imaged from various angles, from which aberration corrections are calculated [77]. Gas bubbles are a good source of point reflections [78], but introducing bubbles into the brain could potentially be problematic if they coalesce and occlude capillaries, and intra-cranial injection of bubbles is challenging. As before, the intravenous injection of small PFC droplets with slow clearance rates provides distributed points of gas in the brain when activated by transcranial ultrasound. ADV of PFC5 droplets has been proposed [79] and then applied in *ex vivo* skull models [76] and tissue mimicking gels [80]. While not yet in the clinic, ADV for aberration correction is a very promising strategy that could be developed for very controlled HIFU treatment of cancer or for precise drug delivery to the brain.

4. Clinical Potential and Application of Acoustic Droplet Vaporization

Applications of ADV in cardiac and vascular imaging first commenced nearly 2 decades ago, and then diminished within 10 years. While currently obsolete, this wave of using PFC5 droplets and microbubbles for imaging occurred because the droplets and perhaps microbubbles were sufficiently small that their clearance was slow and provided sustained ultrasound contrast for imaging the left heart and arterial circulation. Such imaging prior to that time could not be done at that time without intra-arterial injection, which is problematic both then and now. However, the ADV contrast agents were never approved by the FDA following clinical trials. In the late 1990s, the contrast agent Definity appeared. This small microbubble of perfluoropropane apparently found better clinical acceptance than EchoGen and its sister products. In our opinion, the use of ADV for standard clinical imaging of cardiovascular organs and systems will probably not experience any resurgence. Better contrast agents have come along, and hopefully even better contrast agents will arrive in the future. However, the brief use of ADV for vascular imaging set the stage for current and future applications in other areas, including occlusion, drug delivery, molecular imaging, and aberration correction.

To our knowledge, ADV for vascular occlusion has not yet been used clinically, although it has been used in animals [55, 58]. This application of ADV has significant clinical potential for several reasons. First, the perfluorocarbon droplets can be intravenously injected at a convenient site, can remain in the circulatory system, and then can be activated to form gas bubbles only at the site of insonation. Second, the occlusive bodies (gas bubbles) are not permanent and do not need to be retrieved at a later time. They will eventually dissolve away. Thus there is no concern for the retrieval of or the permanent residence of metal, ceramic, or polymeric materials in the tissues. While there will be competition in the clinic from other modes of vascular occlusion, we foresee that there is great potential here for clinical application in vital organ tissues (brain, liver, eye, etc.) in which revascularization after therapeutic healing is desired. One of the challenges is to create droplets that have stealth character and yet when activated to gas bubbles will easily coalesce into bubbles sufficiently large to occlude arterioles and capillaries. Stealth character is usually endowed by incorporating polyethyleneglycol (PEG) chains in the surfactants that stabilize the vesicles [81]. However, the presence of PEG chains may cause bubbles to repel each other and moderate the coalescence. This optimal balance needs to be addressed.

Clinical application of ADV in molecular targeting and therapeutic delivery of drugs and genes is probable but still requires much work. Preclinical animal models (mice) have shown potential. Both applications require very specific molecular targeting to attach the PFC nanodroplets to the correct tissues, although some therapeutic delivery could be done via passive targeting [82]. These applications of ADV in clinical medicine may be delayed until very specific targeting is developed further. The combination of imaging with drug delivery will be very powerful in clinical medicine. However,

this same combination may slow the approval by regulatory agencies that currently do not have infrastructure for approval of combined devices, such as a combined imaging agent and a therapeutic drug [83]. This regulatory obstacle may temper the enthusiasm of pharmaceutical companies to pursue development, given the expense and risk of clinical trials.

While ADV for nucleation of bubbles in HIFU therapy may have clinical application, its use is probably years away for critical tissues such as the brain and vital organs. Similarly, we foresee that ADV for aberration correction may take some time, given that other correction algorithms are also competing for clinical attention.

5. Remaining Critical Issues

As with all therapeutic agents and procedures, thorough research must be done to ensure the safety and efficacy of the therapy. These concerns should guide the future directions of research in therapeutic applications of ADV.

From a medical point of view, issues in safety of targeted agents and safety of contrast agents are fundamentally important. This includes chemical safety (nontoxicity) and physical safety, the main concern of which is premature expansion leading to gas bubble occlusion of capillaries. While the perfluorocarbons of interest are deeded nontoxic, the surfactants that stabilize the droplets must also be considered. Natural phospholipids, polysaccharides, and human proteins may be the best stabilizing agents to use. Stabilization by synthetic polymers will remain suspect until nontoxicity is proven [84].

More data on the kinetics of phase transformation under dynamic shear stresses are needed to ensure to the medical community that premature and nontargeted expansion is a rarity. More measurements need to be done to establish the acoustic thresholds for gas expansion as a function of acoustic parameters (frequency, amplitude, pulse length, etc.) and the characteristics of the droplets (chemical composition, size, stabilizing surfactants, temperature, etc.). The medical community needs a reliable and controllable off/on switch to engender confidence that gas bubble will be formed only when and where they are desired. Uncontrolled formation of microbubbles may cause side effects observed in experimental studies, including hemolysis and endothelial damage [85, 86].

A safety issue (which very few if any studies have mentioned) is cavitation after formation of a gas bubble. If a bubble is formed at the beginning of an acoustic pulse, what possible damage may occur during the remainder of the pulse, caused by the oscillation and collapse of the cavitating bubble? In some cases, such as drug delivery, cavitation may be a desired by-product that may enhance drug delivery. In HIFU, strong cavitation is the desired effect. However, for molecular targeting, occlusion, imaging, and aberration correction, cavitation may produce unwanted tissue damage. In such cases it will be essential to know what combination of intensity and pulse length is necessary to form the gas bubble with minimal subsequent damage by cavitation.

Another safety issue is the development of sensitivity or allergic reactions to the ADV constructs. We have not found any reports of sensitivities to small amounts of perfluorocarbons; this needs to be studied in more depth. Also, attachment of proteins to nanodroplets as targeting ligands may lead to allergies to those proteins.

As a foreign body, microbubbles may be cleared by the phagocytic cells of the reticuloendothelial system [87]. From 5 to 10 minutes after injection, the EchoGen (PFC5 gas) is exhaled via lungs, while the components of the shell are metabolized or filtered by the kidney and eliminated by the liver [88]. The microbubble sizes were 2–5 μm in diameter and circulated in the body. Nonactivated PFC droplets are much smaller and may not be cleared by the same mechanisms as bubbles. More research is needed to estimate the residence times and clearance rates.

From a science and engineering viewpoint, the effectiveness of the nanodroplet is almost as important as safety. There are a number of issues regarding efficacy that still need to be addressed. These include very specific binding for molecular targeting and drug delivery, the size and design of stealth polymers in masking the constructs from the RES system, and the appropriate size for passive accumulation via extravasation. With respect to feasible commercialization, one must always consider the ease of manufacturing and the shelf life and storage of the product.

Acknowledgment

The authors thank the National Science Council of Taiwan (no. NSC: 101-2917-I-082) for funding of postdoctoral research abroad.

References

[1] C. M. Sehgal, P. H. Arger, and C. R. Pugh, "Sonographic enhancement of renal cortex by contrast media," *Journal of Ultrasound in Medicine*, vol. 14, no. 10, pp. 741–748, 1995.

[2] F. Forsberg, J.-B. Liu, D. A. Merton, N. M. Rawool, and B. B. Goldberg, "Parenchymal enhancement and tumor visualization using a new sonographic contrast agent," *Journal of Ultrasound in Medicine*, vol. 14, no. 12, pp. 949–957, 1995.

[3] T. Albrecht, D. O. Cosgrove, J. M. Correas, L. Rallidis, P. Nihoyanopoulos, and N. Patel, "Renal, hepatic, and cardiac enhancement on Doppler and gray-scale sonograms obtained with EchoGen," *Academic Radiology*, vol. 3, pp. S198–S200, 1996.

[4] O. D. Kripfgans, J. B. Fowlkes, D. L. Miller, O. P. Eldevik, and P. L. Carson, "Acoustic droplet vaporization for therapeutic and diagnostic applications," *Ultrasound in Medicine and Biology*, vol. 26, no. 7, pp. 1177–1189, 2000.

[5] R. L. Rowley, W. V. Wilding, J. L. Oscarson, and N. F. Giles, "DIPPR Data Compilation of Pure Chemical Properties," 2012, http://dippr.byu.edu/.

[6] G. M. Lanza, K. D. Wallace, M. J. Scott et al., "A novel site-targeted ultrasonic contrast agent with broad biomedical application," *Circulation*, vol. 94, no. 12, pp. 3334–3340, 1996.

[7] N. Rapoport, K.-H. Nam, R. Gupta et al., "Ultrasound-mediated tumor imaging and nanotherapy using drug loaded, block copolymer stabilized perfluorocarbon nanoemulsions," *Journal of Controlled Release*, vol. 153, no. 1, pp. 4–15, 2011.

[8] W. G. Pitt, K. X. Perez, R. N. Singh, G. A. Husseini, and D. R. Jack, "Phase transitions of perfluorocarbon nanoemulsions induced with ultrasound: a mathematical model," *Ultrasonics Sonochemistry*, 2013.

[9] N. Y. Rapoport, A. M. Kennedy, J. E. Shea, C. L. Scaife, and K.-H. Nam, "Controlled and targeted tumor chemotherapy by ultrasound-activated nanoemulsions/microbubbles," *Journal of Controlled Release*, vol. 138, no. 3, pp. 268–276, 2009.

[10] M. Blander and J. L. Katz, "Bubble nucleation in liquids," *AIChE Journal*, vol. 21, no. 5, pp. 833–848, 1975.

[11] P. C. Hiemenz and R. Rajagopalan, *Principles of Colloid and Surface Chemistry*, Marcel Dekker, New York, NY, USA, 3rd edition, 1997.

[12] L. Y. Clasohm, I. U. Vakarelski, R. R. Dagastine, D. Y. C. Chan, G. W. Stevens, and F. Grieser, "Anomalous pH dependent stability behavior of surfactant-free nonpolar oil drops in aqueous electrolyte solutions," *Langmuir*, vol. 23, no. 18, pp. 9335–9340, 2007.

[13] P. S. Sheeran, S. Luois, P. A. Dayton, and T. O. Matsunaga, "Formulation and acoustic studies of a new phase-shift agent for diagnostic and therapeutic ultrasound," *Langmuir*, vol. 27, no. 17, pp. 10412–10420, 2011.

[14] P. S. Sheeran, S. H. Luois, L. B. Mullin, T. O. Matsunaga, and P. A. Dayton, "Design of ultrasonically-activatable nanoparticles using low boiling point perfluorocarbons," *Biomaterials*, vol. 33, no. 11, pp. 3262–3269, 2012.

[15] *ASME Steam Tables*, American Society of Mechanical Engineers, New York, NY, USA, 2006.

[16] J. L. Green, D. J. Durben, G. H. Wolf, and C. A. Angell, "Water and solutions at negative pressure: Roman spectroscopic study to -80 megapascals," *Science*, vol. 249, no. 4969, pp. 649–652, 1990.

[17] P. S. Sheeran, T. O. Matsunaga, and P. A. Dayton, "Phase-transition thresholds and vaporization phenomena for ultrasound phase-change nanoemulsions assessed via high-speed optical microscopy," *Physics in Medicine and Biology*, vol. 58, no. 13, pp. 4513–4534, 2013.

[18] T. Giesecke and K. Hynynen, "Ultrasound-mediated cavitation thresholds of liquid perfluorocarbon droplets in vitro," *Ultrasound in Medicine and Biology*, vol. 29, no. 9, pp. 1359–1365, 2003.

[19] O. D. Kripfgans, M. L. Fabiilli, P. L. Carson, and J. B. Fowlkes, "On the acoustic vaporization of micrometer-sized droplets," *Journal of the Acoustical Society of America*, vol. 116, no. 1, pp. 272–281, 2004.

[20] N. Rapoport, Z. Gao, and A. M. Kennedy, "Multifunctional nanoparticles for combining ultrasonic tumor imaging and targeted chemotherapy," *Journal of the National Cancer Institute*, vol. 99, no. 14, pp. 1095–1106, 2007.

[21] O. D. Kripfgans, C. M. Orifici, P. L. Carson, K. A. Ives, O. P. Eldevik, and J. B. Fowlkes, "Acoustic droplet vaporization for temporal and spatial control of tissue occlusion: a kidney study," *IEEE Transactions on Ultrasonics, Ferroelectrics, and Frequency Control*, vol. 52, no. 7, pp. 1101–1108, 2005.

[22] M. Zhang, M. L. Fabiilli, K. J. Haworth et al., "Acoustic droplet vaporization for enhancement of thermal ablation by high intensity focused ultrasound," *Academic Radiology*, vol. 18, no. 9, pp. 1123–1132, 2011.

[23] O. Shpak, L. Stricker, M. Versluis, and D. Lohse, "The role of gas in ultrasonically driven vapor bubble growth," *Physics in Medicine and Biology*, vol. 58, no. 8, pp. 2523–2535, 2013.

[24] N. Reznik, O. Shpak, E. C. Gelderblom et al., "The efficiency and stability of bubble formation by acoustic vaporization of submicron perfluorocarbon droplets," *Ultrasonics*, vol. 53, no. 7, pp. 1368–1376, 2013.

[25] C. H. Wang, S. T. Kang, and C. K. Yeh, "Superparamagnetic iron oxide and drug complex-embedded acoustic droplets for ultrasound targeted theranosis," *Biomaterials*, vol. 34, no. 7, pp. 1852–1861, 2013.

[26] K. Shiraishi, R. Endoh, H. Furuhata et al., "A facile preparation method of a PFC-containing nano-sized emulsion for theranostics of solid tumors," *International Journal of Pharmaceutics*, vol. 421, no. 2, pp. 379–387, 2011.

[27] S.-T. Kang and C.-K. Yeh, "Intracellular acoustic droplet vaporization in a single peritoneal macrophage for drug delivery applications," *Langmuir*, vol. 27, no. 21, pp. 13183–13188, 2011.

[28] A. Kabalnov, J. Weers, R. Arlauskas, and T. Tarara, "Phospholipids as emulsion stabilizers—1. Interfacial tensions," *Langmuir*, vol. 11, no. 8, pp. 2966–2974, 1995.

[29] M. Javadi, W. G. Pitt, C. M. Tracy et al., "Ultrasonic gene and drug delivery using eLiposomes," *Journal of Controlled Release*, vol. 167, no. 1, pp. 92–100, 2013.

[30] J. R. Lattin, D. M. Belnap, and W. G. Pitt, "Formation of eLiposomes as a drug delivery vehicle," *Colloids and Surfaces B*, vol. 89, no. 1, pp. 93–100, 2012.

[31] J.-M. Correas and S. D. Quay, "EchoGen emulsion: a new ultrasound contrast agent based on phase shift colloids," *Clinical Radiology*, vol. 51, no. 1, pp. 11–14, 1996.

[32] A. H. Lo, O. D. Kripfgans, P. L. Carson, E. D. Rothman, and J. B. Fowlkes, "Acoustic droplet vaporization threshold: effects of pulse duration and contrast agent," *IEEE Transactions on Ultrasonics, Ferroelectrics, and Frequency Control*, vol. 54, no. 5, pp. 933–945, 2007.

[33] K. C. Schad and K. Hynynen, "In vitro characterization of perfluorocarbon droplets for focused ultrasound therapy," *Physics in Medicine and Biology*, vol. 55, no. 17, pp. 4933–4947, 2010.

[34] R. Williams, C. Wright, E. Cherin et al., "Characterization of submicron phase-change perfluorocarbon droplets for extravascular ultrasound imaging of cancer," *Ultrasound in Medicine and Biology*, vol. 39, no. 3, pp. 475–489, 2013.

[35] G. A. Husseini and W. G. Pitt, "The use of ultrasound and micelles in cancer treatment," *Journal of Nanoscience and Nanotechnology*, vol. 8, no. 5, pp. 2205–2215, 2008.

[36] C.-Y. Lin, T.-M. Liu, C.-Y. Chen et al., "Quantitative and qualitative investigation into the impact of focused ultrasound with microbubbles on the triggered release of nanoparticles from vasculature in mouse tumors," *Journal of Controlled Release*, vol. 146, no. 3, pp. 291–298, 2010.

[37] S. K. Hobbs, W. L. Monsky, F. Yuan et al., "Regulation of transport pathways in tumor vessels: role of tumor type and microenvironment," *Proceedings of the National Academy of Sciences of the United States of America*, vol. 95, no. 8, pp. 4607–4612, 1998.

[38] S. M. Moghimi and S. S. Davis, "Innovations in avoiding particle clearance from blood by Kupffer cells: cause for reflection," *Critical Reviews in Therapeutic Drug Carrier Systems*, vol. 11, no. 1, pp. 31–59, 1994.

[39] M. Ogiwara, "Clearance and maximum removal rate of liposome in normal and impaired liver of rat," *Gastroenterologia Japonica*, vol. 19, no. 1, pp. 34–40, 1984.

[40] Y. E. Rahman, E. A. Cerny, and K. R. Patel, "Differential uptake of liposomes varying in size and lipid composition by

parenchyma and Kupffer cells of mouse liver," *Life Sciences*, vol. 31, no. 19, pp. 2061–2071, 1982.

[41] O. Couture, P. D. Bevan, E. Cherin, K. Cheung, P. N. Burns, and F. S. Foster, "Investigating perfluorohexane particles with high-frequency ultrasound," *Ultrasound in Medicine and Biology*, vol. 32, no. 1, pp. 73–82, 2006.

[42] P. Grayburn, "Perflenapent emulsion (EchoGen): a new long-acting phase-shift agent for contrast echocardiography," *Clinical Cardiology*, vol. 20, no. 10, supplement, pp. 112–118, 1997.

[43] J. D. Kasprzak and F. J. Ten Cate, "New ultrasound contrast agents for left ventricular and myocardial opacification," *Herz*, vol. 23, no. 8, pp. 474–482, 1998.

[44] H. Ragde, G. M. Kenny, G. P. Murphy, and K. Landin, "Transrectal ultrasound microbubble contrast angiography of the prostate," *The Prostate*, vol. 32, no. 4, pp. 279–283, 1997.

[45] P. A. Grayburn, J. L. Weiss, T. C. Hack et al., "Phase III multicenter trial comparing the efficacy of 2% dodecafluoropentane emulsion (EchoGen) and sonicated 5% human albumin (Albunex) as ultrasound contrast agents in patients with suboptimal echocardiograms," *Journal of the American College of Cardiology*, vol. 32, no. 1, pp. 230–236, 1998.

[46] W. G. Hundley, A. M. Kizilbash, I. Afridi, F. Franco, R. M. Peshock, and P. A. Grayburn, "Administration of an intravenous perfluorocarbon contrast agent improves echocardiographic determination of left ventricular volumes and ejection fraction: comparison with cine magnetic resonance imaging," *Journal of the American College of Cardiology*, vol. 32, no. 5, pp. 1426–1432, 1998.

[47] M. L. Main and P. A. Grayburn, "Clinical applications of transpulmonary contrast echocardiography," *American Heart Journal*, vol. 137, no. 1, pp. 144–153, 1999.

[48] J.-M. Correas, A. R. Meuter, E. Singlas, D. R. Kessler, D. Worah, and S. C. Quay, "Human pharmacokinetics of a perfluorocarbon ultrasound contrast agent evaluated with gas chromatography," *Ultrasound in Medicine and Biology*, vol. 27, no. 4, pp. 565–570, 2001.

[49] P. A. Grayburn, J. M. Erickson, J. Escobar, L. Womack, and C. E. Velasco, "Peripheral intravenous myocardial contrast echocardiography using a 2% dodecafluoropentane emulsion: identification of myocardial risk area and infarct size in the canine model of ischemia," *Journal of the American College of Cardiology*, vol. 26, no. 5, pp. 1340–1347, 1995.

[50] F. Forsberg, R. Roy, D. A. Merton et al., "Conventional and hypobaric activation of an ultrasound contrast agent," *Ultrasound in Medicine and Biology*, vol. 24, no. 8, pp. 1143–1150, 1998.

[51] R. Totaro, M. Del Sette, and C. Marini, "Echocontrast agents in neurosonology," *Functional Neurology*, vol. 14, no. 4, pp. 235–239, 1999.

[52] K. Tiemann, S. Lohmeier, S. Kuntz et al., "Real-time contrast echo assessment of myocardial perfusion at low emission power: first experimental and clinical results using power pulse inversion imaging," *Echocardiography*, vol. 16, no. 8, pp. 799–810, 1999.

[53] R. I. White Jr., "Embolotherapy in vascular disease," *American Journal of Roentgenology*, vol. 142, no. 1, pp. 27–30, 1984.

[54] M. R. Lyaker, D. B. Tulman, G. T. Dimitrova, R. H. Pin, and T. J. Papadimos, "Arterial embolism," *International Journal of Critical Illness and Injury Science*, vol. 3, no. 1, pp. 77–87, 2013.

[55] N. Matsuura, R. Williams, I. Gorelikov et al., "Nanoparticle-loaded perfluorocarbon droplets for imaging and therapy," in *Proceedings of the IEEE Interantional Ultrasonic Symposium Proceedings*, 2009.

[56] M. Zhang, M. L. Fabiilli, K. J. Haworth et al., "Initial investigation of acoustic droplet vaporization for occlusion in canine kidney," *Ultrasound in Medicine and Biology*, vol. 36, no. 10, pp. 1691–1703, 2010.

[57] J. R. Lattin, W. G. Pitt, D. M. Belnap, and G. A. Husseini, "Ultrasound-induced calcein release from eLiposomes," *Ultrasound in Medicine and Biology*, vol. 38, no. 12, pp. 2163–2173, 2012.

[58] S. Samuel, A. Duprey, M. L. Fabiilli, J. L. Bull, and J. B. Fowlkes, "In vivo microscopy of targeted vessel occlusion employing acoustic droplet vaporization," *Microcirculation*, vol. 19, no. 6, pp. 501–509, 2012.

[59] M. Zhang, M. Fabiilli, P. Carson et al., "Acoustic droplet vaporization for the enhancement of ultrasound thermal therapy," in *Proceedings of the IEEE International Ultrasonics Symposium (IUS '10)*, pp. 221–224, October 2010.

[60] M. L. Fabiilli, K. J. Haworth, N. H. Fakhri, O. D. Kripfgans, P. L. Carson, and J. B. Fowlkes, "The role of inertial cavitation in acoustic droplet vaporization," *IEEE Transactions on Ultrasonics, Ferroelectrics, and Frequency Control*, vol. 56, no. 5, pp. 1006–1017, 2009.

[61] D. Fukumura and R. K. Jain, "Tumor microvasculature and microenvironment: targets for anti-angiogenesis and normalization," *Microvascular Research*, vol. 74, no. 2-3, pp. 72–84, 2007.

[62] N. Rapoport, A. M. Kennedy, J. E. Shea, C. L. Scaife, and K.-H. Nam, "Ultrasonic nanotherapy of pancreatic cancer: lessons from ultrasound imaging," *Molecular Pharmaceutics*, vol. 7, no. 1, pp. 22–31, 2010.

[63] C.-H. Wang, S.-T. Kang, Y.-H. Lee, Y.-L. Luo, Y.-F. Huang, and C.-K. Yeh, "Aptamer-conjugated and drug-loaded acoustic droplets for ultrasound theranosis," *Biomaterials*, vol. 33, no. 6, pp. 1939–1947, 2012.

[64] Z. Gao, A. M. Kennedy, D. A. Christensen, and N. Y. Rapoport, "Drug-loaded nano/microbubbles for combining ultrasonography and targeted chemotherapy," *Ultrasonics*, vol. 48, no. 4, pp. 260–270, 2008.

[65] D. L. Miller and C. Dou, "The potential for enhancement of mouse melanoma metastasis by diagnostic and high-amplitude ultrasound," *Ultrasound in Medicine and Biology*, vol. 32, no. 7, pp. 1097–1101, 2006.

[66] L. Du, Y. Jin, W. Zhou, and J. Zhao, "Ultrasound-triggered drug release and enhanced anticancer effect of doxorubicin-loaded poly(D,L-lactide-co- glycolide)-methoxy-poly(ethylene glycol) nanodroplets," *Ultrasound in Medicine and Biology*, vol. 37, no. 8, pp. 1252–1258, 2011.

[67] N. Rapoport, D. A. Christensen, A. M. Kennedy, and K.-H. Nam, "Cavitation properties of block copolymer stabilized phase-shift nanoemulsions used as drug carriers," *Ultrasound in Medicine and Biology*, vol. 36, no. 3, pp. 419–429, 2010.

[68] B. E. O'Neill and N. Rapoport, "Phase-shift, stimuli-responsive drug carriers for targeted delivery," *Therapeutic Delivery*, vol. 2, no. 9, pp. 1165–1187, 2011.

[69] N. Y. Rapoport, A. L. Efros, D. A. Christensen, A. M. Kennedy, and K.-H. Nam, "Microbubble generation in phase-shift nanoemulsions used as anticancer drug carriers," *Bubble Science Engineering & Technology*, vol. 1, no. 1-2, pp. 31–39, 2009.

[70] Y. H. Bae and K. Park, "Targeted drug delivery to tumors: myths, reality and possibility," *Journal of Controlled Release*, vol. 153, no. 3, pp. 198–205, 2011.

[71] R. B. Campbell, "Tumor physiology and delivery of nanopharmaceuticals," *Anti-Cancer Agents in Medicinal Chemistry*, vol. 6, no. 6, pp. 503–512, 2006.

[72] P. Zhang and T. Porter, "An in vitro study of a phase-shift nanoemulsion: a potential nucleation agent for bubble-enhanced HIFU tumor ablation," *Ultrasound in Medicine and Biology*, vol. 36, no. 11, pp. 1856–1866, 2010.

[73] Y. F. Zhou, "High intensity focused ultrasound in clinical tumor ablation," *World Journal of Clinical Oncology*, vol. 2, no. 1, pp. 8–27, 2011.

[74] H.-L. Liu, Y.-Y. Chen, W.-S. Chen, T.-C. Shih, J.-S. Chen, and W.-L. Lin, "Interactions between consecutive sonications for characterizing the thermal mechanism in focused ultrasound therapy," *Ultrasound in Medicine and Biology*, vol. 32, no. 9, pp. 1411–1421, 2006.

[75] P. Zhang, J. A. Kopechek, and T. M. Porter, "The impact of vaporized nanoemulsions on ultrasound-medicated ablation," *Journal of Therapeutic Ultrasound*, vol. 1, no. 2, pp. 1–13, 2013.

[76] K. J. Haworth, J. B. Fowlkes, P. L. Carson, and O. D. Kripfgans, "Towards aberration correction of transcranial ultrasound using acoustic droplet vaporization," *Ultrasound in Medicine and Biology*, vol. 34, no. 3, pp. 435–445, 2008.

[77] S.-E. Måsøy, B. Angelsen, and T. Varslot, "Estimation of ultrasound wave aberration with signals from random scatterers," *Journal of the Acoustical Society of America*, vol. 115, no. 6, pp. 2998–3009, 2004.

[78] D. Psychoudakis, J. B. Fowlkes, J. L. Volakis, and P. L. Carson, "Potential of microbubbles for use as point targets in phase aberration correction," *IEEE Transactions on Ultrasonics, Ferroelectrics, and Frequency Control*, vol. 51, no. 12, pp. 1639–1647, 2004.

[79] O. D. Kripfgans, J. B. Fowlkes, M. Woydt, O. P. Eldevik, and P. L. Carson, "In vivo droplet vaporization for occlusion therapy and phase aberration correction," *IEEE Transactions on Ultrasonics, Ferroelectrics, and Frequency Control*, vol. 49, no. 6, pp. 726–738, 2002.

[80] C. M. Carneal, O. D. Kripfgans, J. Krücker, P. L. Carson, and J. B. Fowlkes, "A tissue-mimicking ultrasound test object using droplet vaporization to create point targets," *IEEE Transactions on Ultrasonics, Ferroelectrics, and Frequency Control*, vol. 58, no. 9, pp. 2013–2025, 2011.

[81] A. S. Manjappa, K. R. Chaudhari, M. P. Venkataraju et al., "Antibody derivatization and conjugation strategies: application in preparation of stealth immunoliposome to target chemotherapeutics to tumor," *Journal of Controlled Release*, vol. 150, no. 1, pp. 2–22, 2011.

[82] H. Maeda, H. Nakamura, and J. Fang, "The EPR effect for macromolecular drug delivery to solid tumors: improvement of tumor uptake, lowering of systemic toxicity, and distinct tumor imaging in vivo," *Advanced Drug Delivery Reviews*, vol. 65, pp. 71–79, 2013.

[83] R. Duncan and R. Gaspar, "Nanomedicine(s) under the microscope," *Molecular Pharmaceutics*, vol. 8, no. 6, pp. 2101–2141, 2011.

[84] W. Chang, M. Edirisinghe, and E. Stride, "Ultrasound mediated release from stimuli-responsive core-shell capsules," *Journal of Materials Chemistry B*, vol. 1, no. 32, pp. 3962–3961, 2013.

[85] A. A. Brayman and M. W. Miller, "Acoustic cavitation nuclei survive the apparent ultrasonic destruction of albunex microspheres," *Ultrasound in Medicine and Biology*, vol. 23, no. 5, pp. 793–796, 1997.

[86] T. Ye and J. L. Bull, "Direct numerical simulations of microbubble expansion in gas embolotherapy," *Journal of Biomechanical Engineering*, vol. 126, no. 6, pp. 745–759, 2004.

[87] F. Forsberg, B. B. Goldberg, J.-B. Liu, D. A. Merton, N. M. Rawool, and W. T. Shi, "Tissue-specific US contrast agent for evaluation of hepatic and splenic parenchyma," *Radiology*, vol. 210, no. 1, pp. 125–132, 1999.

[88] E. Quaia, "Microbubble ultrasound contrast agents: an update," *European Radiology*, vol. 17, no. 8, pp. 1995–2008, 2007.

Hindawi Publishing Corporation
BioMed Research International
Volume 2013, Article ID 839683, 8 pages
http://dx.doi.org/10.1155/2013/839683

Review Article

Microfluidics for Synthesis of Peptide-Based PET Tracers

Yang Liu,[1,2,3,4] Mei Tian,[1,2,3,4] and Hong Zhang[1,2,3,4]

[1] *Department of Nuclear Medicine, Second Affiliated Hospital of Zhejiang University School of Medicine, 88 Jiefang Road, Hangzhou, Zhejiang 310009, China*
[2] *Zhejiang University Medical PET Center, Zhejiang University, 88 Jiefang Road, Hangzhou, Zhejiang 310009, China*
[3] *Institute of Nuclear Medicine and Molecular Imaging, Zhejiang University, 88 Jiefang Road, Hangzhou, Zhejiang 310009, China*
[4] *Key Laboratory of Medical Molecular Imaging of Zhejiang Province, 88 Jiefang Road, Hangzhou, Zhejiang 310009, China*

Correspondence should be addressed to Hong Zhang; hzhang21@gmail.com

Received 26 July 2013; Revised 14 September 2013; Accepted 17 September 2013

Academic Editor: Yasuhisa Fujibayashi

Positron emission tomography (PET) is a powerful noninvasive tool for acquisition of the physiological parameters in human and animals with the help of PET tracers. Among all the PET tracers, radiolabeled peptides have been widely explored for cancer-related receptor imaging due to their high affinity and specificity to receptors. But radiochemistry procedures for production of peptide-based PET tracers are usually complex, which makes large-scale clinical studies relatively challenging. New radiolabeling technologies which could simplify synthesis and purification procedures, are extremely needed. Over the last decade, microfluidics and lab-on-a-chip (LOC) technology have boomed as powerful tools in the field of organic chemistry, which potentially provide significant help to the PET chemistry. In this minireview, microfluidic radiolabeling technology is described and its application for synthesis of peptide-based PET tracers is summarized and discussed.

1. Introduction

Positron emission tomography (PET) is increasingly being used for *in vivo* biochemical, physiological, and pharmacological process visualization and is also routinely used for screening, diagnosing, and staging of cancer. With the help of PET tracers and PET scanners, physiological parameters (like blood flow, metabolism, receptor properties, drug distribution, and gene expression) in the living human and animal bodies could be studied noninvasively. These PET tracers, including small molecules, peptides, antibodies, are radiolabeled with short-lived radioisotopes. Among these tracers, radiolabeled peptides have been widely explored for cancer imaging due to their high affinity and specificity to many kinds of cancer-related receptors. Peptide-based PET tracers have the following advantages: (1) peptides usually have very high affinity and specificity to the target (receptor); (2) compared to biomacromolecules like antibodies, peptides are easy to synthesize and characterize; (3) rapid clearance from the blood and nontarget tissues. A lot of peptide-based PET tracers are undergoing clinical trials, like the ^{18}F-labeled RGD and ^{68}Ga-labeled Octreotide [1, 2]. However, large-scale clinical studies and applications are relatively challenging due to the complex radiochemistry procedures for peptide-based PET tracers, especially for ^{18}F-labeled tracers which usually require a laborious and time-consuming multistep process. Radiochemists are continually working on the development of new methods and technologies for the preparation of PET tracers.

During the last several decades, microfluidics and lab-on-a-chip (LOC) technologies have boomed as powerful tools in the field of organic chemistry, showing characteristics like enhanced heat and mass transfer, reduction of reagent consuming and hazardous waste, which potentially provide significant help to the PET chemistry. Applications of microfluidic chemistry in radiopharmaceutical synthesis have also drawn increasing attention [5–9]. Microfluidic system could increase the overall efficiency of radiolabeling reaction remarkably. ^{18}F-FDG production by the microfluidic system has been successfully demonstrated [10], and a lot of other PET tracers have been produced successfully. Compared with small molecules, synthesis of peptide-based PET

Table 1: Receptors for the peptide-based PET tracers [11–14].

Receptors	Peptide	Cancer	Labeling
Somatostatin receptor	Somatostatin	Neuroendocrine tumors	^{68}Ga-DOTA, ^{68}Ga-NOTA, ^{64}Cu-TETA, ^{64}Cu-DOTA, ^{64}Cu-NOTA, ^{64}Cu-CB-TE2A, ^{18}F-NFP, ^{18}F-SFB, and so forth
Gastrin-releasing peptide receptor (GRPR)	Bombesin	Prostate cancer, breast cancer, Gastrointestinal stromal tumor	
$\alpha_v\beta_3$-integrin	RGD	Brain cancer, lung cancer, breast cancer, and so forth	
Melanocortin 1 receptor (MC1R)	α-MSH	Melanomas	^{18}F-SFB, ^{68}Ga-DOTA, ^{64}Cu-TETA, ^{64}Cu-DOTA, ^{64}Cu-CB-TE2A
Cholecystokinin B/gastrin receptor (CCK_2/CCK-B)	CCK/gastrin	Medullary thyroid cancer	^{18}F-SFB, ^{68}Ga-DOTA, ^{64}Cu-DOTA
Glucagon-like peptide-1 receptor (GLP-1)	Exendin	Insulinoma cancer	^{18}F-FBEM, ^{68}Ga-DOTA
Neurotensin receptor (NTR1)	Neurotensin	Small cell lung cancer, colon cancer, and so forth	^{68}Ga-DOTA ^{18}F-FB
Neuropeptide Y receptor (Y1)	NPY	Breast cancer, prostate cancer	^{64}Cu-DOTA
Luteinizing hormone-releasing hormone receptor (LHRH-R)	LHRH	Prostate cancer, breast cancer, and so forth	^{68}Ga-DOTA
Neurokinin 1 receptor (NK-1)	Substance P	Glioblastoma	
Vasoactive intestinal peptide **receptor** (VIP-R)	Vasoactive intestinal peptide (VIP)	Prostate cancer	^{64}Cu-DOTA ^{18}F-FB
Pituitary adenylate cyclase-activating peptide (PACAP) **receptor**	Pituitary adenylate cyclase-activating peptide (PACAP)	Breast cancer	^{64}Cu-DOTA
Chemokine receptor 4 (CXCR4)	CXCR4	Lymphatic system, lung cancer, and so forth	^{18}F-SFB, ^{68}Ga-DOTA, ^{64}Cu-DOTA

Table 2: Commonly used radioisotopes for peptide-based PET tracer.

Radionuclide	Half-life	E_{max} (β^+)/abundance	Production	Chemistry
^{18}F	109.8 min	634 Kev/97%	Cyclotron	Organic chemistry Chelation chemistry
^{64}Cu	12.8 h	656 Kev/19%	Cyclotron	Chelation chemistry
^{68}Ga	67.6 min	1899 Kev/89%	Generator	Chelation chemistry

tracers requires milder reaction conditions and strict chromatographic purification. Microfluidic system allows lower precursor consumption which simplified the purification, and the enhanced heat and mass transfer in microfluidic reactors can provide higher labeling yields under milder reaction conditions, so microfluidic system has good potential to play an important role in production of peptide-based PET tracers.

In this minireview, microfluidic radiolabeling technology is described and its application for synthesis of peptide-based PET tracers is summarized and discussed.

2. Peptide-Based PET Tracers

Biological active peptides are involved in many biochemical processes, like immune response and information transmission, and they play important roles in cellular communication and cell proliferation. On the other hand, a variety of receptors are found to be expressed on the membrane and possess very high affinity to specific peptides. Particular receptors are often massively overexpressed in cancer tissues, so peptide ligands could be utilized as targeting tools for PET imaging. Representative targets for peptide-based PET tracers are listed in Table 1.

Common radioisotopes used for peptide radiolabeling are listed in Table 2; half-lives of these radioisotopes (^{18}F: $t_{1/2}$ = 109.8 min, ^{68}Ga: $t_{1/2}$ = 67.6 min, ^{64}Cu: $t_{1/2}$ = 12.8 h) are suitable for the pharmacokinetics of most peptides. ^{18}F is one of the most widely used radionuclides for diagnostic PET imaging because of its unique nuclear and chemical properties [15]. ^{18}F-labeling of peptides can be achieved via prosthetic groups, such as N-succinimidyl-4-^{18}F-fluorobenzoate (^{18}F-SFB) [16] and 4-nitrophenyl 2-^{18}F-fluoropropionate (^{18}F-NFP) [17]. In recent years, a facile, 1-step Al^{18}F method has been developed and demonstrated as a very promising method for radiofluorination of peptides, which does not require on-site cyclotron by use of the commonly available sodium ^{18}F-fluoride solutions [18–20].

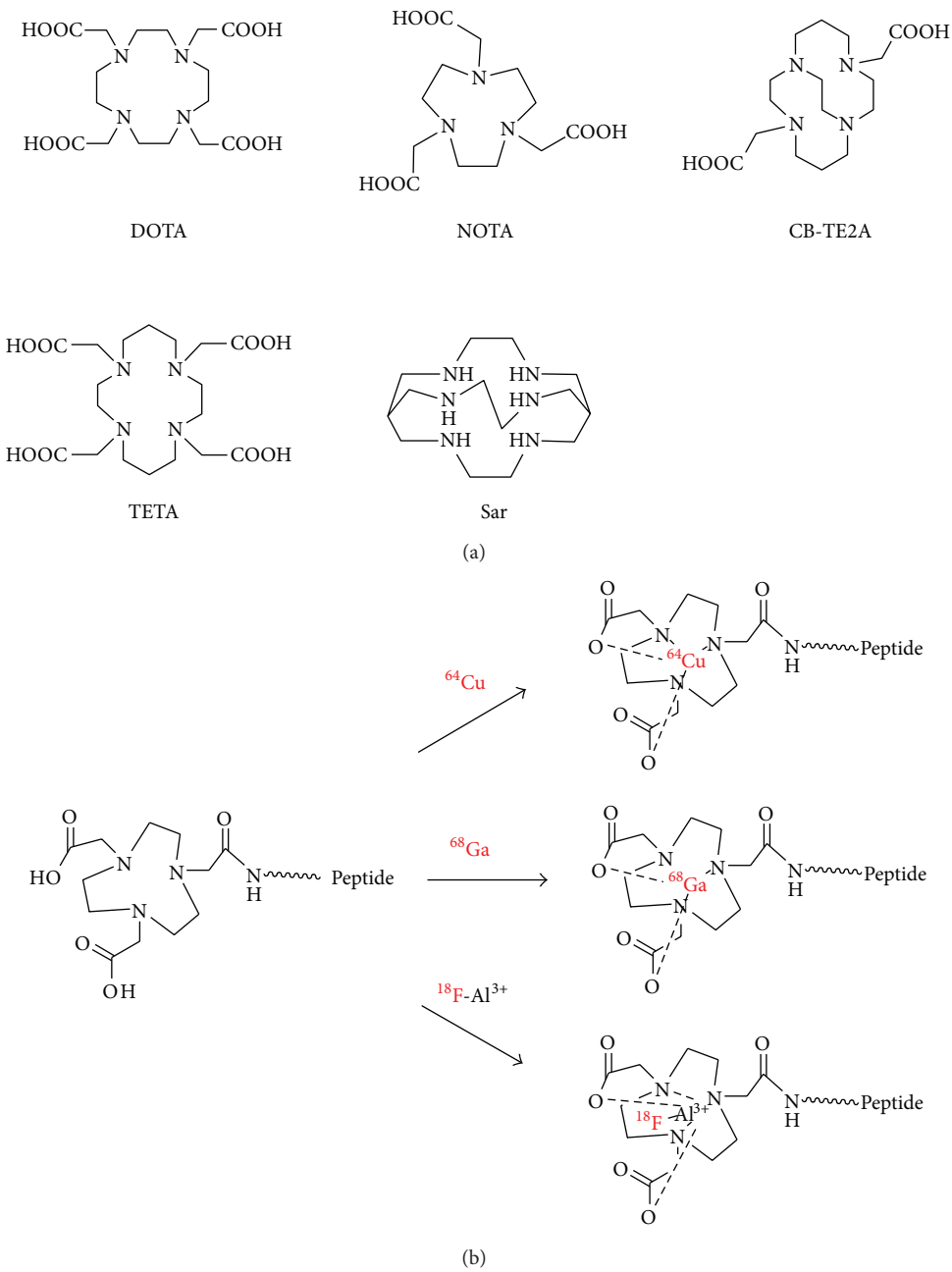

Figure 1: Basic bifunctional chelators (a) and schematic procedure for radiolabeling of peptides (b).

^{68}Ga is available from an in-house generator rendering ^{68}Ga radiopharmacy independent of an on-site cyclotron, which is a big advantage for clinical use. ^{68}Ga-labeled peptides have been developed for the targeting of somatostatin receptors, the melanocortin 1 receptor, the bombesin receptor, HER2 receptor and so forth [21, 22]. ^{64}Cu is another widely used metallic positron emitter, which can be produced on a large scale with a medical cyclotron, and the half-life (12.7 h) and decay properties make it an ideal radioisotope for PET imaging and radiotherapy [23, 24]. Besides, coordination chemistry of copper is well established and a wide variety of chelator systems are available. ^{64}Cu-labeled peptides have also been developed for the targeting of a variety of receptors.

Conventional methods for radiolabeling of peptides can be divided into two catalogs: labeling with radiometals via chelation chemistry [25] (Figure 1) and labeling through prosthetic groups [26] (Figure 2). For example, the BBN peptide and its analogues have been radiolabeled with various radionuclides including ^{64}Cu, ^{68}Ga, and ^{18}F for GRPR-related cancer imaging [27–30]. In addition to the above two methods, direct radiolabelling of peptide analogues with a leaving group with ^{18}F-fluoride was also reported [31].

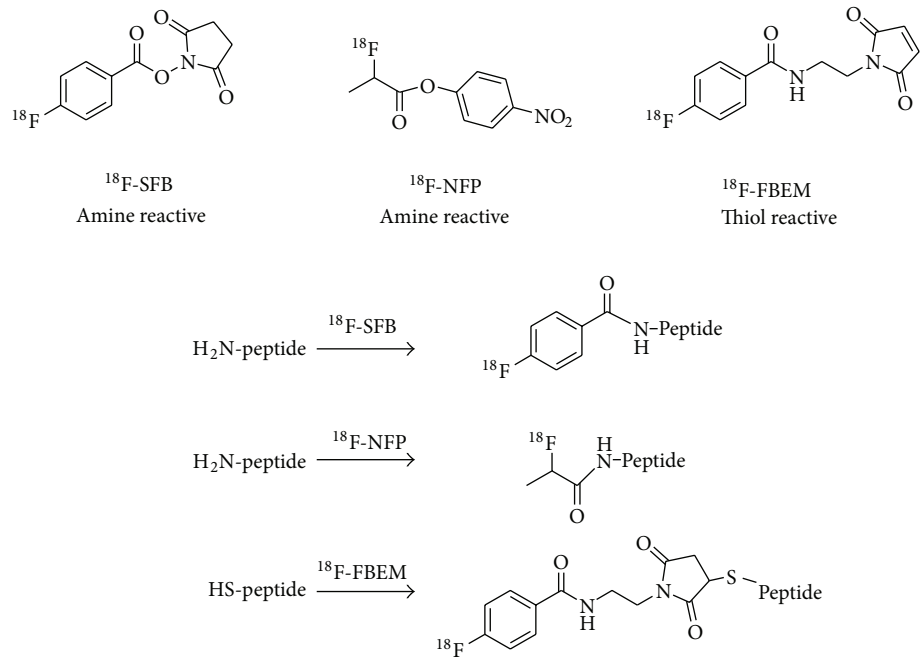

Figure 2: Representative prosthetic groups for radiolabeling of peptides.

Generally speaking, labeling through prosthetic groups is more time consuming, and labeling with radiometals via chelation chemistry is straightforward and usually has higher labeling yields. But some chelation reactions also require high temperature and long reaction time in order to get high yields. New technologies are always desired to improve the radiolabeling efficacy and efficiency.

3. Microfluidic Reactors

Microfluidic reactors, which generally consist of a network of micron-sized channels (typically 10–500 μm) embedded in a glass, metal or plastic solid substrate, have already found broad applications in the fields of organic synthesis [32] and biomolecular labeling [33]. The basic aspects of microfluidic reactors have been well summarized in other reviews [34–37]. In recent years, multistep synthesis has been performed on multistep continuous-flow synthesis systems [38–40], which could be utilized as promising tools for the multistep synthesis and purification of radiopharmaceuticals for PET.

Figure 3 showed representative microfluidic devices and the PET tracers synthesized [3]. Low precursor and reagent consumption, efficient heat transfer, and enhanced mixing are quite beneficial for the overall efficiency of radiolabelling reaction processes. Radiolabeling carried on microfluidic reactors usually results in purer products, higher yields, greater selectivities, and shorter reaction times than conventional methods. Furthermore, more benign and milder reaction conditions could be applied for certain reactions within microfluidic devices, which is very helpful for maintenance of the bioactivities of some peptides.

4. Preparation of Peptide-Based PET Tracers with Microfluidic Reactors

Conventional methods for radiolabeling of peptides have several limitations. (1) Large excess of precursors are needed to promote rapid and efficient labeling, and then extensive purification is required in order to separate the product from precursors; otherwise these cold precursors would occupy the targets and result in lower imaging quality. (2) Strict reaction conditions, which are hard to bear for some peptides, are needed, especially in the case of F-18 labeling. It would be promising to apply microfluidics technology to prepare peptide-based PET tracers.

Recently, a PDMS microreactor was fabricated and tested for the labeling of bifunctional chelate conjugated biomolecules with PET radiometals ^{64}Cu and ^{68}Ga in aqueous solutions (Figure 4) [4, 41]. The results showed that the microfluidic approach overall outperforms conventional radiosynthetic methods. The PDMS microreactor had a serpentine microchannel for mixing, a series of reservoirs for the incubation of the radiometal-ligand mixture, and a thin-film heater for heating the mixture. The reservoir was composed of 5 hexagonal chambers connected in series, with a total volume of 50 μL. DOTA-RGD conjugate was labeled with ^{64}Cu at mild reaction condition (23–47°C, 5–20 minutes). The incorporation yield is considerably better (~90%) than that obtained in classical vessel radiochemistry (~60%). The authors further investigated radiolabeling of both DOTA-peptides and NOTA-peptides conjugate with ^{68}Ga, and similar conclusions were drawn. These results demonstrated that it was possible to achieve high radiolabeling yields without using excess of peptide precursors, and this would eliminate

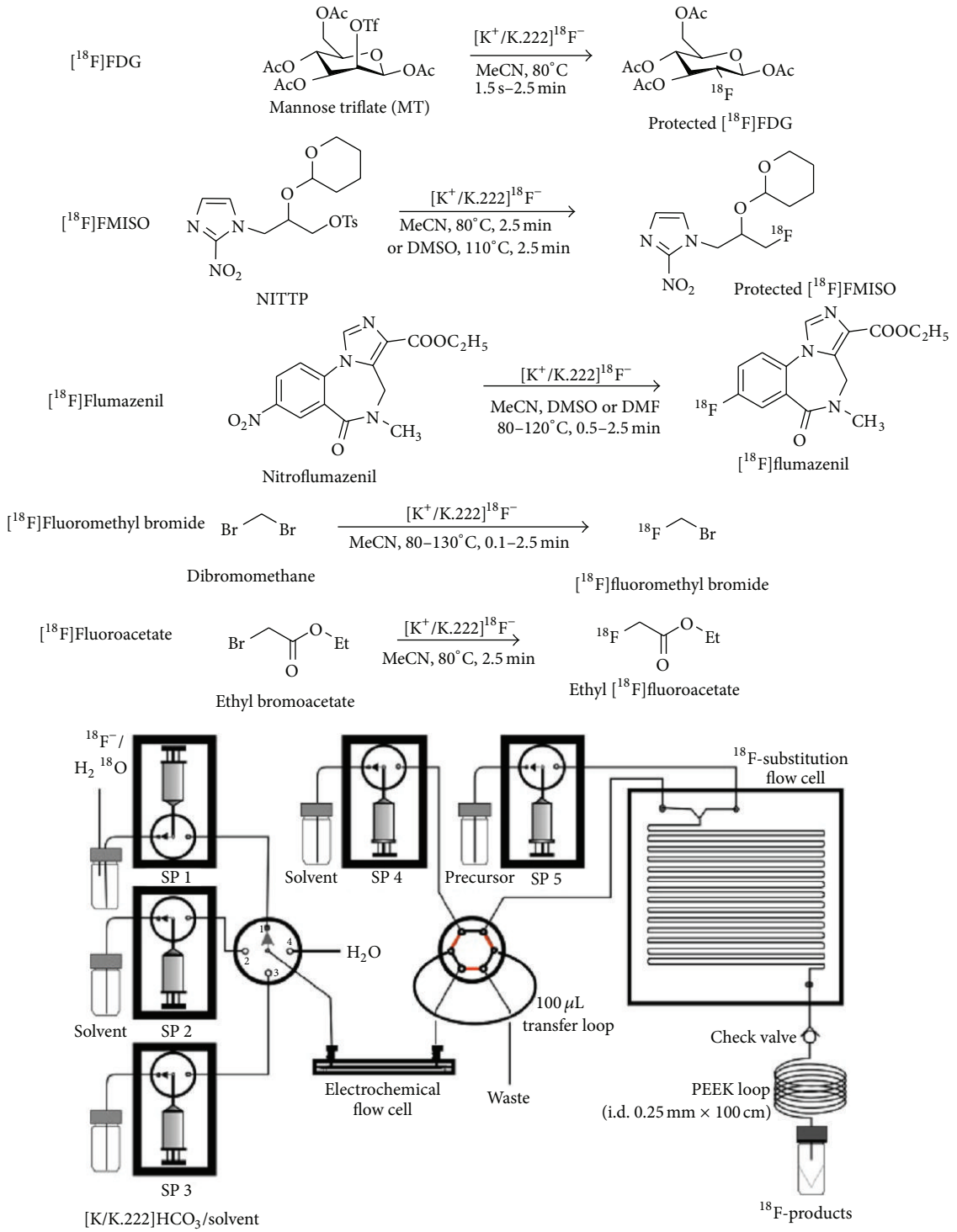

Figure 3: Microfluidic platform showing reaction setup using an electrochemical concentration chip and a reaction flow cell. ^{18}F-fluorination yields for the four ^{18}F-labeled compounds (protected ^{18}F-FDG: 98%, protected ^{18}F-FMISO: 80%, ^{18}F-flumazenil: 20%, ^{18}F-fluoromethyl bromide: 60%) were comparable to or higher than those obtained by conventional means (reproduced from [3] with permission from Elsevier).

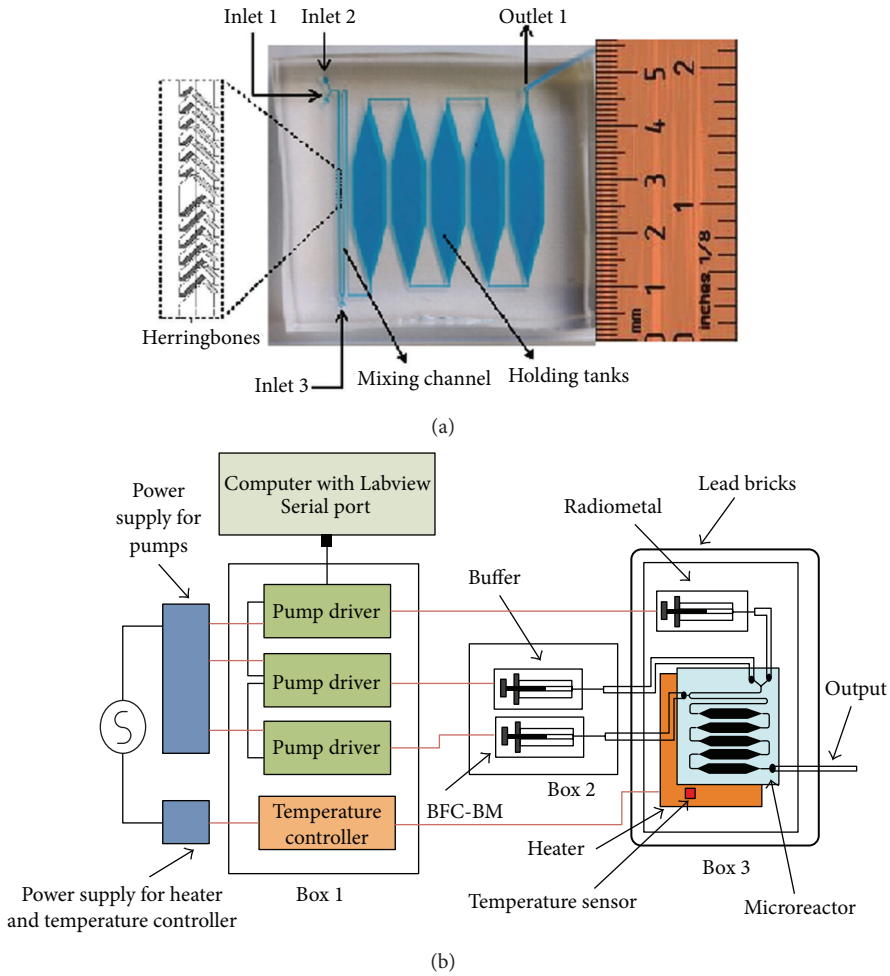

FIGURE 4: Optical micrograph of the microreactor (a) and schematic of the microreactor system for radiolabeling (b). (Reproduced from [4] with permission from Elsevier).

the need for chromatographic purification of the product to remove unlabeled peptides.

Synthesis and purification methods of the widely used prosthetic group ^{18}F-SFB based on microreactor have been developed [42]. It was a good example for multistep synthesis and purification of radiopharmaceuticals for PET. Aqueous ^{18}F-fluoride (100–500 MBq) was concentrated and further eluted to a microreactor for evaporation. ^{18}F-fluorination of the precursor (1.5 mg) was carried out at high temperature (200°C for 4 minutes), followed by hydrolysis and subsequent activation of the 4-^{18}F-fluorobenzoyl group. Purification was performed on a miniaturized solid phase extraction column. It took about 25 minutes, and ^{18}F-SFB was obtained with $55 \pm 6\%$ yield (not decay-corrected) and >98% radiochemical purity.

Radiolabeling of peptides with ^{18}F-SFB utilizing microfluidic technology was reported [43]. In their study, ^{18}F-SFB was firstly synthesized by conventional method and concentrated to a final volume of 50~100 μL in CH_3CN for further use. Then two different approaches were applied for the radiolabeling of the phosphopeptide-cell-penetrating peptide dimers: conventional labeling and microfluidic technology. The isolated radiochemical yields using microfluidic technology (~26%) were much higher than those using conventional labeling methods (2% to 4%). And it was also found that the *N*-terminal acylation of ^{18}F-SFB was more selective in the microfluidic-based reaction compared to the conventional radiolabeling procedure. Liu et al. reported a labeling system for biomolecules via ^{18}F-SFB utilizing a digital microfluidic droplet generation (DMDG) chip which allowed rapid scouting of reaction conditions in nanoliter volumes [44]. This system required only very small amounts of precursors (200- to 2000-fold reduction than conventional method). And it might be utilized for radio-labeling of a diverse spectrum of biomolecules including intact antibodies and their fragments, other proteins, and peptides.

Direct radiolabelling of peptides with ^{18}F-fluoride was also successfully achieved using the Advion NanoTek continuous flow microreactor [45]. These results showed radiochemical yields were dependent on the leaving group, precursor concentration, reaction temperature, and flow rate. The optimal temperature in the microreactor was 70–80°C

yielding labeling efficiency up to 90%. They had some very promising findings: (1) the reaction progressed even at 35°C with 30–40% labelling yields; (2) reactions could be performed even at a concentration of 0.5 mg mL^{-1} with reasonable yields. These results demonstrated that the microreactor may be used for labeling of thermally labile peptide molecules with ^{18}F radioisotope under very mild conditions.

5. Conclusion

Peptide-based PET tracers are valuable tools for peptide receptor imaging in clinical oncology and a large variety of radiolabeled peptides analogues have been developed for *in vivo* detection of tumors overexpressing relevant receptors. And many of them were under clinical and preclinical investigation. Large-scale clinical studies are still relatively challenging due to the complex radiochemistry procedures for peptide-based PET tracers, such as multistep synthesis and purification. Convenient radiolabeling technology, which could simplify the synthesis and purification procedures, is needed. In the last decade, remarkable progress has been achieved in the field of microfluidics-based PET radiochemistry. With the help of microfluidics system, rapid and efficient preparation of peptide-based PET tracers might be achieved. By now, some microfluidic systems have been explored for peptide radiolabeling, which may provide great versatility for the production of imaging agents in a doses-on-demand way for clinic use. In conclusion, microfluidics is a very promising technology to meet the increased demand for peptide-based PET tracers.

Conflict of Interests

No potential conflict of interests was disclosed.

Acknowledgments

This work is partly sponsored by Grants from the Zhejiang Provincial Natural Science Foundation of China (Z2110230), Health Bureau of Zhejiang Province (2010ZA075, 2011ZDA013), Science and Technology Bureau of Zhejiang Province (2012R10040), National Science Foundation of China (81327004, 81000630), China Postdoctoral Science Foundation (201104729), and Ministry of Science and Technology of China (2012BAI13B06).

References

[1] F. T. Chin, B. Shen, S. Liu et al., "First experience with clinical-grade ([^{18}F]FPP(RGD(2)): an automated multi-step radiosynthesis for clinical PET studies," *Molecular Imaging and Biology*, vol. 14, pp. 88–95, 2012.

[2] E. S. Mittra, M. L. Goris, A. H. Iagaru et al., "Pilot pharmacokinetic and dosimetric studies of^{18}F-FPPRGD2: a PET radiopharmaceutical agent for imaging $\alpha v\beta 3$ integrin levels," *Radiology*, vol. 260, no. 1, pp. 182–191, 2011.

[3] R. Wong, R. Iwata, H. Saiki, S. Furumoto, Y. Ishikawa, and E. Ozeki, "Reactivity of electrochemically concentrated anhydrous [^{18}F]fluoride for microfluidic radiosynthesis of^{18}F-labeled compounds," *Applied Radiation and Isotopes*, vol. 70, no. 1, pp. 193–199, 2012.

[4] D. X. Zeng, A. V. Desai, D. Ranganathan, T. D. Wheeler, P. J. A. Kenis, and D. E. Reichert, "Microfluidic radiolabeling of biomolecules with PET radiometals," *Nuclear Medicine and Biology*, vol. 40, pp. 42–51, 2013.

[5] A. M. Elizarov, "Microreactors for radiopharmaceutical synthesis," *Lab on a Chip*, vol. 9, no. 10, pp. 1326–1333, 2009.

[6] H. Audrain, "Positron emission tomography (PET) and microfluidic devices: a breakthrough on the microscale?" *Angewandte Chemie*, vol. 46, no. 11, pp. 1772–1775, 2007.

[7] P. W. Miller, H. Audrain, D. Bender et al., "Rapid carbon-11 radiolabelling for PET using microfluidics," *Chemistry*, vol. 17, no. 2, pp. 460–463, 2011.

[8] G. Pascali, P. Watts, and P. A. Salvadori, "Microfluidics in radiopharmaceutical chemistry," *Nuclear Medicine and Biology*, vol. 40, no. 6, pp. 776–787, 2013.

[9] M. Wang, W. Lin, K. Liu, M. Masterman-Smith, and C. K. Shen, "Microfluidics for positron emission tomography probe development," *Molecular Imaging*, vol. 9, no. 4, pp. 175–191, 2010.

[10] V. Arima, G. Pascali, O. Lade et al., "Radiochemistry on chip: towards dose-on-demand synthesis of PET radiopharmaceuticals," *Lab on a Chip*, vol. 13, pp. 2328–2336, 2013.

[11] M. Fani and H. R. Maecke, "Radiopharmaceutical development of radiolabelled peptides," *European Journal of Nuclear Medicine and Molecular Imaging*, vol. 39, supplement 1, pp. S11–S30, 2012.

[12] V. Ambrosini, M. Fani, S. Fanti, F. Forrer, and H. R. Maecke, "Radiopeptide imaging and therapy in Europe," *Journal of Nuclear Medicine*, vol. 52, supplement 2, pp. 42S–55S, 2011.

[13] M. M. Graham and Y. Menda, "Radiopeptide imaging and therapy in the United States," *Journal of Nuclear Medicine*, vol. 52, pp. 56S–63S, 2011.

[14] M. Schottelius and H. Wester, "Molecular imaging targeting peptide receptors," *Methods*, vol. 48, no. 2, pp. 161–177, 2009.

[15] L. Varagnolo, M. P. M. Stokkel, U. Mazzi, and E. K. J. Pauwels, "^{18}F-labeled radiopharmaceuticals for PET in oncology, excluding FDG," *Nuclear Medicine and Biology*, vol. 27, no. 2, pp. 103–112, 2000.

[16] Z. Cheng, L. Zhang, E. Graves et al., "Small-animal PET of melanocortin 1 receptor expression using a ^{18}F-labeled α-melanocyte-stimulating hormone analog," *Journal of Nuclear Medicine*, vol. 48, no. 6, pp. 987–994, 2007.

[17] H. Jiang, S. J. Moore, S. Liu et al., "A novel radiofluorinated agouti-related protein for tumor angiogenesis imaging," *Amino Acids*, vol. 44, pp. 673–681, 2013.

[18] D. M. Goldenberg, R. M. Sharkey, W. J. McBride, and O. C. Boerman, "Al^{18}F: a new standard for radiofluorination," *Journal of Nuclear Medicine*, vol. 54, p. 1170, 2013.

[19] W. J. McBride, R. M. Sharkey, and D. M. Goldenberg, "Radiofluorination using aluminum-fluoride (Al^{18}F)," *EJNMMI Research*, vol. 3, p. 36, 2013.

[20] S. Liu, H. Liu, H. Jiang, Y. Xu, H. Zhang, and Z. Cheng, "One-step radiosynthesis of^{18}F-AlF-NOTA-RGD2 for tumor angiogenesis PET imaging," *European Journal of Nuclear Medicine and Molecular Imaging*, vol. 38, no. 9, pp. 1732–1741, 2011.

[21] H. R. Maecke, M. Hofmann, and U. Haberkorn, "^{68}Ga-labeled peptides in tumor imaging," *Journal of Nuclear Medicine*, vol. 46, pp. 172S–178S, 2005.

[22] G. Ren, R. Zhang, Z. Liu et al., "A 2-helix small protein labeled with ^{68}Ga for PET imaging of HER2 expression," *Journal of Nuclear Medicine*, vol. 50, no. 9, pp. 1492–1499, 2009.

[23] M. Shokeen and C. J. Anderson, "Molecular imaging of cancer with copper-64 radiopharmaceuticals and positron emission tomography (PET)," *Accounts of Chemical Research*, vol. 42, no. 7, pp. 832–841, 2009.

[24] S. V. Smith, "Molecular imaging with copper-64," *Journal of Inorganic Biochemistry*, vol. 98, no. 11, pp. 1874–1901, 2004.

[25] M. D. Bartholomä, "Recent developments in the design of bifunctional chelators for metal-based radiopharmaceuticals used in Positron Emission Tomography," *Inorganica Chimica Acta*, vol. 389, pp. 36–51, 2012.

[26] Z. Li and P. S. Conti, "Radiopharmaceutical chemistry for positron emission tomography," *Advanced Drug Delivery Reviews*, vol. 62, no. 11, pp. 1031–1051, 2010.

[27] J. C. Garrison, T. L. Rold, G. L. Sieckman et al., "In vivo evaluation and small-animal PET/CT of a prostate cancer mouse model using Cu-64 bombesin analogs: side-by-side comparison of the CB-TE2A and DOTA chelation systems," *Journal of Nuclear Medicine*, vol. 48, no. 8, pp. 1327–1337, 2007.

[28] X. Zhang, W. Cai, F. Cao et al., "^{18}F-labeled bombesin analogs for targeting GRP receptor-expressing prostate cancer," *Journal of Nuclear Medicine*, vol. 47, no. 3, pp. 492–501, 2006.

[29] J. Schuhmacher, H. Zhang, J. Doll et al., "GRP receptor-targeted PET of a rat pancreas carcinoma xenograft in nude mice with a ^{68}Ga-labeled bombesin(6–14) analog," *Journal of Nuclear Medicine*, vol. 46, no. 4, pp. 691–699, 2005.

[30] X. Chen, R. Park, Y. Hou et al., "MicroPET and autoradiographic imaging of GRP receptor expression with Cu-64-DOTA-Lys(3) bombesin in human prostate adenocarcinoma xenografts," *Journal of Nuclear Medicine*, vol. 45, no. 8, pp. 1390–1397, 2004.

[31] M. Honer, L. Mu, T. Stellfeld et al., "^{18}F-labeled bombesin analog for specific and effective targeting of prostate tumors expressing gastrin-releasing peptide receptors," *Journal of Nuclear Medicine*, vol. 52, no. 2, pp. 270–278, 2011.

[32] P. D. I. Fletcher, S. J. Haswell, E. Pombo-Villar et al., "Micro reactors: principles and applications in organic synthesis," *Tetrahedron*, vol. 58, no. 24, pp. 4735–4757, 2002.

[33] C. Wang, J. Ouyang, D. K. Ye, J. J. Xu, H. Y. Chen, and X. H. Xia, "Rapid protein concentration, efficient fluorescence labeling and purification on a micro/nanofluidics chip," *Lab on a Chip*, vol. 12, pp. 2664–2671, 2012.

[34] A. J. deMello, "Control and detection of chemical reactions in microfluidic systems," *Nature*, vol. 442, no. 7101, pp. 394–402, 2006.

[35] K. Geyer, J. D. C. Codée, and P. H. Seeberger, "Microreactors as tools for synthetic Chemists—the chemists' round-bottomed flask of the 21st century?" *Chemistry*, vol. 12, no. 33, pp. 8434–8442, 2006.

[36] R. L. Hartman and K. F. Jensen, "Microchemical systems for continuous-flow synthesis," *Lab on a Chip*, vol. 9, no. 17, pp. 2495–2507, 2009.

[37] G. M. Whitesides, "The origins and the future of microfluidics," *Nature*, vol. 442, no. 7101, pp. 368–373, 2006.

[38] H. R. Sahoo, J. G. Kralj, and K. F. Jensen, "Multistep continuous-flow microchemical synthesis involving multiple reactions and separations," *Angewandte Chemie*, vol. 46, no. 30, pp. 5704–5708, 2007.

[39] N. Pagano, M. L. Heil, and N. D. P. Cosford, "Automated multistep continuous flow synthesis of 2-(1H-Indol-3-yl)thiazole derivatives," *Synthesis-Stuttgart*, vol. 44, pp. 2537–2546, 2012.

[40] X. Y. Liu and K. F. Jensen, "Multistep synthesis of amides from alcohols and amines in continuous flow microreactor systems using oxygen and urea hydrogen peroxide as oxidants," *Green Chemistry*, vol. 15, pp. 1538–1541, 2013.

[41] T. D. Wheeler, D. Zeng, A. V. Desai, B. Önal, D. E. Reichert, and P. J. A. Kenis, "Microfluidic labeling of biomolecules with radiometals for use in nuclear medicine," *Lab on a Chip*, vol. 10, no. 24, pp. 3387–3396, 2010.

[42] R. Bejot, A. M. Elizarov, E. Ball et al., "Batch-mode microfluidic radiosynthesis of N-succinimidyl-4-[^{18}F]fluorobenzoate for protein labelling," *Journal of Labelled Compounds and Radiopharmaceuticals*, vol. 54, no. 3, pp. 117–122, 2011.

[43] S. Richter, V. Bouvet, M. Wuest et al., "F-labeled phosphopeptide-cell-penetrating peptide dimers with enhanced cell uptake properties in human cancer cells," *Nuclear Medicine and Biology*, vol. 39, no. 18, pp. 1202–1212, 2012.

[44] K. Liu, E. J. Lepin, M. Wang et al., "Microfluidic-based^{18}F-labeling of biomolecules for immuno-positron emission tomography," *Molecular Imaging*, vol. 10, no. 3, pp. 168–176, 161–167, 2011.

[45] S. V. Selivanova, L. Mu, J. Ungersboeck et al., "Single-step radiofluorination of peptides using continuous flow microreactor," *Organic and Biomolecular Chemistry*, vol. 10, no. 19, pp. 3871–3874, 2012.

Hindawi Publishing Corporation
BioMed Research International
Volume 2013, Article ID 694075, 12 pages
http://dx.doi.org/10.1155/2013/694075

Clinical Study

Abacus Training Modulates the Neural Correlates of Exact and Approximate Calculations in Chinese Children: An fMRI Study

Fenglei Du,[1] Feiyan Chen,[1] Yongxin Li,[1] Yuzheng Hu,[1] Mei Tian,[2,3,4,5] and Hong Zhang[2,3,4,5]

[1] *Bio-X Laboratory, Department of Physics, Zhejiang University, 38 Zheda Road, Hangzhou 310027, China*
[2] *Department of Nuclear Medicine, The Second Affiliated Hospital of Zhejiang University School of Medicine, 38 Zheda Road, Hangzhou 310009, China*
[3] *Zhejiang University Medical PET Center, Zhejiang University, 38 Zheda Road, Hangzhou 310009, China*
[4] *Institute of Nuclear Medicine and Molecular Imaging, Zhejiang University, 38 Zheda Road, Hangzhou 310009, China*
[5] *Key Laboratory of Medical Molecular Imaging of Zhejiang Province, Hangzhou 310009, China*

Correspondence should be addressed to Feiyan Chen; chenfy@zju.edu.cn

Received 26 July 2013; Accepted 12 September 2013

Academic Editor: Ignasi Carrio

Exact (EX) and approximate (AP) calculations rely on distinct neural circuits. However, the training effect on the neural correlates of EX and AP calculations is largely unknown, especially for the AP calculation. Abacus-based mental calculation (AMC) is a particular arithmetic skill that can be acquired by long-term abacus training. The present study investigated whether and how the abacus training modulates the neural correlates of EX and AP calculations by functional magnetic resonance imaging (fMRI). Neural activations were measured in 20 abacus-trained and 19 nontrained Chinese children during AP and EX calculation tasks. Our results demonstrated that: (1) in nontrained children, similar neural regions were activated in both tasks, while the size of activated regions was larger in AP than those in the EX; (2) in abacus-trained children, no significant difference was found between these two tasks; (3) more visuospatial areas were activated in abacus-trained children under the EX task compared to the nontrained. These results suggested that more visuospatial strategies were used by the nontrained children in the AP task compared to the EX; abacus-trained children adopted a similar strategy in both tasks; after long-term abacus training, children were more inclined to apply a visuospatial strategy during processing EX calculations.

1. Introduction

Arithmetical calculation is executed everywhere in our daily life, for example, statistics of population in the government, management of financial affairs in a company, and calculation of the sum of price at a grocery store. These calculations are mainly performed by physical tools or devices (pencil with paper, calculators, and computers). With these tools, complex calculations can be done more precisely and efficiently. However, it is discommodious for everyone to carry a physical device everywhere. Therefore, it is more convenient to calculate by mental calculation.

Several studies have investigated the cognitive mechanism of exact (EX) and approximate (AP) calculations [1–3]. Within the elementary arithmetic, there are two representative formats corresponding to EX and AP calculations: a language-specific format and a language-independent format. The language-specific format is specified for EX arithmetic which relies on language-based representations, and the language-independent format is specified for AP arithmetic which relies on visuospatial representations [1]. Substantial neuroimaging studies have revealed that the parietal cortex, especially bilateral horizontal segment of the intraparietal sulcus (IPS) and the angular gyrus were potential candidates for neural correlates of mental calculation [1, 2, 4–9]. Furthermore, the left inferior frontal cortex and the angular gyrus were responsible for language-based representations and more activated in EX calculations; the bilateral

parietal areas around IPS and left superior prefrontal gyrus were responsible for visuospatial representations and more activated in AP calculations.

The other studies found that practice and experience of high-level cognitive skills can change the structure of the cerebral cortex [10–19]. For example, long-term training of abacus-based mental calculation (AMC) does change the neural function [15, 16], structure [17, 18], and the number processing system [19]. AMC is a unique strategy for arithmetic, which can be used to solve calculation problems with exceptional speed and high accuracy [20, 21]. AMC experts can acquire their capabilities after long-term training. Initially, they learn to perform calculations on an abacus (a simple device consisted of beads and rods, and numbers can be represented by the spatial locations of beads) with both hands simultaneously. The procedure of solving a calculation problem by abacus is shown in Figure 1(a). After being familiar with the operation of the abacus, they are instructed to imagine moving beads with actual finger movements on an imagined abacus in minds and watching a real one at the same time. Finally, they calculate via an imagined abacus without moving fingers, as if manipulating a "mental abacus" [15, 20–24]. The existence of the "imaginary abacus" has been validated by previous studies, which indicated that the nonverbal visuospatial cerebral networks play an important role during calculation tasks in abacus experts [15, 16, 23–27]. Recently, a study revealed that "mental abacus" was represented by a column-based model, in which the abacus is split into a series of columns and each column is independently stored as a unit with its own detailed substructure [24].

Positive emission tomography (PET) and functional magnetic resonance imaging (fMRI) studies have attempted to explore the neural correlates of the AMC mechanism in EX calculations [15, 16, 23, 25], which showed that the premotor, frontal, and parietal cortices (especially on the right hemisphere) were involved in AMC. One case study on an adult abacus expert confirmed these special regions by the combined methods of electroencephalography (EEG) and fMRI [27]. Furthermore, a lesion study on a skilled abacus expert manifested the importance of the dorsal premotor and parietal cortex in the superior arithmetic ability of AMC experts [26]. These studies indicated that abacus experts adopted the visuospatial strategy instead of the linguistic strategy when performing EX calculations.

However, all those studies only focused on the abacus training effect on EX (simple, complex, or both) calculations. To the best of our knowledge, no study has been done to explore the training effects on the AP calculation or the difference between EX and AP calculations. Since the strategy adopted in the EX calculation was changed by long-term abacus training, the difference of the underlying neural correlates between EX and AP calculations might be altered, too. Thus, we hypothesize that: (1) the neural difference between the simple EX and AP calculations should disappear or decline after the abacus training; (2) for simple EX calculations, the mechanism should be changed and more visuospatial representations should be involved after the abacus training.

Since the combined abacus operation and AMC course was instructed only in a few experimental classes at certain elementary schools, starting from Grade 1 to 4, only children were recruited in this study. Thus, our present fMRI study aimed to explore whether and how the abacus training modulates neural correlates of EX and AP calculations in Chinese children.

2. Materials and Methods

2.1. Subjects. Two groups of children participated in the present study, including an abacus-trained group (10 boys and 10 girls, mean age = 10.60 ± 0.34 years, range: 10.08–11.34 years) and a nontrained group (9 boys and 10 girls, mean age = 10.62 ± 0.31 years, range: 10.12–11.26 years). These two groups were recruited from different classes of the same grade in the same school. At the beginning of this study, all children were randomly divided into two experimental groups. Besides abacus training, all children studied the same curriculum at school. The abacus-trained group was instructed to practice abacus operation and AMC additionally for approximately 3 years and for 2 to 3 hours per week (these combined two practices were named as "abacus training" in this study). In contrast, the nontrained group received no abacus training either at school or after school.

The intelligence quotient (IQ) of each child was assessed by the Wechsler Intelligence Scale for Chinese Children-Revised (WISCC-R) in the same week of MRI study [28].

All participants were right-handed urban Chinese children with normal or corrected-to-normal vision and reported no history of neurological or psychiatric disorders. Written informed consent was obtained from each subject and his/her guardian. This study was approved by the Institutional Ethic Committee and the Institutional Review Boards (IRBs) of the Affiliated Hospital of Medical College of Qingdao University.

2.2. Tasks. EX and AP addition tasks were applied in this study. The addend ranged from 1 to 9, and the sum ranged from 3 to 17. In the EX addition task, one of the two alternative answers was correct, another was wrong (off by two units at most). In the AP addition task, one of the two alternative answers was a number off by one unit which was the one to be chosen, and another was a number off by at least four units.

Subjects were instructed to press the left or right button corresponding to the answer they chose. The buttons of correct answers were counterbalanced: half of them were on the left side and another half on the right. Once the answer-choosing screen appeared, subjects were required to push the correct button by their forefingers as fast as possible.

All subjects received 4 blocks of tasks (2 blocks for each). The blocks were separated by a resting period of 16 s. Each block started with a cue of 4 s to remind the subjects of the type of tasks and followed by 12 continuous addition problems. The sequence of blocks was shown in Figure 1(b) and the procedure of a single trial was shown in Figure 1(c).

The experimental task was carried out on a computer using E-prime 1.2 [29]. Stimuli were projected to a screen behind the MR scanner. The subject can see all the tasks by looking at a mirror right over his/her eyes. The MR scanner and the computer which control tasks were synchronized.

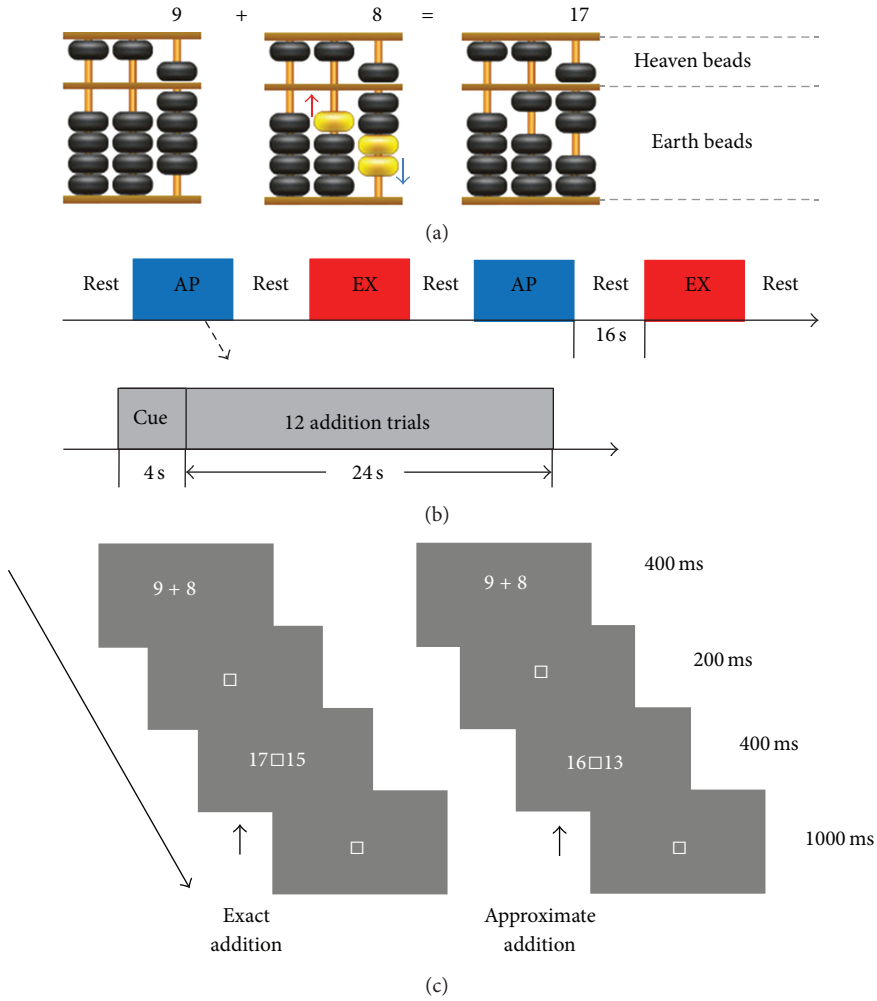

Figure 1: Abacus addition procedure and design of the experimental tasks. (a) An addition example on the abacus (9+8 = 17). The left abacus schematic represents the number 9 (one heaven bead equals to 5 and 4 earth beads equal to 4). The middle abacus schematic represents the addition procedure: subtract the complement of the addend to 10 (2 here) by pushing down the 2 yellow beads (near the blue arrow) with the index finger, then add 1 to the tens column by pushing up the yellow bead (near the red arrow) with the thumb. The right abacus schematic represents the result. (b) The task blocks that were used during data acquisition. The blocks were separated by a resting period of 16 s. Each block started with a cue of 4 s to remind the subject of the type of tasks and followed by 12 continuous addition problems. (c) The task design that is used during data acquisition. On each trial, an addition problem is presented for 400 ms and then followed by two alternative answers (also presented for 400 ms). Subjects are instructed to choose either the correct answer (EX task) or the most plausible answer (AP task) as soon as possible.

Reaction time (RT) and accuracy were recorded by the computer.

2.3. fMRI Data Acquisition. Data acquisition was performed on a 3.0 T Philips MRI scanner using a standard circularly polarized head coil. For fMRI, a whole brain single-shot gradient-echo echo-planer imaging (EPI) sequence was used, which is sensitive to the blood-oxygen-level dependent (BOLD) contrast. Images were acquired in an interleaved order and approximately parallel to the AC-PC line. Acquisition parameters were as follows: TR = 2000 ms, TE = 30 ms, slice thickness = 4 mm, gap between slices = 0.8 mm, flip angle = 90°, field of view = 230 mm, matrix size = 64 × 64, and slices numbers = 33. Heads of the children were stabilized with a foam cushion to minimize motions during imaging.

2.4. Statistical Analysis: Behavioral. Three participants (2 from abacus-trained group, 1 from nontrained group) were excluded due to high error rate (>30%) of the addition tasks. Thus, we got 18 participants for each group.

Trials with RT < 300 ms were discarded from the analysis. Only correct trials were used to calculate the median RTs for each participant under each task condition. These median correct RTs were subjected to a repeated measures of analysis of variance (ANOVA) with task type (the EX and AP task) as a within-subjects factor and group (the abacus-trained and

nontrained group) as a between-subjects factor. The same ANOVA was also applied to accuracies in each condition for all participants.

2.5. Statistical Analysis: fMRI Data Analysis. Image preprocessing and statistical analysis were carried out with SPM8 (FIL, London, http://www.fil.ion.ucl.ac.uk/spm/), as implemented in MATLAB software (MathWorks, Inc., Natick, MA, USA). In the preprocessing stage, images were (1) corrected for slice timing, (2) spatially aligned to the first volume, (3) normalized to the Montreal Neurological Institute (MNI) standard EPI template with a resolution of $3 \times 3 \times 3$ mm, (4) spatially smoothed with a 6 mm full width at half maximum (FHWM) Gaussian smoothing kernel [30].

After preprocessing, statistical analyses based on general linear model (GLM) and the theory of Gaussian fields [31] were performed at a participant level and at a group level. A fixed effects model was applied to the smoothed data to constitute contrast images for each participant. In this step, an appropriate design matrix was specified and the BOLD signals induced by different experimental conditions were assessed voxel by voxel. Three types of contrast images for different conditions were derived here: the EX, AP, and rest contrast (corresponding to the resting periods between blocks). These contrast images were then submitted to appropriate t-tests to identify the activations that were specifically involved in different tasks.

In order to determine brain activations for different addition tasks, paired t-tests were done separately on EX versus rest contrast and AP versus rest contrast in each group. Paired t-tests between EX and AP contrasts were also executed to explore the differences in brain activity between the two addition tasks in each group.

To reveal the differences of brain activity between the abacus-trained and nontrained groups, two-sample t-tests were performed between the two groups on both EX versus rest and AP versus rest contrasts.

3. Results

3.1. Behavior Result. The accuracies and median correct RTs for each task in both groups were summarized in Table 1. A significant difference was detected in median correct RTs between two tasks: $F(1, 1) = 189.209$, $P < 0.001$, $\eta^2 = 0.848$ (533 ± 86 ms, and 676 ± 124 ms for the EX addition and AP addition task, resp.), which demonstrated that the EX addition task was processed much faster than the AP addition task. The main effect of group and its interaction with task type were not significant ($P > 0.05$).

A significant difference was detected in accuracies between two tasks: $F(1, 2) = 18.671$, $P < 0.001$, $\eta^2 = 0.354$ (0.92 ± 0.05 and 0.88 ± 0.07 for the EX addition and AP addition task, resp.), indicating that subjects made more errors in the AP addition task. The difference of accuracies between the groups was also significant: $F(1, 1) = 7.240$, $P = 0.011$, $\eta^2 = 0.176$ (0.91 ± 0.08 and 0.86 ± 0.07 for the abacus-trained and nontrained groups, resp.). Interestingly, unlike the RT analysis, the interaction between group and task type was marginally significant: $F(1, 2) = 2.681$, $P = 0.111$, $\eta^2 = 0.073$. Decomposition into contrasts showed a significant difference in the EX addition task: $F(1, 1) = 16.276$, $P < 0.001$, $\eta^2 = 0.324$ (0.95 ± 0.05 and 0.89 ± 0.04 for the abacus-trained and nontrained groups, resp.), suggesting that nontrained children made more errors in the EX addition task. However, no significant difference was found between the abacus-trained and nontrained groups in the AP addition task ($P = 0.220$).

Table 1: The RTs and accuracies for each task of each group.

Group	Task type	Reaction time (ms)	Accuracy
Abacus-trained	EX addition	526 (101)	0.95 (0.05)
	AP addition	661 (144)	0.89 (0.08)
Non-trained	EX addition	538 (71)	0.89 (0.04)
	AP addition	690 (102)	0.86 (0.05)

Numbers in the parenthesis are standard deviations.

3.2. Brain Activity: General Pattern. Brain regions activated by the AP and EX addition task in the abacus-trained and nontrained groups were investigated separately. A preview of the brain activity was shown in Figure 2. The statistical threshold was set at $P < 0.05$ with false discovery rate (FDR) corrected for multiple comparisons, and a minimal cluster size of 30 voxels was considered to represent regions with significant activations.

In the abacus-trained group, activations elicited by the AP addition task were detected in the supplementary areas (SMA), bilateral precentral sulcus, inferior frontal cortex, bilateral inferior parietal cortices, and bilateral middle temporal and occipital cortices and bilateral insula and thalamus (Figure 2(a)); activations elicited by the EX addition task were detected in the SMA, bilateral precentral sulcus, right middle frontal cortex, bilateral inferior and middle occipital cortices, left inferior parietal cortex, right angular, the bilateral insula and thalamus, right middle and inferior temporal cortices, and the vermis in the cerebellum (Figure 2(b)). The activations for the abacus-trained group were distributed bilaterally in both hemispheres.

In the nontrained group, activations elicited by the AP addition task were detected in the SMA, bilateral inferior and superior parietal cortices, insula, precentral sulcus in the middle frontal cortex, inferior and middle frontal cortices, inferior temporal cortex, thalamus, inferior occipital cortex, and cerebellum (Figure 2(c)); activations elicited by the EX addition task were detected in the SMA, left inferior and superior parietal cortex, left inferior frontal cortex, right angular, left insula, and the bilateral precentral sulcus (Figure 2(d)).

3.3. Brain Activity in AP And EX Addition Tasks within Group Comparisons. In the nontrained group, no significant areas were activated in favor of the EX addition task when compared to the AP addition task ($P > 0.05$ uncorrected, cluster size > 20). While activations in favor of the AP addition

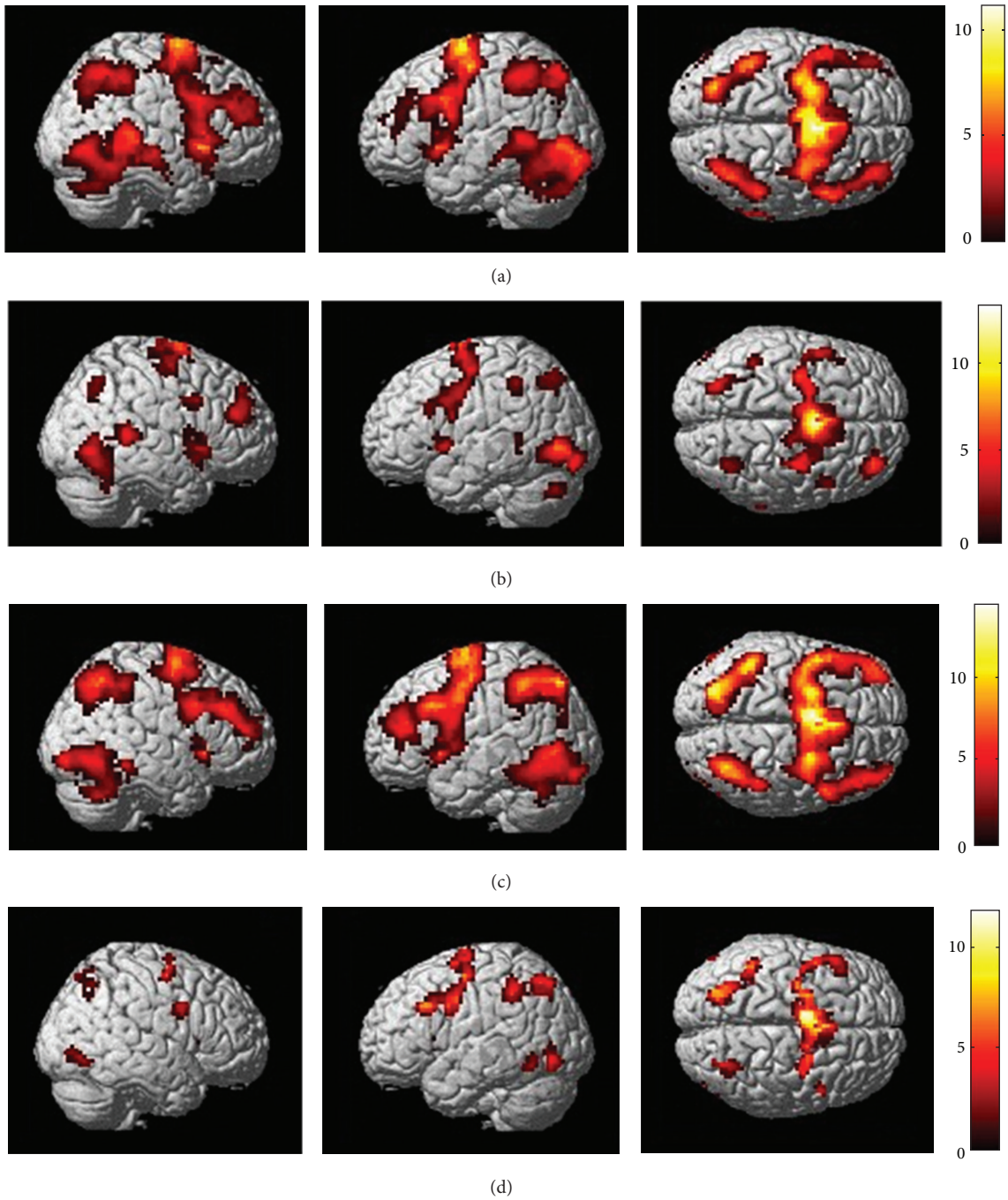

Figure 2: Brain regions activated by the AP and EX addition task in the abacus-trained and nontrained group. (a) The activity pattern revealed by the AP addition task in the abacus-trained group. (b) The activity pattern revealed by the EX addition task in the abacus-trained group. (c) The activity pattern revealed by the AP addition task in the nontrained group. (d) The activity pattern revealed by the EX addition task in the nontrained group. The left column showed the right hemisphere; the middle showed the left hemisphere, and the right showed the vertical view of the brain. ($P < 0.05$, FDR corrected; minimal cluster size = 30 voxels).

task were found in the SMA, bilateral inferior parietal cortices, middle occipital cortex, precentral sulcus, left superior parietal cortex, left precuneus, left cerebellum, right angular and the bilateral thalamus, and striatum, with the threshold of $P < 0.001$ (FDR corrected) and a minimal cluster size of 30 voxels (Table 2 and Figure 3). Figure 3(a) showed brain regions activated by the AP addition task (contrasted to the EX addition task) in the nontrained group; Figure 3(b) showed the mean beta values of activated brain regions in two tasks.

In the abacus-trained group, no significant differences were found in favor of the AP addition task when compared

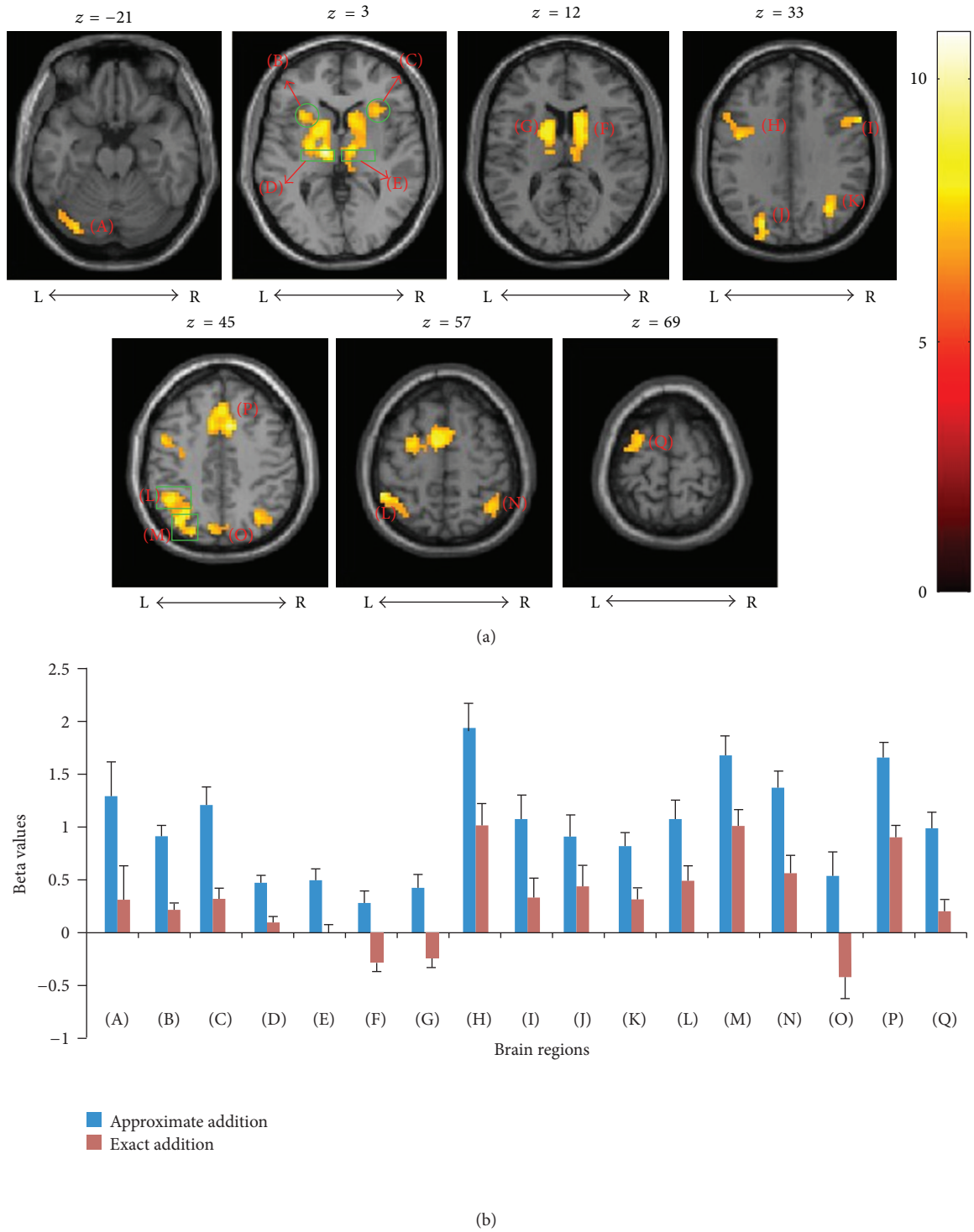

Figure 3: (a) Brain regions activated by the AP addition task (contrasted to the EX addition task) in the nontrained group. (b) Comparison of the mean beta values of these brain regions between two tasks. Uppercase letters in the parenthesis represent these brain regions. (A): cerebellum; (B): left insula; (C): right insula; (D): left thalamus; (E): right thalamus; (F): right striatum; (G): left striatum; (H): left precentral sulcus; (I): right precentral sulcus; (J): left middle occipital lobule; (K): right middle occipital lobule; (L): left inferior parietal lobule; (M): left superior parietal lobule; (N): right angular; (O): left precuneus; (P): SMA; (Q): left superior frontal lobule. ($P < 0.001$, FDR corrected; Voxel sizes > 30).

Table 2: Brain regions activated by the AP addition task (contrasted to the EX addition task) in the non-trained group.

Regions	Voxel size	BA	Hemisphere	T value	MNI coordinate		
					x	y	z
(1) SMA, left precentral sulcus, left superior frontal cortex	696	6/32	L/R	10.72	9	15	48
				8.51	−6	0	57
				8.38	−6	9	51
(2) Thalamus, striatum, insula	953	—	L/R	10.19	−12	−15	3
				7.99	−15	6	9
				7.77	15	12	12
(3) Middle occipital cortex, inferior parietal cortex, superior parietal cortex	454	7/40	L	9.24	−24	−75	30
				8.62	−51	−45	54
				8.48	−30	−63	48
(4) Precentral sulcus	30	9	R	7.96	57	15	36
				5.81	54	6	39
(5) Middle occipital cortex, angular	185	7/40	R	7.40	33	−63	33
				6.85	39	−54	54
				6.62	33	−66	45
(6) Cerebellum	72	—	L	6.62	−33	−81	−21
				6.47	−42	−60	−27
				6.21	−27	−87	−18
(7) Precuneus	43	7	L	6.32	−6	−75	45

BA: Brodmann area. $P < 0.001$ (AP addition contrast versus EX addition contrast, in the non-trained group), FDR corrected.

to the EX addition task ($P < 0.05$, FDR corrected). If the statistical threshold was set at $P < 0.005$ (uncorrected) and minimal cluster size as 20 continuous voxels, differences in favor of the AP addition task were found in the left superior frontal cortex (x, y, z = −24, 3, 69), left inferior parietal cortex (x, y, z = −27, −63, 42), and the right middle temporal cortex (x, y, z = 66, −48, −3); In the reverse contrast, only the anterior cingulate cortex (ACC, x, y, z = −3, 30,−6) was activated with the threshold of $P < 0.01$ (uncorrected) and cluster size > 30. This activity pattern suggested that the neural differences between the EX and AP addition tasks declined for abacus-trained children.

3.4. Brain Activity in AP and EX Addition Tasks between Group Comparisons. In the AP addition task, more activations were elicited in abacus-trained children, including the bilateral middle temporal cortices (x, y, z = −51, −33, −3 on the left; x, y, z = 51, −18, −12 on the right) and the left precuneus (x, y, z = −3, −39, 60), with a threshold of $P < 0.001$ (uncorrected) and a minimal cluster size of 10 voxels. Conversely, more activations were induced in nontrained children, including the left precentral sulcus (x, y, z = −42, −3, 42) and the SMA (x, y, z = −6, 0, 57), with a threshold of $P < 0.005$ (uncorrected) and a minimal cluster size of 10 voxels.

In the EX addition task, more activations were elicited in abacus-trained children, including the medial prefrontal cortex (MPFC), right caudate, right thalamus, right superior temporal cortex, and the right angular gyrus (see Table 3 and Figure 4), with a threshold of $P < 0.011$ (FDR corrected) and a minimal cluster size of 30 voxels. Figure 4(a) showed brain regions activated by the EX addition task in the abacus-trained group (contrasted to the nontrained group); Figure 4(b) showed the mean beta values of activated brain regions in the two groups. Conversely, more activations were induced in nontrained children, including the left precentral sulcus (x, y, z = −36, −6, 36) and the left middle frontal cortex (x, y, z = −30, 15, 27), with a threshold of $P < 0.05$ (uncorrected) and a minimal cluster size of 30 voxels.

4. Discussion

The present study aimed to explore whether and how the long-term abacus training modulates the neural correlates of EX and AP calculations in Chinese children. To address this issue, we compared functional activations between the AP and EX addition task for each group (the abacus-trained and nontrained groups), and we also compared the brain activity patterns between the abacus-trained and nontrained group for each addition task. To the best of our knowledge, this is the first report revealing the specific effect of abacus training on the neural correlates of EX and AP calculations.

The findings confirm our hypothesis. Firstly, the difference between AP and EX addition tasks for abacus-trained children existed only in the FDR-corrected result, demonstrating that the neural correlates underlying the two addition tasks were similar after the abacus training, and the pattern of brain activity during the two addition tasks in the nontrained group was consistent with previous neuroimaging studies [1, 9], revealing that AP arithmetic relied primarily on a quantity representation implemented in visuospatial networks of the left and right parietal lobes.

Table 3: Brain regions activated by the EX addition task in the abacus-trained group (contrast to the non-trained group).

Regions	Voxel size	BA	Hemisphere	T value	MNI coordinate		
					x	y	z
(1) Medial prefrontal cortex	115	8/9	R	5.56	18	42	18
				5.29	27	36	15
				5.05	12	39	36
(2) Superior temporal cortex	31	22	R	5.13	66	−33	9
				4.80	66	−24	3
				4.77	63	−42	0
(3) Caudate	48	—	R	5.00	15	18	15
				4.43	18	21	−3
(4) Angular	46	39	R	4.90	57	−63	27
				4.80	48	−57	27
(5) Thalamus	51	—	R	4.84	12	−3	3
				4.67	18	−12	6

BA: Brodmann area. $P < 0.011$ (the abacus-trained group versus the non-trained group, in the EX addition task), FDR corrected.

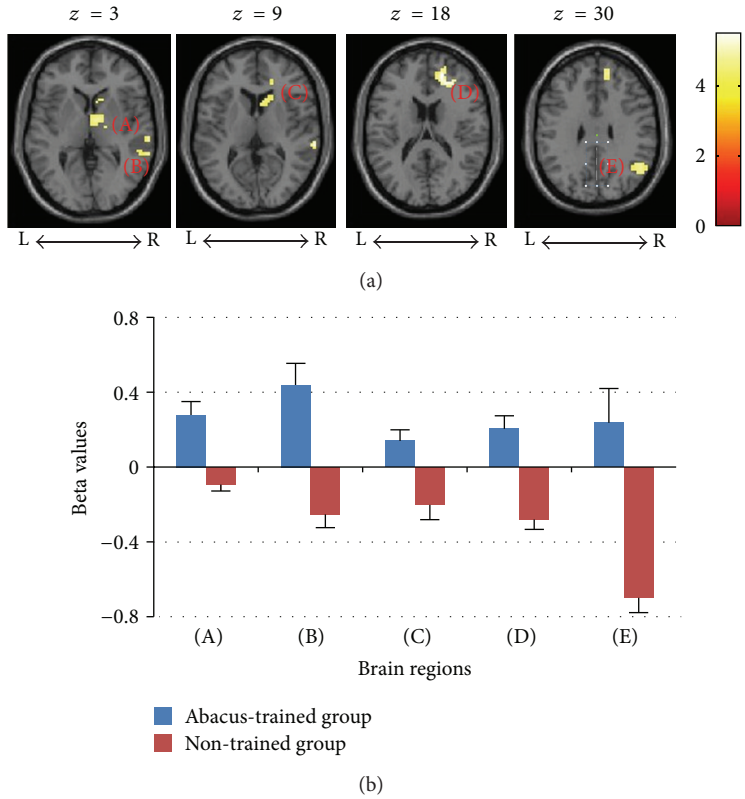

Figure 4: (a) Brain regions activated by the EX addition task in the abacus-trained group (contrasted to the nontrained group). (b) Comparison of the mean beta values of these brain regions between groups. Uppercase letters in the parenthesis represent these brain regions. (A): thalamus; (B): superior temporal lobule; (C): caudate; (D): MPFC; (E): right angular. ($P < 0.011$, FDR corrected; Voxel sizes > 30).

Secondly, no differences were detected between the two groups in the AP addition task; while, in the EX addition task, hyperactivity was detected for the abacus-trained children in the right MPFC, right caudate, right thalamus, right superior temporal cortex, and the right angular. These results illustrated that the processing of AP addition task for abacus-trained children was similar to that for nontrained children, but the long-term training changed the neural correlates of the EX addition task; a frontal-temporal circuit was observed, which was also found in a previous study by our group [15].

Furthermore, no differences were detected between the IQs of the two groups, indicating that both groups had comparative intelligence. This supported the argument that the observed differences were likely to correspond to specific neuronal differences.

4.1. Behavior Performance. Both of the RT and accuracy analysis showed differences between EX and AP addition tasks. However, the difference between the two groups was only detected for the accuracy of EX addition problems, revealing that abacus-trained children were more accurate than nontrained children in the EX addition task. This was in accordance with previous studies that the abacus experts performed computation tasks with a higher accuracy than control [23, 32]. The vanish of speed effect that the abacus-trained children performed computation tasks with faster speed [23, 32] was probably due to the fact that the abacus-trained children in the present study were not as expert as that in previous studies. Anyway, our results still demonstrated the superior capability of numerical processing for abacus-trained children. A possible account for the better performance of abacus-trained children was that they may employ a different problem-solving strategy induced by the long-term abacus training. After the training, a "mental abacus" was formed in their brains [15, 20], which may be helpful when they performed the arithmetical problems. This "mental abacus" may be the key reason for the improved performance of abacus-trained children in the EX calculation task.

4.2. Brain Activations. From the general pattern of brain activities in two addition tasks for both groups, we found that the AP addition task that related brain activations for both groups were distributed bilaterally, while the EX addition that related brain activations were lateralized to the left hemisphere, especially for nontrained children. Moreover, common regions were induced among different addition tasks for both groups, including the SMA, left precentral sulcus (BA 6), insula, IPS, and adjacent parietal areas. Interestingly, the inferior frontal cortex was also activated except in the EX addition task for the abacus-trained group. Basically, these frontal-premotor-parietal areas were specified in numerical representation and calculation, and were consistent with the regions that are engaged in mental calculation tasks in human imaging studies [1, 4–6, 8, 9, 15, 25, 33, 34].

4.3. Neural Differences between the AP And EX Addition Task in Each Group. In the nontrained group, common activations across addition tasks covered a cortical network comprised mostly of left-sided superior parietal cortex, SMA, and left precentral sulcus, and these regions were mainly involved in the number of representation and operation tasks [1, 6, 8, 34].

A significant difference was detected between the activity patterns of two addition tasks. More activities were induced by the AP addition task, especially in the bilateral parietal areas around the IPS, the precuneus and the superior frontal cortex, indicating that the language-independent visuospatial strategy, were adopted in the AP addition task. This was consistent to the result of previous adult studies [1, 9]. Compatible with previous findings, a greater activation was elicited in the medial frontal cortex (mostly in the pre-SMA), which was associated with the cognitive motor control processes, including sensory discrimination and decision making or motor selection for the action after stimuli [35, 36]. Besides, the medial frontal cortex was also suggested to have a role in mental calculation [37, 38]. The involvement of thalamus and cerebellum which showed a small area of activation in the favor of AP addition task was also detected by a previous study focused on mental calculations [7]. The dorsal basal ganglia, including the caudate and putamen, were known to be critical for procedural memory [39, 40], and this region also played a role in the maintenance of information in working memory in mental arithmetic tasks [41]. The activation of insula also signified the engagement of visuospatial resources when children performed the task [5].

Taken together, these findings provided evidence for the greater involvement of and greater reliance on language-independent strategy and visuospatial working memory in AP addition tasks for nontrained children.

On the other hand, no hyperactivity was detected in favor of the EX addition task. This was dissimilar from previous adults studies in which they found significant activations for EX calculation in the language-dependent areas located in the left hemisphere [1, 9]. One possible reason of the mismatch between the present and previous results may be due to the differences in culture such as educational systems and mathematics learning strategies. For example, Yiyuan Tang et al. [42] detected a functional distinction between native Chinese and English speakers in the brain network that was involved in number representation tasks. Another reason may be due to the strategy and the development of the neural networks adopted by children. A comparative study of children and adults suggested that both verbal and spatial number representations might be involved in AP and EX calculations, and the cerebral networks were still developing around the age of 10 years old [3].

In the abacus-trained group, common activations across addition tasks covered a distributed cortical network that was comprised of bilateral superior parietal cortices, bilateral middle occipital cortices, bilateral inferior temporal cortices, bilateral precentral gyrus, bilateral insula, the SMA, left inferior parietal cortex, and cerebellum. These regions were also found in previous abacus studies [15, 23, 25, 26, 36]. Only slight differences were detected between the AP and EX addition tasks by the uncorrected results; hyperactivity was found in the left superior frontal cortex and left inferior parietal cortex during the AP addition task and in the ACC during the EX addition task. These areas fall outside of traditional perisylvian language areas [43, 44]. The inferior parietal cortex was involved in various visuospatial and analogical mental transformations [45, 46], and the superior frontal-intraparietal network was very important for visuospatial working memory [47]. The ACC that is involved in attentional processes [48] was also found in a previous study in children [49]. These results demonstrated that a similar visuospatial-specific strategy was adopted by abacus-trained children in AP and EX addition tasks, and more visuospatial networks were engaged when they performed AP addition tasks.

4.4. Neural Differences between the Abacus-Trained and Nontrained Group in Each Task. In the AP addition task, no significant differences were found between the two groups in the corrected result, indicating that a similar strategy was adopted in the AP addition task for both groups, whereas, slight differences were detected in the uncorrected result; the spatial related area (left precuneus) and the bilateral middle temporal cortices were more activated in abacus-trained children, while premotor regions (SMA and precentral sulcus) were more activated in nontrained children. Additionally, from the general pattern of the brain activity, we knew that bilateral inferior parietal cortices were activated in both groups during the AP addition task, suggesting the engagement of a visuospatial strategy. These results indicated that a similar but slightly different visuospatial strategy was adopted during the AP addition task in both groups.

In the EX addition task, the abacus-trained group revealed more activations than the nontrained group, including the right MPFC, right caudate, right superior temporal cortex, and the right angular. This activity pattern was specifically lateralized to the right hemisphere, which is consistent to previous abacus studies [15, 23, 25]. The right parietal cortex was suggested to play a role in mental calculation of abacus experts [23]. The right angular was considered to be associated with visuospatial attention [6, 8], and the caudate was suggested to be involved in learning and memory [40]. Besides, the thalamus was also activated. These corticothalamic circuits recruited here may be responsible for the rapid arithmetic processing of abacus-trained children.

More interestingly, the MPFC were mainly included in the default mode network (DMN) which contained a group of areas that exhibit higher metabolic activity at rest than during tasks [50–52]. Additionally, the MPFC was considered to play an important role in cognitive control [53]. This activity pattern indicated that abacus-trained children need fewer resources to accomplish EX addition tasks or the resource allocation was optimized by the long-term abacus training, which might account for the exceptional computational skills of abacus experts.

All these areas may constitute a circuit involved in the visuospatial-specific retrieval and the processing of imaginary abacus.

5. Conclusion

With two matched groups of Chinese children aged about 10 years, the present study investigated the abacus training effect on children's behavioral performance and brain activity pattern during AP and EX addition tasks. Our findings showed that: (1) nontrained children engaged more visuospatial representations in the AP calculation task with contrast to the EX; (2) abacus-trained children adopted a similar strategy for both tasks; (3) after the abacus training, children were more inclined to apply a visuospatial strategy when processing EX problems. For the first time, this study provided evidence for the specific effects of abacus training on EX and AP number processing in children.

However, there were limitations in our study. The lacking of adult contrast made our comparative result between children and adults less persuasive. Furthermore, only one group of abacus-trained children participated in our study; children with different training intensities should be involved in future studies.

Nonetheless, our results still demonstrated an obvious effect of the long-term abacus training on both of the behavior performance and neural correlates of addition tasks. The present study might be helpful for understanding the neural mechanism of abacus training and also have some positive significance for children's early educations.

Conflict of Interests

The authors declare that they have no conflict of interests.

Acknowledgments

The authors thank the contribution of the Chinese Abacus and Mental Arithmetic Association, Finance Departments and Abacus and Mental Arithmetic Association of Weifang for their kind supports. The authors thank also to the children from Beiguan Primary School of Weifang for their kind supports in data collection. The Project was partially supported by NSFC (no. 81271601, no. 30900389, no. 31270026).

References

[1] S. Dehaene, E. Spelke, P. Pinel, R. Stanescu, and S. Tsivkin, "Sources of mathematical thinking: behavioral and brain-imaging evidence," *Science*, vol. 284, no. 5416, pp. 970–974, 1999.

[2] P. Pica, C. Lemer, V. Izard, and S. Dehaene, "Exact and approximate arithmetic in an Amazonian indigene group," *Science*, vol. 306, no. 5695, pp. 499–503, 2004.

[3] K. Kucian, M. von Aster, T. Loenneker, T. Dietrich, and E. Martin, "Development of neural networks for exact and approximate calculation: a fMRI study," *Developmental Neuropsychology*, vol. 33, no. 4, pp. 447–473, 2008.

[4] S. Dehaene, M. Piazza, P. Pinel, and L. Cohen, "Three parietal circuits for number processing," *Cognitive Neuropsychology*, vol. 20, no. 3–6, pp. 487–506, 2003.

[5] L. Zago, M. Pesenti, E. Mellet, F. Crivello, B. Mazoyer, and N. Tzourio-Mazoyer, "Neural correlates of simple and complex mental calculation," *NeuroImage*, vol. 13, no. 2, pp. 314–327, 2001.

[6] V. Menon, S. M. Rivera, C. D. White, G. H. Glover, and A. L. Reiss, "Dissociating prefrontal and parietal cortex activation during arithmetic processing," *NeuroImage*, vol. 12, no. 4, pp. 357–365, 2000.

[7] R. H. Grabner, D. Ansari, G. Reishofer, E. Stern, F. Ebner, and C. Neuper, "Individual differences in mathematical competence predict parietal brain activation during mental calculation," *NeuroImage*, vol. 38, no. 2, pp. 346–356, 2007.

[8] M. Arsalidou and M. J. Taylor, "Is 2+2=4? Meta-analyses of brain areas needed for numbers and calculations," *NeuroImage*, vol. 54, no. 3, pp. 2382–2393, 2011.

[9] R. Stanescu-Cosson, P. Pinel, P.-F. van de Moortele, D. Le Bihan, L. Cohen, and S. Dehaene, "Understanding dissociations in dyscalculia: a brain imaging study of the impact of number size on the cerebral networks for exact and approximate calculation," *Brain*, vol. 123, no. 11, pp. 2240–2255, 2000.

[10] B. Kolb and I. Q. Whishaw, "Brain plasticity and behavior," *Annual Review of Psychology*, vol. 49, pp. 43–64, 1998.

[11] D. V. Buonomano and M. M. Merzenich, "Cortical plasticity: from synapses to maps," *Annual Review of Neuroscience*, vol. 21, pp. 149–186, 1998.

[12] J. N. Sanes and J. P. Donoghue, "Plasticity and primary motor cortex," *Annual Review of Neuroscience*, vol. 23, pp. 393–415, 2000.

[13] P. J. Olesen, H. Westerberg, and T. Klingberg, "Increased prefrontal and parietal activity after training of working memory," *Nature Neuroscience*, vol. 7, no. 1, pp. 75–79, 2003.

[14] A. Holtmaat and K. Svoboda, "Experience-dependent structural synaptic plasticity in the mammalian brain," *Nature Reviews Neuroscience*, vol. 10, no. 9, pp. 647–658, 2009.

[15] F. Y. Chen, Z. H. Hu, X. H. Zhao et al., "Neural correlates of serial abacus mental calculation in children: a functional MRI study," *Neuroscience Letters*, vol. 403, no. 1-2, pp. 46–51, 2006.

[16] T.-H. Wu, C.-L. Chen, Y.-H. Huang, R.-S. Liu, J.-C. Hsieh, and J. J. S. Lee, "Effects of long-term practice and task complexity on brain activities when performing abacus-based mental calculations: a PET study," *European Journal of Nuclear Medicine and Molecular Imaging*, vol. 36, no. 3, pp. 436–445, 2009.

[17] Y. Hu, F. Geng, L. Tao et al., "Enhanced white matter tracts integrity in children with abacus training," *Human Brain Mapping*, vol. 32, no. 1, pp. 10–21, 2011.

[18] Y. Li, Y. Wang, Y. Hu, Y. Liang, and F. Chen, "Structural changes in left fusiform areas and associated fiber connections in children with abacus training: evidence from morphometry and tractography," *Frontiers in Human Neuroscience*, vol. 7, article 335, 2013.

[19] Y. Q. Wang, F. J. Geng, Y. Z. Hu, F. L. Du, and F. Y. Chen, "Numerical processing efficiency improved in experienced mental abacus children," *Cognition*, vol. 127, pp. 149–158, 2013.

[20] J. W. Stigler, "'Mental abacus': the effect of abacus training on Chinese children's mental calculation," *Cognitive Psychology*, vol. 16, no. 2, pp. 145–176, 1984.

[21] G. Hatano, Y. Miyake, and M. G. Binks, "Performance of expert abacus operators," *Cognition*, vol. 5, no. 1, pp. 47–55, 1977.

[22] S. Hishitani, "Imagery experts: how do expert abacus operators process imagery?" *Applied Cognitive Psychology*, vol. 4, no. 1, pp. 33–46, 1990.

[23] T. Hanakawa, M. Honda, T. Okada, H. Fukuyama, and H. Shibasaki, "Neural correlates underlying mental calculation in abacus experts: a functional magnetic resonance imaging study," *NeuroImage*, vol. 19, no. 2, pp. 296–307, 2003.

[24] M. C. Frank and D. Barner, "Representing exact number visually using mental abacus," *Journal of Experimental Psychology*, vol. 141, no. 1, pp. 134–149, 2012.

[25] C. L. Chen, T. H. Wu, M. C. Cheng et al., "Prospective demonstration of brain plasticity after intensive abacus-based mental calculation training: an fMRI study," *Nuclear Instruments and Methods in Physics Research A*, vol. 569, no. 2, pp. 567–571, 2006.

[26] S. Tanaka, K. Seki, T. Hanakawa et al., "Abacus in the brain: a longitudinal functional MRI study of a skilled abacus user with a right hemispheric lesion," *Frontiers in Psychology*, vol. 3, article 315, 2012.

[27] Y. Ku, B. Hong, W. Zhou, M. Bodner, and Y.-D. Zhou, "Sequential neural processes in abacus mental addition: an EEG and fMRI case study," *PLoS ONE*, vol. 7, no. 5, Article ID e36410, 2012.

[28] Y. Gong and T. Cai, *Manual of Chinese Revised Wechsler Intelligence Scale for Children*, Hunan Atlas Publishing House, Changsha, China, 1993.

[29] W. Schneider, A. Eschman, and A. Zuccolotto, *E-Prime Reference Guide: Psychology Software Tools*, 2002.

[30] J. Talairach and P. Tournoux, *Co-Planar Stereotaxic Atlas of the Human Brain*, 1988.

[31] K. J. Friston, A. P. Holmes, K. J. Worsley, J.-P. Poline, C. D. Frith, and R. S. J. Frackowiak, "Statistical parametric maps in functional imaging: a general linear approach," *Human Brain Mapping*, vol. 2, no. 4, pp. 189–210, 1994.

[32] T. Hatta and M. Miyazaki, "Visual imagery processing in Japanese abacus experts," *Imagination, Cognition and Personality*, vol. 9, no. 2, pp. 91–102, 1990.

[33] S. M. Rivera, A. L. Reiss, M. A. Eckert, and V. Menon, "Developmental changes in mental arithmetic: evidence for increased functional specialization in the left inferior parietal cortex," *Cerebral Cortex*, vol. 15, no. 11, pp. 1779–1790, 2005.

[34] H. Zhang, C. Chen, and X. Zhou, "Neural correlates of numbers and mathematical terms," *NeuroImage*, vol. 60, no. 1, pp. 230–240, 2012.

[35] M. X. Cohen, A. S. Heller, and C. Ranganath, "Functional connectivity with anterior cingulate and orbitofrontal cortices during decision-making," *Cognitive Brain Research*, vol. 23, no. 1, pp. 61–70, 2005.

[36] T. Hanakawa, M. Honda, T. Okada, H. Fukuyama, and H. Shibasaki, "Differential activity in the premotor cortex subdivisions in humans during mental calculation and verbal rehearsal tasks: a functional magnetic resonance imaging study," *Neuroscience Letters*, vol. 347, no. 3, pp. 199–201, 2003.

[37] F. Lucchelli and E. De Renzi, "Primary dyscalculia after a medial frontal lesion of the left hemisphere," *Journal of Neurology Neurosurgery and Psychiatry*, vol. 56, no. 3, pp. 304–307, 1993.

[38] T. Hanakawa, A. Ikeda, N. Sadato et al., "Functional mapping of human medial frontal motor areas: the combined use of functional magnetic resonance imaging and cortical stimulation," *Experimental Brain Research*, vol. 138, no. 4, pp. 403–409, 2001.

[39] M.-F. Ghilardi, C. Ghez, V. Dhawan et al., "Patterns of regional brain activation associated with different forms of motor learning," *Brain Research*, vol. 871, no. 1, pp. 127–145, 2000.

[40] A. M. Graybiel, "The basal ganglia: learning new tricks and loving it," *Current Opinion in Neurobiology*, vol. 15, no. 6, pp. 638–644, 2005.

[41] V. Menon, R. T. Anagnoson, G. H. Glover, and A. Pfefferbaum, "Basal ganglia involvement in memory-guided movement sequencing," *NeuroReport*, vol. 11, no. 16, pp. 3641–3645, 2000.

[42] Y. Tang, W. Zhang, K. Chen et al., "Arithmetic processing in the brain shaped by cultures," *Proceedings of the National Academy of Sciences of the United States of America*, vol. 103, no. 28, pp. 10775–10780, 2006.

[43] A. R. Damasio and N. Geschwind, "The neural basis of language," *Annual Review of Neuroscience*, vol. 7, pp. 127–147, 1984.

[44] C. J. Price, "The functional anatomy of word comprehension and production," *Trends in Cognitive Sciences*, vol. 2, no. 8, pp. 281–288, 1998.

[45] E. Bonda, M. Petrides, S. Frey, and A. Evans, "Neural correlates of mental transformations of the body-in-space," *Proceedings of the National Academy of Sciences of the United States of America*, vol. 92, no. 24, pp. 11180–11184, 1995.

[46] S. Lambrey, C. Doeller, A. Berthoz, and N. Burgess, "Imagining being somewhere else: neural basis of changing perspective in space," *Cerebral Cortex*, vol. 22, no. 1, pp. 166–174, 2012.

[47] T. Klingberg, "Development of a superior frontal-intraparietal network for visuo-spatial working memory," *Neuropsychologia*, vol. 44, no. 11, pp. 2171–2177, 2006.

[48] M. M. Botvinick, J. D. Cohen, and C. S. Carter, "Conflict monitoring and anterior cingulate cortex: an update," *Trends in Cognitive Sciences*, vol. 8, no. 12, pp. 539–546, 2004.

[49] N. Davis, C. J. Cannistraci, B. P. Rogers et al., "The neural correlates of calculation ability in children: an fMRI study," *Magnetic Resonance Imaging*, vol. 27, no. 9, pp. 1187–1197, 2009.

[50] M. E. Raichle, A. M. MacLeod, A. Z. Snyder, W. J. Powers, D. A. Gusnard, and G. L. Shulman, "A default mode of brain function," *Proceedings of the National Academy of Sciences of the United States of America*, vol. 98, no. 2, pp. 676–682, 2001.

[51] M. E. Raichle and M. A. Mintun, "Brain work and brain imaging," *Annual Review of Neuroscience*, vol. 29, pp. 449–476, 2006.

[52] M. E. Raichle and A. Z. Snyder, "A default mode of brain function: a brief history of an evolving idea," *NeuroImage*, vol. 37, no. 4, pp. 1083–1090, 2007.

[53] K. R. Ridderinkhof, M. Ullsperger, E. A. Crone, and S. Nieuwenhuis, "The role of the medial frontal cortex in cognitive control," *Science*, vol. 306, no. 5695, pp. 443–447, 2004.

Hindawi Publishing Corporation
BioMed Research International
Volume 2013, Article ID 683768, 8 pages
http://dx.doi.org/10.1155/2013/683768

Research Article

Changes of Regulatory T and B Cells in Patients with Papillary Thyroid Carcinoma after ^{131}I Radioablation: A Preliminary Study

Lei Jiang,[1] Yanxia Zhan,[2] Yusen Gu,[1] Yi Ye,[3] Yunfeng Cheng,[2,3] and Hongcheng Shi[1]

[1] *Department of Nuclear Medicine, Zhongshan Hospital, Fudan University, 180 Fenglin Road, Shanghai 200032, China*
[2] *Department of Hematology, Zhongshan Hospital, Fudan University, 180 Fenglin Road, Shanghai 200032, China*
[3] *Biomedical Research Center, Zhongshan Hospital, Fudan University, Shanghai 200032, China*

Correspondence should be addressed to Hongcheng Shi; shi.hongcheng@zs-hospital.sh.cn

Received 24 July 2013; Accepted 2 September 2013

Academic Editor: Hong Zhang

Introduction. Lymphocytic infiltration and specific lymphocytes subsets may play important roles in papillary thyroid carcinoma (PTC) progression and prognosis. In this study, we try to understand the influence of ^{131}I radioablation on the important lymphocytes subtypes of regulatory T and B cells (Tregs and Bregs). *Methods*. Peripheral blood mononuclear cells from 30 PTC patients before and after ^{131}I therapy, and 20 healthy donors were collected. The expression of Tregs ($CD4^+CD25^+CD127^{-/low}$) and B cell ($CD5^+CD19^+$) and production and secretion of interleukin 10 (IL-10) were analyzed by FACS and ELISA assay, respectively. *Results*. For Tregs percentage in peripheral blood lymphocytes, there was no difference between pretreatment and control and between posttreatment and control. Compared with pretherapy, increased Tregs infiltration was noted in posttherapy ($P < 0.05$). Although no difference was between pretreatment and control, compared with these two groups, decreased $CD19^+$ and $CD5^+CD19^+$ B cell percentage in posttreatment was observed ($P < 0.05$). Among these groups, no significant difference was displayed in intracellular IL-10 production and extracellular IL-10 secretion. *Conclusions*. ^{131}I Radioablation increased Tregs and decreased $CD19^+$ and $CD5^+CD19^+$ B cells percentage after treatment. However, it has no effect on IL-10 and lymphocytes in peripheral blood. Therefore, longer follow-up of Tregs and Bregs should be further investigated.

1. Introduction

Thyroid cancer is the most common endocrine malignancy, which constitutes approximately 1% of all human malignancies [1, 2]. Papillary thyroid carcinoma (PTC) accounts for about 70% of all thyroid carcinomas [3]. Although it has a relatively good prognosis, the incidence of thyroid carcinomas is rapidly increasing, and 10–30% of patients have recurrence and/or metastases [4, 5].

At present, many mechanisms are involved in the development of thyroid cancer, and the dysfunction of the immune systems is increasing being considered [6]. Regulatory T cells (Tregs) are subtypes of $CD4^+$ T cells, which play an important role in the immune response [7, 8]. In general, Tregs is identified as $CD4^+CD25^+CD127^{-/low}$ or $CD4^+CD25^+Foxp3^+$ [9, 10], which are commonly rich in primary tumors, draining lymph nodes, and peripheral blood of cancer patients [11–16]. An increased frequency of Tregs has been proven to be related with poor prognosis of many tumors [3, 17–19]. In contrast to Tregs, regulatory B cells (Bregs) mainly suppress immune response via the production of interleukin 10 (IL-10) [20, 21]. However, there are no specific transcriptions or surface molecular makers identified as Bregs. The most well-established concept of Bregs is the subtype of B cells producing IL-10, which are regulatory B10 cells. Furthermore, lots of studies demonstrated that the surface membrane marker CD5 was expressed on B10 cells. Meantime, CD19 is the well-established marker to identify B cells from peripheral

blood mononuclear cells (PBMCs). Thus, it seems that the expression of $CD5^+CD19^+$ is a common feature or hallmark of regulatory B cells [20–23].

In clinic, large studies have proven that, compared with thyroidectomy alone, the combination of ^{131}I radioablation and thyroidectomy for PTC patients could reduce recurrence and/or metastases [24–26]. In addition to that, the previous study demonstrated that Tregs and IL-10 level are related with invasiveness and prognosis of thyroid cancer [3, 5, 27, 28]. Therefore, it is necessary to understand the role of specific lymphocytes subsets in PTC patients before and after ^{131}I radiotherapy to evaluate the relationship between immune response and ^{131}I ablation.

2. Materials and Methods

2.1. Patients and Controls. From October 2012 to December 2012, PTC patients, with total or near-total thyroidectomy, were admitted and carried out the first radioiodine ablation in the Department of Nuclear Medicine, Zhongshan Hospital. On the basis of laboratory tests and imaging modalities (ultrasound, CT, whole body ^{131}I scan, and ^{18}F-FDG PET/CT examinations, etc.), the patients with thyroiditis and/or long distant metastases (such as lung and bone) were excluded. The follow-up examination was one month after the 1st ^{131}I therapy, and 30 patients had serum thymoglobulin level less than 2 μIU/mL (normal: 0.27–4.2 μIU/mL), that is to say, the ^{131}I therapy was successful, were enrolled in this study. Moreover, the healthy control group consisted of 20 adult volunteers.

The study was approved by local Medical Ethics Committees of Zhongshan Hospital, Fudan University. Informed consents were signed by all the patients before they were included in the study.

2.2. Radioiodine Ablation. In this study, all patients were firstly administrated for radioiodine ablation, and the received dose was 3,700 MBq (100 mCi) (Shanghai GMS Pharmaceutical Co., Ltd.). The venous blood samples of patients were collected within one week before the radioiodine therapy and one month after treatment, respectively. Meanwhile, the thyroid function tests and routine hematological parameters were analyzed.

2.3. Isolation of PBMCs. Venous blood samples were collected into ethylenediaminetetraacetic acid-treated tubes and diluted at 1 : 2 with Hanks balanced salt solution (HBSS) before Ficoll-Hypaque gradient centrifugation (2,000 rpm at room temperature for 15 min). Washed and resuspended, PBMCs were cryopreserved in fetal bovine serum containing 10% dimethyl sulfoxide (DMSO) and stored in liquid nitrogen for future cell-surface staining and cell culture.

2.4. Cell Culture. Cryopreserved PBMCs were thawed at 37°C and washed twice with HBSS. Then, PBMCs were seeded at a density of 5×10^5/mL in 24-well tissue culture plates. The culture medium was RPMI 1640 medium supplemented with 10% heat-inactivated fetal bovine serum, 2 mM L-glutamine, 200 U/mL penicillin, and 100 μg/mL streptomycin. For intracellular staining of IL-10, cells were stimulated with 50 ng/mL phorbol-12-myristate-13-acetate (PMA) and 500 ng/mL ionomycin for 24 h and the additional presence of 1 mM Brefeldin A (BFA) for last 4 h.

2.5. Flow Cytometric Analysis of Tregs. ~2×10^5 PBMCs were incubated with FITC-conjugated anti-CD4/PE-Cy7-conjugated anti-CD25/APC-conjugated anti-CD127, or isotypes (BD, USA) for 30 min at 4°C, washed twice and resuspended in staining buffer for analysis of T cell subpopulations. Acquisitions were performed on a FACS Aria II flow cytometer (BD, USA) and then analyzed using Flowjo software version 7.6.

2.6. Flow Cytometric Analysis of CD5, CD19, and IL-10. The flow cytometry was performed as above described. Briefly, ~2×10^5 PBMCs were incubated with APC-conjugated anti-CD5/FITC-conjugated anti-CD19 or isotypes (BD, USA) for 20 min at 4°C, washed twice, and resuspended in staining buffer for analysis of B cell subpopulations.

For intracellular IL-10 detection, cultured cells were then fixed and permeabilized before PE-conjugated anti-IL-10 or isotype (BioLegend, USA) staining. Acquisitions were performed on a FACSAria II flow cytometer (BD, USA) and then analyzed using Flowjo software version 7.6.

2.7. IL-10 Enzyme-Linked Immunosorbent Assay (ELISA). According to the manufacturer's instructions of Human IL-10 Quantikine ELISA kits (R&D, USA), concentration of IL-10 in supernatants of cell culture was detected. The lower detection limit of this assay was 0.78 pg/mL. Pure RPMI 1640 medium was used as negative control.

2.8. Statistical Analysis. SPSS 18.0 software for Windows (SPSS Inc., Chicago, Iee, USA) was used for statistical analysis. Data were expressed as mean ± SD. Means were compared using the Student's t-test. When multiple groups were compared, one-way ANOVA and Kruskal-Wallis test were used for data fulfilling normal distribution and for those did not, respectively. A 95% confidence level was chosen to determine the significance between groups, with P values of less than 0.05 indicating significant differences.

3. Results

3.1. Clinical Data. As shown in Table 1, 30 PTC patients were enrolled in this study, including 20 females and 10 males, with age range 26–70 years, median 45 years. Twenty healthy donors were also included, consisted of 11 females and 9 males, with age range 22–63 years, median 43 years.

The absolute number of lymphocytes in the pretreatment ($[2.45 \pm 0.68] \times 10^9$/L) and posttreatment group ($[1.52 \pm 0.41] \times 10^9$/L) is within normal levels (1.1–3.2 $\times 10^9$/L). However, there is significant difference between the pretreatment and posttreatment group ($P < 0.05$).

Table 1: Clinical data of patients and healthy donors.

Variable	Patients		Healthy donors
	Pre-T	Post-T	
Gender (female/male)	20/10		11/9
Age (median, range, yr)	45 (26–70)		43 (22–63)
Free T3 (normal: 2.8–7.1 pmoL/L)	1.38 ± 0.77	5.31 ± 2.87	4.54 ± 1.60
Free T4 (normal: 12.0–22.0 pmoL/L)	2.60 ± 0.85	19.1 ± 13.1	16.72 ± 2.67
TSH (normal: 0.27–4.2 μIU/mL)	84.56 ± 17.11	2.39 ± 2.73	2.14 ± 1.13
Tg (normal: 1.4–78 ng/mL)	13.32 ± 14.2	0.73 ± 0.65	22.72 ± 17.46
Anti-Tg (normal: <115 IU/mL)	15.36 ± 4.72	12.94 ± 4.10	20.82 ± 11.47
Anti-TPO (normal: <34 IU/mL)	10.99 ± 5.45	10.00 ± 5.27	8.86 ± 5.42

For PTC patients, the blood samples of pretreatment and aftertreatment were collected under different conditions. Patients were inhibited to take levothyroxine sodium tablets or similar euthyrox drugs for at least 3 weeks before the ^{131}I ablation. One month posttreatment, patients do the blood tests with routine suppressive therapy of thyroid hormone.

3.2. $CD4^+$ T Cells and Tregs Screening by Flow Cytometry Analysis. Blood samples of PTC patients and the healthy donors were analyzed by flow cytometry for $CD4^+$ T cells and $CD4^+CD25^+CD127^{-/low}$ T cells (Tregs), respectively (Figure 1(a)). The $CD4^+$ percentage in peripheral blood lymphocytes of the pretreatment, posttreatment, and control groups was (31.40 ± 6.09)%, (30.38 ± 8.00)%, and (34.74 ± 8.84)%, respectively. There was no significant difference among the above groups ($P > 0.05$) (Figure 1(b)).

Compared with Tregs (expressed as percentage of $CD4^+$ T cells) in blood of PTC patients before ^{131}I therapy (2.52 ± 0.87)%, Tregs was significantly higher in the posttherapy group (3.23 ± 0.84)% ($P < 0.05$) (Figures 1(c) and 1(d)). Tregs in the healthy donor was (2.69 ± 0.72)%. However, no significant difference was noted between the pretreatment and control group and between posttreatment and control, respectively ($P > 0.05$) (Figure 1(c)).

3.3. $CD19^+$ and $CD5^+CD19^+$ B Cells Screening by Flow Cytometry Analysis. Blood samples of patients with PTC and the healthy donors were analyzed by flow cytometry for $CD19^+$ and $CD5^+CD19^+$ B cells, respectively (Figure 2(a)). The $CD19^+$ percentage of total peripheral blood lymphocytes among the pretreatment, posttreatment, and control groups was (6.00 ± 2.31)%, (3.99 ± 1.16)%, and (6.96 ± 1.24)%, respectively.

No significant difference was found between pretherapy and control ($P > 0.05$), but the significant difference was noted between posttreatment and control ($P < 0.05$) (Figure 2(b)). Compared with $CD5^+CD19^+$ B cells (expressed as percentage of total lymphocytes) in blood of PTC patients before the ^{131}I ablation (2.07 ± 0.97)%, $CD5^+CD19^+$ B cells were significantly lower in the posttreatment group (1.63 ± 0.59)% ($P < 0.05$). $CD5^+CD19^+$ B cells in the healthy donors were (2.39 ± 0.43)%. Similar to the results of $CD19^+$ B cells, there was no significant difference between pretreatment and control ($P > 0.05$), but the significant difference was observed between posttreatment and control, respectively ($P < 0.05$) (Figures 2(b) and 2(c)).

3.4. Accumulated Intracellular IL-10 in $CD5^+CD19^+$ B Cells by Flow Cytometry Analysis. The intracellular production of IL-10 in $CD5^+CD19^+$ B cell percentage by flow cytometry analysis in the pretreatment, posttreatment, and the healthy donors was (6.77 ± 5.80)%, (11.96 ± 17.25)%, and (11.72 ± 10.81)%, respectively. There was no significant difference among these groups ($P > 0.05$) (Figure 3(a)).

3.5. IL-10 Production by $CD5^+$ B Cells by ELISA Analysis. The IL-10 production by $CD5^+$ B cells by ELISA analysis in the pretreatment, posttreatment, and the healthy donors was 9.02 ± 1.55, 9.44 ± 1.18, and 9.79 ± 0.57 pg/mL, respectively. There was no significant difference among these groups ($P > 0.05$) (Figure 3(b)).

4. Discussion

The lymphocytic infiltration is frequently observed in PTC, and specific lymphocytes subsets may be the important regulators of PTC progression and prognosis [3, 5, 27, 28]. Therefore, in this work, lymphocytes subpopulations of Tregs and $CD5^+$ B cells (putative B cells that have regulatory functions) are studies in blood samples of PTC patient before and after ^{131}I ablation. To our knowledge, no previous study focused on this control research.

Although Tregs have been studied and analyzed in many tumors, such as breast cancer, pancreas cancer, and melanoma [17–19], the studies on Tregs infiltration in thyroid tissues and peripheral blood samples are limited. Gogali et al. [3] and French et al. [5] proved that increased Tregs infiltration in thyroid tissue was positively correlated with advanced disease stage. In addition, Gogali et al. [3] showed that there was no difference in Tregs percentage in blood samples between PTC patients and the healthy control. Different from the patients included in previous studies [3, 5, 28], the population in the present study was PTC patients with total or near-total thyroidectomy, whose Tregs percentage in the peripheral blood samples was supposed to be within normal level [29]. The pretreatment Tregs in our study were consistent with previous studies. Compared with

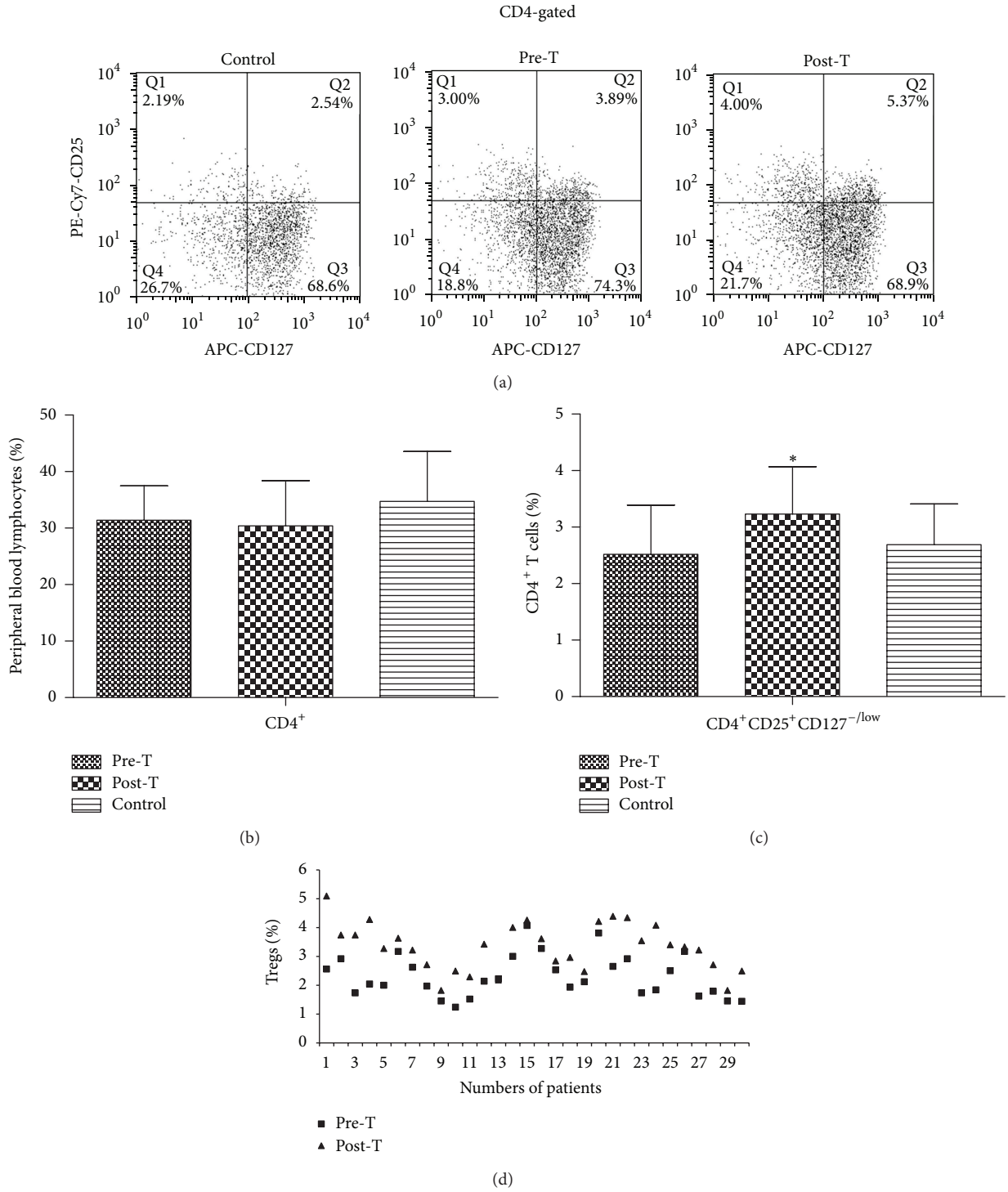

Figure 1: Expression of $CD4^+CD25^+CD127^{-/low}$ T cells (Tregs) in blood sample of pretreatment, posttreatment, and control groups (Pre-T: pretreatment, Post-T: posttreatment). (a) $CD4^+CD25^+CD127^{-/low}$ lymphocytes shown by FACS. (b) $CD4^+$ T cells percentage in peripheral blood lymphocytes. (c) $CD4^+CD25^+CD127^{-/low}$ T cells percentage in $CD4^+$ T cells ($^*P < 0.05$, compared with Pre-T). (d) Comparison of peripheral blood Tregs in individual patients with thyroid papillary carcinoma before and after ^{131}I radioablation.

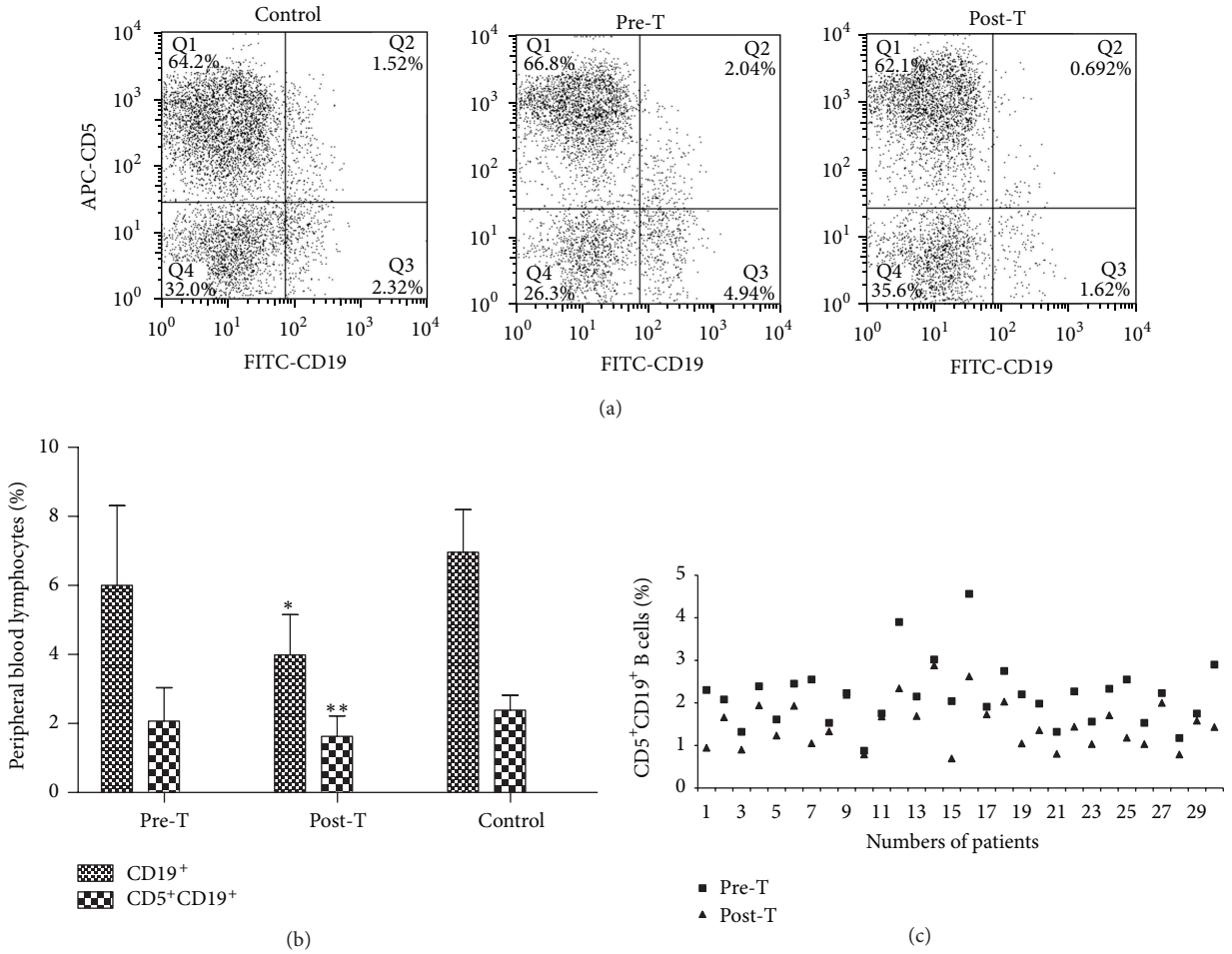

Figure 2: Expression of $CD5^+CD19^+$ B cells in blood sample of pretreatment, posttreatment, and control groups. (a) $CD5^+CD19^+$ B cells shown by FACS. (b) $CD19^+$ and $CD5^+CD19^+$ B cells percentage in peripheral blood lymphocytes ($^*P < 0.05$, compared with Pre-T and control; $^{**}P < 0.05$, compared with Pre-T and control). (c) Comparison of peripheral blood $CD5^+CD19^+$ B cells in individual patients with thyroid papillary carcinoma before and after ^{131}I radioablation.

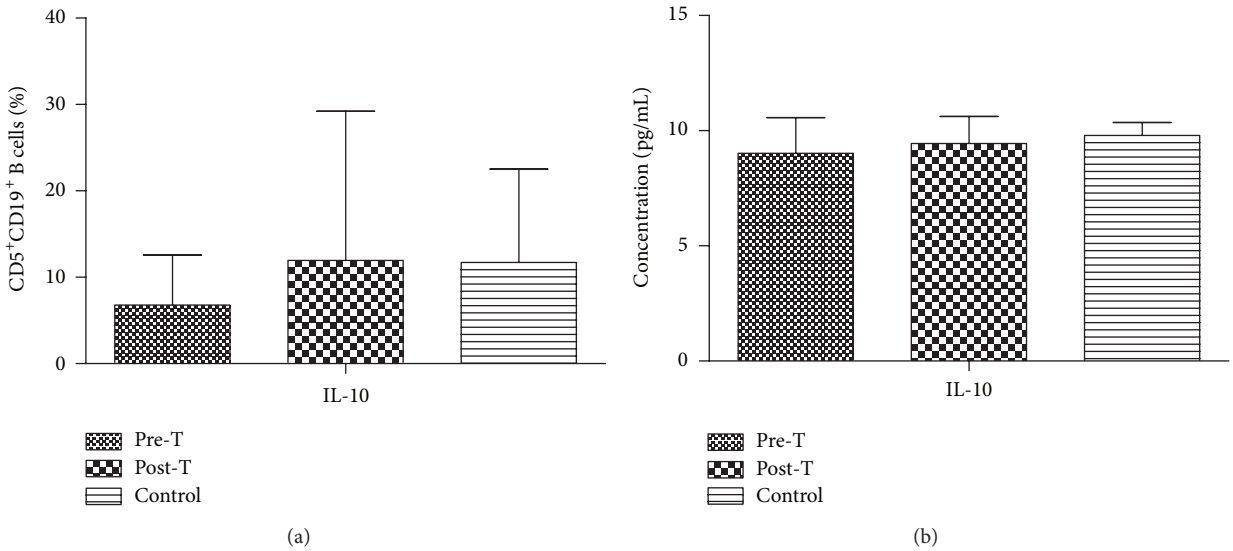

Figure 3: Intracellular and extracellular IL-10 in $CD5^+CD19^+$ B cells. (a) Intracellular IL-10 analyzed by FACS. (b) Extracellular IL-10 concentration tested by ELISA.

pretreatment, Tregs after the ^{131}I treatment were significantly higher. However, the posttreatment Tregs percentage in peripheral blood lymphocytes was found to have no significant difference with the healthy donors. The main function of human immune system is the body protection from a diverse range of agents, including tumor cells and radionuclide [3]. Elevating Tregs may be the immune response to ^{131}I, which was not beyond the self-tolerant extent and normalized the numbers of $CD4^+$ T cells. Moreover, it is demonstrated that ^{131}I ablation for PTC patients was a safe and effective therapy.

In addition to Tregs, certain B cell subpopulations could also exhibit potential regulation of immune response by functioning as cellular adjuvants for $CD4^+$ T cell activation and are involved in immune pathology through the production of cytokines that regulate T-cell function [30–33]. Given that regulatory B-cell subsets are likely to exist, one of the factors produced by regulatory B cells is the immunosuppressive cytokine IL-10 [20–23]. In this work, there was no significant difference between the pretreatment and control of $CD19^+$ B cells and between the pretreatment and control of $CD5^+CD19^+$ B cells. However, compared with healthy donors and PTC patients before ^{131}I ablation, both $CD19^+$ and $CD5^+CD19^+$ B cells after the ^{131}I therapy were significantly decreasing. The reasons are probably as followed: compared with T cells, B cells are more sensitive to radiation and prone to radiation-induced inhibition [34]. Moreover, although some clinical observations supported that the increasing of B cells was contributed to the limitation of autoimmune and malignant diseases, they are testified to have rather aggravating potential in other cases [35, 36]. Our results also showed there was no obvious correlation between decreasing B cells and bad prognosis. In addition, compared with the pretreatment group, the absolute number of lymphocytes in the posttreatment group significantly decreased, which was consistent with the analysis of regulatory B cells. We assume that in patients with thyroid papillary carcinoma before and after ^{131}I radioablation, regulatory B cells prior to regulatory T cells play more important role in the regulation of peripheral blood lymphocytes.

IL-10 was initially associated with Th2 cells and was described to inhibit Th1 cytokine production [37–39]. However, at present, IL-10 is not only involved in the inhibition of Th1 polarization but also prevents Th2 responses and exerts anti-inflammatory and suppressive effects on most hematopoietic cells. IL-10 produced by monocytes and cells other than T cells is required to maintain Treg-suppressive function and other autoimmune diseases [40]. In our study, the intracellular and extracellular IL-10 production and secretion were found to have no significant difference between the pretreatment, posttreatment, and control groups, which are in accordance with results of $CD4^+$ T cells and Tregs. However, the numbers of posttreatment $CD19^+$ and $CD5^+CD19^+$ B cells were lower than those of pretreatment, which suggests that the synthesis and secretion of IL-10 were relatively increased. It could develop and maintain that posttherapy Tregs were higher than pretherapy ones in this study.

Moreover, there were some potential limitations in this study. One is considering the clinical effect of ^{131}I, only one time-point after treatment was chosen, which couldn't reflect the dynamic change in patients' peripheral blood lymphocytes. Another limitation is the small population. Large sample of analysis of regulatory T and B cells in patients with thyroid papillary carcinoma before and after ^{131}I radioablation should be further investigated.

5. Conclusion

^{131}I radioablation increased Tregs percentage and decreased $CD19^+$ and $CD5^+CD19^+$ B cells percentage at one month after treatment. However, it has no effect on the production and secretion of IL-10, and the percentage and absolute number of lymphocytes in peripheral blood are within normal levels. Therefore, longer follow-up of changes of regulatory T and B cells should be further investigated.

Conflict of Interests

The authors have no conflict of interest.

Authors' Contribution

Lei Jiang and Yanxia Zhan equally contributed to this work.

Acknowledgments

This study is in part supported by the National Science Foundation for Scholars of China (Grant no. 81271608 to Hongcheng Shi and 81170473 to Yunfeng Cheng), the National Science Foundation for Young Scholars of China (Grant no. 81101072 to Lei Jiang), and Funding from Shanghai Institute of Medical Imaging (Grant no. Y-2013-12 to Lei Jiang). Moreover, the authors would like to thank Chao Ma, M.D., Ph.D., from Xinhua Hospital, Shanghai, China, for the discussion part.

References

[1] E. L. Mazzaferri, "Thyroid cancer," in *Principles and Practice of Endocrinology and Metabolism*, K. L. Becker, Ed., pp. 319–331, J. B. Lippincott, Philadelphia, Pa, USA, 1990.

[2] J. Robbins, M. J. Merino, J. D. Boice Jr. et al., "Thyroid cancer: a lethal endocrine neoplasm," *Annals of Internal Medicine*, vol. 115, no. 2, pp. 133–147, 1991.

[3] F. Gogali, G. Paterakis, G. Z. Rassidakis et al., "Phenotypical analysis of lymphocytes with suppressive and regulatory properties (Tregs) and NK cells in the papillary carcinoma of thyroid," *The Journal of Clinical Endocrinology & Metabolism*, vol. 97, pp. 1474–1482, 2012.

[4] E. L. Mazzaferri and S. M. Jhiang, "Long-term impact of initial surgical and medical therapy on papillary and follicular thyroid cancer," *The American Journal of Medicine*, vol. 97, no. 5, pp. 418–428, 1994.

[5] J. D. French, Z. J. Weber, D. L. Fretwell, S. Said, J. P. Klopper, and B. R. Haugen, "Tumor-associated lymphocytes and increased

FoxP3$^+$ regulatory T cell frequency correlate with more aggressive papillary thyroid cancer," *Journal of Clinical Endocrinology and Metabolism*, vol. 95, no. 5, pp. 2325–2333, 2010.

[6] B. Müller-Hübenthal, M. Azemar, D. Lorenzen et al., "Tumour biology: tumour-associated inflammation versus antitumor immunity," *Anticancer Research*, vol. 29, no. 11, pp. 4795–4805, 2009.

[7] A. M. Thornton and E. M. Shevach, "CD4$^+$CD25$^+$ immunoregulatory T cells suppress polyclonal T cell activation in vitro by inhibiting interleukin 2 production," *Journal of Experimental Medicine*, vol. 188, no. 2, pp. 287–296, 1998.

[8] S. Sakaguchi, N. Sakaguchi, M. Asano, M. Itoh, and M. Toda, "Immunologic self-tolerance maintained by activated T cells expressing IL- 2 receptor α-chains (CD25): breakdown of a single mechanism of self- tolerance causes various autoimmune diseases," *Journal of Immunology*, vol. 155, no. 3, pp. 1151–1164, 1995.

[9] W. Liu, A. L. Putnam, Z. Xu-yu et al., "CD127 expression inversely correlates with FoxP3 and suppressive function of human CD4$^+$ T reg cells," *Journal of Experimental Medicine*, vol. 203, no. 7, pp. 1701–1711, 2006.

[10] B. Bisikirska, J. Colgan, J. Luban, J. A. Bluestone, and K. C. Herold, "TCR stimulation with modified anti-CD3 mAb expands CD8$^+$ T cell population and induces CD8$^+$CD25$^+$ Tregs," *Journal of Clinical Investigation*, vol. 115, no. 10, pp. 2904–2913, 2005.

[11] T. J. Curiel, G. Coukos, L. Zou et al., "Specific recruitment of regulatory T cells in ovarian carcinoma fosters immune privilege and predicts reduced survival," *Nature Medicine*, vol. 10, no. 9, pp. 942–949, 2004.

[12] L. R. Javia and S. A. Rosenberg, "CD4$^+$CD25$^+$ suppressor lymphocytes in the circulation of patients immunized against melanoma antigens," *Journal of Immunotherapy*, vol. 26, no. 1, pp. 85–93, 2003.

[13] U. K. Liyanage, T. T. Moore, H.-G. Joo et al., "Prevalence of regulatory T cells is increased in peripheral blood and tumor microenvironment of patients with pancreas or breast adenocarcinoma," *Journal of Immunology*, vol. 169, no. 5, pp. 2756–2761, 2002.

[14] D. Wolf, A. M. Wolf, H. Rumpold et al., "The expression of the regulatory T cell-specific forkhead box transcription factor FoxP3 is associated with poor prognosis in ovarian cancer," *Clinical Cancer Research*, vol. 11, no. 23, pp. 8326–8331, 2005.

[15] C. Jandus, G. Bioley, D. E. Speiser, and P. Romero, "Selective accumulation of differentiated FOXP3$^+$ CD4$^+$ T cells in metastatic tumor lesions from melanoma patients compared to peripheral blood," *Cancer Immunology, Immunotherapy*, vol. 57, no. 12, pp. 1795–1805, 2008.

[16] A. M. Miller, K. Lundberg, V. Özenci et al., "CD4$^+$CD25 high T cells are enriched in the tumor and peripheral blood of prostate cancer patients," *Journal of Immunology*, vol. 177, no. 10, pp. 7398–7405, 2006.

[17] A. Bamias, V. Koutsoukou, E. Terpos et al., "Correlation of NK T-like CD3$^+$CD56$^+$ cells and CD4$^+$CD25$^+$(hi) regulatory T cells with VEGF and TNFα in ascites from advanced ovarian cancer: association with platinum resistance and prognosis in patients receiving first-line, platinum-based chemotherapy," *Gynecologic Oncology*, vol. 108, no. 2, pp. 421–427, 2008.

[18] T. Schneider, S. Kimpfler, A. Warth et al., "Foxp3$^+$ regulatory T cells and natural killer cells distinctly infiltrate primary tumors and draining lymph nodes in pulmonary adenocarcinoma," *Journal of Thoracic Oncology*, vol. 6, no. 3, pp. 432–438, 2011.

[19] S. Hinz, L. Pagerols-Raluy, H.-H. Oberg et al., "Foxp3 expression in pancreatic carcinoma cells as a novel mechanism of immune evasion in cancer," *Cancer Research*, vol. 67, no. 17, pp. 8344–8350, 2007.

[20] D. J. Dilillo, T. Matsushita, and T. F. Tedder, "B10 cells and regulatory B cells balance immune responses during inflammation, autoimmunity, and cancer," *Annals of the New York Academy of Sciences*, vol. 1183, pp. 38–57, 2010.

[21] P. A. Blair, L. Y. Noreña, F. Flores-Borja et al., "CD19$^+$CD24^{hi}CD38^{hi} B cells exhibit regulatory capacity in healthy individuals but are functionally impaired in systemic lupus erythematosus patients," *Immunity*, vol. 32, no. 1, pp. 129–140, 2010.

[22] D. Maseda, S. H. Smith, D. J. DiLillo et al., "Regulatory B10 cells differentiate into antibody-secreting cells after transient IL-10 production in vivo," *Journal of Immunology*, vol. 188, no. 3, pp. 1036–1048, 2012.

[23] F. Hua, L. Ji, Y. Zhan et al., "Pulsed high-dose dexamethasone improves interleukin 10 secretion by CD5$^+$ B cells in patients with primary immune thrombocytopenia," *Journal of Clinical Immunology*, vol. 32, no. 6, pp. 1233–1242, 2012.

[24] Q. Y. Luo, "Clinical value and indications of ^{131}I treatment after surgery for differentiated thyroid cancer," *Journal of Nuclear Medicine & Radiation Therapy*, vol. 3, article e104, 2012.

[25] M. Schlumberger, B. Catargi, I. Borget et al., "Strategies of radioiodine ablation in patients with low-risk thyroid cancer," *The New England Journal of Medicine*, vol. 366, no. 18, pp. 1663–1673, 2012.

[26] R. J. Robbins and M. J. Schlumberger, "The evolving role of ^{131}I for the treatment of differentiated thyroid carcinoma," *Journal of Nuclear Medicine*, vol. 46, no. 1, p. 28, 2005.

[27] L. L. Cunha, A. J. Tincani, L. V. M. D. Assumpção, F. A. Soares, J. Vassallo, and L. S. Ward, "Interleukin-10 but not interleukin-18 may be associated with the immune response against well differentiated thyroid cancer," *Clinics*, vol. 66, no. 7, pp. 1203–1208, 2011.

[28] L. L. Cunha, E. C. Morari, S. Nonogaki, F. A. Soares, J. Vassallo, and L. S. Ward, "Foxp3 expression is associated with aggressiveness in differentiated thyroid carcinomas," *Clinics*, vol. 67, no. 5, pp. 483–488, 2012.

[29] A. Sellitto, G. Galizia, U. De Fanis et al., "Behavior of circulating CD4$^+$CD25$^+$Foxp3$^+$ regulatory T cells in colon cancer patients undergoing surgery," *Journal of Clinical Immunology*, vol. 31, no. 6, pp. 1095–1104, 2011.

[30] T. W. Lebien and T. F. Tedder, "B lymphocytes: how they develop and function," *Blood*, vol. 112, no. 5, pp. 1570–1580, 2008.

[31] K. Yanaba, J.-D. Bouaziz, T. Matsushita, C. M. Magro, E. W. St.Clair, and T. F. Tedder, "B-lymphocyte contributions to human autoimmune disease," *Immunological Reviews*, vol. 223, no. 1, pp. 284–299, 2008.

[32] J.-D. Bouaziz, K. Yanaba, G. M. Venturi et al., "Therapeutic B cell depletion impairs adaptive and autoreactive CD4 $^+$ T cell activation in mice," *Proceedings of the National Academy of Sciences of the United States of America*, vol. 104, no. 52, pp. 20878–20883, 2007.

[33] F. E. Lund, "Cytokine-producing B lymphocytes: key regulators of immunity," *Current Opinion in Immunology*, vol. 20, no. 3, pp. 332–338, 2008.

[34] Q. Y. Luo, L. B. Chen, Y. L. Yu, H. K. Lu, and R. S. Zhu, "Changs in lymphocytes subsets in differentiated thyroid cancer treated with ^{131}I," *Chinese Journal of Endocrinology and Metabolism*, vol. 22, pp. 52–54, 2006.

[35] F. Martin and A. C. Chan, "B cell immunobiology in disease: evolving concepts from the clinic," *Annual Review of Immunology*, vol. 24, pp. 467–496, 2006.

[36] S. Lindner, K. Dahlke, K. Sontheimer et al., "Interleukin 21-induced granzyme B-expressing B cells infiltrate tumors and regulate T cells," *Cancer Research*, vol. 15, no. 73, pp. 2468–2479, 2013.

[37] C. Asseman, S. Mauze, M. W. Leach, R. L. Coffman, and F. Powrie, "An essential role for interleukin 10 in the function of regulatory T cells that inhibit intestinal inflammation," *Journal of Experimental Medicine*, vol. 190, no. 7, pp. 995–1003, 1999.

[38] F. Cottrez, S. D. Hurst, R. L. Coffman, and H. Groux, "T regulatory cells 1 inhibit a Th2-specific response in vivo," *Journal of Immunology*, vol. 165, no. 9, pp. 4848–4853, 2000.

[39] A. O'Garra, G. Stapleton, V. Dhar et al., "Production of cytokines by mouse B cells: B lymphomas and normal B cells produce interleukin 10," *International Immunology*, vol. 2, no. 9, pp. 821–832, 1990.

[40] M. Murai, O. Turovskaya, G. Kim et al., "Interleukin 10 acts on regulatory T cells to maintain expression of the transcription factor Foxp3 and suppressive function in mice with colitis," *Nature Immunology*, vol. 10, no. 11, pp. 1178–1184, 2009.

Hindawi Publishing Corporation
BioMed Research International
Volume 2013, Article ID 275805, 8 pages
http://dx.doi.org/10.1155/2013/275805

Review Article

The Predictive Value of Interim and Final [18F] Fluorodeoxyglucose Positron Emission Tomography after Rituximab-Chemotherapy in the Treatment of Non-Hodgkin's Lymphoma: A Meta-Analysis

Yuyuan Zhu,[1,2] Jianda Lu,[3] Xin Wei,[3] Shaoli Song,[1] and Gang Huang[1]

[1] *Department of Nuclear Medicine, Renji Hospital, Jiaotong University, Shanghai 200127, China*
[2] *Department of Nuclear Medicine, Renji Hospital, Shanghai Jiaotong University School of Medicine, Shanghai 200127, China*
[3] *Renji Hospital, School of Medicine, Shanghai Jiaotong University, Shanghai 200127, China*

Correspondence should be addressed to Gang Huang; huang2802@163.com

Received 17 March 2013; Revised 13 June 2013; Accepted 2 July 2013

Academic Editor: Ignasi Carrio

Background and Purpose. The aim of this study is to determine the prognostic value of interim and final FDG-PET in major histotypes of B-cell NHL patients treated with rituximab containing-chemotherapy. *Methods*. We searched for articles published in English, limited to lymphoma, rituximab, and FDG-PET, and dedicated to deal with the impact on progression and survival. The log hazard ratios (HR) and their variances were estimated. *Results*. A PubMed and Scopus review of published trials identified 13 studies of Progression-free survival (PFS) and overall survival (OS) which were set as the main outcome measures. The combined HRs of I-PET for PFS and OS in DLBCL were 4.4 ($P = 0.11$) and 3.99 ($P = 0.46$), respectively. The combined HRs of F-PET for PFS and OS in DLBCL were 5.91 ($P = 0.39$) and 6.75 ($P = 0.92$), respectively. Regarding to non-DLBCL with F-PET, the combined HRs of F-PET for PFS and OS were 4.05 ($P = 0.79$) and 5.1 ($P = 0.51$), respectively. No publication bias existed. *Conclusion*. In DLBCL, both I-PET and F-PET can be performed for survival and progression analysis. But in other B-cell subtypes such as follicular lymphoma (FL) and mantle cell lymphoma (MCL), it would be necessary to perform F-PET for predictive purposes.

1. Introduction

The use of [18F] fluorodeoxyglucose positron emission tomography (^{18}F-FDG PET) imaging in the management of lymphoma has remarkably expanded after the realization of the metabolic features of lymphoma cells [1, 2]. PET/CT imaging provides both anatomic and functional information which is fundamentally altering staging, guiding the choice of treatment modality, response monitoring, and response assessment for lymphomas. Meanwhile, it can provide useful information concerning prognosis for the risk stratified therapy. The application of interim FDG-PET in the risk stratification of Hodgkin's lymphoma is very successful [3]. But the benefits of FDG-PET/CT in the management of NHL are uncertain. Previous meta-analysis about the prognostic value of PET in Hodgkin's lymphoma or non-Hodgkin's Lymphoma showed no consistent conclusions due to the heterogeneity caused by different study populations, variations of imaging condition, inconsistent imaging interpretation criteria, and lack of uniformed treatment regimens [4]. All these factors impact on the PET results which may coinstantaneousy influence the management of the progression and survival of lymphoma patients in most clinical situations. NHL is a heterogeneous group of tumors with different aggressiveness. Subtypes like diffuse large B-cell lymphoma, follicular lymphoma, and mantle cell lymphoma are all FDG-avid [5], so that FDG-PET could be a potential prognostic imaging modality for survival prediction. Therefore, we, through the literature review, performed a meta-analysis concentrating on interim and final FDG-PET in major histological subtypes

of B-cell NHL patients (including DLBCL and non-DLBCL) treated with first-line rituximab containing-chemotherapy to assess the prognostic value of PET.

2. Materials and Methods

2.1. Literature Search. Studies were identified by a comprehensive electronic literature search [6] of abstracts of studies assessing the predictive value of PET for the human lymphoma. We conducted a search on the MEDLINE and Scopus databases, using keywords (PET, positron emission tomography, or SUV), lymphoma (rituximab, R-CHOP, or R), humans, and English.

2.2. Selection of Studies. Four investigators, including three physicians and one biostatistician, reviewed each publication independently and scored them according to a quality scale as described in the appendix. Each item was graded with a value between 0 and 2. This quality scale evaluated several dimensions of the methodology, grouped into four main categories: the scientific design, the generalization of the results, the analysis of the study data, and the PET reports. This quality scale was modified on the basis of the European lung cancer working party quality scale for biological prognostic factors for lung cancer introduced by Steels et al. [20]. To assess the PET reports, the scoring items previously introduced by Berghmans et al. [21] were used. The scores were compared and a consensus value for each item was reached in meetings at which at least two-thirds of the investigators needed to be present.

The participation of many readers was a guarantee for the correct interpretation of the articles. As the scores were objective, a consensus was always obtainable. The final scores were expressed as percentages, with higher values reflecting a better methodological quality. Each category had a maximum score of 10 points; hence, the overall maximum score was 40 points. Two reviewers independently assessed the quality items, and discrepancies were resolved by consensus. When an item was not applicable in a study, the theoretically attributable points were not taken into account in the total of the concerned category.

The studies about NHL patients mainly treated with rituximab-regimen plus CHOP (cyclophosphamide, doxorubicin, vincristine, and prednisone) or CHOP-like intensive chemotherapy monitored by FDG-PET providing survival data for the meta-analysis were potential for full-text evaluation. Only the studies reporting or providing data to make univariate analysis or results for survival were considered for the aggregation of the survival data.

Detailed inclusion criteria are as follows:

(1) Including more than 10 patients with histologically proven NHL patients treated with first-line R-chemo regimen with or without proceeding treatment such as radioimmunotherapy (RIT), BEAM chemotherapy (carmustine, etoposide, cytarabine, and melphalan regimen), and autologous stem cell transplantation (ASCT).

(2) Use interim and/or final PET to monitor therapy response and predict the survival of lymphoma patients.

(3) Use positive and negative results of FDG-PET as a predicting factor according to SUV cutoff value or visual analysis.

(4) Survival data of hazard ratio was extractable.

(5) Treatment of lymphoma is not risk-adapted by the result of FDG-PET.

2.3. Statistical Methods. Survival data from each study were analyzed in terms of the Kaplan-Meier curves, unless hazard ratios (HRs) were reported, and compared to calculate HR and 95% confidence intervals (CI) as previously described by Parmar et al. [22] and Tierney et al. [23]. In brief, effects were measured from the observed minus expected difference (O−), and variance (V) was generated using the reported summary statistics, by the one step approximation exp [(O−)/V]. These effects were combined to estimate the overall (pooled) effect of the PET-positive versus PET-negative arm. An HR < 1 denotes the survival benefit from a positive PET scan, whereas an HR > 1 indicates an increased risk of progression and death.

Statistical heterogeneity was measured using the chi-squared Q test ($P < 0.10$ was considered to represent significant statistical heterogeneity) and the I^2 statistic, as described by Higgins et al. [24]. Subgroup analysis was performed if heterogeneity existed. Publication bias including funnel plot and Egger's test was performed.

Survival rates on the graphical representation of the survival curves were read by Engauge Digitizer version 2.5. HRs and their variations were calculated by STATA version 12.0 and Review Manager 5.2.0.

3. Results

3.1. Study Selection and Characteristics Analysis. The detailed study selection process was described in Figure 1. The electronic searches yield 676 potentially eligible articles from all databases. Of all these articles, 45 were analyzed. Thirty two of these studies were excluded because of the following: unable to calculate the log HR and its variance ($n = 6$), not using rituximab regimen in every patient of the study ($n = 18$), using a relatively high SUV cutoff or MTV as a prognostic factor ($n = 4$), not exactly related to the research subject ($n = 3$), and its treatment being risk-adapted to the result of PET ($n = 1$) [25]. Finally, a total of 13 studies (all in English, 8 retrospective and 5 prospective) [7–19] were used for the analysis.

The principal characteristics of the 13 studies evaluated for the meta-analysis were described in Table 1. A total of 1160 patients, with a predominance of male DLBCL patients, were included in this prognostic meta-analysis. About half of the patients were graded intermediate or high IPI score. The median follow-up period ranged from 20 to 38 months. Seven studies [8–10, 12, 13, 16, 17] used FDG-PET/CT, and six studies [7, 11, 14, 15, 18, 19] used FDG-PET. Nine [7, 9–11, 13, 16–19] of

Table 1: Characteristics of the 13 studies included in the meta-analysis.

Study	Publication year	No. of NHL patients	Study design	Stage	Functional imaging	PET timing	Survival data	PET (+) as prognostic factor for survival	Methodology score (%)
Zinzani et al. [7]	2011	DLBCL ($n = 78$) PMLBCL ($n = 13$)	Retrospective	Stage II–IV	PET	I-PET	OS & PFS	Significant	65.79%
Yoo et al. [8]	2011	DLBCL ($n = 155$)	Retrospective	Stage I–IV	PET/CT	I-PET, final PET	OS & PFS	Undetermined	78.95%
Yang et al. [9]	2011	DLBCL ($n = 159$)	Prospective	Stage I–IV	PET/CT	I-PET	OS & PFS	Significant	89.47%
Trotman et al. [10]	2011	FL ($n = 122$)	Prospective	Stage III-IV	PET/CT	F-PET	OS & PFS	Significant	71.05%
Safar et al. [11]	2012	DLBCL ($n = 112$)	Retrospective	Stage III-IV	PET	I-PET	OS & PFS	Significant	71.05%
Pregno et al. [12]	2012	DLBCL ($n = 88$)	Retrospective	Stage I–IV	PET/CT	I-PET, F-PET	PFS	Undetermined	78.95%
Le Dortz et al. [13]	2010	FL ($n = 45$)	Retrospective	Stage I–IV	PET/CT	F-PET	PFS	Significant	71.05%
Han et al. [14]	2009	DLBCL ($n = 38$) MCL ($n = 13$)	Retrospective	Stage I–IV	PET	I-PET, F-PET	OS & PFS	Undetermined	63.16%
Cox et al. [15]	2012	DLBCL ($n = 73$) PMLBCL ($n = 12$)	Prospective	Stage I–IV	PET	I-PET	OS & PFS	Undetermined	76.68%
Cashen et al. [16]	2011	DLBCL ($n = 50$)	Prospective	Stage III-IV	PET/CT	I-PET, F-PET	OS & PFS	Significant	71.05%
Mato et al. [17]	2012	MCL ($n = 148$)	Retrospective	N/A	PET/CT	I-PET, F-PET	OS & PFS	F-PET: significant I-PET: undetermined	50.00%
Lanic et al. [18]	2012	DLBCL ($n = 57$)	Retrospective	N/A	PET	I-PET	OS & PFS	Significant	71.05%
Dupuis et al. [19]	2012	FL ($n = 111$)	Prospective	Grade 1 to 3A	PET	I-PET, F-PET	OS & PFS	Significant (OS of I-PET: undetermined)	84.21%

these studies achieved definite statistical significance, while other four showed undetermined results [8, 12, 14, 15]. Ten studies included a single histotype of NHL [8–13, 16–19] and three studies [7, 14, 15] included a mixed subtype of NHL with a majority of DLBCL. In order to ensure enough included articles, the latter three were categorized into DLBCL subgroups for pooling data instead of being excluded. Meta-analysis was performed based on each lymphoma subtype, for the clinical interpretation of FDG-PET is usually on the basis of patient diagnosis. As I-PET is not routinely performed in non-DLBCL patients [26], and few existing researches about I-PET showed a positive predictive value in non-DLBCL patients [17, 19], only I-PET and F-PET in patients with DLBCL and F-PET in non-DLBCL were evaluated separately (Table 1).

In a majority of DLBCL patients, nine studies dealt with the prognostic value of I-PET which was performed after 2–4 cycles of R-chemotherapy [7–9, 11, 12, 14–16, 18], in which 9 studies presented an extractable HR value for PFS (progression-free survival) and 8 studies for OS (overall survival) (Table 1). Four studies dealt with the prognostic value of F-PET which was performed after the 6–8 cycles of R-chemotherapy [12, 14–16], in which 4 studies presented an extractable HR value for PFS and 3 studies for OS. In non-DLBCL patients, four studies dealt with the prognostic value of F-PET [10, 13, 17, 19], in which 4 studies presented an extractable HR value for PFS and 3 studies for OS (Table 1). On the whole, approximately 34 HRs were extracted, of which 8 HR values and their confidence intervals were directly from the articles, whereas the other 26 HRs were extracted from the K-M curves. Six meta-analyses were performed for both OS and PFS of I-PET and F-PET in NHL patients afterwards. One study by Le Dortz et al. [13] concerning the response monitor of follicular lymphoma combined I-PET and F-PET together

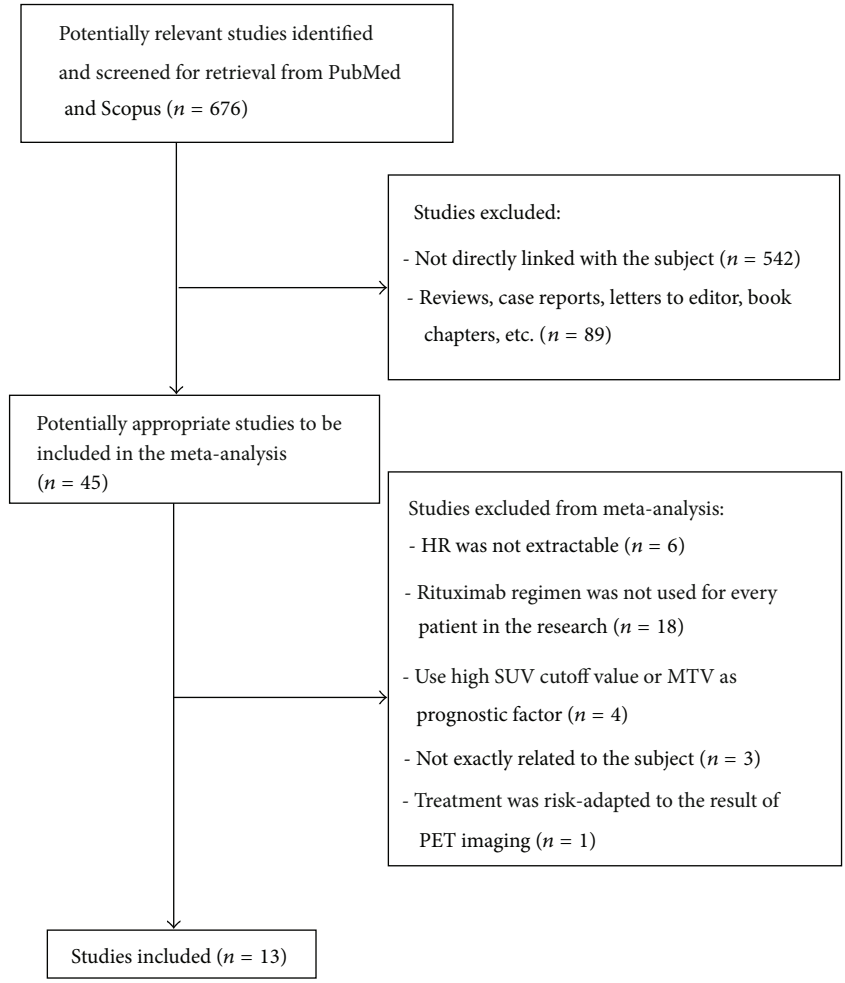

Figure 1: The study selection process (HR: hazard ratios; SUV: standardized uptake value).

with a majority of final data, and it was categorized into the final group.

3.2. Quality Assessment. Overall, the global quality score ranged from 50 to 89%, with a median score of 72.3% (Table 1). An attempt was made to contact the authors, if necessary, to obtain missing details of the methodological quality.

3.3. Meta-Analysis. Regarding the DLBCL with an I-PET, 9 studies for PFS and 8 studies for OS were included. In a fixed effect model, the combined HRs of I-PET for PFS and OS were 4.4 (95% CI: 3.34–5.81, $P = 0.11$) (Figure 2) and 3.99 (95% CI: 2.63–6.06, $P = 0.46$) (Figure 3), respectively. Regarding the DLBCL with F-PET, there were 4 studies for PFS and 3 studies for OS. The combined HRs of F-PET for PFS and OS were 5.91 (95% CI: 3.15–11.09, $P = 0.39$) (Figure 4) and 6.75 (95% CI: 1.72–26.50, $P = 0.92$) (Figure 5), respectively. Regarding the non-DLBCL with F-PET, 4 studies for PFS and 3 studies for OS were included. The combined HRs of F-PET for PFS and OS were 4.05 (95% CI: 2.68–6.1, $P = 0.79$) (Figure 6) and 5.1 (95% CI: 2.54–10.23, $P = 0.51$) (see Figure S3 in supplementary material available online at http://dx.doi.org/10.1155/2013/275805). All pooling data were statistically homogeneous. Meaning that for both I-PET and F-PET in DLBCL patients, a positive PET scan indicated a worse survival prognosis and a higher risk of progression than a negative PET scan, and in non-DLBCL patients, a positive F-PET could be predictive of more recurrence and worse survival.

3.4. Publication Bias for HR of I-PET in DLBCL Patients. The evaluation of publication bias showed that Egger's test results for PFS and OS were both insignificant ($P = 0.119$, $P = 0.485$). The funnel plots for publication bias of I-PET for PFS and OS (Figures S1 and S2) show little asymmetry. These results indicated no publication bias for the HR pooling of I-PET in DLBCL patients for either PFS or OS.

4. Discussion

As one of the ten leading cancer types in both men and women, non-Hodgkin's Lymphoma caused 70,130 estimated new cancer cases and 18,940 estimated deaths in

Study or subgroup	log(hazard ratio)	SE	Weight	Hazard ratio IV, fixed, 95% CI
Cashen et al. 2011	1.4677	0.486929	8.4%	4.34 [1.67, 11.27]
Cox et al. 2012	0.7419	0.561427	6.3%	2.1 [0.7, 6.31]
Han et al. 2009	0.9226	0.967988	2.1%	2.52 [0.38, 16.77]
Lanic et al. 2012	1.548345	0.830548	2.9%	4.7 [0.92, 23.96]
Pregno et al. 2012	0.8961	0.451549	9.8%	2.45 [1.01, 5.94]
Safar et al. 2012	1.569	0.48734	8.4%	4.8 [1.85, 12.48]
Yang et al. 2011	1.9463	0.272213	27%	7 [4.11, 11.94]
Yoo et al. 2011	0.5743	0.414608	11.6%	1.78 [0.79, 4]
Zinzani et al. 2011	1.8601	0.292575	23.4%	6.42 [3.62, 11.4]
Total (95% CI)			**100%**	**4.4 [3.34, 5.81]**

Heterogeneity: $\chi^2 = 13.7$, df = 8 ($P = 0.11$); $I^2 = 39\%$
Test for overall effect: $Z = 10.48$ ($P < 0.00001$)

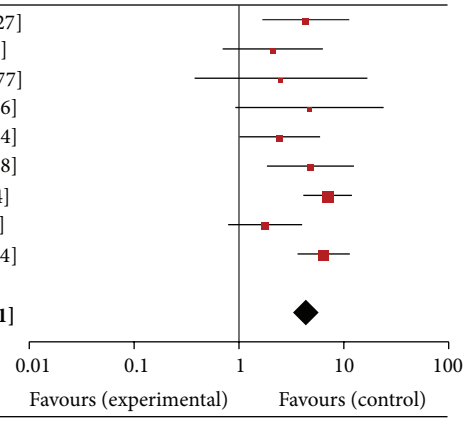

Figure 2: Forest plot of nine included studies in DLBCL (I-PET PFS). Pooled effect (HR) and heterogeneity test of an I-PET-positive scan on PFS in DLBCL patients (PET: positron emission tomography; PFS: progression-free survival; HR: hazard ratio; DLBCL: diffuse large B-cell lymphoma).

Study or subgroup	log(hazard ratio)	SE	Weight	Hazard ratio IV, fixed, 95% CI
Cashen et al. 2011	1.145	1.166833	3.3%	3.14 [0.32, 30.94]
Cox et al. 2012	1.3541	0.705833	9.1%	3.87 [0.97, 15.45]
Han et al. 2009	0.8787	1.372443	2.4%	2.41 [0.16, 35.47]
Lanic et al. 2012	1.719682	0.938835	5.1%	5.58 [0.89, 35.15]
Safar et al. 2012	0.941	0.530094	16.1%	2.56 [0.91, 7.24]
Yang et al. 2011	1.8898	0.31257	46.2%	6.62 [3.59, 12.21]
Yoo et al. 2011	0.5023	0.504282	17.8%	1.65 [0.62, 4.44]
Zinzani et al. 2011	6.9056	79.732394	0%	997.85 [0, 7.369E70]
Total (95% CI)			**100%**	**3.99 [2.63, 6.06]**

Heterogeneity: $\chi^2 = 6.69$, df = 7 ($P = 0.46$); $I^2 = 0\%$
Test for overall effect: $Z = 6.51$ ($P < 0.00001$)

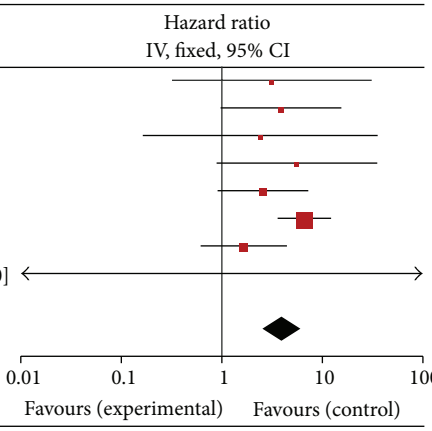

Figure 3: Forest plot of eight included studies in DLBCL (I-PET, OS). Pooled effect (HR) and heterogeneity test of an I-PET-positive scan on OS in DLBCL patients (PET: positron emission tomography; OS: overall survival; HR: hazard ratio; DLBCL: diffuse large B-cell lymphoma).

Study or subgroup	log(hazard ratio)	SE	Weight	Hazard ratio IV, fixed, 95% CI
Cashen et al. 2011	1.7441	0.829216	70.8%	5.72 [1.13, 29.06]
Cox et al. 2012	2.3004	1.292169	29.1%	9.98 [0.79, 125.59]
Han et al. 2009	6.9731	26.339596	0.1%	1067.53 [0, 2.810E25]
Total (95% CI)			**100%**	**6.75 [1.72, 26.5]**

Heterogeneity: $\chi^2 = 0.17$, df = 2 ($P = 0.92$); $I^2 = 0\%$
Test for overall effect: $Z = 2.74$ ($P = 0.006$)

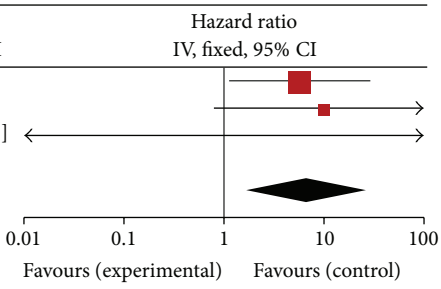

Figure 4: Forest plot of three included studies in DLBCL (F-PET, PFS). Pooled effect (HR) and heterogeneity test of an F-PET-positive scan on PFS in DLBCL patients (PET: positron emission tomography; PFS: progression-free survival; HR: hazard ratio; DLBCL: diffuse large B-cell lymphoma).

the USA during the year of 2012 [27]. The combination of the anti-CD20 monoclonal antibody rituximab (R) with the standard doses of chemotherapy has dramatically improved the clinical outcomes of NHL patients. Nevertheless, significant proportions of patients show disease progression or relapse after a good initial response [28, 29]. These patients may require alternative approaches, such as early intensive chemotherapy followed by ASCT

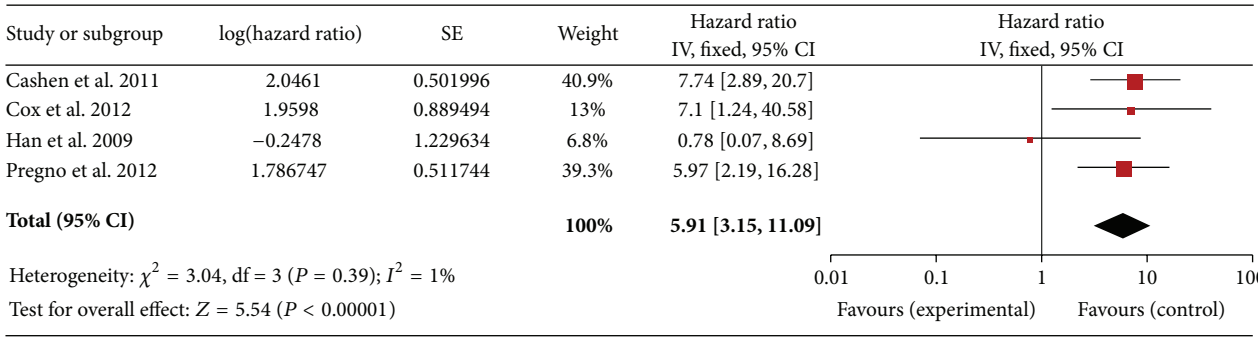

Figure 5: Forest plot of four included studies in DLBCL (F-PET, OS). Pooled effect (HR) and heterogeneity test of an F-PET-positive scan on OS in a majority of DLBCL patients (PET: positron emission tomography; OS: overall survival; HR: hazard ratio; DLBCL: diffuse large B-cell lymphoma).

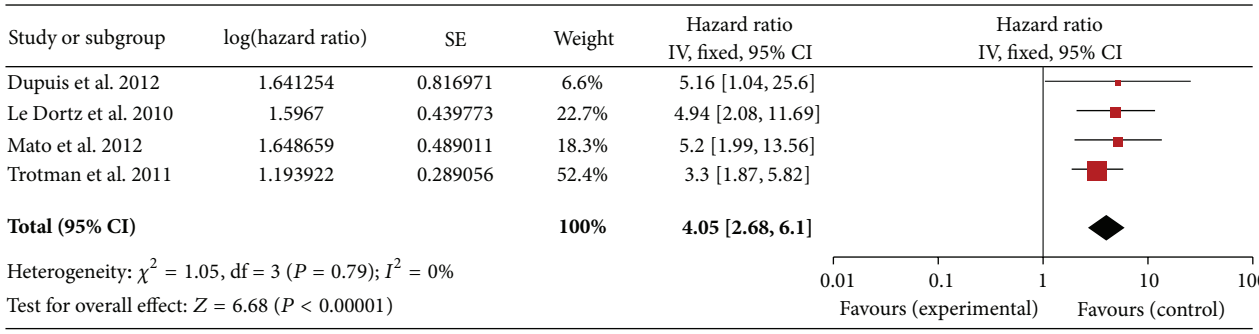

Figure 6: Forest plot of four included studies in non-DLBCL (F-PET, PFS). Pooled effect (HR) and heterogeneity test of F-PET-positive scan on PFS in non-DLBCL patients (PET: positron emission tomography; PFS: progression-free survival; HR: hazard ratio; DLBCL: diffuse large B-cell lymphoma).

or participation in clinical trials of new molecular targeted agents. It is essential to identify these patients as early as possible, so that they can be switched to other treatments for a longer survival.

Consequently, finding reliable prognostic indicators would be very helpful in the management of NHL patients. The most commonly used factors are histopathological subtypes and the International Prognostic Index (IPI). The previousy used IPI for aggressive lymphoma was developed specifically to stratify NHL patients for overall survival, but it may not be reliable for patients with different outcomes from the same IPI group [7, 30]. Other than that, it was suggested that I-PET or F-PET, immunephenotypes, and gene expressions could also be additional predictive factors [19, 31–33].

Based on the statistical analysis of a total of 1160 NHL patients, with a predominance of male DLBCL patients, our study confirms the independent prognostic value of FDG-PET in NHL patients treated with first-line R-chemotherapy. I-PET and F-PET in DLBCL and F-PET in non-DLBCL are all independent prognostic factors for survival and recurrence without statistical heterogeneity.

NHL consists of approximately 80% of B-cell lymphoma cases, and the remaining 20% are of T-cell and natural killer (NK) cell origin [5]. Most CD20+ B-cell lymphomas are suggested for R-chemotherapy if clinically available. Though FDG-PET has an excellent accuracy in baseline detection in cases of diffuse large B-cell lymphoma, follicular lymphoma, and mantle cell lymphoma [34], the FDG uptake of B-cell lymphoma varies according to diverse histotypes and aggressiveness and so does the predictive value of ^{18}F-FDG PET. The baseline FDG uptake of DLBCL is much higher which makes the visual and semiquantitative interpretation of the SUV percentage change more sensitive. While the mean uptakes of FL and MCL are relatively lower [35], the lymphoma subtypes could be a major potential source of heterogeneity to the predictive value of FDG-PET suggested in the previous meta-analysis.

Therefore, in patients with DLBCL, I-PET and F-PET should be performed for the prognosis evaluation and risk stratification. That would be more valuable for the management of DLBCL patients. As for patients with other subtypes of NHL such as FL and MCL, it would be necessary to perform final FDG-PET.

There are several limitations of our meta-analysis. First, only published articles were included, and the articles were restricted to the articles published in English. Second, studies with statistically significant results were more often published, whereas those with no statistically significant results were not. Third, even though they were published, more often than not, they were not assessable because of the more concise reports of results. These reasons may have led to

the publication bias found in the present paper. Fourth, most of the HRs were extrapolated from the survival curves. Although three readers independently read the survival rates on the graphical representation of the survival curves, the strategy could not ensure a complete accuracy in the extracted survival rates. Fifth, studies included were retrospective and we suggest that larger prospective, high-quality, and multicenter studies should be conducted according to different histological subtypes of NHL especially in NHL subtypes other than DLBCL. In conclusion, further studies of cost-effectiveness analysis should be conducted with regard to the techniques predicting the survival of B-cell NHL.

Conflicts of Interests

The authos declare that there is no conflict of interests.

Authors' Contribution

Yuyuan Zhu and Jianda Lu contributed equally to this meta-analysis.

Acknowledgments

This work was funded in part by the National Natural Science Foundation of China (Grants 81071180, 81101073), the Shanghai Pujiang Program (no. 11PJD018), and the Shanghai Jiao Tong University Medical Engineering Cross Research Fund (no. YG2012MS13).

References

[1] M. E. Juweid, S. Stroobants, O. S. Hoekstra et al., "Use of positron emission tomography for response assessment of lymphoma: consensus of the imaging subcommittee of international harmonization project in lymphoma," *Journal of Clinical Oncology*, vol. 25, no. 5, pp. 571–578, 2007.

[2] B. J. Krause, S. Schwarzenbock, and M. Souvatzoglou, "FDG PET and PET/CT," *Recent Results in Cancer Research*, vol. 187, pp. 351–369, 2013.

[3] A. Gallamini, F. Fiore, R. Sorasio, and M. Meignan, "Interim positron emission tomography scan in Hodgkin lymphoma: definitions, interpretation rules, and clinical validation," *Leukemia and Lymphoma*, vol. 50, no. 11, pp. 1761–1764, 2009.

[4] T. Terasawa, J. Lau, S. Bardet et al., "Fluorine-18-fluorodeoxyglucose positron emission tomography for interim response assessment of advanced-stage Hodgkin's lymphoma and diffuse large B-cell lymphoma: a systematic review," *Journal of Clinical Oncology*, vol. 27, no. 11, pp. 1906–1914, 2009.

[5] "A clinical evaluation of the International Lymphoma Study Group classification of non-Hodgkin's lymphoma. The non-Hodgkin's lymphoma classification project," *Blood*, vol. 89, no. 11, pp. 3909–3918, 1997.

[6] W. L. J. M. Devillé, P. D. Bezemer, and L. M. Bouter, "Publications on diagnostic test evaluation in family medicine journals: an optimal search strategy," *Journal of Clinical Epidemiology*, vol. 53, no. 1, pp. 65–69, 2000.

[7] P. L. Zinzani, L. Gandolfi, A. Broccoli et al., "Midtreatment18F-fluorodeoxyglucose positron-emission tomography in aggressive non-Hodgkin lymphoma," *Cancer*, vol. 117, no. 5, pp. 1010–1018, 2011.

[8] C. Yoo, D. H. Lee, J. E. Kim et al., "Limited role of interim PET/CT in patients with diffuse large B-cell lymphoma treated with R-CHOP," *Annals of Hematology*, vol. 90, no. 7, pp. 797–802, 2011.

[9] D. H. Yang, J. J. Min, H. C. Song et al., "Prognostic significance of interim18F-FDG PET/CT after three or four cycles of R-CHOP chemotherapy in the treatment of diffuse large B-cell lymphoma," *European Journal of Cancer*, vol. 47, no. 9, pp. 1312–1318, 2011.

[10] J. Trotman, M. Fournier, T. Lamy et al., "Positron emission tomography-computed tomography (PET-CT) after induction therapy is highly predictive of patient outcome in follicular lymphoma: analysis of PET-CT in a subset of PRIMA trial participants," *Journal of Clinical Oncology*, vol. 29, no. 23, pp. 3194–3200, 2011.

[11] V. Safar, J. Dupuis, E. Itti et al., "Interim [18F]fluorodeoxyglucose positron emission tomography scan in diffuse large B-cell lymphoma treated with anthracycline-based chemotherapy plus rituximab," *Journal of Clinical Oncology*, vol. 30, no. 2, pp. 184–190, 2012.

[12] P. Pregno, A. Chiappella, M. Bellò et al., "Interim 18-FDG-PET/CT failed to predict the outcome in diffuse large B-cell lymphoma patients treated at the diagnosis with rituximab-CHOP," *Blood*, vol. 119, no. 9, pp. 2066–2073, 2012.

[13] L. le Dortz, S. de Guibert, S. Bayat et al., "Diagnostic and prognostic impact of 18F-FDG PET/CT in follicular lymphoma," *European Journal of Nuclear Medicine and Molecular Imaging*, vol. 37, no. 12, pp. 2307–2314, 2010.

[14] H. S. Han, M. P. Escalón, B. Hsiao, A. Serafini, and I. S. Lossos, "High incidence of false-positive PET scans in patients with aggressive non-Hodgkin's lymphoma treated with rituximab-containing regimens," *Annals of Oncology*, vol. 20, no. 2, pp. 309–318, 2009.

[15] M. C. Cox, V. Ambrogi, V. Lanni et al., "Use of interim [18F]fluorodeoxyglucose-positron emission tomography is not justified in diffuse large B-cell lymphoma during first-line immunochemotherapy," *Leukemia and Lymphoma*, vol. 53, no. 2, pp. 263–269, 2012.

[16] A. F. Cashen, F. Dehdashti, J. Luo, A. Homb, B. A. Siegel, and N. L. Bartlett, "18F-FDG PET/CT for early response assessment in diffuse large B-cell lymphoma: poor predictive value of international harmonization project interpretation," *Journal of Nuclear Medicine*, vol. 52, no. 3, pp. 386–392, 2011.

[17] A. R. Mato, J. Svoboda, T. Feldman et al., "Post-treatment (not interim) positron emission tomography-computed tomography scan status is highly predictive of outcome in mantle cell lymphoma patients treated with R-HyperCVAD," *Cancer*, vol. 118, no. 14, pp. 3565–3570, 2012.

[18] H. Lanic, S. Mareschal, F. Mechken et al., "Interim positron emission tomography scan associated with international prognostic index and germinal center B cell-like signature as prognostic index in diffuse large B-cell lymphoma," *Leukemia and Lymphoma*, vol. 53, no. 1, pp. 34–42, 2012.

[19] J. Dupuis, A. Berriolo-Riedinger, A. Julian et al., "Impact of [18F]fluorodeoxyglucose positron emission tomography response evaluation in patients with high-tumor burden follicular lymphoma treated with immunochemotherapy: a prospective study from the Groupe d'Etudes des Lymphomes de l'Adulte

and GOELAMS," *Journal of Clinical Oncology*, vol. 30, no. 35, pp. 4317–4322, 2012.

[20] E. Steels, M. Paesmans, T. Berghmans et al., "Role of p53 as a prognostic factor for survival in lung cancer: a systematic review of the literature with a meta-analysis," *European Respiratory Journal*, vol. 18, no. 4, pp. 705–719, 2001.

[21] T. Berghmans, M. Dusart, M. Paesmans et al., "Primary tumor standardized uptake value (SUVmax) measured on fluorodeoxyglucose positron emission tomography (FDG-PET) is of prognostic value for survival in non-small cell lung cancer (NSCLC): a systematic review and meta-analysis (MA) by the european lung cancer working party for the IASLC lung cancer staging project," *Journal of Thoracic Oncology*, vol. 3, no. 1, pp. 6–12, 2008.

[22] M. K. Parmar, V. Torri, and L. Stewart, "Extracting summary statistics to perform meta-analyses of the published literature for survival endpoints," *Statistics in Medicine*, vol. 17, no. 24, pp. 2815–2834, 1998.

[23] J. F. Tierney, L. A. Stewart, D. Ghersi, S. Burdett, and M. R. Sydes, "Practical methods for incorporating summary time-to-event data into meta-analysis," *Trials*, vol. 8, article 16, 2007.

[24] J. P. T. Higgins, S. G. Thompson, J. J. Deeks, and D. G. Altman, "Measuring inconsistency in meta-analyses," *The British Medical Journal*, vol. 327, no. 7414, pp. 557–560, 2003.

[25] R. Casasnovas, M. Meignan, A. Berriolo-Riedinger et al., "SUVmax reduction improves early prognosis value of interim positron emission tomography scans in diffuse large B-cell lymphoma," *Blood*, vol. 118, no. 1, pp. 37–43, 2011.

[26] A. D. Zelenetz, W. G. Wierda, J. S. Abramson et al., "Non-Hodgkin's lymphomas, version 1.2013," *Journal of the National Comprehensive Cancer Network*, vol. 11, no. 3, pp. 257–273, 2013.

[27] R. Siegel, D. Naishadham, and A. Jemal, "Cancer statistics, 2013," *CA: A Cancer Journal for Clinicians*, vol. 63, no. 1, pp. 11–30, 2013.

[28] M. Pfreundschuh, L. Trümper, A. Österborg et al., "CHOP-like chemotherapy plus rituximab versus CHOP-like chemotherapy alone in young patients with good-prognosis diffuse large-B-cell lymphoma: a randomised controlled trial by the MabThera International Trial (MInT) group," *Lancet Oncology*, vol. 7, no. 5, pp. 379–391, 2006.

[29] P. Feugier, A. van Hoof, C. Sebban et al., "Long-term results of the R-CHOP study in the treatment of elderly patients with diffuse large B-cell lymphoma: a study by the Groupe d'Etude des Lymphomes de l'Adulte," *Journal of Clinical Oncology*, vol. 23, no. 18, pp. 4117–4126, 2005.

[30] M. A. Shipp, D. P. Harrington, J. R. Andersen et al., "A predictive model for aggressive non-Hodgkin's lymphoma," *The New England Journal of Medicine*, vol. 329, no. 14, pp. 987–994, 1993.

[31] A. Rosenwald, G. Wright, W. C. Chan et al., "The use of molecular profiling to predict survival after chemotherapy for diffuse large-B-cell lymphoma," *The New England Journal of Medicine*, vol. 346, no. 25, pp. 1937–1947, 2002.

[32] G. Lenz, G. Wright, S. S. Dave et al., "Stromal gene signatures in large-B-cell lymphomas," *The New England Journal of Medicine*, vol. 359, no. 22, pp. 2313–2323, 2008.

[33] B. D. Cheson, "Role of functional imaging in the management of lymphoma," *Journal of Clinical Oncology*, vol. 29, no. 14, pp. 1844–1854, 2011.

[34] J. W. Friedberg and V. Chengazi, "PET scans in the staging of lymphoma: current status," *Oncologist*, vol. 8, no. 5, pp. 438–447, 2003.

[35] H. Schöder, A. Noy, M. Gönen et al., "Intensity of 18fluorodeoxyglucose uptake in positron emission tomography distinguishes between indolent and aggressive non-Hodgkin's lymphoma," *Journal of Clinical Oncology*, vol. 23, no. 21, pp. 4643–4651, 2005.

Hindawi Publishing Corporation
BioMed Research International
Volume 2013, Article ID 145427, 10 pages
http://dx.doi.org/10.1155/2013/145427

Clinical Study

Comparison of ^{99m}Tc-N-DBODC5 and ^{99m}Tc-MIBI of Myocardial Perfusion Imaging for Diagnosis of Coronary Artery Disease

Haiyan Ma, Sijin Li, Zhifang Wu, Jianzhong Liu, Haiyan Liu, and Xiaoshan Guo

Department of Nuclear Medicine, First Affiliated Hospital of Shanxi Medical University, 85 Jiefang South Road, Taiyuan, Shanxi 030001, China

Correspondence should be addressed to Sijin Li; lisj-nm@hotmail.com

Received 20 April 2013; Accepted 20 May 2013

Academic Editor: Hong Zhang

Despite recent advances in therapeutic and diagnostic approaches, coronary artery disease (CAD) and its related cardiac disorders represent the most common cause of death in the United States. Nuclear myocardial perfusion imaging (MPI) technologies play a pivotal role in the diagnosis and treatment design for CAD. Recently, in order to develop improved MPI agents for diagnosis of CAD, ^{99m}Tc-[bis(dimethoxypropylphosphinoethyl)-ethoxyethyl-amine(PNP5)]-[bis(N-ethoxyethyl)dithiocarbamato(DBODC)]nitride(N-DBODC5)(^{99m}Tc-N-DBODC5) with a faster liver clearance than conventional single-photon emission computed tomography (SPECT) imaging agents (technetium 99m sestamibi (^{99m}Tc-MIBI) or technetium 99m tetrofosmin) has been introduced. In preclinical and phase I studies, ^{99m}Tc-N-DBODC5 has shown characteristics of an essentially ideal MPI tracer. Importantly, however, there is no data to support the use of ^{99m}Tc-N-DBODC5 to evaluate myocardial ischemia in patients with suspected CAD. The present study was designed to assess the clinical value of this agent; the findings of stress and rest MPI after the administration of this agent were compared to those of stress and rest ^{99m}Tc-MIBI, as well as those of coronary angiography, with respect to the detection of CAD. Our findings indicated the usefulness of ^{99m}Tc-N-DBODC5 as a promising MPI agent.

1. Introduction

Coronary artery disease (CAD) remains the single greatest cause of death in men and women in the USA, despite a declining total death rate. Using 2005 data, over 445,000 (or 1 in every 5) deaths in the USA were due to CAD, and it ranked highest among all disease categories in hospital discharges [1]. CAD also remains the third leading cause of death of the Chinese population, creating a significant socioeconomic burden [2]. Therefore, the reduction of the morbidity and mortality due to CAD is of primary importance to physicians and patients.

Nuclear cardiology, cardiovascular magnetic resonance, cardiac computed tomography, position emission computed tomography, and coronary angiography (CA) are imaging modalities that have been used to measure myocardial perfusion, left ventricular function, and coronary anatomy for clinical management and research [3]. Based on current guidelines, invasive CA is a suitable diagnostic procedure for patients with a high pretest likelihood of significant coronary artery disease either with or without troublesome symptoms or clinical findings [4, 5]. In this population, the reported diagnostic yield of invasive CA is 44–48% [6–8]. However, in reality, invasive CA has an even lower diagnostic yield of obstructive CAD of approximately 38% [9]. Noninvasive testing could be of value to defer from invasive diagnostic procedures. Stress myocardial perfusion imaging (MPI) has emerged as an important noninvasive mean of evaluating patients with suspected CAD, with over 8.5 million evaluations performed annually in the USA [10].

The most commonly used imaging modality for this purpose is single-photon emission computed tomography (SPECT) [11]. The advantages of nuclear MPI for the detection of CAD are as follows: first, it enables the simple, safe, and noninvasive assessment of myocardial ischemia and reduction of coronary flow reserve using exercise or pharmacological stress. In addition, it provides left ventricular functional information on coronary arteries, which

is different from the morphological information provided by CA [12]. Furthermore, CA is the standard technique for assessing epicardial coronary anatomy, and MPI is the standard technique for assessing myocardial perfusion and is appropriate for the quantitative evaluation of myocardial perfusion conditions [13].

Thallium-201 (^{201}Tl), technetium 99m sestamibi (^{99m}Tc-MIBI), and technetium 99m tetrofosmin (^{99m}Tc-tetrofosmin) are three traditional, routinely used, MPI tracers and are clinical-validated tracers for evaluation of SPECT MPI [14–16]. Because ^{201}Tl is a cyclotron-produced isotope, it is expensive, and it is not easily available for routine clinical use in many developing countries. Therefore, from a practical standpoint, ^{99m}Tc-MIBI or ^{99m}Tc-tetrofosmin is the preferred agent for a gated SPECT study. However, tracer activity below the diaphragm is commonly seen with ^{99m}Tc-MIBI and ^{99m}Tc-tetrofosmin, and this can reduce accuracy in some studies [17, 18].

Recently, ^{99m}Tc-N-DBODC5 with a faster liver clearance than conventional SPECT imaging agents has been introduced. It is a new lipophilic, monocationic ^{99m}Tc-labeled compound that is currently under clinical investigation as a MPI agent [19–24]. Basic research and phase I studies have shown the safety, excellent biodistribution, and high image quality of this radiopharmaceutical [22, 25, 26]. Like ^{99m}Tc-MIBI and ^{99m}Tc-tetrofosmin, ^{99m}Tc-N-DBODC5, also a monocationic lipophilic complex, is possibly localized in the mitochondrial fraction. Marmion et al. [27] and Bolzati et al. [28] reported that the lipophilic characteristics and electronic charge of the tracer were thought to be important. Importantly, however, the clinical value of diagnosis of CAD has not been fully explored.

In order to evaluate the clinical value of this agent, the findings of stress and rest MPI after the administration of this agent were compared to those of stress and rest ^{99m}Tc-MIBI MPI, as well as those of CA, with respect to the detection of CAD.

2. Methods

2.1. Patient Population. Of 120 patients admitted to the hospital because of chest pain from March 2010 to December 2011, 46 (31 males; mean age, 60.08 ± 8.58 years (Table 1)) who underwent stress-rest ^{99m}Tc-N-DBODC5 SPECT, ^{99m}Tc-MIBI SPECT, and coronary arteriography were included in this study. If the creatine kinase concentration was more than twice the upper normal limit or there was positive troponin T, or if there was evidence of previous myocardial infarction, coronary angioplasty, or a coronary artery bypass graft surgery, the patients were excluded.

2.2. Preparation of ^{99m}Tc-N-DBODC5. ^{99m}Tc-N-DBODC5 was prepared using a lyophilized kit formulation purchased from Beijing Shihong Pharmaceutical Center. The saline solution of sodium pertechnetate (1.0 mL, 1110 MBq) was added to an SDH vial (Vail A: 5.0 mg of succinate dehydrogenase, 5.0 mg of 1,2-diaminopropane-N,N,N′,N′-tetraacetic acid, and 0.05 mg of $SnCl_2 \cdot 2H_2O$). Then, the solution was kept at room temperature for 15 min to form a $[^{99m}TcN]^{2+}$ intermediate. The other two lyophilized vials (Vail B: 2.0 mg of PNP5, Vail C: 2.0 mg of DBODC) were dissolved with 1.0 mL of saline solution, respectively. And then the saline solutions of Vails B and C were added to the vial of $[^{99m}TcN]^{2+}$ intermediate (Vail A). The resulting solution was heated at 100°C for 15 min. Before injection, the solution was filtrated through a 0.22-μm membrane. The ^{99m}Tc-MIBI was obtained using a lyophilized kit formulation (Beijing Shihong Pharmaceutical Center) in the First Affiliated Hospital of Shanxi Medical University.

Table 1: Study group.

Parameter	Value
n	46
M/F	31/15
Age (yr)	60.08 ± 8.58 (39–74)
Hypertension	31
Hyperlipidemia	19
Diabetes mellitus	14
Smoking	26
Trigger of chest pain	
Effort	22
Rest	13
Not specific	11
ECG abnormality	11
ST-T elevation	3
ST-T depression	8
≥50% of luminal narrowing	29
One-vessel disease	14
Two-vessel disease	11
Three-vessel disease	4

Data are presented as mean ± SD or number (%) as appropriate.

Radiochemical purity (RCP) was determined by thin-layer chromatography (TLC). TLC was conducted on polyamide film as the station phase and saline/acetone (v / v = 6 : 1) as the mobile phase. Retention factor (Rf) for ^{99m}Tc-N-DBODC5 is 0.3–0.6. The RCP was more than 95% in each experimental study, and the purity was still greater than 95% at least 6 h.

2.3. Exercise Protocol. Figure 1 shows that a two-day protocol was used for both ^{99m}Tc-MIBI and ^{99m}Tc-N-DBODC5 MPI. Image acquisition procedures conformed to the ASNC imaging guidelines [29, 30], and the aged-adjusted maximal heart rate was the endpoint on an ergometer, but other endpoints included physical exhaustion, uncommon arrhythmia, severe angina, or significant hypotension. At the endpoint of the symptom-limited bicycle ergometer exercise, 740 MBq of ^{99m}Tc-N-DBODC5 (mean injected activity, 740.8 ± 11.1 MBq) was injected; exercise was continued for a further 2 min.

Each patient underwent an exercise ^{99m}Tc-MIBI study within 7 days of the ^{99m}Tc-N-DBODC5 study. For the ^{99m}Tc-MIBI (741.5 ± 12.3 MBq) SPECT study, the exercise protocol

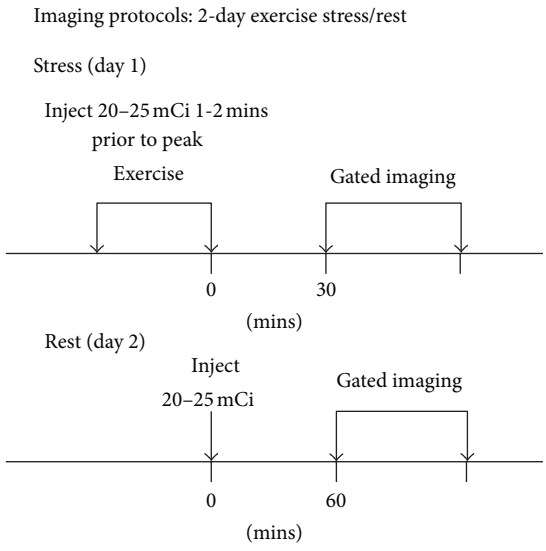

Figure 1: ^{99m}Tc-N-DBODC5 and ^{99m}Tc-MIBI imaging protocols: two-day exercise stress/rest.

of patients was identical to that for the ^{99m}Tc-N-DBODC5 study. ^{99m}Tc-N-DBODC5 and ^{99m}Tc-MIBI were used as myocardial perfusion agents in a random sequence.

2.4. Gated SPECT Acquisition and Image Reconstruction. Patients were imaged in the supine position with their arms raised. SPECT images were acquired with a fixed 90° two-headed gamma camera (Infinia VC Hawkeye, General Electric, USA), using a low-energy, high-resolution, parallel-hole collimator, from the 45° right anterior oblique to the 45° left posterior position. Acquisition parameters were as follows: detectors at 90°, 180° rotation at 3° steps with automatic body contouring, 35 s acquisition per step, 64 × 64 matrix, zoom ×1.28, and energy window 140 keV ± 10%. The total acquisition time was approximately 20 min. The same filters were used for both tracers. The raw projection datasets were filtered with a Butterworth filter (cut off frequency 0.50 cycles/pixel and power 6.0 for rest images, cut off frequency 0.50 cycles/pixel and power 5.0 for stress images). No scatter or attenuation correction was performed.

2.5. Heart-to-Organ Analysis. ^{99m}Tc-N-DBODC5 and ^{99m}Tc-MIBI heart-to-organ count ratios were calculated from the anterior projection of each tomographic acquisition. Regions of interests (ROIs) were drawn around the entire left ventricular myocardium, over the hepatic margin adjacent to the inferoapical wall of the left ventricle, excluding the biliary tree, and over the inferior left ventricular wall adjacent large intestine activity. The mean counts per pixel in the three ROIs were normalized to the injected tracer activity after decay correction and to a standard acquisition time of 1 min. Heart-to-liver and heart-to-intestine ratios were then computed [31].

2.6. Image Quality Assessing. For MPI analyses, at first, two experienced observers judged which image sets from ^{99m}Tc-MIBI and ^{99m}Tc-N-DBODC5 were superior in image quality on the basis of patient motion, statistical noise, tracer activity below the diaphragm, heart-to-organ count ratio, and sharpness, without knowledge of the radiopharmaceutical or patient identity [32].

2.7. MPI Image Interpretation. Both overall qualitative diagnosis and semiquantitative 17 segment with 5-point [33] (0 = normal, 4 = absent tracer uptake) scorings were employed in the independent, blinded read by two expert readers who were experienced in SPECT MPI interpretation. In this model, the left anterior descending artery (LAD) distribution territory comprises seven segments (segments 1-2, 7-8, 13-14, and 17), the left circumflex artery (LCX) comprises five segments (segments 3-4, 9-10, and 15), and the right coronary artery (RCA) comprises five segments (segments 5-6, 11-12, and 16). SPECT stress/rest studies were classified for each myocardial region in the following manner: normal if all the segments were normal after stress; ischemic if at least one segments improved at rest; and scar if no segments improved at rest. In addition, the summed stress (SSS), summed rest (SRS), and summed difference scores (SDSs) were calculated, and ischemia was defined as SDS ≥ 2 [34]. The ^{99m}Tc-MIBI and ^{99m}Tc-N-DBODC5 images were separately interpreted without knowing the clinical histories, results of coronary angiography, or other radionuclide findings.

2.8. Coronary Angiography Interpretation. All coronary angiograms were interpreted with quantitative CA in a coronary angiography core laboratory blinded to the clinical or imaging results. A coronary stenosis was considered present when there was a stenosis ≥ 50% in diameter in any epicardial coronary artery. The presence of one or more coronary stenoses defined the presence of significant CAD.

2.9. Statistical Analysis. All statistical analyses were performed using the statistical package SPSS 16.0 (Chicago, IL, USA). The results were expressed as the mean value ± SD. The difference in left ventricular function parameters and perfusion scores were compared using a paired Student's t-test. Comparison of the proportion was made with the McNemar test. CA results were used as the "gold standard." Agreements between CA and SPECT results were defined as the kappa (κ) value. $P < 0.05$ was considered significant.

3. Results

3.1. Coronary Angiography. Of the 46 patients studied, 29 had ≥50% luminal diameter stenosis in at least one major coronary vessel. Fourteen had single-vessel disease, 11 had two-vessel disease, and four had three-vessel disease; 15 patients showed significant stenosis in the RCA, 19 in the LAD, and 14 in the LCX. The remaining 17 patients had normal or nonsignificantly stenosed coronary arteries.

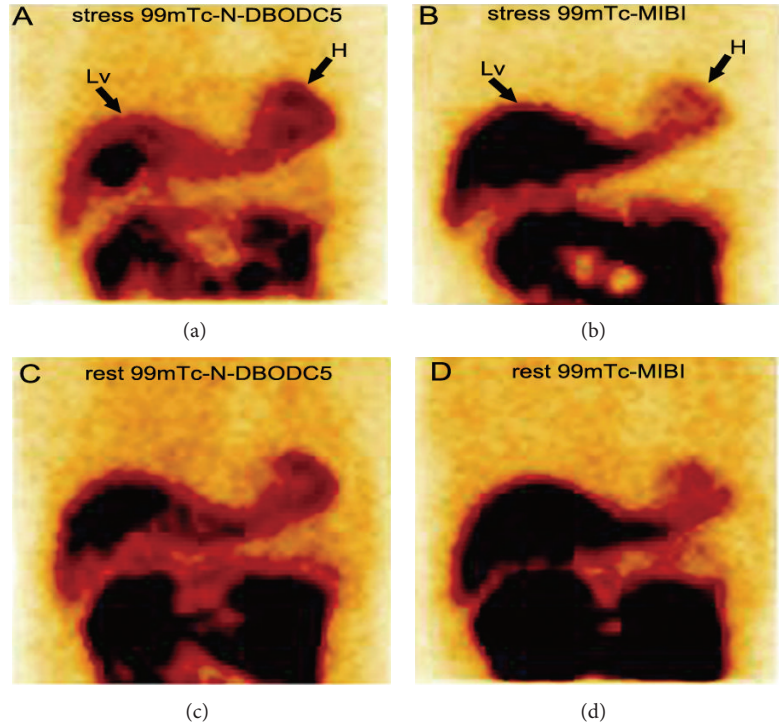

FIGURE 2: Comparison of liver clearance of the two tracers in anterior tomographic planar images of a patient (as shown in the black arrow; H, heart; Lv, liver). (a) Exercise stress ^{99m}Tc-N-DBODC5, (b) Exercise stress ^{99m}Tc-MIBI, (c) rest ^{99m}Tc-N-DBODC5 and (d) rest ^{99m}Tc-MIBI.

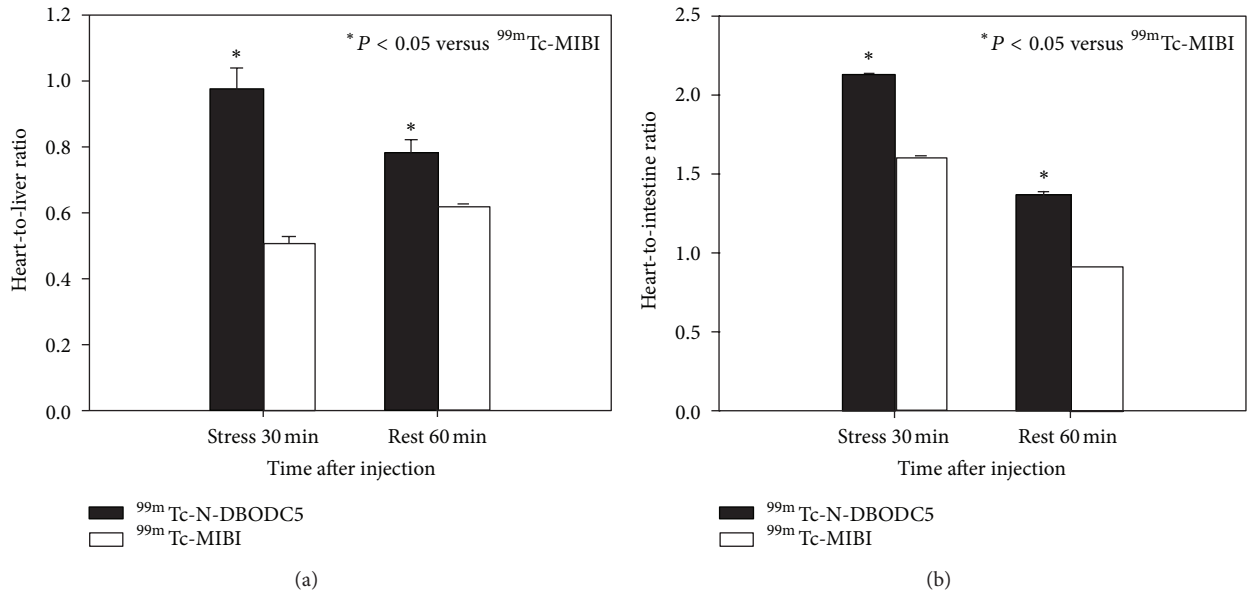

FIGURE 3: Heart-to-liver ratio and heart-to-intestine ratio measured with an anterior projection images at stress for 30 min and rest for 60 min for ^{99m}Tc-N-DBODC5 and ^{99m}Tc-MIBI in 46 patients.

3.2. Heart-to-Organ Count Ratio. Qualitative analyses of images acquired of ^{99m}Tc-N-DBODC5 both at rest and during stress revealed no significant overlap between tracer accumulation in the inferior wall of the ventricle and in the subdiaphragmatic region (Figure 2).

Figure 3 depicts the heart-to-liver count ratios (a) and heart-to-intestine count ratios (b) of ^{99m}Tc-N-DBODC5 and ^{99m}Tc-MIBI in 46 patients. The myocardium-to-liver ratios of ^{99m}Tc-N-DBODC5 and ^{99m}Tc-MIBI studies were 0.97 ± 0.07 and 0.51 ± 0.02, respectively, at stress. The myocardium-to-liver ratios of ^{99m}Tc-N-DBODC5 and ^{99m}Tc-MIBI MPI were 0.78 ± 0.04 and 0.62 ± 0.01, respectively, at rest. On the other hand, the mean heart-to-intestine ratios of ^{99m}Tc-N-DBODC5 were 2.12 ± 0.01 and 1.36 ± 0.02 for stress and

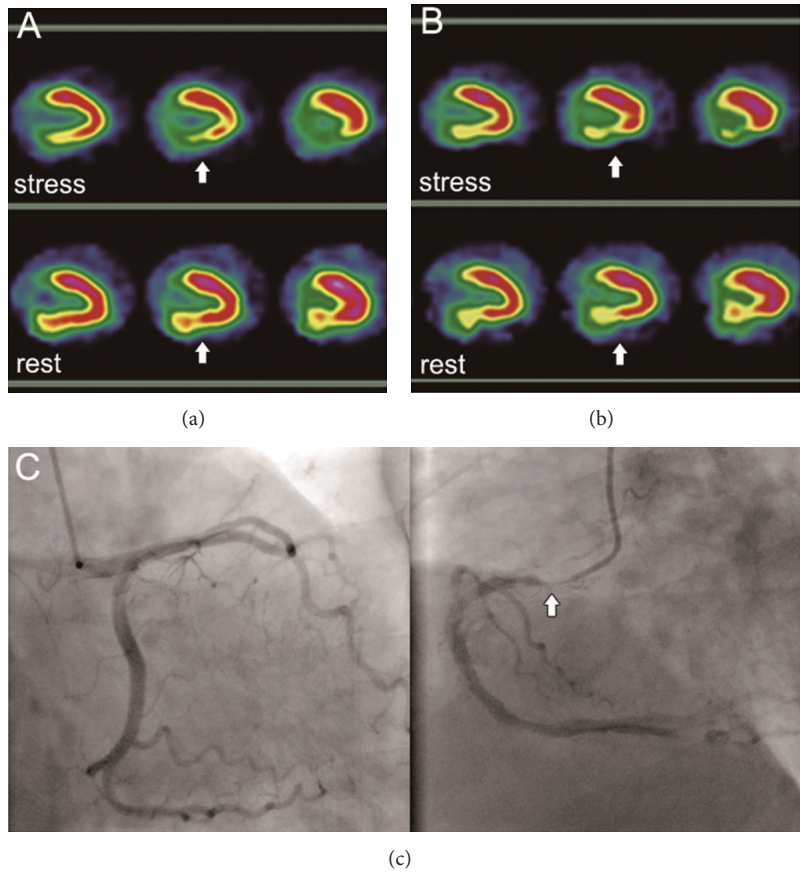

(a) (b)

(c)

Figure 4: Abnormal MPI in the vertical long-axis slices of a representative patient. Both ^{99m}Tc-N-DBODC5 (a) and ^{99m}Tc-MIBI (b) images demonstrate an inferoposterior defect (white arrows). The defect is well visualized on two tracer images corresponding to the CA result. This coronary angiography (c) detected a stenosis of 90% in the RCA. The concordance for diagnosis of myocardial ischemia was seen on ^{99m}Tc-N-DBODC5 and ^{99m}Tc-MIBI studies.

rest images, respectively. The average heart-to-intestine ratios of ^{99m}Tc-MIBI were 1.62 ± 0.01 and 0.91 ± 0.00 for stress and rest images, respectively. ^{99m}Tc-N-DBODC5 studies had a significantly higher heart-to-organ count ratio compared with ^{99m}Tc-MIBI studies ($P < 0.05$).

3.3. Image Quality. In the stress perfusion imaging, ^{99m}Tc-N-DBODC5 MPI was superior in quality to ^{99m}Tc-MIBI MPI in 37 of the 46 patients studied. In the remaining nine patients, the MPI was judged to be of equal quality. In the resting perfusion imaging, ^{99m}Tc-N-DBODC5 images were superior in all the patients studied. In general, the ^{99m}Tc-N-DBODC5 MPI had more counts with less statistical noise, less tracer activity below the diaphragm, and desirable heart-to-organ count ratio compared with ^{99m}Tc-MIBI MPI.

3.4. Gated SPECT Findings. Table 2 shows the results of scan segments between the ^{99m}Tc-N-DBODC5 and ^{99m}Tc-MIBI MPI. Of the 782 segments that could be interpreted by both techniques, 302 were concordantly normal, 119 were concordantly reversible, and 136 were concordantly nonreversible. ^{99m}Tc-N-DBODC5 SPECT detected more reversible, defects than did ^{99m}Tc-MIBI SPECT (240 versus 140, $P < 0.05$, McNemar test). ^{99m}Tc-MIBI SPECT identified more nonreversible defects than did ^{99m}Tc-N-DBODC5 SPECT (312 versus 152, $P < 0.001$, McNemar test). Seventy-one segments interpreted as normal on ^{99m}Tc-N-DBODC5 corresponded to nonreversible defects on ^{99m}Tc-MIBI SPECT images. In contrast, 12 normal ^{99m}Tc-MIBI segments corresponded to nonreversible defects on ^{99m}Tc-N-DBODC5 images. When the patterns of uptake (normal, reversible defect, and nonreversible defect) of ^{99m}Tc-N-DBODC5 and ^{99m}Tc-MIBI were compared, there was concordance in 71% (557/782) of segments.

Table 3 shows the results of left ventricular function parameters in the two techniques used. In this study, the end-diastolic volume (EDV), end-systolic volume (ESV), left ventricular ejection fraction (LVEF), and transient ventricular dysfunction (TID) were assessed by MPI using two tracers. No statistically significant differences in MPI parameters were observed between the ^{99m}Tc-MIBI and ^{99m}Tc-N-DBODC5 studies. However, the scores of myocardial perfusion defects for the detection of CAD were higher with ^{99m}Tc-MIBI than with ^{99m}Tc-N-DBODC5 ($P = 0.012$, for SSS; $P = 0.020$, for SDS, resp.).

3.5. Detection of CAD. Table 4 shows the sensitivity and specificity of two tracers in diagnosing CAD. Based on CA,

Table 2: The comparison of myocardial perfusion in a total of 782 segments with ^{99m}Tc-N-DBODC5 and ^{99m}Tc-MIBI SPECT exercise imaging.

^{99m}Tc-N-DBODC5	^{99m}Tc-MIBI			Total
	Normal	Reversible defect	Nonreversible defect*	
Normal	302 (39%)	17 (2%)	71 (9%)	390
Reversible defect*	16 (2%)	119 (15%)	105 (13%)	240
Nonreversible defect	12 (2%)	4 (1%)	136 (17%)	152
Total	330	140	312	782

Data are presented as number; $^{*}P < 0.001$, ^{99m}Tc-MIBI versus ^{99m}Tc-N-DBODC5 for nonreversible defect segments; $^{*}P < 0.05$, ^{99m}Tc-N-DBODC5 versus ^{99m}Tc-MIBI for reversible defect segments; McNemar test was used.

Table 3: MPI findings of two tracers on left ventricular function parameters and ischemia scores in 46 patients.

Parameter	^{99m}Tc-MIBI	^{99m}Tc-N-DBODC5
LVEF (%)		
Exercise	54.2 ± 11.3	56.7 ± 9.2
Rest	63.1 ± 8.5	64.8 ± 7.9
EDV (mL)		
Exercise	81.5 ± 18.6	83.2 ± 16.3
Rest	97.3 ± 16.4	99.1 ± 13.7
ESV (mL)		
Exercise	43.2 ± 9.7	41.4 ± 12.3
Rest	59.4 ± 13.6	60.2 ± 9.8
SSS	12.1 ± 1.4*	9.6 ± 1.6
SRS	7.2 ± 0.8	7.9 ± 0.9
SDS	4.2 ± 0.5*	3.6 ± 0.4
TID	0.96 ± 0.06	0.94 ± 0.02

Data are presented as mean ± SD or number (%) as appropriate; *statistically significant ^{99m}Tc-MIBI versus ^{99m}Tc-N-DBODC5 ($P < 0.05$); paired Student's t-test was used; LVEF: left ventricular ejection fraction; EDV: end-diastolic volume; ESV: end-systolic volume; SSS: summed stress scores; SRS: summed rest scores; SDS: summed difference scores; TID: transient ventricular dysfunction.

overall figures for sensitivity and specificity in identification of CAD were 86% (25/29) and 65% (11/17) for ^{99m}Tc-MIBI imaging. On the other hand, the overall sensitivity and specificity for the detection of CAD were 86% (25/29) and 88% (15/17) for ^{99m}Tc-N-DBODC5 SPECT studies. The concordance of ischemia diagnosis sensitivity of a representative patient for the two tracers is shown in Figure 4. The accuracy was 0.78 for ^{99m}Tc-MIBI and 0.87 for ^{99m}Tc-N-DBODC5. Angiography agreement was very good for ^{99m}Tc-N-DBODC5 ($\kappa = 0.73$) and moderate for ^{99m}Tc-MIBI ($\kappa = 0.52$). Specificity and accuracy were not significantly different but better for the ^{99m}Tc-N-DBODC5 group when compared to ^{99m}Tc-MIBI SPECT (specificity, 88-65%; accuracy, 87-78%).

3.6. Detection of Disease in Individual Coronary Vessels. Table 4 also shows the sensitivity and specificity of the two tracers in detecting individual-stenosed vessels. Of a total of 138 arteries in 46 patients, 48 arteries had significant stenoses, and 90 had insignificant lesions or were normal. Overall figures for sensitivity and specificity in identifying individual-stenosed vessels were 67% (32/48) and 86% (77/90) for ^{99m}Tc-MIBI imaging; overall sensitivity and specificity to diagnose individual significantly stenosed vessels were 69% (33/48) and 92% (83/90) for ^{99m}Tc-N-DBODC5 SPECT studies.

On the other hand, sensitivity and specificity for RCA stenosis vessel lesion detection using ^{99m}Tc-MIBI MPI were 87% and 68% compared to 87% and 87% for ^{99m}Tc-N-DBODC5 MPI, LAD stenosis (53% sensitivity and 96% specificity for ^{99m}Tc-MIBI, 63% sensitivity and 96% specificity for ^{99m}Tc-N-DBODC5, resp.), and left circumflex (LCX) (64% sensitivity and 94% specificity for ^{99m}Tc-MIBI, 57% sensitivity and 94% specificity for ^{99m}Tc-N-DBODC5, resp.). Angiography agreement was very good for ^{99m}Tc-N-DBODC5 ($\kappa = 0.63$ for LAD; $\kappa = 0.71$ for RCA, resp.) and moderate for ^{99m}Tc-MIBI ($\kappa = 0.52$ for LAD; $\kappa = 0.48$ for RCA, resp.). In contrast, the angiography agreement was very good for ^{99m}Tc-MIBI ($\kappa = 0.62$ for LCX) and moderate for ^{99m}Tc-N-DBODC5 ($\kappa = 0.55$ for LCX) (Table 4). Overall, the specificity of ^{99m}Tc-N-DBODC5 SPECT to detect individual RCA stenosis was better (27/31, 87%) than that of ^{99m}Tc-MIBI SPECT (21/31, 68%), despite having no statistical significance.

4. Discussion

These preliminary results demonstrate that stress-rest myocardial perfusion SPECT with ^{99m}Tc-N-DBODC5 is a sensitive method for detecting CAD and identifying stenosed coronary arteries. For the detection of CAD, more importantly, ^{99m}Tc-N-DBODC5 MPI reached good agreement compared with CA ($\kappa = 0.73$).

4.1. Advantages of ^{99m}Tc-N-DBODC5. ^{99m}Tc-N-DBODC5 is a new lipophilic, monocationic, and nitride ^{99m}Tc-labeled tracer that is rapidly cleared from the liver after intravenous injection. It possesses good stability under physiological conditions. Importantly, ^{99m}Tc-N-DBODC5 exhibits more rapid liver washout than either ^{99m}Tc-MIBI or ^{99m}Tc-tetrofosmin. For example, at 60 min after injection in rats, the heart/liver ratio of ^{99m}Tc-N-DBODC5 is approximately ten times higher than that of ^{99m}Tc-MIBI or ^{99m}Tc-tetrofosmin. Preclinical studies have shown that ^{99m}Tc-N-DBODC5 SPECT can identify previous ischemia as areas of reduced tracer uptake [25, 26]. Furthermore, the rapid liver clearance and high uptake in the myocardium of ^{99m}Tc-N-DBODC5 will allow

Table 4: Sensitivity, specificity, and diagnostic accuracy of scintigraphic perfusion studies and agreement with coronary angiography.

	Overall		LAD		LCX		RCA	
	MIBI	DBODC	MIBI	DBODC	MIBI	DBODC	MIBI	DBODC
No. of disease	25	25	10	12	9	8	13	13
Sensitivity (%)	86	86	53	63	64	57	87	87
Specificity (%)	65	88	96	96	94	94	68	87
Accuracy (%)	78	87	78	83	85	83	74	87
▲Kappa (κ)	0.53	0.73	0.52	0.63	0.62	0.55	0.48	0.71

Data are presented as number (%); MIBI = ^{99m}Tc-MIBI, DBODC = ^{99m}Tc-N-DBODC5; LAD: left anterior descending coronary artery; LCX: left circumflex coronary artery; RCA: right coronary artery. ▲CA was used as the "gold standard" for the calculation of the κ, which is determine between SPECT MPI and CA. If there is no agreement, κ = 0.20–0.39; moderate agreement, κ = 0.40–0.59; very good agreement, κ = 0.60–0.79; excellent agreement, κ = 0.80–1.00.

SPECT images of the left ventricle to be acquired early and with excellent quality [22]. The ratios of heart-to-liver were consistent with the previous report study [22]. These characteristics are suitable, particularly for patients with suspected acute coronary syndromes and without diagnostic electrocardiogram, because early diagnosis is needed in such patients for timely therapeutic decision making. ^{99m}Tc-MIBI, on the other hand, may require a wait time of up to 1 h for imaging.

In the present study, the heart-to-organ count ratio of ^{99m}Tc-N-DBODC5 MPI was superior to that of ^{99m}Tc-MIBI in 46 patients. Compared with ^{99m}Tc-MIBI MPI, ^{99m}Tc-N-DBODC5 MPI had better image quality in most patients. Furthermore, in this study, exercise stress myocardial images were performed 30 min after ^{99m}Tc-N-DBODC5 injection, and excellent MPI with high contrast was possible.

4.2. Clinical Value of ^{99m}Tc-N-DBODC5 for the Detection of CAD. This clinical trial assesses the diagnostic value of this agent to detect CAD comparing it with stress ^{99m}Tc-MIBI MPI and CA.

In this study, compared with ^{99m}Tc-MIBI MPI, ^{99m}Tc-N-DBODC5 MPI indicates the same sensitivity and better specificity and accuracy to detect coronary disease in patients, although none of the differences were significant. On the other hand, more importantly, angiography agreement was very good for ^{99m}Tc-N-DBODC5 (κ = 0.73) and moderate for ^{99m}Tc-MIBI (κ = 0.52); thus, compared with ^{99m}Tc-MIBI MPI, it provides a high degree of concordance for the evaluation of CAD, specifically in excluding perfusion abnormalities in patients with suspected CAD. Possible reasons for this difference may be fast liver clearance, favorable heart-to-organ ratio, and high image quality. ^{99m}Tc-N-DBODC5 with rapid liver clearance may significantly reduce the photon scatter from the liver into the inferoposterior walls. This reduces the artifactual decreased myocardial perfusion and improves the diagnostic accuracy for the detection of CAD compared with other ^{99m}Tc-labeled perfusion agents [24].

Unsurprisingly, Braat et al. [35] and Germano et al. [36] noted that technetium-labeled MPI agents with a fast liver clearance can significantly reduce the photon scatter from the liver into the inferior walls, but the radioactivity may be transferred to the gastrointestinal area, and increased bowel and gastric activity were seen as a problem associated with high liver uptake in the visual and quantitative interpretation of the inferoposterior myocardial walls. In this study, bowel uptake was frequently seen on the ^{99m}Tc-N-DBODC5 images, but did not result in any nondiagnostic scans.

For the detection of coronary disease in patients, ^{99m}Tc-MIBI produced abnormal results for MPI in four patients who had no angiographically detected stenosis. Some of these false-positive results may be due, in part, to the liver-to-heart artifacts. In this study, we could classify fixed perfusion defects as soft-tissue attenuation artifacts or infarcts by using gated SPECT. Because an artifactual defect would show normal contraction (wall motion or thickening) on a gated image, artifacts can be differentiated from a true infarct [37].

For the detection of individual vessel stenosis, on the other hand, angiography agreement was very good for ^{99m}Tc-N-DBODC5 (κ = 0.71 for RCA) and moderate for ^{99m}Tc-MIBI (κ = 0.48 for RCA). For LAD and LCX arteries stenosis, the diagnosis of myocardial ischemia on ^{99m}Tc-N-DBODC5 and ^{99m}Tc-MIBI study had the same specificity; and it was similar to that of two tracer to diagnose sensitivity and accuracy of myocardial ischemia. Abnormal results of myocardial images in individual RCA vessel stenosis (six arteries-stenosed vessels for RCA) were obtained in the ^{99m}Tc-MIBI studies, while CA and ^{99m}Tc-N-DBODC5 studies showed normal findings in the same individual RCA vessel territories. Some of these false-positive results may be due to photon scatter from the liver and intestine into the inferoposterior walls. ^{99m}Tc-MIBI concentration located below the left diaphragm (i.e. liver and bowel) may cause an artifactual perfusion defect in the adjacent myocardial, a phenomenon known as the "liver-heart artifact" [36, 38]. Moreover, the inferior and inferoposterior regions were dominated mainly by RCA territories corresponding to the myocardial short axis and vertical long axis; while arteries regions which LAD and LCX dominated were less interfered from "liver-heart artifact." Finally, for clinical applications, ^{99m}Tc-N-DBODC5 offers better determination of detects, particularly in the inferoposterior wall on myocardial images. A typical example of a false-positive perfusion defect in the inferior wall is shown in Figure 5.

On a segment-to-segment basis, complete agreement between the two imaging agents occurred in 71% of segments.

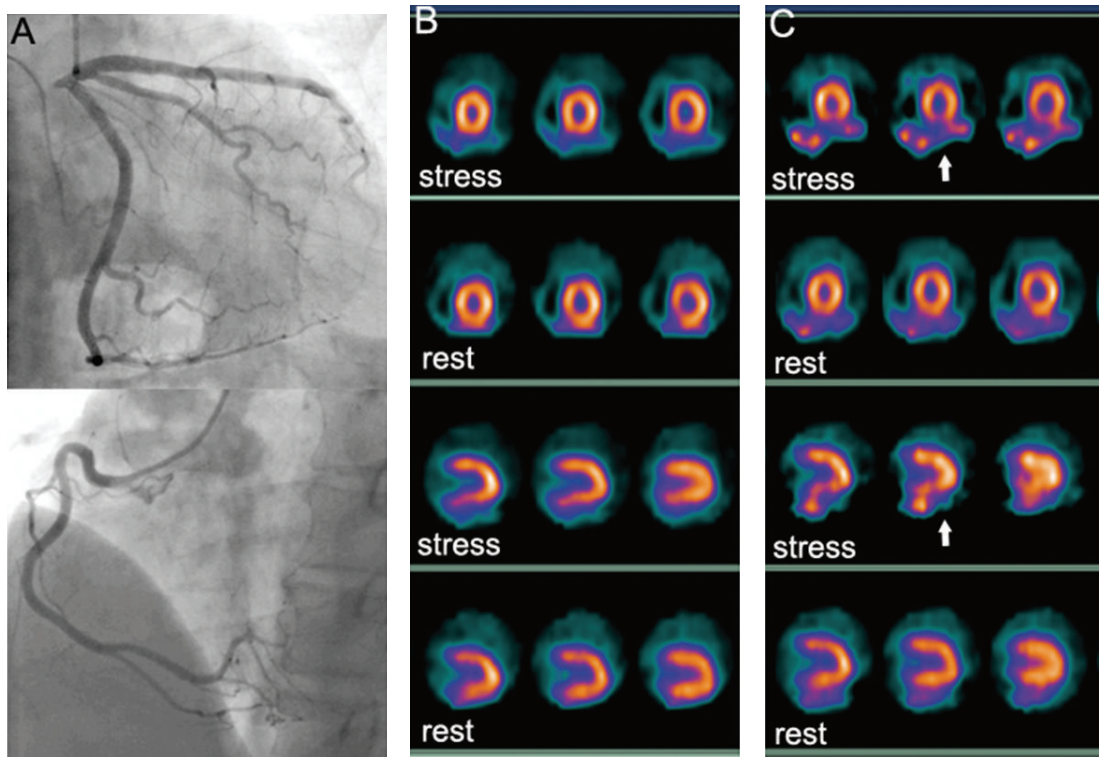

(a) (b) (c)

Figure 5: Serial short-axis and vertical long-axis slices of stress-rest ^{99m}Tc-N-DBODC5 images (b) and stress-rest ^{99m}Tc-MIBI images (c) of a representative patient with normal CA (a). Because of intense uptake of technetium ^{99m}Tc-MIBI in the liver, high liver background activity can be observed. Furthermore, a false-positive myocardial perfusion defect was also seen in the inferoposterior wall segments supplied by the RCA territory (white arrows). Importantly, however, at stress and rest, the inferoposterior wall segments of ^{99m}Tc-N-DBODC5 images are clearly separated from the subdiaphragmatic activity.

However, more myocardial segments were nonreversible on ^{99m}Tc-MIBI images than on ^{99m}Tc-N-DBODC5 images. On the contrary, ^{99m}Tc-N-DBODC5 MPI had a higher reversible defect than that of ^{99m}Tc-MIBI. A possible reason for this difference may be due, in part, to the "liver-heart artifact." The presence of high liver activity adjacent to the inferior wall results from oversubtraction of activity from the inferior wall. Therefore, the more "liver-heart artifact" in the inferoposterior wall on myocardial images, the more false nonreversible defects in the inferoposterior wall on myocardial perfusion segmental analysis. In other words, the less reversible defects in the inferoposterior wall were deduced on ^{99m}Tc-MIBI MPI segmental analysis.

More importantly, however, the main advantage and clinical value of ^{99m}Tc-N-DBODC5 can improve diagnostic specificity and reduce the false-positive diagnosis of patients and associated treatment fees.

5. Limitations

In this study, we did not attempt to assess the absolute diagnostic accuracy of ^{99m}Tc-N-DBODC5, because definitive conclusions in this regard can only be drawn by studying larger patient cohort. In addition, although ^{99m}Tc-N-DBODC5 did not track flow as well as ^{201}Tl, the magnitudes of the pharmacologic stress-induced perfusion defects were comparable to those previously reported for ^{99m}Tc-tetrofosmin. Thus, direct comparison between ^{99m}Tc-N-DBODC5 and ^{99m}Tc-tetrofosmin should be further proved in the same patient population. Overall, ^{99m}Tc-N-DBODC5 MPI will become an important diagnostic tool in the evaluation of myocardial perfusion.

6. Conclusion

This preliminary clinical study showed that ^{99m}Tc-N-DBODC5 and ^{99m}Tc-MIBI MPI provide comparable diagnostic information for patients undergoing exercise rest for detection of CAD. In addition, ^{99m}Tc-N-DBODC5 does not exhibit the disadvantages of ^{99m}Tc-MIBI in this study. By contrast, because of its high heart-organ count ratio in comparison to ^{99m}Tc-MIBI, it improves high degree of diagnostic concordance in defining or excluding perfusion abnormalities in patients with CAD. Therefore, it can become

the agent of choice for the evaluation of myocardial perfusion and ventricular function in patients with CAD.

Abbreviations

CAD:	Coronary artery disease
MPI:	Myocardial perfusion imaging
CA:	Coronary angiography
SPECT:	Single-photon emission computed tomography
PET:	Positron emission computed tomography
^{99m}Tc-MIBI:	Technetium 99m sestamibi
^{99m}Tc-N-DBODC5:	^{99m}Tc(N)(DBODC)(PNP5)
^{201}Tl:	Thallium-201
^{99m}Tc-tetrofosmin:	Technetium-99m-tetrofosmin
ROI:	Regions of interest
LAD:	Left anterior descending artery
LCX:	Left circumflex artery
RCA:	Right coronary artery
SSS:	Summed stress score
SRS:	Summed rest score
SDS:	Summed difference score
EDV:	End-diastolic volume
ESV:	End-systolic volume
LVEF:	Left ventricular ejection fraction.

Ethics Statement

This study was conducted in accordance with the Helsinki Declaration. All subjects provided written informed consent before MPI, acknowledging that they understood their rights and obligations. This study was approved by the Research Ethics Committee of Shanxi Medical University.

Conflict of Interests

The authors declare that they have no conflict of interest.

Acknowledgments

This research is partly supported by Grants from the Youth Science and Technology Research Foundation of Shanxi Province (no. 2009021043-3). The authors acknowledge the members of the participating staff for their contribution to this clinical study.

References

[1] National Hospital Discharge Survey, National Health Statistics Report, no. 5, 2006.

[2] J. He, D. Gu, X. Wu et al., "Major causes of death among men and women in China," *The New England Journal of Medicine*, vol. 353, no. 11, pp. 1124–1134, 2005.

[3] M. D. Cerqueira, N. J. Weissman, V. Dilsizian et al., "Standardized myocardial sementation and nomenclature for tomographic imaging of the heart: a statement for healthcare professionals from the Cardiac Imaging Committee of the Council on Clinical Cardiology of the American Heart Association," *Circulation*, vol. 105, no. 4, pp. 539–542, 2002.

[4] R. J. Gibbons, J. Abrams, K. Chatterjee et al., "ACC/AHA 2002 guideline update for the management of patients with chronic stable angina—summary article: a report of the American College of Cardiology/American Heart Association Task Force on Practice Guidelines (Committee on the Management of Patients With Chronic Stable Angina)," *Journal of the American College of Cardiology*, vol. 41, no. 1, pp. 159–168, 2003.

[5] W. Wijns, P. Kolh, N. Danchin et al., "Guidelines on myocardial revascularization," *European Heart Journal*, vol. 31, pp. 2501–2555, 2010.

[6] J. M. Jensen, K. A. Øvrehus, L. H. Nielsen, J. K. Jensen, H. M. Larsen, and B. L. Nørgaard, "Paradigm of pretest risk stratification before coronary computed tomography," *Journal of Cardiovascular Computed Tomography*, vol. 3, no. 6, pp. 386–391, 2009.

[7] N. R. Mollet, F. Cademartiri, C. Van Mieghem et al., "Adjunctive value of CT coronary angiography in the diagnostic work-up of patients with typical angina pectoris," *European Heart Journal*, vol. 28, no. 15, pp. 1872–1878, 2007.

[8] R. G. E. J. Groutars, J. F. Verzijlbergen, M. M. C. Tiel-Van Buul et al., "The accuracy of 1-day dual-isotope myocardial SPECT in a population with high prevalence of coronary artery disease," *International Journal of Cardiovascular Imaging*, vol. 19, no. 3, pp. 229–238, 2003.

[9] M. R. Patel, E. D. Peterson, D. Dai et al., "Low diagnostic yield of elective coronary angiography," *The New England Journal of Medicine*, vol. 362, no. 10, pp. 886–895, 2010.

[10] "Pharmacologic stress testing," in *Nuclear Cardiac Imaging Priniciples and Applications*, A. E. Iskandrian and E. V. Garcia, Eds., pp. 293–315, Oxford University Press, New York, NY, USA, 4th edition, 2008.

[11] R. R. Russell III and B. L. Zaret, "Nuclear cardiology: present and future," *Current Problems in Cardiology*, vol. 31, no. 9, pp. 557–629, 2006.

[12] G. Germano, H. Kiat, P. B. Kavanagh et al., "Automatic quantification of ejection fraction from gated myocardial perfusion SPECT," *Journal of Nuclear Medicine*, vol. 36, no. 11, pp. 2138–2147, 1995.

[13] S. R. Underwood, C. Anagnostopoulos, M. Cerqueira et al., "Myocardial perfusion scintigraphy: the evidence," *European Journal of Nuclear Medicine and Molecular Imaging*, vol. 31, pp. 261–291, 2004.

[14] J. Heo and A. S. Iskandrian, "Technetium-labeled myocardial perfusion agents," *Cardiology Clinics*, vol. 12, no. 2, pp. 187–198, 1994.

[15] B. L. Zaret, P. Rigo, F. J. T. Wackers et al., "Myocardial perfusion imaging with 99mTc tetrofosmin: comparison to 201Tl imaging and coronary angiography in a phase III multicenter trial," *Circulation*, vol. 91, no. 2, pp. 313–319, 1995.

[16] J. J. Mahmarian and M. S. Verani, "Exercise thallium-201 perfusion scintigraphy in the assessment of coronary artery disease," *American Journal of Cardiology*, vol. 67, no. 14, pp. 2D–11D, 1991.

[17] D. D. Miller, L. T. Younis, B. R. Chaitman, and H. Stratmann, "Diagnostic accuracy of dipyridamole technetium 99m-labeled sestamibi myocardial tomography for detection of coronary artery disease," *Journal of Nuclear Cardiology*, vol. 4, no. 1, pp. 18–24, 1997.

[18] Z. He, A. S. Iskandrian, N. C. Gupta, and M. S. Verani, "Assessing coronary artery disease with dipyridamole technetium-99m-tetrofosmin SPECT: a multicenter trial," *Journal of Nuclear Medicine*, vol. 38, no. 1, pp. 44–48, 1997.

[19] A. Boschi, C. Bolzati, L. Uccelli et al., "A class of asymmetrical nitrido 99mTc heterocomplexes as heart imaging agents with improved biological properties," *Nuclear Medicine Communications*, vol. 23, no. 7, pp. 689–693, 2002.

[20] A. Boschi, L. Uccelli, C. Bolzati et al., "Synthesis and biologic evaluation of monocationic asymmetric 99mTc-nitride heterocomplexes showing high heart uptake and improved imaging properties," *Journal of Nuclear Medicine*, vol. 44, no. 5, pp. 806–814, 2003.

[21] C. Bolzati, M. Cavazza-Ceccato, S. Agostini, S. Tokunaga, D. Casara, and G. Bandoli, "Subcellular distribution and metabolism studies of the potential myocardial imaging agent [99mTc(N)(DBODC)(PNP5)]+," *Journal of Nuclear Medicine*, vol. 49, no. 8, pp. 1336–1344, 2008.

[22] C. Cittanti, L. Uccelli, M. Pasquali et al., "Whole-body biodistribution and radiation dosimetry of the new cardiac tracer 99mTc-N-DBODC," *Journal of Nuclear Medicine*, vol. 49, no. 8, pp. 1299–1304, 2008.

[23] K. Hatada, L. M. Riou, M. Ruiz et al., "99mTc-N-DBODC5, a new myocardial perfusion imaging agent with rapid liver clearance: comparison with 99mTc-sestamibi and 99mTc-tetrofosmin in rats," *Journal of Nuclear Medicine*, vol. 45, no. 12, pp. 2095–2101, 2004.

[24] T. Takeda, J. Wu, and T. T. Lwin, "99mTc-N-DBODC5: a novel myocardial perfusion imaging agent for diagnosis of coronary artery disease, a review," *Recent Patents on Cardiovascular Drug Discovery*, vol. 1, no. 2, pp. 161–166, 2006.

[25] K. Hatada, M. Ruiz, L. M. Riou et al., "Organ biodistribution and myocardial uptake, washout, and redistribution kinetics of Tc-99m N-DBODC5 when injected during vasodilator stress in canine models of coronary stenoses," *Journal of Nuclear Cardiology*, vol. 13, no. 6, pp. 779–790, 2006.

[26] W. Zhang, W. Fang, B. Li, X. Wang, and Z. He, "Experimental study of [99mTc(PNP5) (DBODC)]+ as a new myocardial perfusion imaging agent," *Cardiology*, vol. 112, no. 2, pp. 89–97, 2009.

[27] M. E. Marmion, S. R. Woulfe, W. L. Neumann, D. L. Nosco, and E. Deutsch, "Preparation and characterization of technetium complexes with Schiff base and phosphine coordination. 1. Complexes of technetium-99g and -99m with substituted acac2en and trialkyl phosphines (where acac2en = N,N′-ethylenebis[acetylacetone iminato])," *Nuclear Medicine and Biology*, vol. 26, no. 7, pp. 755–770, 1999.

[28] C. Bolzati, L. Uccelli, A. Boschi et al., "Synthesis of a novel class of nitrido Tc-99m radiopharmaceuticals with phosphino-thiol ligands showing transient heart uptake," *Journal of Inorganic Biochemistry*, vol. 78, no. 3, pp. 369–374, 2000.

[29] M. J. Henzlova, M. D. Cerqueira, J. J. Mahmarian, and S. Yao, "Stress protocols and tracers," *Journal of Nuclear Cardiology*, vol. 13, no. 6, pp. e80–e90, 2006.

[30] C. L. Hansen, R. A. Goldstein, D. S. Berman et al., "Myocardial perfusion and function single photon emission computed tomography," *Journal of Nuclear Cardiology*, vol. 13, no. 6, pp. e97–e120, 2006.

[31] P. Flamen, A. Bossuyt, and P. R. Franken, "Technetium-99m-tetrofosmin in dipyridamole-stress myocardial SPECT imaging: intraindividual comparison with technetium-99m-sestamibi," *Journal of Nuclear Medicine*, vol. 36, no. 11, pp. 2009–2015, 1995.

[32] N. Tamaki, N. Takahashi, M. Kawamoto et al., "Myocardial tomography using technetium-99m-tetrofosmin to evaluate coronary artery disease," *Journal of Nuclear Medicine*, vol. 35, no. 4, pp. 594–600, 1994.

[33] M. D. Cerqueira, N. J. Weissman, V. Dilsizian et al., "Standardized myocardial segmentation and nomenclature for tomographic imaging of the heart: a statement for healthcare professionals from the Cardiac Imaging Committee of the Council on Clinical Cardiology of the American Heart Association," *Journal of Nuclear Cardiology*, vol. 9, no. 2, pp. 240–245, 2002.

[34] T. Sharir, G. Germano, X. Kang et al., "Prediction of myocardial infarction versus cardiac death by gated myocardial perfusion SPECT: risk stratification by the amount of stress-induced ischemia and the poststress ejection fraction," *Journal of Nuclear Medicine*, vol. 42, no. 6, pp. 831–837, 2001.

[35] S. H. Braat, B. Leclercq, R. Itti, A. Lahiri, B. Sridhara, and P. Rigo, "Myocardial imaging with technetium-99m-tetrofosmin: comparison of one-day and two-day protocols," *Journal of Nuclear Medicine*, vol. 35, no. 10, pp. 1581–1585, 1994.

[36] G. Germano, T. Chua, H. Kiat, J. S. Areeda, and D. S. Berman, "A quantitative phantom analysis of artifacts due to hepatic activity in technetium-99m myocardial perfusion SPECT studies," *Journal of Nuclear Medicine*, vol. 35, no. 2, pp. 356–359, 1994.

[37] A. K. Paul and H. A. Nabi, "Gated myocardial perfusion SPECT: basic principles, technical aspects, and clinical applications," *Journal of Nuclear Medicine Technology*, vol. 32, no. 4, pp. 179–187, 2004.

[38] J. Nuyts, P. Dupont, V. Van den Maegdenbergh, S. Vleugels, P. Suetens, and L. Mortelmans, "A study of the liver-heart artifact in emission tomography," *Journal of Nuclear Medicine*, vol. 36, no. 1, pp. 133–139, 1995.

Hindawi Publishing Corporation
BioMed Research International
Volume 2013, Article ID 759057, 11 pages
http://dx.doi.org/10.1155/2013/759057

Research Article

Molecular Imaging of Hepatocellular Carcinoma Xenografts with Epidermal Growth Factor Receptor Targeted Affibody Probes

Ping Zhao,[1,2] Xiaoyang Yang,[3] Shibo Qi,[2] Hongguang Liu,[2] Han Jiang,[2] Susan Hoppmann,[2] Qizhen Cao,[2] Mei-Sze Chua,[3] Samuel K. So,[3] and Zhen Cheng[2]

[1] *Department of Digestive, China-Japan Union Hospital, Jilin University, Changchun, Jilin 130033, China*
[2] *Department of Radiology and Bio-X Program, Molecular Imaging Program at Stanford (MIPS), Canary Center at Stanford for Cancer Early Detection, 1201 Welch Road, Lucas Center, P095, Stanford University, Stanford, CA 94305, USA*
[3] *Department of Surgery, Asian Liver Center, Stanford University School of Medicine, Stanford University, Stanford, CA 94305, USA*

Correspondence should be addressed to Zhen Cheng; zcheng@stanford.edu

Received 12 March 2013; Accepted 22 March 2013

Academic Editor: Hong Zhang

Hepatocellular carcinoma (HCC) is a highly aggressive and lethal cancer. It is typically asymptomatic at the early stage, with only 10%–20% of HCC patients being diagnosed early enough for appropriate surgical treatment. The delayed diagnosis of HCC is associated with limited treatment options and much lower survival rates. Therefore, the early and accurate detection of HCC is crucial to improve its currently dismal prognosis. The epidermal growth factor receptor (EGFR) has been reported to be involved in HCC tumorigenesis and to represent an attractive target for HCC imaging and therapy. In this study, an affibody molecule, Ac-Cys-$Z_{EGFR:1907}$, targeting the extracellular domain of EGFR, was used for the first time to assess its potential to detect HCC xenografts. By evaluating radio- or fluorescent-labeled Ac-Cys-$Z_{EGFR:1907}$ as a probe for positron emission tomography (PET) or optical imaging of HCC, subcutaneous EGFR-positive HCC xenografts were found to be successfully imaged by the PET probe. Thus, affibody-based PET imaging of EGFR provides a promising approach for detecting HCC *in vivo*.

1. Introduction

Primary liver cancer, also known as hepatocellular carcinoma (HCC), is the fifth most common neoplasm and the third leading cause of cancer-related deaths worldwide [1–3]. Symptoms of HCC at early stage are usually atypical, and thus, HCC patients often present with symptoms at an advanced stage. Only 10%–20% of HCC are diagnosed early enough for appropriate surgical treatment [4–6]. The poor prognosis of this disease is largely due to the lack of effective and accurate early diagnostic methods, causing most patients to be diagnosed at the late stages, which seriously limits treatment options. Therefore, highly sensitive and accurate molecular imaging techniques that allow early HCC detection are urgently needed.

Currently, the most commonly used positron emission tomography (PET) probe for tumor imaging is ^{18}F-fluoro-deoxy-glucose (^{18}F-FDG). However, the use of ^{18}F-FDG-PET in the detection of HCC is rather limited, and it was reported that ^{18}F-FDG could even miss 30%–50% of HCC lesions in the liver [7]. Another PET probe commonly used for detection of HCC is ^{11}C-labeled acetate, which was reported to show higher sensitivity than ^{18}F-FDG [8, 9]. It plays a complementary role to ^{18}F-FDG in both HCC cell lines and human HCC detection, being able to detect HCC tumors with low ^{18}F-FDG uptake only. But similar as ^{18}F-FDG, ^{11}C-labeled acetate is a largely nonspecific probe for HCC imaging, as it typically enters the tricarboxylic acid cycle as a substrate for β-oxidation in fatty acid synthesis [10].

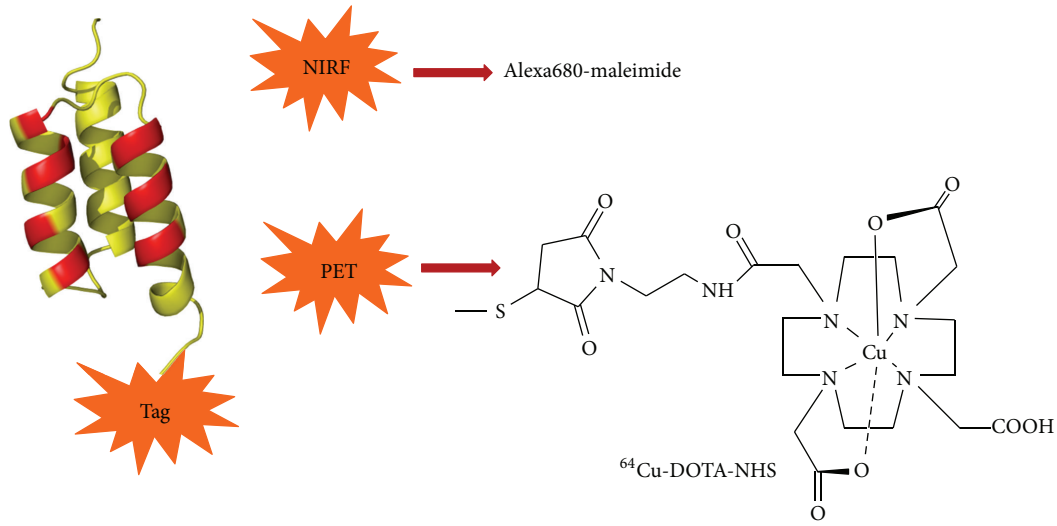

FIGURE 1: Schematic structure of affibody-based PET and NIRF probes. Different probes were used in various imaging studies (^{64}Cu-DOTA-$Z_{EGFR:1907}$ for PET and Alex680-$Z_{EGFR:1907}$ for optical imaging).

Development of molecular probes suitable for imaging other HCC associated biomarkers is thus considered as a promising strategy whereas a largely unexplored field.

The contextual complexity of understanding HCC is defined by the functional involvement of several signaling cascades (epidermal growth factor, insulin-like growth factor, RAS, WNT-β catenin, etc.) as well as multiple risk factors (such as hepatitis B and C viral infection and alcohol abuse) [1, 11, 12]. Among them, epidermal growth factor (EGF) signaling is one of the most thoroughly evaluated signaling cascades in human HCC development. EGF is demonstrated to control proliferation, differentiation, and cell survival and is overexpressed in a wide range of solid tumors including HCC [13, 14]. The growth factor receptor (EGFR) is a receptor tyrosine kinase that regulates a number of key processes, including cell proliferation and differentiation, tissue homeostasis, and tumorigenesis [15, 16]. Dysregulation of EGFR expression is associated with several key features of cancer, such as autonomous cell growth, apoptosis inhibition, invasion, and metastasis [17, 18]. Overexpression of EGFR has been frequently detected in a wide range of human tumors, including non-small-cell lung cancer, gastric cancer, breast cancer, as well as liver cancer [19]. In HCC, there is increasing evidence demonstrating a correlation between EGFR overexpression and tumor aggressiveness, metastasis formation, therapy resistance, and poor prognosis of this disease [15, 20–22]. Functional involvement of EGFR in HCC development was best demonstrated by the observation that EGFR inhibitor, Gefitinib, can significantly reduce HCC incidence in a genotoxic animal model of HCC [23]. Taken together, EGFR represents an attractive target for small molecules or antibodies in applications such as tumor-targeted imaging and therapy.

Several anti-EGFR affibody molecules (Z_{EGFR}) with high affinities (in nanomolar range) have been reported recently. Among them, the affibody molecule, $Z_{EGFR:1907}$, has been shown to specifically bind EGFR with no cross-binding to other growth factor receptors [24], as well as fast tumor targeting and excellent tumor-to-normal tissue contrast on EGFR-expressing xenografted epithelial cancer models [25–29]. Affibody molecules are small (approximately 7 kDa), engineered proteins with 58-amino acid residues and a three-helix bundle scaffold structure [24, 30]. Its small molecular weight, high stability, high binding specificity, and affinity make it an excellent probe for tumor-targeted imaging *in vivo* [31, 32]. In this study, we hypothesized that EGFR targeted affibody probes can be promising molecular probes for HCC detection. Two types of affibody-based probes, ^{64}Cu-DOTA-$Z_{EGFR:1907}$ for PET, and Alexa680-$Z_{EGFR:1907}$ for near-infrared fluorescent (NIRF) imaging (Figure 1), were evaluated and compared for molecular imaging of three type of HCC xenograft models. It is expected that the EGFR targeted NIRF probe can not only image HCCs noninvasively but also provides a tool for image-guided therapy, whereas the PET probe can find more broad applications for clinical cancer imaging.

2. Materials and Methods

2.1. Preparation of Affibody-Based Molecular Probes. The affibody molecule Ac-Cys-$Z_{EGFR:1907}$ (Ac-CVDNKFNKEMWAAWEEIRNLPNLN GWQMTAFIA SLVDDPSQSANLLAEAKKLNDAQAPK-NH_2) was synthesized and analyzed as previously described [25]. 1,4,7,10-Tetraazacyclododecane-1,4,7,10-tetraacetic acid mono-N hydroxysuccinimidide ester (DOTA-NHS ester) was obtained from Macrocyclics Inc. (Dallas, TX). Near-infrared fluorescent dye Alexa Fluor 680 C2 maleimide was purchased from Invitrogen Life Technologies (Carlsbad, CA). The general procedure for the conjugation of maleimido-mono-amide-DOTA and Alexa Fluor 680 C2 maleimide with Ac-Cys-$Z_{EGFR:1907}$ was performed as previously reported [25]. The purity and molecular mass of the resulting affibody derivatives, DOTA-$Z_{EGFR:1907}$ and Alexa680-$Z_{EGFR:1907}$,

were determined by analytical scale reverse phase high-performance liquid chromatography (RP-HPLC) and matrix-assisted laser desorption/ionization-time of flight mass spectrometry (MALDI-TOF-MS). $^{64}CuCl_2$ was purchased from the Department of Medical Physics, University of Wisconsin at Madison. ^{64}Cu radiolabeling of DOTA-$Z_{EGFR:1907}$ was performed as reported previously [12].

2.2. Cell Culture and Animal Models. The human HCC cell lines HepG2, PLC/PRF/5, and Hep3B were purchased from American Type Culture Collection (ATCC) (Manassas, VA). PLC/PRF/5 and Hep3B cells were cultured in Dulbecco's Modified Eagle's Medium (DMEM), and HepG2 cells were cultured in ATCC-formulated Eagle's Minimum Essential Medium (MEM), supplemented with 10% fetal bovine serum (FBS), and 1% penicillin-streptomycin (Invitrogen Life Technologies, Carlsbad, CA). All cell lines were maintained in a humidified atmosphere of 5% CO_2 at 37°C.

All animal studies were carried out in compliance with Federal and local institutional rules for the conduct of animal experiments. The animal protocol was approved by the Stanford University Administrative Panels on Laboratory Animal Care. In brief, male athymic nude (nu/nu) mice were obtained from Charles River Laboratories, Inc. (Cambridge, MA) at 4 weeks of age. To generate animal tumor models, approximately, 10×10^6 HepG2 cells were injected subcutaneously into the upper left shoulder. On separate mice, approximately 5×10^6 of Hep3B or PLC/PRF/5 cells were injected into the upper right shoulder. Tumors were allowed to grow to a size of approximately 1.0 cm in largest diameter (3-4 weeks after inoculation), and tumor-bearing mice were subjected to *in vivo* imaging and biodistribution studies (n = 3 for each tumor models).

2.3. Quantitative Real-Time PCR. Total RNA was extracted from human HCC cell lines using the RNeasy mini kit (Qiagen, Valencia, CA). First-strand cDNA was generated using Taqman Reverse Transcription Reagent with random primers. Quantitative real-time PCR assays were performed using Taqman EGFR gene expression assay and Universal PCR Master Reagent in a Stratagene MX3000P Q-PCR system (Stratagene, La Jolla, CA). The EGFR expression level was assessed in terms of threshold cycle value using Stratagene MxPro software and normalized to the internal control, human 18S rRNA (Eukaryotic 18S rRNA endogenous control). All the reagents were purchased from Applied Biosystems (Foster City, CA).

2.4. Western Blotting. Whole proteins from either cell pellets or tumor tissues were harvested using T-PER Tissue Protein Extraction Reagent (Pierce Biotechnology, Rockford, IL). Protein concentration was assessed by BCA™ protein assay kit (Pierce Biotechnology, Rockford, IL). Protein (20 μg) was then resolved using NuPAGE 4%–12% Bis-Tris gels (Invitrogen Life Technologies, Carlsbad, CA). Immunoblotting was carried out using EGFR polyclonal antibody (Ab2430, Abcam, Cambridge, MA) at 1 : 5,000 dilution.

2.5. Fluorescence Microscopy. Hep3B, PLC/PRF/5, and HepG2 cells were seeded onto cover slips approximately 24 h prior to the experiment. Staining using EGFR polyclonal antibody was performed at 1 : 500 dilution and AlexaFlour 660 goat anti-rabbit IgG (H + L) (Invitrogen Life Technologies, Carlsbad, CA). For staining using Alexa680-$Z_{EGFR:1907}$, cover slips were washed with PBS and then incubated with Alexa680-$Z_{EGFR:1907}$ (100 nM) at 37°C for 1 h in the dark. The EGFR-binding specificity of Alexa680-$Z_{EGFR:1907}$ in cells was verified by coincubation with or without large excess of blocking dose of nonfluorescent-labeled Ac-Cys-$Z_{EGFR:1907}$ peptide (10 μM). Stained slides were imaged using the Talamasca 2P confocal microscope (Zeiss LSM510, Thornwood, NY) on the same day using 40x oil immersion lens.

For immunohistochemistry (IHC) on subcutaneous xenograft tumors, tissue treatment and fixation were performed by the Department of Surgical Pathology, Stanford University. IHC staining of EGFR was performed using polyclonal EGFR antibodies (Ab2430, Abcam, Cambridge, MA) at 1 : 500 dilution and DAKO Envision Plus Kit (Dako, Carpinteria, CA). For immunofluorescence on human tissue microarrays, 100 nM of Alexa680-$Z_{EGFR:1907}$ was incubated with the slides for 1 h in the dark. Stained slides were imaged using Talamasca 2P confocal microscope on the same day.

2.6. Optical Imaging and Image Analysis. In vivo optical imaging was performed with an IVIS 200 small animal imaging system (Caliper, Alameda, California). A filter set (excitation 615 to 655 nm; emission 695 to 770 nm) was used for acquiring Alexa680-$Z_{EGFR:1907}$ fluorescence *in vivo*. Identical illumination settings were used to acquire all images, and fluorescence emission was normalized to photons per second per centimeter squared per steradian (p/sec/cm^2/sr). Images were analyzed using Living Image 3.0 software (Caliper, Alameda, CA). A prescan image before injection was acquired to eliminate autofluorescence. Mice (n = 3) were injected with 500 pmol of Alexa680-$Z_{EGFR:1907}$ *via* tail vein and subjected to optical imaging at 0.5, 1, 2, 4, and 24 h post injection (p.i.). For blocking experiments, mice (n = 3) were injected with a mixture of 300 μg nonfluorescent Ac-Cys-$Z_{EGFR:1907}$ and 500 pmol of Alexa680-$Z_{EGFR:1907}$. IVIS-200 NIR fluorescent images were acquired using a 1 s exposure time. After the final scan at 24 h p.i., animals were euthanized and imaged *ex vivo*. Tumor and other major tissues were dissected out and fluorescence images acquired to obtain the mean fluorescence flux (p/sec/cm^2/sr) for each sample.

2.7. Small Animal PET, Biodistribution, and Image Analysis. Small animal PET of tumor-bearing mice (n = 3 each group) was performed using a microPET R4 rodent-model scanner (Siemens Medical Solutions USA, Knoxville, TN). Imaging studies were conducted at 1, 2, 4, and 24 h after tail vein injection of ~3.7 MBq (~100 μCi) ^{64}Cu-DOTA-$Z_{EGFR:1907}$ with or without coinjection of 300 μg of nonradioactive (blocking) Ac-Cys-$Z_{EGFR:1907}$. At different time points after injection, the mice were anesthetized with 2% isoflurane and placed in the prone position near the center of the field of view of

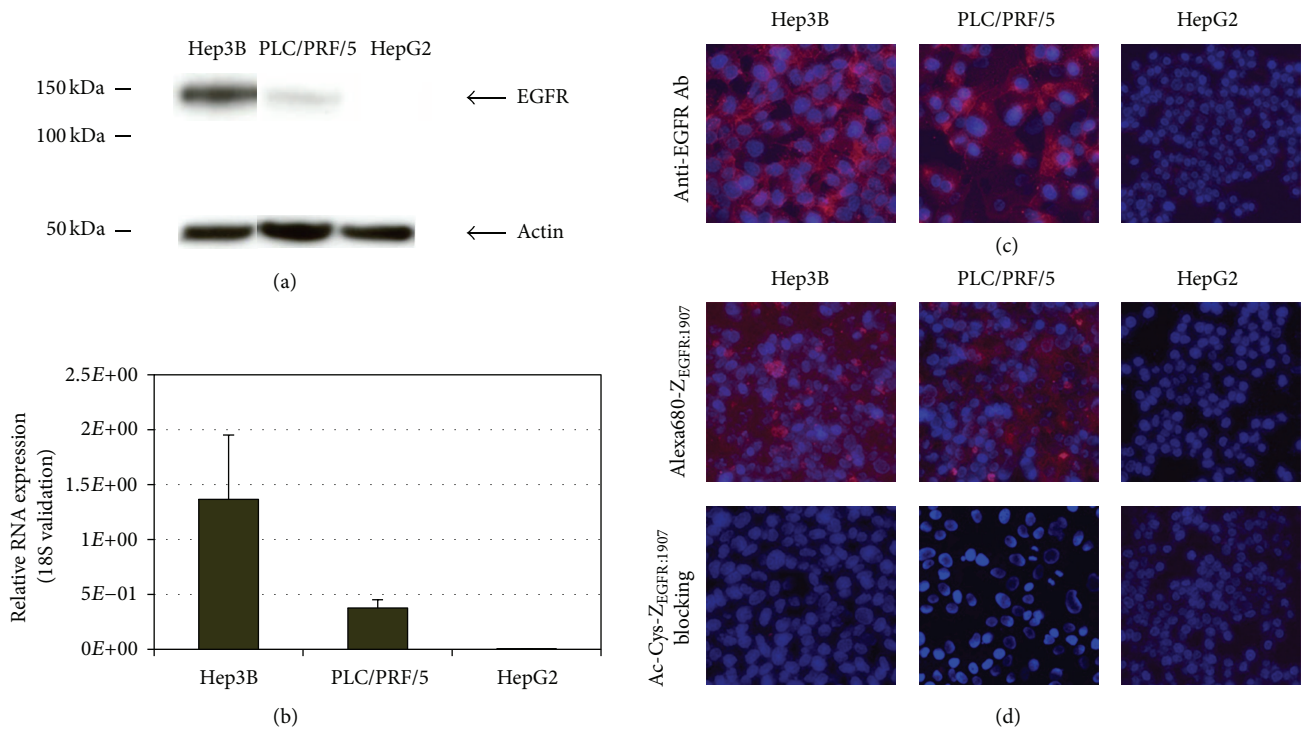

FIGURE 2: Human hepatocellular carcinoma cell line characterization. (a) Assessment of EGFR expression in HCC cell lines, including Hep3B, PLC/PRF/5, and HepG2 cells. Protein ladders are indicated in kDa. Bands for EGFR and β-actin are indicated by arrowheads. (b) EGFR expression in HCC cell lines at mRNA level was assessed by quantitative real-time PCR. Relative quantification of EGFR RNA expression was validated by 18S RNA. (c) Immunofluorescence staining of Hep3B, PLC/PRF/5, and HepG2 cells using FITC labeled anti-EGFR antibody. Positive staining of EGFR was shown in red. Nuclei staining using DAPI is shown in blue. (d) Immunofluorescence staining of Hep3B, PLC/PRF/5, and HepG2 cells using Alexa680-$Z_{EGFR:1907}$. Staining using unlabeled Ac-Cys-$Z_{EGFR:1907}$ as a blocking reagent was also shown. Positive staining of EGFR was shown in red. Nuclei staining using DAPI is shown in blue.

the scanner. The 3-minute static scans were obtained, and the images were reconstructed by a two-dimensional ordered subsets expectation maximum (OSEM) algorithm. Quantification analysis of the images was performed as previously reported [33]. After the final scan, the animals were sacrificed by cervical dislocation under deep anesthesia and dissected. Tumors and organs of interest were excised, weighed, and their radioactivity was measured using the CobraII auto-gamma counter B5002 (Packard, Virginia Beach, VA). Results were expressed as percent of injected dose per gram of tissue (%ID/g).

2.8. Statistical Analysis. Quantitative data were expressed as mean ± standard deviation (SD). Statistical analysis was performed using one-way ANOVA and the Student's two-tailed t-test for unpaired data. P values less than 0.05 were considered statistically significant.

3. Results

3.1. Characterization of Human HCC Cell Lines. To assess the endogenous EGFR expression in human HCC cell lines, we first detected EGFR protein level by Western blotting in a panel of three human HCC cell lines (Hep3B, PLC/PRF/5, and HepG2). Among these cell lines, Hep3B cells have the highest level of EGFR expression, PLC/PRF/5 cells have moderate level of EGFR expression, whereas HepG2 cells have undetectable EGFR expression (Figure 2(a)). The varying levels of EGFR expression in these cell lines were confirmed by quantitative real-time PCR (Figure 2(b)). Immunohistochemistry using polyclonal anti-EGFR antibody also showed highest level of EGFR staining in Hep3B cells, moderate level of EGFR staining in PLC/PRF/5 cells, and absence of EGFR staining in HepG2 cells (Figure 2(c)).

To demonstrate the EGFR binding specificity and subcellular localization of the fluorescently labeled affibody, Alexa680-$Z_{EGFR:1907}$, in HCC cells, immunofluorescence staining was done in Hep3B, PLC/PRF/5, and HepG2 cells. Fluorescence signal was observed mainly on the cell surface of Hep3B cells (Figure 2(d)), consistent with the fact that this probe was designed to primarily target the extracellular domain of EGFR [24]. Furthermore, the fluorescence signal from the Hep3B cells could be significantly reduced by incubation with large excess (10 μM) of the unlabeled Ac-Cys-$Z_{EGFR:1907}$, indicating binding specificity of the probe. In PLC/PRF/5 cells, reduced fluorescence signals were detected, consistent with the lower level of EGFR expression in these cells. Coincubation of PLC/PRF/5 cells with large excess (10 μM) of unlabeled Ac-Cys-$Z_{EGFR:1907}$ resulted in loss of positive signals, again demonstrating binding specificity

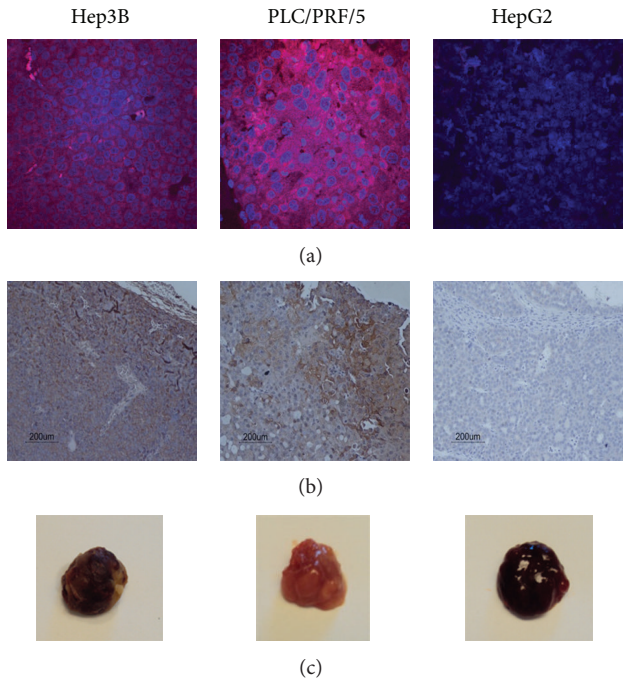

Figure 3: Immunofluorescence and immunohistochemistry staining on subcutaneous HCC xenografts. (a) Immunofluorescence staining of Hep3B, PLC/PRF/5, and HepG2 xenografts using Alex680-$Z_{EGFR:1907}$. (b) Immunohistochemistry (IHC) staining on paraffin-embedded subcutaneous tumor tissues, including Hep3B, PLC/PRF/5, and HepG2 tumors. Anti-EGFR antibody was used in 1 : 200 dilution. Nuclei staining was performed using Dako Cytomation Mayer's hematoxylin histological staining reagent. (c) Representative photograph of PLC/PRF/5, Hep3B, and HepG2 subcutaneous tumors.

(Figure 2(d)). Only background fluorescence was detected in HepG2 cells.

3.2. EGFR Expression in HCC Xenografts. Based on the previous results, HCC mice xenografts with Hep3B, PLC/PRF/5, and HepG2 cells were generated to represent HCC tumors with high-, moderate-, and no-EGFR expression, respectively, for subsequent imaging studies. The subcutaneous xenografts ($n = 3$ for each tumor model) were harvested for assessment of EGFR protein expression. Immunofluorescence using Alex680-$Z_{EGFR:1907}$ showed that Hep3B and PLC/PRF/5 xenografts express high levels of EGFR expression, whereas HepG2 xenografts showed no detectable EGFR expression (Figure 3(a)). Immunohistochemistry of paraffin-embedded tissue sections from Hep3B, PLC/PRF/5, and HepG2 xenografts showed that Hep3B xenografts have extensive staining of EGFR, whereas PLC/PRF/5 xenografts showed regional positive staining, and HepG2 tumor did not show any positive regions (Figure 3(b)). Visual inspection of tumor xenografts revealed that Hep3B and HepG2 are highly vascularized, and both tumor samples showed much darker color than that of PLC/PRF/5 tumors (Figure 3(c)).

3.3. In Vivo and Ex Vivo Tumor Targeting by Optical Imaging. After demonstrating the specific binding of Alexa680-$Z_{EGFR:1907}$ toward EGFR in both *in vitro* cell culture and *in vivo* xenografts of human HCC cell lines, this fluorescent affibody probe was used for optical imaging of nude mice bearing subcutaneous Hep3B, PLC/PRF/5, or HepG2 xenografts. The PLC/PRF/5 xenografts could be clearly distinguished from the surrounding background tissue from prescan, 1 h to 4 h p.i. (Figure 4(a)). Based on quantification analysis of region-of-interest (ROI), PLC/PRF/5 tumor accumulations are significant higher than those of normal tissues at 0.5, 1, 2, and 4 h ($P < 0.001$, resp.) (Figure 4(b) left), with tumor-to-normal tissue ratio reaching a peak around 1.60 at 1 h p.i. (Figure 4(b) right). Minimum fluorescent signals were detected in the HepG2 xenografts which are EGFR negative. Even though Hep3B xenografts express reasonably high levels of EGFR (Figure 3), only very weak fluorescent signals could be detected. All xenografts from imaged mice ($n = 3$ for each groups) were harvested for assessment of EGFR expression by Western blotting, which showed high levels of EGFR expression in Hep3B and PLC/PRF/5 tumors but undetectable EGFR expression in HepG2 tumors (Figure 4(c)).

Receptor specificity of the Alexa680-$Z_{EGFR:1907}$ probe was further verified by blocking experiments in mice bearing PLC/PRF/5 xenografts. After coinjection of a large excess of nonfluorescent Ac-Cys-$Z_{EGFR:1907}$, tumor as well as overall uptake was significantly reduced at 2 h and 4 h p.i. (Figure 4(d)). Tumor-to-background contrasts as quantified by ROI analysis of images at 2 h and 4 h p.i. are shown in Figure 4(e). Significant differences ($P < 0.05$) between the ratios for blocking and nonblock group at both time points were observed.

After the final scan at 24 h p.i., animals were euthanized and *ex vivo* fluorescence imaging on tumor and major organs were performed (Figure 4(f)). Quantitative analysis showed that PLC/PRF/5 tumors have much stronger fluorescence signals than HepG2 tumor, and that a significant level of signal remained in the liver and kidney. The stomach and intestine also showed some level of probe accumulation.

3.4. Small Animal PET of HCC. Ac-Cys-$Z_{EGFR:1907}$ was also conjugated with DOTA and radiolabeled with ^{64}Cu for PET of HCC small animal models. Decay-corrected coronal PET images of mice bearing Hep3B and PLC/PRF/5 tumors at 1, 2, 4, and 24 h after tail vein injection of ^{64}Cu-DOTA-$Z_{EGFR:1907}$ are shown (Figure 5(a)). Hep3B xenografts, which express high levels of EGFR, were clearly visualized starting at 1 h p.i., with the excellent tumor imaging quality at later time points (4 and 24 h p.i.). PLC/PRF/5 xenografts, which express low levels of EGFR, also showed distinct tumor accumulation, with clear tumor imaging and high tumor-to-background ratios at 4 and 24 h p.i. (Figures 5(a) and 5(b)). Quantification analysis showed that the PET probe uptake into both Hep3B and PLC/PRF/5 xenografts increased with time (Figure 5(c)), with the highest tumor uptakes for Hep3B and PLC/PRF/5 xenografts occurring at 24 h p.i. (8.52 ± 1.10% and 6.46 ± 0.59%, resp.). In addition to the tumor, high radioactivity accumulations were also observed in the liver of mice bearing

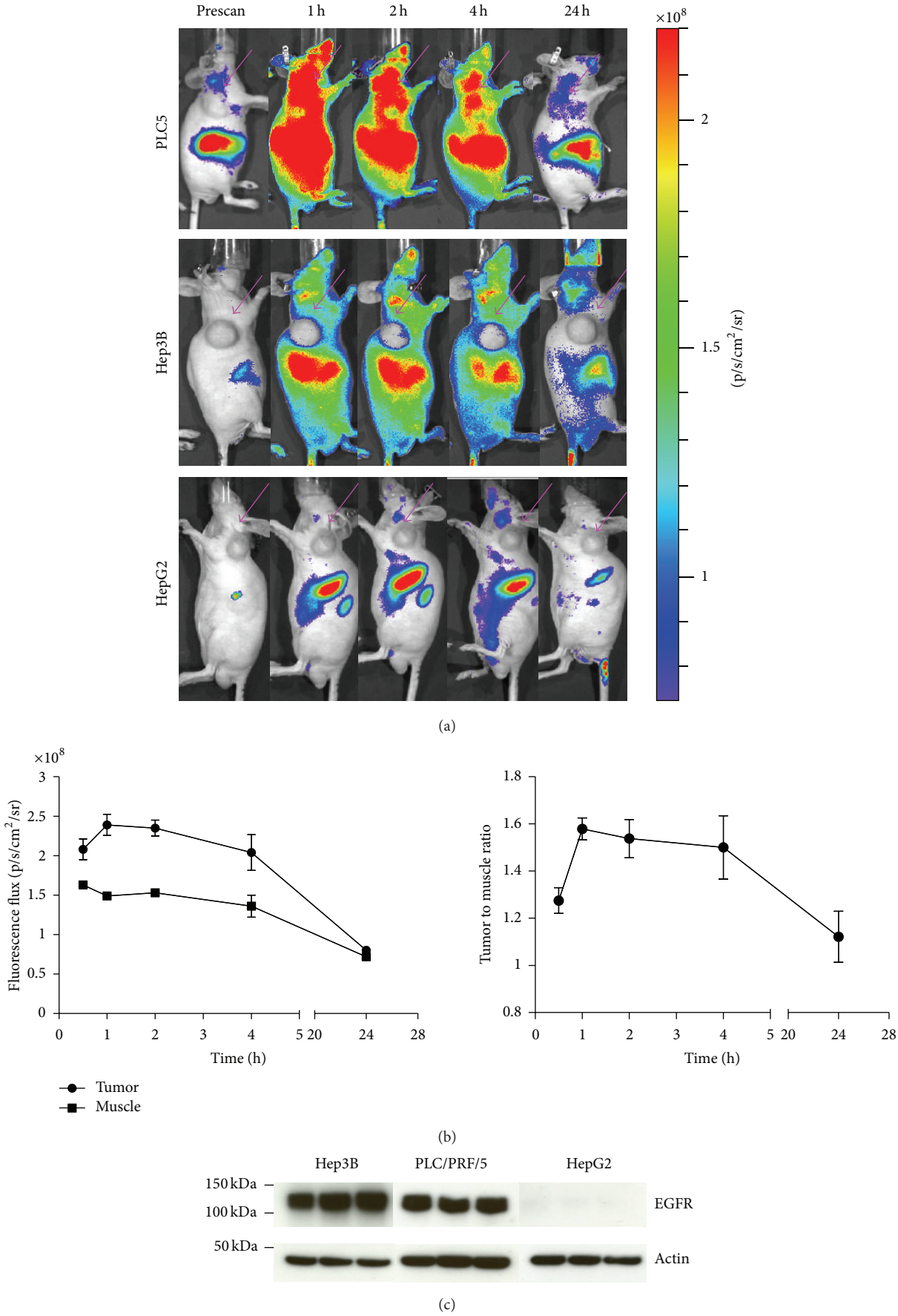

Figure 4: Continued.

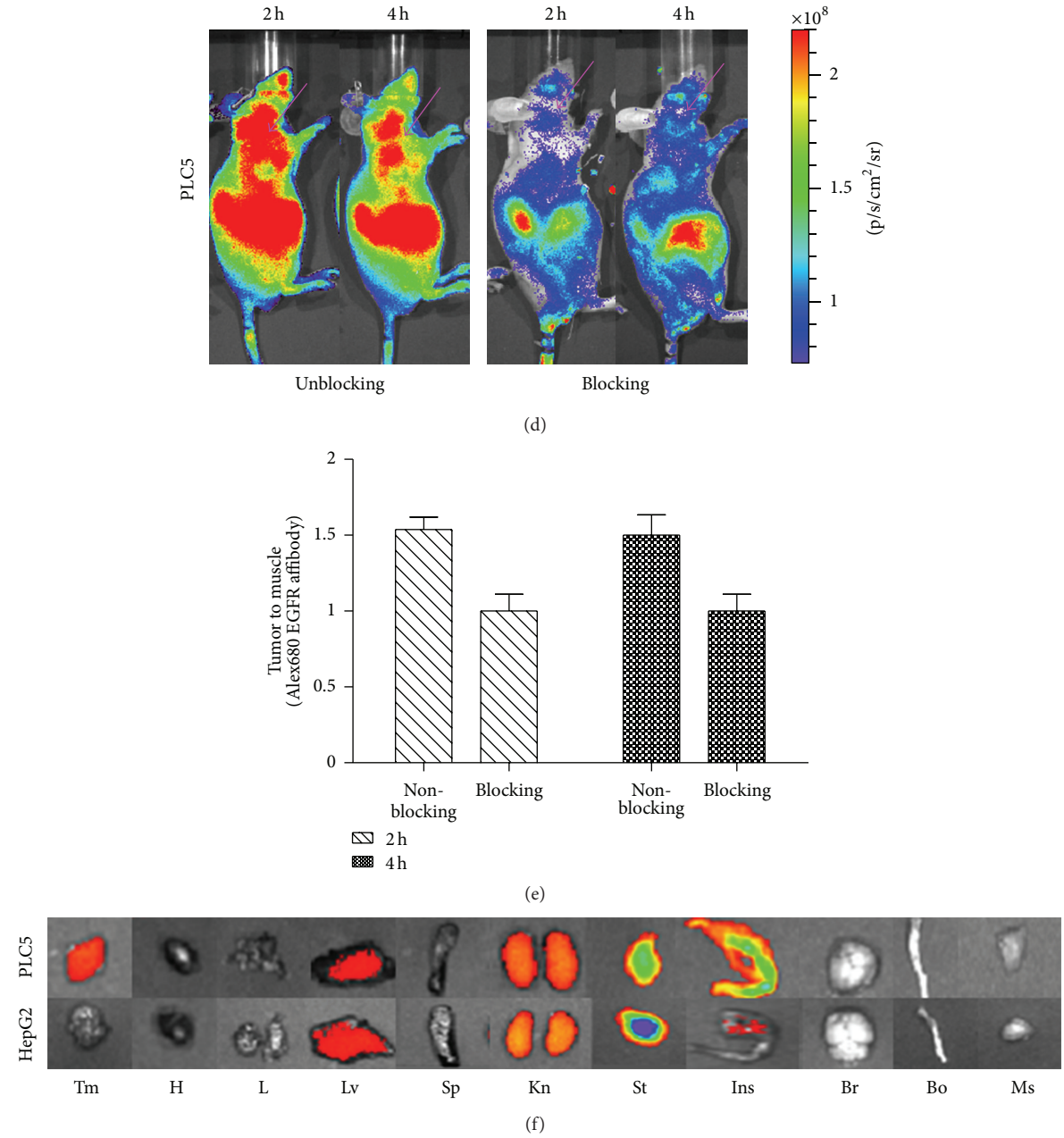

FIGURE 4: Optical Imaging and quantification. (a) *In vivo* fluorescence imaging of subcutaneous PLC/PRF/5 (labeled as PLC5 in the figure), Hep3B, and HepG2 tumor-bearing nude mice at prescan, 1 h, 2 h, 4 h, and 24 h p.i. Approximately 500 pmol Alex680-$Z_{EGFR:1907}$ was injected. Arrows indicate the location of tumors. (b) ROI analysis of tumor and normal tissue (muscle) fluorescence flux and tumor-to-muscle ratio after tail vein injection of Alex680-$Z_{EGFR:1907}$ in mice bearing PLC/PRF/5 tumor ($n = 3$). (c) Protein extractions from subcutaneous tumor tissues were harvested and assessed for EGFR expression. Bands for EGFR and β-actin are indicated by arrowheads. Protein ladders are indicated in kDa. (d) Contrast of *in vivo* fluorescence imaging of subcutaneous PLC/PRF/5 tumor-bearing nude mice at 2 h and 4 h. Alex680-$Z_{EGFR:1907}$ with (right) or without (left) coinjection of unlabeled Ac-Cys-$Z_{EGFR:1907}$ (300 μg). (e) Fluorescence intensity ratio of tumor to muscle in blocking and unblocking PLC/PRF/5 tumor-bearing nude mice at 2 h and 4 h p.i. (f) *Ex vivo* imaging of tumor and normal tissues of PLC/PRF/5 tumor-bearing animals injected with Alex680-$Z_{EGFR:1907}$ and sacrificed at 24 h p.i.. Tm: tumor; H: heart; L: lung; Lv: liver; Sp: spleen; Kn: kidney; St: stomach; Ins: intestine; Br: brain; Bo: bone; Ms: muscle.

either xenografts. The level of liver accumulation, however, decreased with time (from 26.19 ± 2.89% at 1 h p.i. to 16.04 ± 1.19% at 24 h p.i. in mice bearing Hep3B xenografts, and from 16.79 ± 1.64% at 1 h p.i. to 12.89 ± 0.69% at 24 h p.i. in mice bearing PLC/PRF/5 xenografts) (Figure 5(c)).

When a large excess of nonlabeled affibody was co-injected with ^{64}Cu-DOTA-$Z_{EGFR:1907}$ in mice bearing PLC/PRF/5 xenografts, the overall uptake of ^{64}Cu-DOTA-$Z_{EGFR:1907}$ was significantly decreased, and the xenografts were barely visible by PET at all time points (Figure 5(a)).

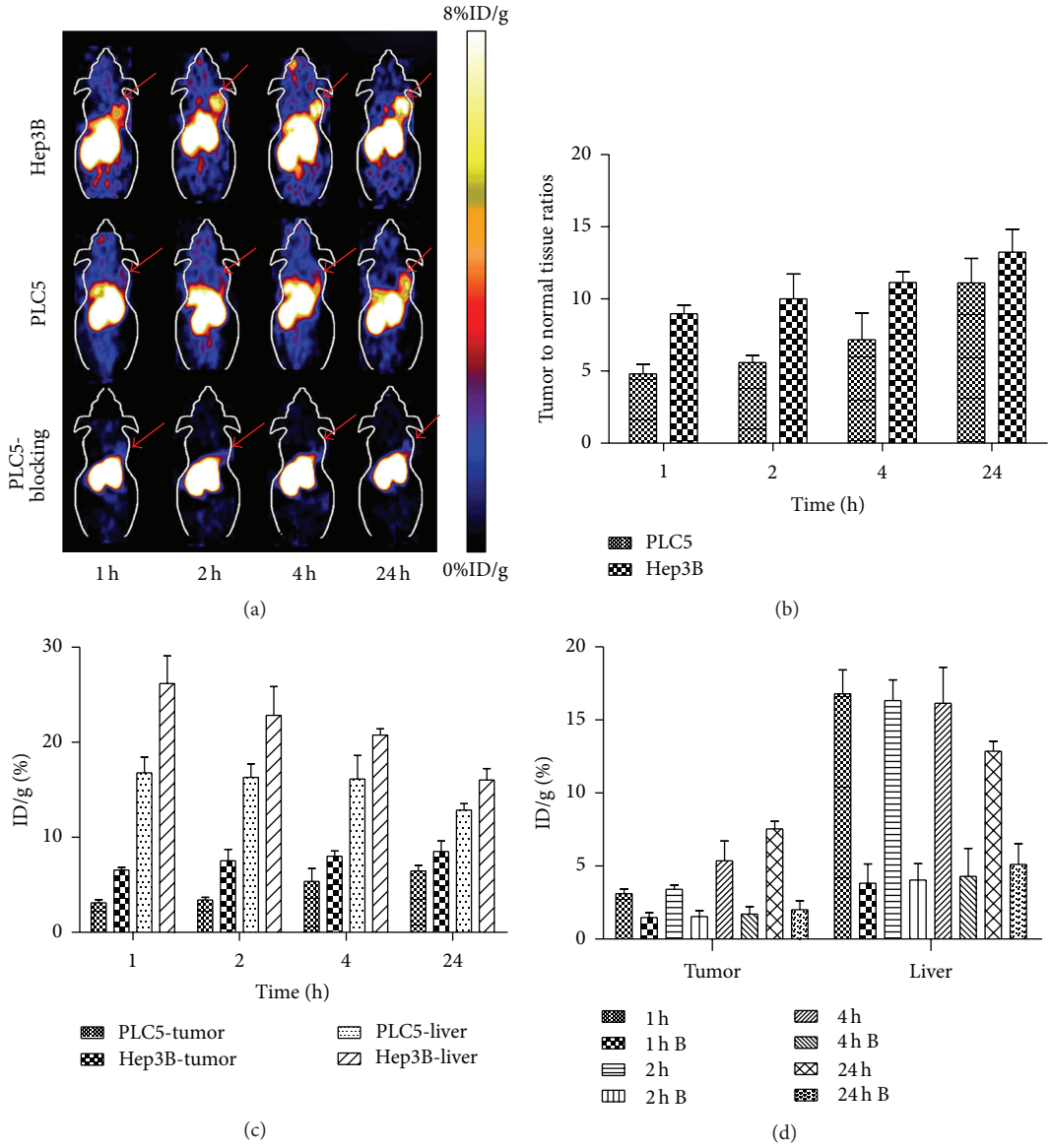

Figure 5: Small-animal PET and quantification analysis. (a) Small animal PET imaging of tumor-bearing mice at 1 h, 2 h, 4 h, and 24 h after tail vein injection of 110 μCi of ^{64}Cu-DOTA-$Z_{EGFR:1907}$. Representative decay-corrected coronal PET images were shown on different tumor-bearing animals, including Hep3B, PLC/PRF/5, and PLC/PRF/5 with blocking dose of unlabeled Ac-Cys-$Z_{EGFR:1907}$. Arrows indicate the location of tumors. (b) Quantification analysis of tumor-to-normal organ ratio in Hep3B and PLC/PRF/5 tumor-bearing mice, respectively, at 1 h, 2 h, 4 h and 24 h after tail vein injection. (c) Quantification analysis of tumor or liver uptake of ^{64}Cu-DOTA-$Z_{EGFR:1907}$ in PLC/PRF/5 tumor models (represented as PLC5 in Figure) and Hep3B tumor models at different time points after injection of the PET probe. (d) Quantification analysis of the probe accumulation in PLC/PRF/5 tumor with (represent as time point B) or without coinjection of unlabeled Ac-Cys-$Z_{EGFR:1907}$ at 1 h, 2 h, 4 h, and 24 h p.i.

Quantification analysis of PET images showed much lower tumor as well as liver uptake at all time points ($P < 0.05$, Figure 5(d)), suggesting successful blocking by the nonlabeled affibody and implying the high specificity of ^{64}Cu-DOTA-$Z_{EGFR:1907}$ for EGFR.

To further validate the PET tumor imaging study, biodistribution analysis was done after the final PET scan at 24 h p.i.. Biodistribution patterns of ^{64}Cu-DOTA-$Z_{EGFR:1907}$ in the tumor, liver, and kidney of mice bearing Hep3B and PLC/PRF/5 xenografts were similar (Figure 6(a)). High kidney and liver uptakes and moderate tumor uptakes were observed. The tumor-to-normal tissue ratios, including tumor/blood and tumor/muscle ratios, were not significantly different between the two tumor models (Figure 6(b)). Blocking experiment using coinjection of a large excess of Ac-Cys-$Z_{EGFR:1907}$ caused a significant decrease in overall uptake of ^{64}Cu-DOTA-$Z_{EGFR:1907}$ (Figure 6(c)). The probe uptake in the PLC/PRF/5 xenograft dropped significantly from 7.84 ± 0.43% to 3.39 ± 1.25% ($P < 0.05$), whereas the radioactivity uptake in the liver dropped significantly from 18.20±2.73% to

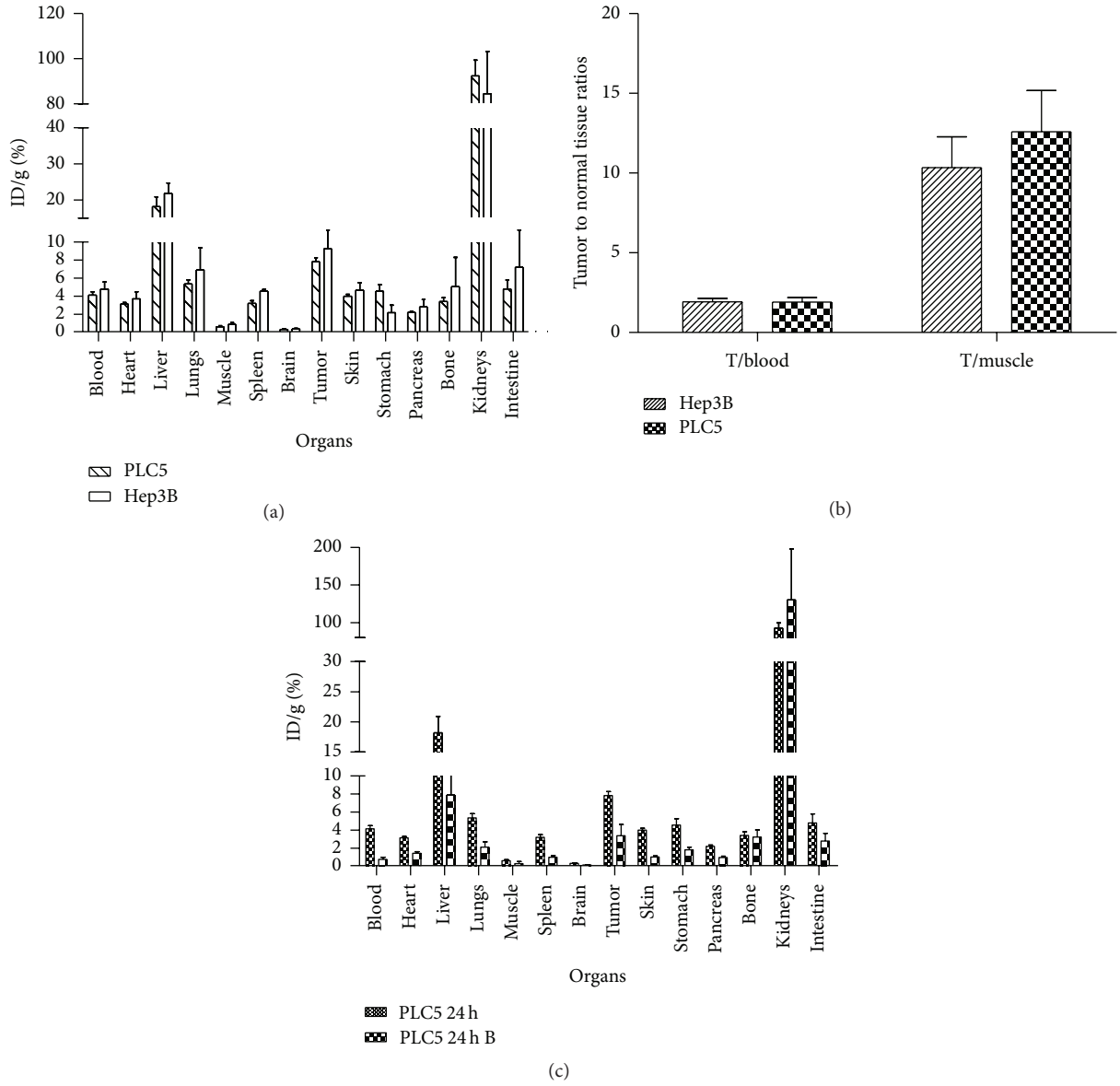

Figure 6: Biodistribution of ^{64}Cu-DOTA-$Z_{EGFR:1907}$ in nude mice bearing subcutaneous PLC/PRF/5 and Hep3B xenografts at 24 h. (a) Comparison of different organs in PLC/PRF/5 and Hep3B tumor-bearing animals after tail vein injection of ^{64}Cu-DOTA-$Z_{EGFR:1907}$ ($n = 3$). (b) Comparison of tumor-to-blood (T/blood) and tumor-to-muscle (T/muscle) ratios in Hep3B and PLC/PRF/5 tumors ($n = 3$). (c) Comparison of different organs in PLC/PRF/5 tumor-bearing animals with (represented as PLC5 24 h B in figure) and without (represented as PLC5 24 h in figure) coinjection of unlabeled Ac-Cys-$Z_{EGFR:1907}$ ($n = 3$).

7.9 ± 2.11% ($P < 0.05$). Radioactivity uptakes in the kidneys were unaffected by blocking.

4. Discussion

Our study reports the first use of an engineered, EGFR-targeted affibody molecule, Ac-Cys-$Z_{EGFR:1907}$, as a probe for the detection of human HCC lesions. Affibody molecules are small scaffold proteins that have recently emerged as a promising platform for molecular imaging and therapy in oncology. Several anti-EGFR affibodies with high binding affinity and specificity have been reported [24, 31]. Among them, Ac-Cys-$Z_{EGFR:1907}$ showed high specific binding to EGFR without cross-binding to other EGFR isoforms [24]. Earlier studies have reported the high tumor-specific uptake and good tumor-to-background ratio of the $Z_{EGFR:1907}$ affibody in EGFR-expressing A431 tumor xenografts using optical and PET imaging modalities [25]. High EGFR expression in a subset of HCC suggests that Ac-Cys-$Z_{EGFR:1907}$ may also be useful for the detection of HCC.

Indeed, fluorescently labeled Ac-Cys-$Z_{EGFR:1907}$ was able to specifically bind to and identify endogenous EGFR protein expressed in human HCC cell lines *in vitro*. Additionally, the expression of EGFR in subcutaneous xenografts generated from these cell lines corresponded with their expression *in vitro*, suggesting that Alexa680-$Z_{EGFR:1907}$ could be used

for detecting HCC xenografts derived from these cell lines. Surprisingly, when Alexa680-$Z_{EGFR:1907}$ was used in near-infrared fluorescence imaging of HCC xenografts, only PLC/PRF/5 tumors could be clearly visualized. Xenografts from Hep3B cells, which express even higher EGFR levels than that of PLC/PRF/5 cells, could not be delineated. This observation reveals a limitation of optical imaging, in that fluorescence signals may be blocked and/or absorbed by tumor tissues enriched with blood vessels, such as Hep3B xenografts (Figure 3(c)). However, when Ac-Cys-$Z_{EGFR:1907}$ based PET probe, ^{64}Cu-DOTA-$Z_{EGFR:1907}$, was used, both Hep3B and PLC/PRF/5 xenografts could be clearly imaged. The targeting specificity of the both optical and PET probes was further confirmed by coinjection of nonlabeled Ac-Cys-$Z_{EGFR:1907}$ into mice bearing EGFR-positive tumors. Furthermore, ^{64}Cu-DOTA-$Z_{EGFR:1907}$ was found to have good PET imaging quality and very similar biodistribution patterns in animals bearing Hep3B and PLC/PRF/5 xenografts. Therefore, PET imaging using ^{64}Cu-DOTA-$Z_{EGFR:1907}$ to target EGFR may be more useful than optical imaging using Alexa680-$Z_{EGFR:1907}$ in detecting the heterogeneous subtypes of HCC tumors.

During the course of our study, Sogawa et al. reported the use of a novel human monoclonal antibody against EGFR for HCC imaging [34], confirming the value of EGFR-based diagnostic imaging of HCC and highlighting the challenge of detecting HCC tumors *in vivo*. Since the liver is the major organ for drug/reagent clearance and metabolism, it can take up and even retain large amounts of imaging agents, giving rise to high background signals. Even though the enhanced permeability and retention (EPR) effect of the tumor (due to the leaky vasculature and lack of lymphatic drainage in the tumor) or receptor-mediated targeted uptake of imaging agents may facilitate probe accumulation in the tumor over other tissues [35], the liver background for nonspecific probe accumulation can still be high. Reducing the nonspecific liver accumulation continues to be a major obstacle in HCC imaging. Our previous studies and reports by other groups have found that affibodies were mainly cleared through the kidneys which showed high renal accumulation, with relatively lower liver uptake [24, 33, 36, 37]. Thus, it is advantageous to use affibody-based probes to image biomarkers expressed in HCC because of the preferred renal clearance. Our current data confirmed the higher renal uptakes of both affibody probes, although liver accumulations could also be detected (likely caused by the expression of basal levels of EGFR in normal liver tissue [38]). In PET quantitative analysis of ^{64}Cu-DOTA-$Z_{EGFR:1907}$ in both Hep3B and PLC/PRF/5 xenografts, probe uptake in the xenografts increased over time, while the uptake in normal liver decreased over time. Thus, it is reasonable to propose that introduction of a longer half-life radionuclide, which will allow imaging at later time points, may enhance the tumor-to-liver ratios, making it more clinically useful [39].

5. Conclusion

We have successfully demonstrated that EGFR-expressing HCC lesions can be specifically detected by using the EGFR-targeted affibody Ac-Cys-$Z_{EGFR:1907}$. In particular, *in vivo* PET imaging based on a modified version of this affibody appears to have greater diagnostic value than optical imaging based on the same affibody. The early and sensitive detection of HCC based on molecular cancer markers, such as EGFR, is a critical step in improving the currently dismal prognosis of HCC patients.

Conflict of Interests

The authors declare no conflict financial of interests.

Authors' Contribution

Ping Zhao and Xiaoyang Yang contributed equally to this work.

Acknowledgments

This work was supported, in part, by the DOE Stanford Molecular Imaging Research and Training Program (DE-SC0008397), Scientific Research Foundation of Jilin Province (20120706), National Cancer Institute (NCI) R01 CA128908-03, and NCI In Vivo Cellular Molecular Imaging Center (ICMIC) Grant P50 CA114747.

References

[1] J. M. Llovet, A. Burroughs, and J. Bruix, "Hepatocellular carcinoma," *The Lancet*, vol. 362, no. 9399, pp. 1907–1917, 2003.

[2] K. Okuda, "Hepatocellular carcinoma," *Journal of Hepatology*, vol. 32, no. 1, pp. 225–237, 2000.

[3] D. M. Parkin, P. Pisani, and J. Ferlay, "Global cancer statistics," *Ca: A Cancer Journal for Clinicians*, vol. 49, no. 1, pp. 33–64, 1999.

[4] J. Bruix and M. Sherman, "Management of hepatocellular carcinoma," *Hepatology*, vol. 42, no. 5, pp. 1208–1236, 2005.

[5] M. Capurro, I. R. Wanless, M. Sherman et al., "Glypican-3: a novel serum and histochemical marker for hepatocellular carcinoma," *Gastroenterology*, vol. 125, no. 1, pp. 89–97, 2003.

[6] N. N. Massarweh, J. O. Park, F. Farjah et al., "Trends in the utilization and impact of radiofrequency ablation for hepatocellular carcinoma," *Journal of the American College of Surgeons*, vol. 210, no. 4, pp. 441–448, 2010.

[7] M. A. Khan, C. S. Combs, E. M. Brunt et al., "Positron emission tomography scanning in the evaluation of hepatocellular carcinoma," *Journal of Hepatology*, vol. 32, no. 5, pp. 792–797, 2000.

[8] J. W. Park, H. K. Ji, K. K. Seok et al., "A prospective evaluation of 18F-FDG and 11C-acetate PET/CT for detection of primary and metastatic hepatocellular carcinoma," *Journal of Nuclear Medicine*, vol. 49, no. 12, pp. 1912–1921, 2008.

[9] M. Yun, S. H. Bang, W. K. Jae, Y. P. Jun, S. K. Kyoung, and D. L. Jong, "The importance of acetyl coenzyme A synthetase for 11C-acetate uptake and cell survival in hepatocellular carcinoma," *Journal of Nuclear Medicine*, vol. 50, no. 8, pp. 1222–1228, 2009.

[10] M. Yoshimoto, A. Waki, Y. Yonekura et al., "Characterization of acetate metabolism in tumor cells in relation to cell proliferation: acetate metabolism in tumor cells," *Nuclear Medicine and Biology*, vol. 28, no. 2, pp. 117–122, 2001.

[11] M. Daveau, M. Scotte, A. François et al., "Hepatocyte growth factor, transforming growth factor α, and their receptors as

combined markers of prognosis in hepatocellular carcinoma," *Molecular Carcinogenesis*, vol. 36, no. 3, pp. 130–141, 2003.

[12] H. Jiang, H. Wang, Z. Tan et al., "Growth suppression of human hepatocellular carcinoma xenografts by a monoclonal antibody CH12 directed to epidermal growth factor receptor variant III," *Journal of Biological Chemistry*, vol. 286, no. 7, pp. 5913–5920, 2011.

[13] K. de Bruin, N. Ruthardt, K. von Gersdorff et al., "Cellular dynamics of EGF receptor-targeted synthetic viruses," *Molecular Therapy*, vol. 15, no. 7, pp. 1297–1305, 2007.

[14] R. S. Herbst, "Review of epidermal growth factor receptor biology," *International Journal of Radiation Oncology Biology Physics*, vol. 59, no. 2, pp. 21–26, 2004.

[15] J. Lupberger, M. B. Zeisel, F. Xiao et al., "EGFR and EphA2 are host factors for hepatitis C virus entry and possible targets for antiviral therapy," *Nature Medicine*, vol. 17, no. 5, pp. 589–595, 2011.

[16] M. R. Schneider and E. Wolf, "The epidermal growth factor receptor ligands at a glance," *Journal of Cellular Physiology*, vol. 218, no. 3, pp. 460–466, 2009.

[17] J. Mendelsohn and J. Baselga, "Status of epidermal growth factor receptor antagonists in the biology and treatment of cancer," *Journal of Clinical Oncology*, vol. 21, no. 14, pp. 2787–2799, 2003.

[18] J. Schlessinger, "Cell signaling by receptor tyrosine kinases," *Cell*, vol. 103, no. 2, pp. 211–225, 2000.

[19] F. X. Real, W. J. Rettig, and P. G. Chesa, "Expression of epidermal growth factor receptor in human cultured cells and tissues: relationship to cell lineage and stage of differentiation," *Cancer Research*, vol. 46, no. 9, pp. 4726–4731, 1986.

[20] A. F. Buckley, L. J. Burgart, V. Sahai, and S. Kakar, "Epidermal growth factor receptor expression and gene copy number in conventional hepatocellular carcinoma," *American Journal of Clinical Pathology*, vol. 129, no. 2, pp. 245–251, 2008.

[21] L. A. DeCicco, J. Kong, and D. P. Ringer, "Carcinogen-induced alteration in liver epidermal growth factor receptor distribution during the promotion stage of hepatocarcinogenesis in rat," *Cancer Letters*, vol. 111, no. 1-2, pp. 149–156, 1997.

[22] S. Kira, T. Nakanishi, S. Suemori, M. Kitamoto, Y. Watanabe, and G. Kajiyama, "Expression of transforming growth factor alpha and epidermal growth factor receptor in human hepatocellular carcinoma," *Liver*, vol. 17, no. 4, pp. 177–182, 1997.

[23] E. Schiffer, C. Housset, W. Cacheux et al., "Gefitinib, an EGFR inhibitor, prevents hepatocellular carcinoma development in the rat liver with cirrhosis," *Hepatology*, vol. 41, no. 2, pp. 307–314, 2005.

[24] M. Friedman, E. Nordberg, I. Höidén-Guthenberg et al., "Phage display selection of Affibody molecules with specific binding to the extracellular domain of the epidermal growth factor receptor," *Protein Engineering, Design and Selection*, vol. 20, no. 4, pp. 189–199, 2007.

[25] J. Gao, K. Chen, Z. Miao et al., "Affibody-based nanoprobes for HER2-expressing cell and tumor imaging," *Biomaterials*, vol. 32, no. 8, pp. 2141–2148, 2011.

[26] S. Hoppmann, Z. Miao, S. Liu et al., "Radiolabeled affibody-albumin bioconjugates for HER2-positive cancer targeting," *Bioconjugate Chemistry*, vol. 22, no. 3, pp. 413–421, 2011.

[27] Z. Miao, G. Ren, H. Liu, S. Qi, S. Wu, and Z. Cheng, "PET of EGFR expression with an 18F-labeled affibody molecule," *Journal of Nuclear Medicine*, vol. 53, no. 7, pp. 1110–1118, 2012.

[28] S. Qi, Z. Miao, H. Liu, Y. Xu, Y. Feng, and Z. Cheng, "Evaluation of four affibody-based near-infrared fluorescent probes for optical imaging of epidermal growth factor receptor positive tumors," *Bioconjugate Chemistry*, vol. 23, no. 6, pp. 1149–1156, 2012.

[29] M. Yang, K. Cheng, S. Qi et al., "Affibody modified and radiolabeled gold-iron oxide hetero-nanostructures for tumor PET, optical and MR imaging," *Biomaterials*, vol. 34, no. 11, pp. 2796–2806, 2013.

[30] K. Nord, E. Gunneriusson, J. Ringdahl, S. Stahl, M. Uhlén, and P. A. Nygren, "Binding proteins selected from combinatorial libraries of an α-helical bacterial receptor domain," *Nature Biotechnology*, vol. 15, no. 8, pp. 772–777, 1997.

[31] M. Friedman, A. Orlova, E. Johansson et al., "Directed evolution to low nanomolar affinity of a tumor-targeting epidermal growth factor receptor-binding affibody molecule," *Journal of Molecular Biology*, vol. 376, no. 5, pp. 1388–1402, 2008.

[32] Z. Miao, J. Levi, and Z. Cheng, "Protein scaffold-based molecular probes for cancer molecular imaging," *Amino Acids*, vol. 41, no. 5, pp. 1037–1047, 2011.

[33] Z. Cheng, O. P. De Jesus, M. Namavari et al., "Small-animal PET imaging of human epidermal growth factor receptor type 2 expression with site-specific 18F-labeled protein scaffold molecules," *Journal of Nuclear Medicine*, vol. 49, no. 5, pp. 804–813, 2008.

[34] C. Sogawa, A. B. Tsuji, C. Yoshida et al., "Novel human monoclonal antibody against epidermal growth factor receptor as an imaging probe for hepatocellular carcinoma," *Nuclear Medicine Communications*, vol. 33, no. 7, pp. 719–725, 2012.

[35] H. Maeda, J. Wu, T. Sawa, Y. Matsumura, and K. Hori, "Tumor vascular permeability and the EPR effect in macromolecular therapeutics: a review," *Journal of Controlled Release*, vol. 65, no. 1-2, pp. 271–284, 2000.

[36] V. Tolmachev, A. Orlova, R. Pehrson et al., "Radionuclide therapy of HER2-positive microxenografts using a 177Lu-labeled HER2-specific affibody molecule," *Cancer Research*, vol. 67, no. 6, pp. 2773–2782, 2007.

[37] A. Orlova, J. Feldwisch, L. Abrahmsén, and V. Tolmachev, "Update: affibody molecules for molecular imaging and therapy for cancer," *Cancer Biotherapy and Radiopharmaceuticals*, vol. 22, no. 5, pp. 573–584, 2007.

[38] Z. Miao, G. Ren, H. Liu, L. Jiang, and Z. Cheng, "Small-animal PET imaging of human epidermal growth factor receptor positive tumor with a 64Cu labeled affibody protein," *Bioconjugate Chemistry*, vol. 21, no. 5, pp. 947–954, 2010.

[39] W. B. Nagengast, E. G. De Vries, G. A. Hospers et al., "In vivo VEGF imaging with radiolabeled bevacizumab in a human ovarian tumor xenograft," *Journal of Nuclear Medicine*, vol. 48, no. 8, pp. 1313–1319, 2007.